

## Additive Fabrication of Microsupercapacitors

Présentée le 28 août 2023

Faculté des sciences et techniques de l'ingénieur  
Laboratoire des technologies de fabrication avancées  
Programme doctoral en science et génie des matériaux

pour l'obtention du grade de Docteur ès Sciences

par

**Amin HODAEI**

Acceptée sur proposition du jury

Prof. D. Grundler, président du jury  
Prof. V. Subramanian, directeur de thèse  
Dr J. Heier, rapporteur  
Prof. J. Dutta, rapporteur  
Prof. J. Brugger, rapporteur



“Man’s search for meaning is the chief motivation of his life.”

–Viktor E. Frankl

To my family



# Acknowledgements

First and foremost, I would like to thank my advisor Prof. Vivek Subramanian for all his exceptional support throughout my PhD study. Vivek, you have truly helped me learn through all the challenges and grow scientifically. You gave me tremendous freedom in pursuit of my research objectives and taught me to think critically and beyond limitations. Words cannot express my heartfelt gratitude towards all your kind support in shaping me to who I have become. The positive impact you have created in my life will last forever.

I also would like to express my gratitude towards Prof. Dirk Grundler, Prof. Jürgen Brugger, Dr. Jakob Heier, and Prof. Joydeep Dutta to be the members of my thesis committee. I would like to specially thank Prof. Dirk Grundler for chairing the examination session and for all his kind support throughout the years of my PhD study as my academic mentor. Dirk, I am truly thankful to you for all the guidance and kind support you have shown to me since the first year of my PhD.

Besides, I would like to thank all my past and current lab members, colleagues, and friends from LAFT; Laurence, Annalies, Mohammed, Babak, Mustafa, Mengmeng, Jake, Sanjay, Sara, Jinhui, Biruktait, Kyle, Fatma, Tugce, and Claude. I am truly thankful for all your help you have been doing to me, and for all the fruitful scientific discussions we have had and also for all the time we have spent together in these years. I would also like to thank the LMTS lab—our immediate neighbors at the Microcity campus in Neuchâtel; Prof. Herbert Shea, Myriam, Morgan, Giulio, Silvia, Fabio, James, Robert, Nicolas, Jaemin, Florian, Valentin, Ronan, Edouard, Vito, Sylvain, Bekir, Danick, Djen, Mike, and Mehdi. I am truly thankful to you for all the nice quality time we have spent over the years together and also for all the support you showed to me when it came to using tools/machines at your lab. I would like to specially thank Prof. Herbert Shea for being a member of my candidacy exam committee and also the follow-up annual report presentations throughout my PhD years. Herb, I am so much thankful to you for having been guiding me with your feedback and support in the last years.

I also would like to thank my friends, Samuel Youcef Benketaf, Ernesto Gribaudo, and Hubert Schneegans for being great movie and outing buddies. I also would like to express my heartfelt acknowledgement to Mr. Peter Giesinger who have been a great source of support for me out

of EPFL. Peter, you have been truly like my grandfather. You helped me settle in my new place in St-Sulpice and have been always there for me when I needed help. You are really an amazing human that deserves all the good in life. Words cannot express how much thankful to you I am for all the pure support you have shown to me. I am honored to have known you and have been able to learn from you all these years. Your sense of humor, cooking style, and taste in art, specially, painting are awesome. You truly changed me to be a better person.

I also would like to acknowledge the scientists and technical collaborators at EPFL who tremendously helped me progress my research— Dr. Rita Therisod, Dr. Mounir Mensi, Albert Taureg, Yann Lavanchy, Wen Hua (David) Bi, and Aurélien Bornet. I am so much thankful to you for all the support you showed to me.

I would also like to thank all my close and far family members, and all my other friends including, Amirmohammad, Ali, Mehdi, Mahshid, and Hengameh who have always supported me.

Last but not least, I would like to thank my dearest parents who did all the best for me throughout my life. You believed in me from the beginning and showed me pure love in every moments of my life. For sure, I cannot thank you enough for even the slightest things you have done for me. I also would like to thank my lovely sister for always having been there for me. I love you from the bottom of my heart. I also would like to thank my nephew, Behrad, who since being born three years ago, has made my life much sweeter. Thank you, Behrad, for talking with me every time you learn a new word.



# Abstract

Microsupercapacitors (with footprints from -mm up to -cm scale) have attracted attention for use as electrochemical energy storage devices to power wearables, IoT, and other small microsystems due to their high power density, excellent charge/discharge reversibility, and long cycle stability. Additive fabrication, with its spatial accuracy and versatile material manipulation capabilities will facilitate easy integration of these devices into a range of ubiquitous microsystem platforms.

This thesis demonstrates the additive fabrication of hybrid microsupercapacitors, which simultaneously, benefit from electrical double-layer capacitance (EDLC) and pseudocapacitance charge storage mechanisms. We have been able to elucidate the charge storage mechanism contributions of the microsupercapacitors, which are found to be dependent on the composition of the electrode and electrolytes. For the first time, this thesis reports the complete integration of such a microsupercapacitor through additive fabrication, including all component layers and encapsulation. We report on several novel materials, including electrodes based on edge-oxide graphene oxide (EOGO)/Cerium Oxide nanocomposites) and electrolytes based on (poly (ethylene glycol) diacrylate (PEGDA) + LiCl + lithium phenyl-2,4,6-trimethylbenzoylphosphinate (LAP). Our results show that, through optimization of all component structures within a microsupercapacitor, it is possible to realize unprecedented levels of performance. We systematically study the dimensional scaling of the microsupercapacitors in the sub-mm<sup>3</sup> range and investigate how this scaling affects the performance of the microsupercapacitors.

The research outcomes of this thesis include realization of the smallest microsupercapacitors that are fully additively fabricated reported to date, with the highest levels of observed performance. We report on scaling behavior in these devices for the first time as well. Thus, this thesis provides important steps towards realization of additive fabrication of high-performance microsupercapacitors for embedded energy applications.

**Keywords:** microsupercapacitors, additive fabrication, 3D printing, dimensional scaling, edge-oxidized graphite oxide (EOGO), cerium oxide



# Résumé

Les microsupercondensateurs (avec des empreintes allant de  $\mu\text{m}$  à  $\text{cm}$ ) ont attiré l'attention pour être utilisés comme dispositifs de stockage d'énergie électrochimique pour alimenter les appareils portables, l'IoT et d'autres petits microsystèmes en raison de leur densité de puissance élevée, de leur excellente réversibilité charge/décharge et de leur stabilité à long cycle. La fabrication additive, avec sa précision spatiale et ses capacités de manipulation de matériaux polyvalentes, facilitera l'intégration de ces dispositifs dans une gamme de plateformes de microsystèmes omniprésentes.

Cette thèse démontre la fabrication additive de microsupercondensateurs hybrides, qui bénéficient à la fois de capacités électriques à double couche (EDLC) et de mécanismes de stockage de charge de pseudocapacité. Nous avons pu élucider les contributions des mécanismes de stockage de charge des microsupercondensateurs, qui se révèlent dépendantes de la composition de l'électrode et des électrolytes. Pour la première fois, cette thèse rapporte l'intégration complète d'un tel microsupercondensateur par fabrication additive, y compris toutes les couches de composants et l'encapsulation. Nous rapportons plusieurs nouveaux matériaux, y compris des électrodes à base d'oxyde de graphène (EOGO)/nanocomposites d'oxyde de cérium) et des électrolytes à base de (diacrylate de poly (éthylène glycol) (PEGDA) + LiCl + lithium phényl-2,4,6- triméthylbenzoylphosphinate (LAP). Nos résultats montrent que, grâce à l'optimisation de toutes les structures de composants dans un microsupercondensateur, il est possible d'atteindre des niveaux de performance sans précédent. Nous étudions systématiquement la mise à l'échelle dimensionnelle des microsupercondensateurs dans la gamme inférieure au  $\text{mm}^3$  et étudions comment cette mise à l'échelle affecte les performances des microsupercondensateurs.

Les résultats de recherche de cette thèse incluent la réalisation des plus petits microsupercondensateurs entièrement fabriqués de manière additive signalés à ce jour, avec les niveaux de performance observés les plus élevés. Nous rapportons également pour la première fois le comportement de mise à l'échelle de ces appareils. Ainsi, cette thèse fournit des étapes importantes vers la réalisation de la fabrication additive de microsupercondensateurs hautes performances pour des applications énergétiques embarquées.

**Mots-clés:** microsupercondensateurs, fabrication additive, impression 3D, mise à l'échelle dimensionnelle, oxyde de graphite oxydé par les bords (EOGO), oxyde de cérium



# List of Figures

|  |    |
|--|----|
| <b>Figure 1.1.</b> Historic timeline for the development of supercapacitors (EC in the figure refers to electrochemical capacitors, which are also called supercapacitors). Adapted from [3].....  | 1  |
| <b>Figure 1.2.</b> Schematic of charge storage mechanisms: (a) electrochemical double-layer capacitance (EDLC) and (b) pseudocapacitance. Adapted from [11].....   | 3  |
| <b>Figure 1.3.</b> Different categories of supercapacitors based on their materials of electrodes and their respective charge storage mechanism. Adapted from [12].....  | 4  |
| <b>Figure 1.4.</b> Different categories of the electrolytes for supercapacitor. Adapted from [111].....  | 7  |
| <b>Figure 1.5.</b> Components of typical electrochemical energy storage systems such as supercapacitors, namely, current collectors, electrodes, electrolyte/separator, and casing/packaging. Adapted from [14].....   | 10 |
| <b>Figure 1.6.</b> Ragone plot demonstrating the differences of specific energy and specific power of batteries and supercapacitors. The start shows the target of the research community for advancing the specific energy and power of these devices (the diagonal dotted lines and timescales represent characteristic operation timescales, obtained by dividing the energy by the power). Adapted from [9]..... | 15 |
| <b>Figure 2.1.</b> Different configurations of microsupercapacitors, left: stacked, right: planar. Adapted from [199].....   | 19 |
| <b>Figure 2.2.</b> Fabrication of a microsupercapacitor through a photolithographic process. Adapted from [210].....   | 21 |
| <b>Figure 2.3.</b> Fabrication of microsupercapacitors by laser processing. Adapted from [221].....  | 22 |

**Figure 2.4.** Exhibition of the plasma jet etching fabrication of a microsupercapacitor. Adapted from [222].....23

**Figure 2.5.** Fabrication of microsupercapacitors using the stamping technique. Adapted from [226].....24

**Figure 2.6.** An example of screen printed microsupercapacitor. Adapted from [185].....25

**Figure 2.7.** Schematics showing the gravure printing process. Adapted from [233].....26

**Figure 2.8.** An example of gravure printed microsupercapacitors. Adapted from [236].....26

**Figure 2.9.** Spray printing process in combination with laser processing (scribing) for fabrication of microsupercapacitors. Adapted from [240].....27

**Figure 2.10.** Schematic representation of FDM printed electrodes of microsupercapacitors. Adapted from [245].....28

**Figure 2.11.** An example of inkjet printing of microsupercapacitors. Scale bars, 500 mm. Adapted from [253].....29

**Figure 2.12.** Demonstration of the principles of extrusion-based 3D printing—three different types of barrels and the mechanisms of extrusion of the inks (pastes), namely, pneumatic, piston-driven and screw-driven, and extrusion of the ink out of the nozzles, and subsequent deposition of the ink on a target substrate. Adapted from [256].....30

**Figure 2.13.** An example of a microsupercapacitor fabricated by extrusion-based 3D printing. Adapted from [181].....31

**Figure 2.14.** Rheological properties: a) viscosity as a function of shear rate, demonstrating shear thinning behavior, and b) oscillatory behavior of the ink showing the storage modulus ( $G'$ ) and loss modulus ( $G''$ ) of the ink and the intersection of them representing the yield stress

of an ink used for extrusion-based 3D printing of microsupercapacitors. Adapted from [275].....35

**Figure 2.15.** Layer thickness and printing resolution as a function of ink viscosity attained by different printing techniques. Adapted from [235].....35

**Figure 3.1.** Schematic of the fabrication procedure of the microsupercapacitors, A) 3D printing (extrusion-based) of the silver current collectors on a wet-oxidized silicon wafer and heat treatment of the current collectors, B) 3D printing of the package using PCL through fused deposition modeling (FDM) printing, C) 3D printing (extrusion-based) the electrodes on the current collectors (inside the package), D) Deposition of UV-curable electrolytes inside the package and immersing the electrodes and UV curing the electrolyte, E) Deposition of an encapsulant on top of the UV-cured electrolyte and subsequently UV curing it, F) An image of one of our fully-fabricated microsupercapacitors (top view), G) An image of a fully-fabricated microsupercapacitor (the same as in (F)) (side view).....41

**Figure 3.2.** A) Sheet resistance of the silver paste used for the current collector fabrication as a function of heat treatment temperature and duration in air, B) current collectors fabricated via extrusion-based 3D printing of the silver paste; these were subsequently heat treated at 450 °C for 10 minutes.....43

**Figure 3.3.** MSCs before encapsulation, A) A fabricated MSC only waiting for the encapsulation step, B) the same MSC after 1 hour resting in ambient conditions. As it can be seen, there is no leakage of the electrolyte to outside over time, however, the electrolyte started to face evaporation and shrinkage although being UV-cured (the red arrows show surfacing of the electrodes due to evaporation of the electrolyte solvent (see the red circles).....44

**Figure 3.4.** Effect of A) UV curing duration of the electrolyte and B) Electrolyte LiCl concentration, and C) the UV curing duration of the encapsulant on the areal capacitance of the MSCs all as a function loading of ceria NPs in the electrode.....46

**Figure 3.5.** Microstructural characterization of EOGO precursor the we used as one of the components in formulating the electrode inks, A) XRD pattern, B) Raman spectroscopy data, C) XPS results showing the c1s region and the deconvoluted peaks after fitting, D) contribution of different bonds that the carbon atoms form in EOGO, TEM images of the EOGO E) showing their size and morphology, and F) the edges of the stacked graphene layers.....49

**Figure 3.6.** A) XRD patterns of the bare EOGO, 5 wt.% ceria loaded electrode, and 32 wt.% ceria loaded electrode (the ceria containing electrodes were dried in air at room temperature), TEM images of B) 32 wt.% ceria loaded electrode, and C) 5 wt.% ceria loaded electrode; rheological characterizations of 5 wt.% ceria loaded, and 32 wt.% ceria loaded electrode inks, D) viscosity as a function of shear rate, and E) oscillation amplitude measurements determining the storage ( $G'$ ) and loss ( $G''$ ) moduli of the inks.....51

**Figure 3.7.** Electrochemical characterization of the microsupercapacitors: A) CV curves at the scan rate 5 mV/s, B) areal capacitances of the microsupercapacitors as a function of ceria NPs loading at the scan rate of 5 mV/s, C) GCD curves of the microsupercapacitors at a current density of 1.42 mA/cm<sup>2</sup>, TEM images of D) 5 wt.% ceria-containing electrodes—inset shows higher magnification of the same image, and E) 32 wt.% ceria-containing electrode—inset exhibits higher magnification of the same image, F) Specific surface area measurements as a function ceria NPs loading, G) The ratio of Ce<sup>3+</sup>/Ce<sup>4+</sup> oxidation states in the electrodes with varying concentrations of ceria NPs, H) kinetic analysis on the charge storage of the MSCs comprising electrodes with varying amounts of ceria NPs to investigate the contributions of electrical double layer capacitance (EDLC), diffusive mechanisms.....54

**Figure 3.8.** Electrochemical characterization of the best performing microsupercapacitor (5 wt.% ceria-containing electrode), A) CV curves at different scan rates (2 mVs<sup>-1</sup> to 100 mVs<sup>-1</sup>), B) GCD curves at different current densities (1.43 mAcm<sup>-2</sup> to 5.72 mAcm<sup>-2</sup>), C) areal and volumetric capacitance values as a function of scan rate (2 mVs<sup>-1</sup> to 100 mVs<sup>-1</sup>), D) EIS data—the inset shows the high-frequency region in more details, E) comparison of the cyclic life and areal capacitance values of a selected number of microsupercapacitors with respect to their active charge storage area (i.e., electrode) and our system, F) the Ragone plot showing the energy and power densities of some of the selected system as shown in part (E) including our

result, G) cyclic life of our system—the inset demonstrates the GCD curves of the first and the last cycles, H) X-ray tomography images of the fully-fabricated microsupercapacitor—the insets are two cross-section images showing the different components of the system with their geometrical dimensions.....57

**Figure 3.9.** Thermogravimetric analysis (TGA) plots of all the electrode active materials.....62

**Figure 3.10.** TGA and DSC curves of the silver paste used for 3D printing of the current collector. A peak in the DSC plot is gradually formed from temperatures around 300 °C that extends up to 570 °C.....63

**Figure 3.11.** A) a TEM image, B) EDX elemental maps, and C) EDX spectrum of the electrode containing 3 wt.% ceria NPs.....65

**Figure 3.12.** A) a TEM image, B) EDX elemental maps, and C) EDX spectrum of the electrode containing 5 wt.% ceria NPs.....66

**Figure 3.13.** A) a TEM image, B) EDX elemental maps, and C) EDX spectrum of the electrode containing 9 wt.% ceria NPs.....67

**Figure 3.14.** A) a TEM image, B) EDX elemental maps, and C) EDX spectrum of the electrode containing 22 wt.% ceria NPs.....68

**Figure 3.15.** A) a TEM image, B) EDX elemental maps, and C) EDX spectrum of the electrode containing 32 wt.% ceria NPs.....69

**Figure 3.16.** N<sub>2</sub> adsorption isotherms of all the electrode materials.....71

**Figure 3.17.** Deconvoluted Ce 3d region of XPS spectra of the electrode materials in high resolution, A) 3 wt.% ceria NPs, B) 5 wt.% ceria NPs, C) 9 wt.% ceria NPs, D) 22 wt.% ceria NPs, E) 32 wt.% ceria NPs.....73



**Figure 3.18.** XRD patterns of all the electrode materials showing the assigned peaks of EOGO and ceria.....75

**Figure 3.19.** Determination of the active area of the MSCs used in the calculations of areal capacitance, area energy density and areal power density. The image shows a fully 3D printed MSC just before the deposition and subsequent UV curing of the encapsulant.....77

**Figure 3.20.** The plots of A)  $C_A$  vs.  $u^{-0.5}$  and B)  $C_A^{-1}$  vs.  $u^{0.5}$  of the MSC constructed by the electrode containing no ceria and the optimum electrolyte composition.....79

**Figure 3.21.** The plots of A)  $C_A$  vs.  $u^{-0.5}$  and B)  $C_A^{-1}$  vs.  $u^{0.5}$  of the MSC constructed by the electrode containing 3 wt.% ceria and the optimum electrolyte composition.....79

**Figure 3.22.** The plots of A)  $C_A$  vs.  $u^{-0.5}$  and B)  $C_A^{-1}$  vs.  $u^{0.5}$  of the MSC constructed by the electrode containing 5 wt.% ceria and the optimum electrolyte composition.....80

**Figure 3.23.** The plots of A)  $C_A$  vs.  $u^{-0.5}$  and B)  $C_A^{-1}$  vs.  $u^{0.5}$  of the MSC constructed by the electrode containing 9 wt.% ceria and the optimum electrolyte composition.....80

**Figure 3.24.** The plots of A)  $C_A$  vs.  $u^{-0.5}$  and B)  $C_A^{-1}$  vs.  $u^{0.5}$  of the MSC constructed by the electrode containing 22 wt.% ceria and the optimum electrolyte composition.....81

**Figure 3.25.** The plots of A)  $C_A$  vs.  $u^{-0.5}$  and B)  $C_A^{-1}$  vs.  $u^{0.5}$  of the MSC constructed by the electrode containing 32 wt.% ceria and the optimum electrolyte composition.....81

**Figure 4.1.** The Schematics of the fabrication steps of the microsupercapacitors, A) Extrusion-based 3D printing the current collectors on a wet-oxidized silicon wafer using a silver paste and subsequently, heat treating the current collectors, B) FDM printing of the package using PCL, C) Extrusion-based 3D printing of the electrodes on the current collectors (inside the package space), D) Deposition of UV-curable electrolytes inside the package to immerse the electrodes and subsequently, UV curing the electrolyte, E) Deposition of an encapsulant on top of the UV-cured electrolyte and subsequently UV curing it, F) Illustration of the design of

dimensional scaling of the microsupercapacitors by changing the diameter of the nozzles used to 3D print the electrodes with different lengths, G) A top view image of one of the fully 3D printed microsupercapacitors (nozzle diameter of 510  $\mu\text{m}$  and electrode length of 2.5 mm), and H) A side view image the same fully 3D printed microsupercapacitor as in (G) scale bars are 500  $\mu\text{m}$ .....87

**Figure 4.2.** A) XRD characterization of the bare EOGO powder and the air-dried electrode ink comprising 5 wt.% ceria nanoparticles, rheological characterizations of the aqueous electrodes ink (EOGO/ceria nanocomposite — 5 wt.% ceria nanoparticles) B) viscosity as a function of shear rate, C) oscillation measurement demonstrating the storage modulus ( $G'$ ) and the loss modulus ( $G''$ ) of the same ink as a function of oscillation stress, and D) TEM images of the air-dried electrodes, the same used for XRD characterization as shown in (A).....89

**Figure 4.3.** Galvanostatic charge discharge diagrams of the additively fabricated MSCs as a function of electrode length and the nozzle diameter with which the electrodes are printed, A) nozzle diameter: 250  $\mu\text{m}$ , B) nozzle diameter: 330  $\mu\text{m}$ , C) nozzle diameter: 510  $\mu\text{m}$ , D) nozzle diameter: 840  $\mu\text{m}$ .....91

**Figure 4.4.** Capacitance (non-normalized per area or volume) of all the MSCs as a function of their electrode length and the diameter of the nozzle used for printing them.....92

**Figure 4.5.** A) Capacitance (non-normalized per area or volume) of the MSCs as a function of the electrode length and thickness, B) the ESR values of the MSCs, C) kinetic study of charge storage of two of the fabricated MSCs with 2.5 mm long electrodes printed with the smallest (i.e., 250  $\mu\text{m}$ ) and the largest (i.e., 840  $\mu\text{m}$ ) nozzles, D) cyclic life the MSC possessing 3.75 mm long electrodes printed with a 840  $\mu\text{m}$  nozzle.....94

**Figure 4.6.** CV curves of the MSCs with an electrode length of 3.75 mm and printed with a nozzle diameter of A) 250  $\mu\text{m}$ , and B) 840  $\mu\text{m}$ , and GCD curves with an electrode length of 3.75 mm and printed with a nozzle diameter of C) 250  $\mu\text{m}$ , and D) 840  $\mu\text{m}$ , and areal and volumetric capacitance values of the MSCS (as a function of scan rates used in CV measurements) with an

electrode length of 3.75 mm and printed with a nozzle diameter of E) 250  $\mu\text{m}$ , and F) 840  $\mu\text{m}$ .....97

**Figure 4.7.** Ragone plot exhibiting areal energy and power densities of our microsupercapacitors possessing an electrode length of 3.75 and printed with a nozzle diameter of 250  $\mu\text{m}$  and 840  $\mu\text{m}$  in comparison with some of the selected examples of printed MSCs from literature.....99

**Figure 4.8.** The geometrical details of the design of the current collectors of the MSC with the sample ID XS1.....102

**Figure 4.9.** The geometrical details of the design of the current collectors of the MSC with the sample ID XS2.....102

**Figure 4.10.** The geometrical details of the design of the current collectors of the MSC with the sample ID XS3.....103

**Figure 4.11.** The geometrical details of the design of the current collectors of the MSC with the sample ID S1.....103

**Figure 4.12.** The geometrical details of the design of the current collectors of the MSC with the sample ID S2.....104

**Figure 4.13.** The geometrical details of the design of the current collectors of the MSC with the sample ID S3.....104

**Figure 4.14.** The geometrical details of the design of the current collectors of the MSC with the sample ID M1.....105

**Figure 4.15.** The geometrical details of the design of the current collectors of the MSC with the sample ID M2.....105

**Figure 4.16.** The geometrical details of the design of the current collectors of the MSC with the sample ID M3.....106

**Figure 4.17.** The geometrical details of the design of the current collectors of the MSC with the sample ID L1.....106

**Figure 4.18.** The geometrical details of the design of the current collectors of the MSC with the sample ID L2.....107

**Figure 4.19.** The geometrical details of the design of the current collectors of the MSC with the sample ID L3.....107

**Figure 4.20.** The plots of A)  $C_A$  vs.  $u^{-0.5}$  and B)  $C_A^{-1}$  vs.  $u^{0.5}$  of the microsupercapacitor constructed by the electrode with the length of 3.75 mm, which is printed with a nozzle of diameter 250  $\mu\text{m}$ .....109

**Figure 4.21.** The plots of A)  $C_A$  vs.  $u^{-0.5}$  and B)  $C_A^{-1}$  vs.  $u^{0.5}$  of the microsupercapacitor constructed by the electrode with the length of 3.75 mm, which is printed with a nozzle of diameter 840  $\mu\text{m}$ .....109





## List of Tables

|   |     |
|---|-----|
| <b>Table 3.1.</b> Proportion of the precursors used in the synthesis of electrode materials with varying Ceria NPs concentrations.....                                    | 59  |
| <b>Table 3.2.</b> Ceria NPs concentrations of different electrode materials determined by TGA.....  | 62  |
| <b>Table 3.3.</b> Assignment of Ce oxidation state associated with deconvoluted peaks in the Ce 3d region of XPS spectra of the electrode materials.....                  | 74  |
| <b>Table 3.4.</b> The contribution of fast-kinetic and slow-kinetic processes involved in the charge storage of the electrodes as a function their ceria NPs loading..... | 82  |
| <b>Table 4.1.</b> The IDs of the 3D printed microsupercapacitors and their related geometrical feature dimensions.....  | 101 |





# Contents

|                              |      |
|------------------------------|------|
| <b>Acknowledgement</b> ..... | V    |
| <b>Abstract</b> .....        | VIII |
| <b>Résumé</b> .....          | IX   |
| <b>List of Figures</b> ..... | XII  |
| <b>List of Tables</b> .....  | XXII |

## Chapter 1. Introduction

|  |    |
|--|----|
| 1.1. Supercapacitors as energy storage devices.....                              | 1  |
| 1.2. Different types of supercapacitors and their charge storage mechanisms..... | 2  |
| 1.3. Components of supercapacitors.....  | 4  |
| 1.3.1. Electrodes.....   | 4  |
| 1.3.2. Electrolyte and separator.....  | 6  |
| 1.3.3. Current collector.....  | 9  |
| 1.3.4. Casing/packaging.....   | 9  |
| 1.4. Performance metrics of supercapacitors.....                                 | 10 |
| 1.5. Supercapacitors vs. Batteries.....  | 14 |

## Chapter 2. Fabrication of microsupercapacitors

|   |    |
|---|----|
| 2.1. Background on microsupercapacitors.....                                  | 18 |
| 2.2. Fabrication techniques of microsupercapacitors.....                      | 19 |
| 2.3. Rheological characteristics of the inks for 3D printing.....             | 31 |
| 2.4. Challenges and opportunities in fabrication of microsupercapacitors..... | 36 |

## Chapter 3. Additive Fabrication of High-Performance Millimeter-Scale Microsupercapacitors: Fine-Tuning Chemistry to Maximize Performance

|   |    |
|---|----|
| 3.1. Introduction.....  | 39 |
| 3.2. Fabrication and Characterization of microsupercapacitors ..... | 39 |
| 3.2.1. Fabrication of Microsupercapacitors.....                     | 39 |
| 3.2.2. Component Structures of the Microsupercapacitors.....        | 42 |
| 3.2.3. Fabrication of the current collectors.....                   | 42 |



|  |    |
|--|----|
| 3.2.4. Fabrication of the package walls.....   | 43 |
| 3.2.5. Selection of the electrolyte, the encapsulant and their UV curing conditions..... | 44 |
| 3.2.6. Optimization of electrode active materials.....                                   | 47 |
| 3.2.7. Realization of microsupercapacitors with optimal performance.....                 | 55 |
| 3.3. Materials and Methods.....  | 58 |
| 3.3.1. Chemicals.....  | 58 |
| 3.3.2. Synthesis of edge-oxidized graphite oxide (EOGO)/ceria nanocomposites...          | 58 |
| 3.3.3. Preparation of the UV-curable electrolytes.....                                   | 59 |
| 3.3.4. 3D printing of the microsupercapacitors.....                                      | 59 |
| 3.3.5. Characterizations methods.....  | 61 |
| 3.3.6. Electrochemical performance calculations.....                                     | 76 |
| 3.3.7. Kinetic study of charge storage mechanisms.....                                   | 77 |
| 3.4. Conclusions.....  | 82 |

## **Chapter 4. Sub-mm<sup>3</sup> Dimensional Scaling of High-Performance Additively-Fabricated Microsupercapacitors**

|   |     |
|---|-----|
| 4.1. Introduction.....  | 85  |
| 4.2. Fabrication, scaling procedures, and characterization.....                         | 85  |
| 4.2.1. Fabrication of microsupercapacitors and designing their dimensional scaling..... | 85  |
| 4.2.2. Chemistries of the components of the microsupercapacitors.....                   | 88  |
| 4.2.3. Performance evaluation of the fabricated microsupercapacitors.....               | 90  |
| 4.3. Materials and Methods.....   | 100 |
| 4.3.1. Details of dimensional scaling of the microsupercapacitors.....                  | 100 |
| 4.3.2. Electrochemical performance calculations.....                                    | 108 |
| 4.3.3. Kinetic study of charge storage mechanisms.....                                  | 108 |
| 4.4. Conclusions.....   | 110 |

## **Chapter 5. Conclusions and Outlook**

|                                       |     |
|---------------------------------------|-----|
| 5.1. Key outcomes of the thesis ..... | 112 |
| 5.2. Discussion of future work.....   | 115 |

|                          |            |
|--------------------------|------------|
| <b>Bibliography.....</b> | <b>119</b> |
|--------------------------|------------|

|                             |            |
|-----------------------------|------------|
| <b>Curriculum Vitæ.....</b> | <b>140</b> |
|-----------------------------|------------|



# 1. Introduction

## 1.1. Supercapacitors as energy storage devices

Powering internet of things (IoT), wearables, and future electronic systems necessitates designing energy storage devices that can fulfill the energy and power requirements of such systems[1]. Supercapacitors are ideal energy storage devices to supply the power needs of these systems. Moreover, when supercapacitors are coupled with other energy storage devices, such as batteries and solar cells, they can complement the performance limitations of those devices in IoT, wearables, or other microelectronic applications. By definition, supercapacitors (also called electrochemical capacitors) are electrochemical energy storage devices that store energy at the interface of electrodes and an electrolyte [2]. Historically, the first example of a capacitor emerged as early as 18<sup>th</sup> century with the invention of the “Leyden jar”, which was constructed of two pieces of metal foil, water, and a conductive chain inside a glass jar [3]. Since then, research on the development of supercapacitors and understanding their working principles and mechanisms have continued (as shown in Figure 1.1).

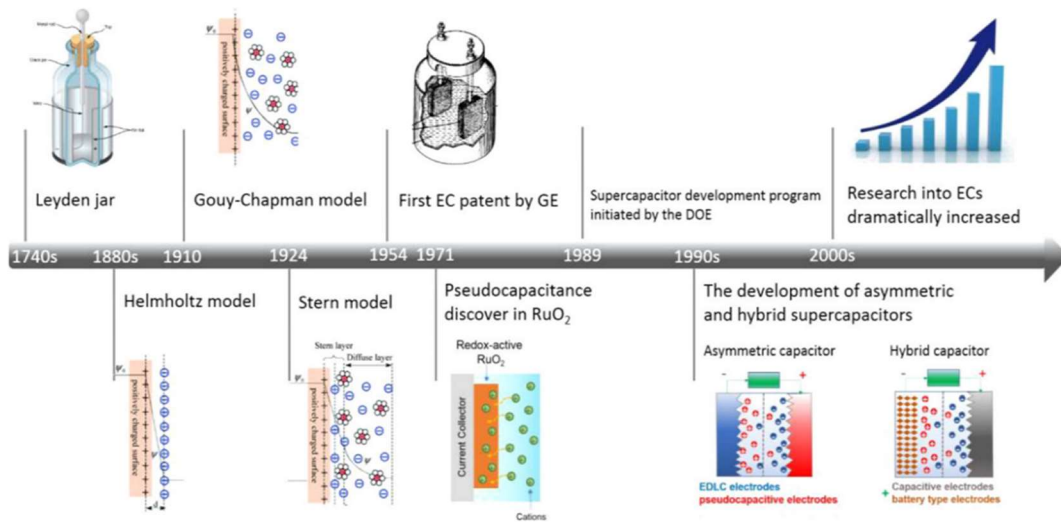


Figure 1.1. Historic timeline for the development of supercapacitors (EC in the figure refers to electrochemical capacitors, which are also called supercapacitors). Adapted from [3].

The developmental history of supercapacitors is intertwined with the story of discovering charge storage mechanisms, which resulted in the emergence of models describing these mechanisms—in chronological order, by Helmholtz [4], Gouy [5], Chapman [6], Stern [7], and

Grahame[8]. In the last decades, extensive research has been devoted to development of novel materials systems to improve the performance of supercapacitors and to advance our understanding of their working mechanisms.

In the upcoming sections of this chapter, we will discuss different types of supercapacitors and their charge storage mechanisms, the components of supercapacitors and the materials of construction for the components, the performance metrics of supercapacitors, and also how supercapacitors compare to batteries.

### **1.2. Different types of supercapacitors and their charge storage mechanisms**

Based on their charge storage mechanism, supercapacitors are grouped into three categories: i) electrochemical double-layer capacitors (EDLC), ii) pseudocapacitors, iii) hybrid supercapacitors that combine the EDLC and pseudocapacitive mechanisms [9]. EDLC capacitors store charge based on electrostatic charge separation at the interface of the electrodes and the electrolyte (non-Faradaic), pseudocapacitors store charge electrochemically through Faradaic reactions (through redox reactions) at the interface between the electrodes and the electrolyte, and hybrid supercapacitors synergistically benefit from both of these two charge storage mechanisms as they combine EDLC and pseudocapacitance [10]. Figure 1.2 schematically demonstrates the process of charge storage in EDLC and pseudocapacitance mechanisms.

## Chapter 1

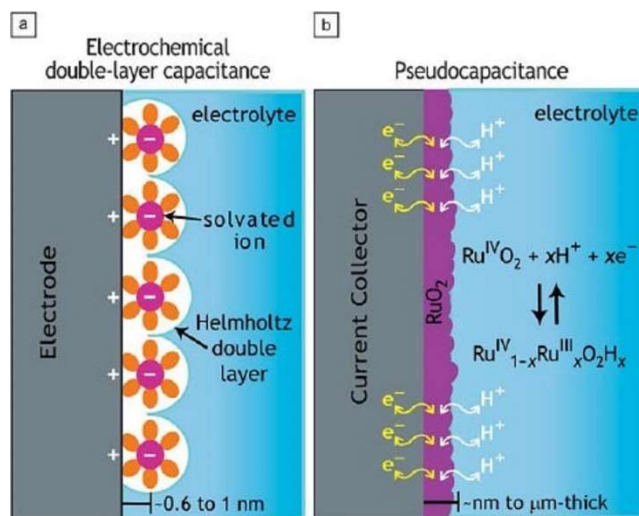


Figure 1.2. Schematic of charge storage mechanisms: (a) electrochemical double-layer capacitance (EDLC) and (b) pseudocapacitance. Adapted from [11]

Determination of the charge storage mechanism in a supercapacitor is usually done based on their active electrode materials (see Figure 1.3.). The EDLC mechanism is typically observed in carbonaceous materials such as, graphene, carbon nanotubes, and activated carbon, etc., due to their high specific surface areas. EDLC happens as a result of electrostatic charge separation at the interface of electrode/electrolyte. Moreover, the EDLC mechanism does not involve any charge transfer among species of the system. Since it is purely an electrostatic charge separation process, the higher the surface area, the easier the EDLC formation. This is why, it predominantly occurs in carbonaceous materials. On the other hand, pseudocapacitance is observed in conductive polymers, metal oxide/carbides/nitrides, etc. where charge transfer occurs among the species of the system at the interface of electrode/electrolyte (i.e., it is not an electrostatic charge separation process). These charge transfer reactions are Faradaic reactions in nature where electron transfer causes redox reaction (i.e., oxidation/reduction reactions) to take place. When these two categories of materials, and subsequently, these two charge storage mechanisms are combined, the resultant supercapacitor is designated as a hybrid supercapacitor[12]. The main reason behind formulation of these hybrid systems is to benefit from both EDLC and pseudocapacitive charge storage mechanisms synergistically[13].

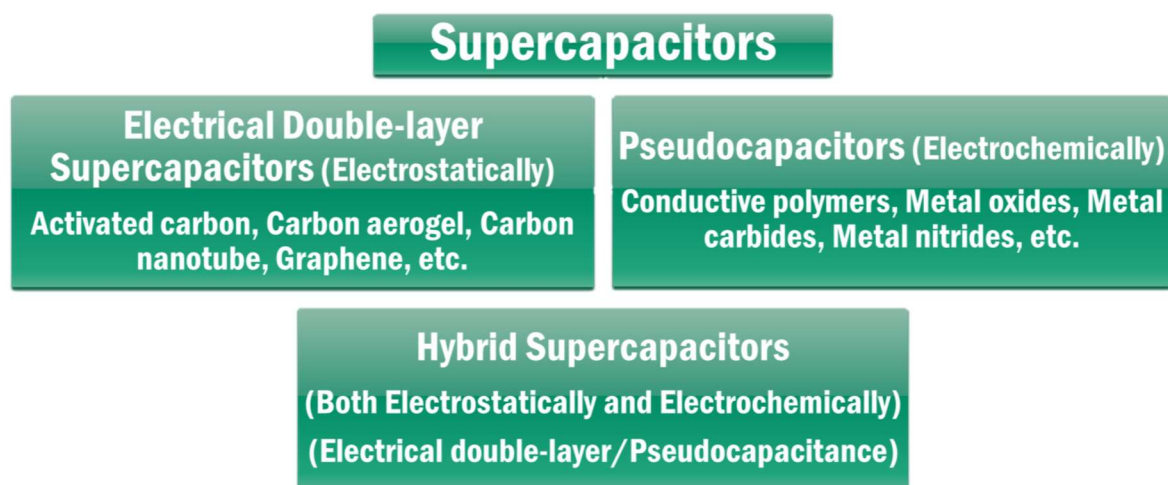


Figure 1.3. Different categories of supercapacitors based on their materials of electrodes and their respective charge storage mechanism. Adapted from [12]

To this end, design and synthesis of novel classes of (nano)-composite structures which deliver both EDLC and pseudocapacitance (as a hybrid system) has been one of the main research foci in supercapacitor development [14].

### 1.3. Components of supercapacitors

The main components of supercapacitors are, electrodes, an electrolyte, current collectors, and a separator (which would not be needed most of the time when using solid-state or semi solid-state electrolytes). All these components should be assembled in a packaging in order to make the supercapacitor as a stand-alone device.

#### 1.3.1. Electrodes

Electrodes are the main components of supercapacitors as their role is to store the electrical charge on their surface. Thus, the majority of the research conducted on supercapacitors has been focused on development of electrodes with novel chemistries and structures. Wide ranges of materials have been used as electrode active materials in supercapacitors. Conventionally, these electrode active materials are mixed with binders or some other

## Chapter 1

---

additives. In this section, we will focus on the electrode active materials that have been used in supercapacitors.

In general, electrode active materials can be divided into four groups: i) carbonaceous materials, ii) conductive polymers, iii) metal oxides and metal carbides/nitrides, and iv) nanocomposites of two or more of the aforementioned groups of materials.

One of the most widely studied type of materials in supercapacitors are carbonaceous materials. Carbonaceous materials are attractive candidates for use as electrode active materials due to their relatively large surface area, which is favorable for the function of the electrodes of supercapacitors. These materials mostly store charge based EDLC formation which is a reversible adsorption/desorption process, hence, they show relatively long cyclic life. These electrode materials include graphene and its family (e.g., graphite, graphene, graphene oxide, reduced graphene oxide, graphene quantum dots)[2], [15]–[26], carbon aerogel [27]–[31], carbon nanotubes (CNTs) [32]–[35], and activated carbon [36]–[40]. The majority of these materials, however, require post-processing such as chemical reduction \*to get rid of oxygen functional groups) in order to increase their electrical conductivity. Besides, for the case of graphene, for instance, organic solvents should be used as dispersants for processing of their slurries, which are, most of the time, toxic chemicals.

As the second group, conductive polymers have been widely used in supercapacitors as electrode active materials due to their attractive properties, such as their relatively high electrical conductivity in doped state and their suitable redox reactivity, to name a few. Examples of conductive polymers including polyaniline (PANI) [41]–[46], polypyrrole (PPy) [47]–[51], polythiophene (PTh) [52], [53] and Poly-(3,4-ethylenedioxythiophen)-poly-(styrolsulfonat) (PEDOT:PSS) [54]–[56] have been extensively used as electrodes of supercapacitors. In comparison to the carbonaceous family of materials, conductive polymers show higher nominal capacitance values, however, they suffer from shorter cyclic life as a result of their structural destruction (shrinking/swelling) throughout the process of charge/discharge.[57]

The third group of electrode materials are metal oxides, which are widely used as electrode materials mainly due to their redox reactivity which enables them to undergo Faradaic reactions to store charge through these reactions. Examples of metal oxides, such as transition metal oxides, NiO [58]–[62], RuO<sub>2</sub> [63]–[65], MnO<sub>2</sub> [66]–[70], V<sub>2</sub>O<sub>5</sub> [71]–[76], lanthanide oxides, such as CeO<sub>2</sub> [77]–[80] and La<sub>2</sub>O<sub>3</sub> [81], [82]. Moreover, carbides and nitrides of transition metals (also known as MXenes) [83] have been another class of materials of interest for the electrodes of supercapacitors [84]–[90]. The main disadvantage of these materials is their relatively low electrical conductivity, which is the main reason behind compositing them with other types of electrode materials.

In order to benefit from the inherent properties of these groups of materials, many examples of their composites have been developed and used as electrodes in supercapacitors. Some of these examples are graphene/polyaniline (PANI) [91], [92], activated carbon/polyaniline (PANI) [93] NiO/carbon nanotubes (CNTs) [94], Polypyrrole/MXene [95], [96], activated carbon/MXene [97], MXene/polyaniline (PANI) [98]–[100], MXene/MnO<sub>2</sub>[101], MXene/CNT[102], MXene/CNT/PANI[103], MnO<sub>2</sub>/graphene oxide/PANI[104], reduced graphene oxide/CNT/MnO<sub>2</sub> [105], NiO/V<sub>2</sub>O<sub>5</sub>/MnO<sub>2</sub> [106], reduced graphene oxide/MnO<sub>2</sub>/polypyrrole[107], polypyrrole/graphene oxide/CNT[108], V<sub>2</sub>O<sub>5</sub>/CNT[109], and graphene oxide/CNT/RuO<sub>2</sub>[110].

### 1.3.2. Electrolyte and separator

The ionic species in the electrolytes form an ionic layer at the interface with electrodes, which causes the electrical charge to be stabilized on the electrodes' surface (i.e., charge storage). Thus, without electrolytes, the amount of stored charge at the electrodes will be low. Compared to the dipoles in the dielectrics utilized in the conventional capacitors, ionic species in the electrolytes are more mobile and can have higher concentrations and unlike the dipoles in the dielectrics, ionic species in the electrolytes do not need relatively large voltages to be arranged as a layer of opposite charges at the interface of electrodes/electrolyte. Moreover, due to better mobility of ionic species in the electrolytes, they can enter the pores of the



## Chapter 1

---

electrodes at micro/nano-scale which enables electrolytes to be more effective in utilizing the maximum of electrode surfaces. Thus, using electrolytes provides ionic conductivity which is a more facile way to form a layer of opposite charges at the interface of electrodes/electrolytes, which ultimately, stabilizes charges more efficiently (i.e., better charge storage—higher capacitance values). Electrolytes generally determine the working voltage window of supercapacitors and by providing ionic conductivity, they can alter the power density of the supercapacitors [111]. Electrolytes are categorized into two main groups: liquid electrolytes and solid electrolytes. While liquid electrolytes possess higher ionic conductivity compared to the solid electrolytes due to the freedom of movement of the ionic species in them, they suffer from leakage issues and evaporation of their solvents over time if not suitably sealed. Hence, selection of electrolytes is always a compromise between chemical stability and performance and structural stability influenced by their leakage and/or evaporation. Figure 1.4 demonstrates the subgroups to which the liquid and solid electrolytes are divided.

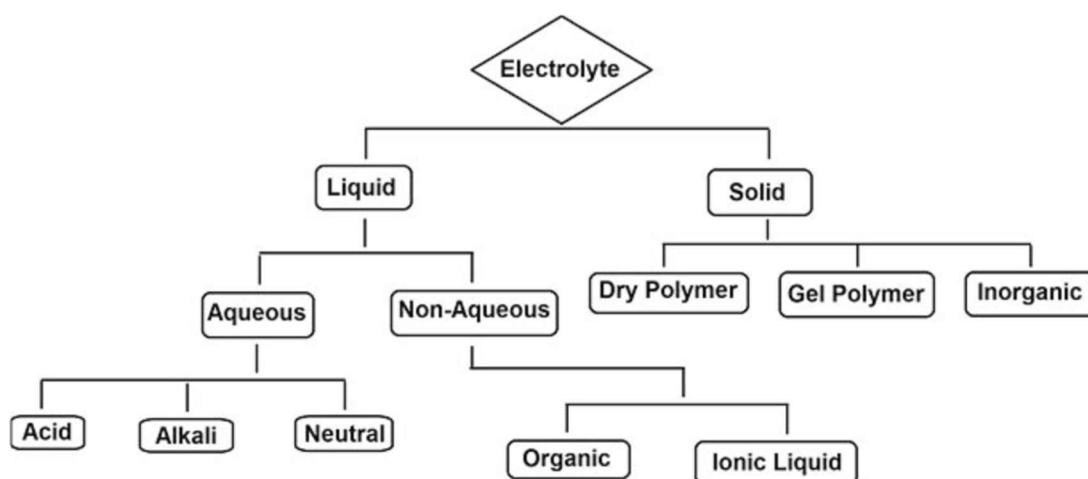


Figure 1.4. Different categories of the electrolytes for supercapacitor. Adapted from [111]

Based on the focus of my thesis, I only discuss the aqueous liquid electrolytes from the main category of “liquid electrolytes” and gel polymer electrolytes from the “solid electrolytes”. Aqueous electrolytes, can be grouped into sub-divisions of alkali[112], [113], acid[114]–[116], and neutral[117], [118] electrolytes. These electrolyte are quite cheap, easy to formulate, and

they provide good solubility for many salts, however, their typical operating working potential is limited to 1.23V which is the hydrolysis potential of water[119].

Among the solid electrolytes, “gel polymer” electrolytes, are the other category of the electrolytes that we will discuss in this section. Gel polymer electrolytes have the highest ionic conductivity among solid electrolytes and they are categorized into the sub-groups of “aqueous” and “organic” gel also known as “organogel” electrolytes[111]. Aqueous gel electrolytes, also known as hydrogel electrolytes, are composed of water, monomers or polymeric chains, and salts, acids or bases. Examples of hydrogel electrolytes include, Polyvinyl alcohol (PVA)/LiCl[120]–[122], PVA/H<sub>2</sub>SO<sub>4</sub>[37], [123], PVA/H<sub>3</sub>PO<sub>4</sub>[124], PVA/KOH[125]–[127], PEO/KOH[128], sodium alginate-grafted-dopamine/KCl[129]. Organogel electrolytes, on the other hand, are composed of organic solvents (or organic dispersing media), and polymeric hosts[130]. Examples of such electrolytes include cyanoethyl polyvinyl alcohol[131], TBAPF<sub>6</sub> (tetrabutylammoniumhexafluorophosphate):PMMA (poly(methyl methacrylate)):PC (propylene carbonate):ACN (acetonitrile)[132], TBAPF<sub>6</sub> in acetonitrile:Poly(methyl methacrylate)[133], sulphonated PEEK/dimethyl sulfoxide (DMSO)/ LiClO<sub>4</sub>[134], poly(acrylonitrile)-*b*-poly(ethylene glycol)-*b*-poly(acrylonitrile) (PAN-*b*-PEG-*b*-PAN)/dimethylformamide/LiClO<sub>4</sub>[135].

Separators, also known as membranes, are one of the components of the supercapacitors that are used to ensure that the electrodes do not contact each other (i.e., avoiding short circuit). Their porous structure, optimum thickness, and chemical stability provide suitable ionic pathways for the electrolyte species towards the electrodes[136]. In other words, they separate electrodes to ensure no electrical charge passage between them, while they do not obstruct ionic conduction in the electrolyte. Some of the most common materials used for separators are poly(vinylidene fluoride) (PVDF)[137], [138], cellulose-based[139]–[141], agar-based[142], chitosan-based[143], [143], Nafion[144]–[146], inorganic-based (such as aluminum silicate[147], hydroxyapatite[148]), composite-based (such as PVDF/BaTiO<sub>3</sub>[149], and Al<sub>2</sub>O<sub>3</sub> nanowires/Polyvinyl butyral[150]). In order to minimize the design, materials selection and fabrication steps of supercapacitors, gel polymer electrolytes can act both as separators and electrolytes in supercapacitors[151].

### **1.3.3. Current collectors**

The main function of the current collectors in supercapacitors is to direct the charges stored on the electrodes to the outer circuit of the supercapacitor[152]. The current collectors must be electrically conductive and chemically stable[153], [154]. For instance, the electrical conductivity of current collectors must be high enough (i.e., higher than that of the electrodes) not to limit the passage of electron to/from the supercapacitor. Some of the most common materials used for current collectors of the supercapacitors are aluminum[155], [156], copper[157], [158], silver[159], [160], gold[161], [162], stainless steel[163], [164], nickel[165], [166], carbon[167]–[169].

### **1.3.4. Casing/packaging**

To prepare the supercapacitors for integration in circuits and use them in real applications, they need to have proper casing/packaging[170]. The casing/packaging should provide hermeticity to ambient humidity, low processing temperature, chemical compatibility with the electrolyte, and good electrical connections to the circuit out of the package[171]. Since these packaging/casing processing is more relevant to smaller-sized supercapacitors (also known as microsupercapacitors) for integration into microelectronic systems, we will discuss the types of materials and the involved processing for them in the next chapter. Figure 1.5 illustrates the components of the supercapacitors (as a member of the electrochemical energy storage systems), namely, current collectors, electrodes, separator/electrolyte, and casing/packaging assembled as a device.

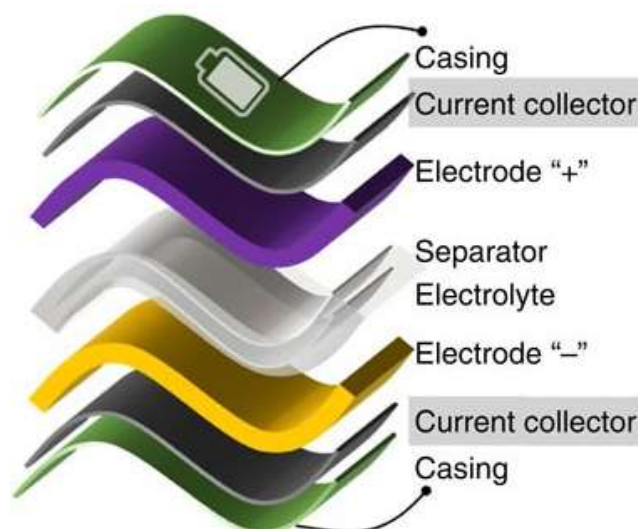


Figure 1.5. Components of typical electrochemical energy storage systems such as supercapacitors, namely, current collectors, electrodes, electrolyte/separator, and casing/packaging. Adapted from[14]

#### 1.4. Performance metrics of supercapacitors

In order to evaluate the performance of the supercapacitors, several metrics are used that are summarized in Figure 1.6. To compare the performances of different supercapacitors, these metrics are normalized per mass, area, or volume of the supercapacitors.

Some of the most important performance metrics of supercapacitors are: i) operating potential window, ii) capacitance, iii) energy density, iv) power density, v) cyclic stability, vi) coulombic efficiency, vii) self-discharge, and viii) equivalent series resistance (ESR)[172].

These performance metrics are crucial since they determine if a supercapacitor can act successfully in a desired application. As supercapacitors always need to be coupled with other electronic components in circuits, they need to be rated based on their performance metrics so that they can be reliably used for any specific applications. Moreover, these performance metrics enable us to compare different supercapacitors with each other.

**Operating potential window:** this is the maximum potential that supercapacitor can operate at without decomposition of the electrolyte and/or electrodes. We should make sure that the supercapacitor is used within a certain voltage range that provides chemical stability

## Chapter 1

---

for both the electrolyte and the electrodes. Practically, it is possible to enlarge the voltage range at which a supercapacitor operates, however, that might shorten the life cycle of the supercapacitor since undesirable reactions (e.g., decomposition of electrolyte species, or hydrolysis of water molecules in aqueous electrolytes) might occur. Hence, it is necessary to select a safe operating voltage window, within which we can ensure the maximum life cycle of any given supercapacitors. There have been reports on supercapacitors with operating potential windows as large as  $\sim 3.5$  V [173]. For fully assembled microsupercapacitors, an operating potential window ranging from 0.5 V [174] up to 3 V has been reported [175].

**Capacitance:** capacitance is the proportionality of the charge that is stored in a supercapacitor with respect to its operating voltage range and it is normalized per mass of the electrodes/whole system (i.e., gravimetric capacitance — with the unit of F/g), or per area of the electrodes/whole system (i.e., areal capacitance — with the unit of F/cm<sup>2</sup>), or volume of the electrodes/whole system (i.e., volumetric capacitance — with the unit of F/cm<sup>3</sup>). The higher the capacitance of supercapacitors, the higher the capability of them to store charge. However, this comes at the cost of longer times needed to store and release charges when they are larger in quantity. Thus, although we aim at increasing the capacitance of supercapacitors, we should make sure that the pace of the storage/release of charge in them is fast. While there are examples of supercapacitors with capacitances of magnitudes exceeding 2000 F/g [176], [177] (usually capacitance is reported in F/g unit for supercapacitors), capacitance values as high as 2100 mF/cm<sup>2</sup> [178] have been reported for microsupercapacitors.

**Energy density:** also known as specific energy, is the amount of energy that a supercapacitor can provide, which can be normalized per mass (gravimetric energy density — with the unit of Wh/kg), area (areal energy density — with the unit of Wh/cm<sup>2</sup>), or volume (volumetric energy density — with the unit of Wh/cm<sup>3</sup> or Wh/L) of the electrode or the whole system. This performance metric is one of the bottlenecks of the fabrication of supercapacitors. In most examples of supercapacitors, energy density is relatively low (specially compared to batteries) and increasing the energy density of supercapacitors is one

of the major research goals in development of supercapacitors. Energy densities as high as tens of Wh/kg [179], [180] and tens of  $\mu\text{Wh}/\text{cm}^2$  have been reported [181], [182] (similar to capacitance, energy density is also reported per mass for the supercapacitors) for supercapacitors and microsupercapacitors, respectively.

**Power density:** also known as the specific power, is the amount of power that can be generated by a supercapacitor (i.e., how fast they can deliver energy) normalized per mass (gravimetric power density — with the unit of W/kg), area (areal power density — with the unit of  $\text{W}/\text{cm}^2$ ), or volume (volumetric power density — with the unit of  $\text{W}/\text{cm}^3$  or  $\text{W}/\text{L}$ ) of the electrode or the whole system. One of the main advantages of supercapacitors compared to batteries is their relatively higher power density. It is crucial to increase power density of supercapacitors while increasing their energy density. In other words, the ideal supercapacitors should store/deliver more energy (high energy density) at a faster pace (high power density) so that they could ultimately replace batteries. Power densities as high as thousands of W/kg [183], [184] and hundreds of  $\text{mW}/\text{cm}^2$  [185] have been reported (similar to capacitance and energy density, power density is also reported per mass for the supercapacitors) for supercapacitors and microsupercapacitors, respectively.

**Cyclic stability:** the number of cycles that a supercapacitor can be fully charged and discharged before their capacitance falls below 80% of their initial capacitance value is called their cyclic stability [182], [186], [187]. Although there is not a comprehensive definition for this term, the abovementioned definition is one that has been used quite frequently. This performance metric determines the service life time of supercapacitors, thus, one of the main goals of research on supercapacitors is to maximize this metric. Supercapacitors with cyclic stability of 100000 cycles have already been reported [188]. However, for microsupercapacitors, cyclic stability of up to 17000 charge/discharge cycles has been shown in the literature [185].

**Coulombic efficiency:** the ratio of the amount of charge that is released from a supercapacitor during discharging to the amount of charge that is stored in it during charging is called coulombic efficiency. As it is a measure of efficiency, we would like to see a value of

## Chapter 1

---

100% for coulombic efficiency of a supercapacitor which means that at a fixed and equal current for charge and discharge, the times taken for charging and discharging should be equal. Maximum coulombic efficiency means no unwanted loss of charge during charge/discharge cycles. This is why we aim at maximizing coulombic efficiency. It has been shown in the literature that supercapacitors can operate with +90% coulombic efficiency [189].

**Self-discharge:** electrochemical energy storage systems such as supercapacitors, are discharged spontaneously even when they are in an open circuit condition. This phenomenon occurs since the system tends to go back to its equilibrium state, for instances, by charge redistribution at the interface of electrode/electrolyte[172], [190]. This characteristics of supercapacitors is important to determine how long these devices can keep their charges once being at rest. Hence, the longer the self-discharge time of a supercapacitor, the less the need for recharging them. (Micro)-supercapacitors usually experience self-discharge in time-scales on the order of few hours up to a few days [191].

**Equivalent series resistance (ESR):** Equivalent series resistance (ESR), also known as the internal resistance of the electrochemical energy storage systems, is an indication of the energy loss of such systems and is defined as the sum of the bulk electrolyte resistance, the resistance of the electrode, and the contact resistance between the electrode and the current collector[192]. One way to improve the performance of the supercapacitors is to decrease their ESR. In other words, the lower the ESR of the supercapacitors, the lower their energy loss, and the better overall their performance. ESR values of couple of milliohms [193] up to hundreds of ohms [194] have been reported for (micro)-supercapacitors. As the supercapacitor size is reduced, i.e., when they are microsupercapacitors, their ESR values typically increase (as the smaller they get, the available surface for charge transfer gets smaller).

## 1.5. Supercapacitors vs. Batteries

In this section, we will discuss the main differences of supercapacitors and batteries. Both these systems are electrochemical energy storage systems, however, they have fundamental differences in their performance. The most important parameters that elucidate the differences between supercapacitors and batteries are energy density, power density, and cyclic life. While batteries have higher energy densities compared to supercapacitors, they suffer from low power densities. Figure 1.6 exhibits a Ragone plot (which is a demonstration of power density (specific power) vs. energy density (specific energy)) that demonstrates the ranges of these performance metric in supercapacitors and batteries. One of the main goals of research in the field of supercapacitors is to increase their energy density without sacrificing their power density. On the other hand, supercapacitors provide much longer cyclic life compared to batteries which enables them to have longer service lifetime and subsequently, it results in less requirements for their maintenance.



# Chapter 1

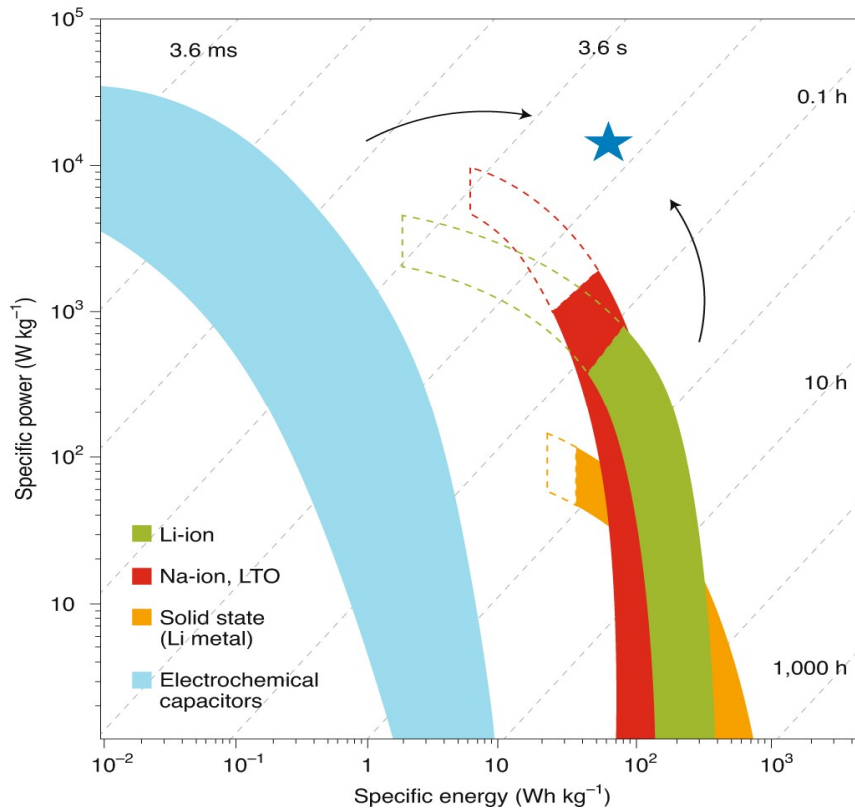


Figure 1.6. Ragone plot demonstrating the differences of specific energy and specific power of batteries and supercapacitors. The start shows the target of the research community for advancing the specific energy and power of these devices (the diagonal dotted lines and timescales represent characteristic operation timescales, obtained by dividing the energy by the power). Adapted from[9]

Moreover, the charging/discharging time of supercapacitors is much shorter than that of the batteries which means that they can be charged and discharged at a much faster pace[172]. Besides, the charge storage in supercapacitors occur at the outmost surface (outmost surface or near surface) of the electrode, unlike batteries, where the charge storage takes place in bulk of the electrode[10].

In summary, the main goals pursued in this thesis are as follows:

- Design, synthesis, and optimization of novel chemistries for different components of the microsupercapacitors— we designed and synthesized electrode and electrolytes and use commercially available materials for current collectors, packaging, and encapsulation and ultimately, optimized the overall performance of the fully-printed microsupercapacitors.
- Achieving highest level of integration for printed microsupercapacitors to date, by full printing of all components at as small as possible footprints. Particularly, we aimed at realizing mm-scale microsupercapacitors—sub-cm<sup>2</sup> area and mm level total height.
- Systematically studying the effect of dimensional scaling on the performance of the fully-additively fabricated microsupercapacitors at such low footprints and heights, for the first time, which would elucidate how scaling the size at the component level and subsequently at the whole system level could alter their electrochemical performance.

In chapter 2 of the thesis, we will discuss the background on microsupercapacitors—what materials and fabrication processes have been reported for them, rheological characterization of the inks utilized in additive fabrication of microsupercapacitors, and finally, discussing the challenges and opportunities in fabrication of microsupercapacitors.

We devoted chapter 3 of the thesis to the optimization of the performance of microsupercapacitors as a function of the chemistries of their components. We systematically investigate how the optimized chemistries can realize the maximized performance of the microsupercapacitors. The reason behind studying the effects of the chemistries of the components on the performance of the additively-fabricated microsupercapacitors is that it enables us to optimize the compositions and processing conditions for all the components to maximize the performance of the microsupercapacitors.

In chapter 4, we systematically investigate the effects of dimensional scaling of these fully-additively fabricated microsupercapacitors on their performance using the optimized

## Chapter 1

---

chemistries of the components as determined in chapter 3. Performing dimension scaling study of the fully-additively fabricated microsupercapacitors is crucial as it reveals the relationship between size of the system and its overall performance. To the best of our knowledge, dimensional scaling study of fully-additively fabricated microsupercapacitors, where all components (i.e., electrodes, electrolyte, current collectors, packaging/encapsulation) are printed, and more specifically, which are benefiting from both EDLC and pseudocapacitance charge storage mechanisms is a glaring hole in the literature. We designed the dimensional scaling study in such a way that the performance of the microsupercapacitors are evaluated as a function of change in the length of the electrodes and also the inner diameter of the nozzles with which the electrodes are 3D printed.

Finally, in chapter 5, we discuss the key outcomes of the thesis, why these outcomes are important, in addition to specific and detailed discussion of future work that can be potentially pursued on fully-additively microsupercapacitors.

## 2. Fabrication of Microsupercapacitors

### 2.1. Background on microsupercapacitors

Microsupercapacitors (MSCs) have emerged as a relatively new class of miniaturized electrochemical energy storage devices that can be integrated into microsystems[195], [196]. They possess submillimeter-scale features with a typical footprint area of up to few  $\text{cm}^2$ [197]. In recent years, novel materials and fabrication procedures/techniques for their components and new applications for them have been developed.

Similar to supercapacitors, microsupercapacitors also are composed of current collectors, electrodes, electrolytes/separator, and packaging/casing. Due to their relatively small size, their fabrication is generally challenging, hence, it is necessary to develop materials and processes to enable their replicable fabrication [198].

In this chapter, we will discuss the fabrication techniques of microsupercapacitors, examples of materials used in the related fabrication techniques, a summary of performance records of state-of-the-art microsupercapacitors, challenges and opportunities in the fabrication of microsupercapacitors, and the research goals of this thesis.

Microsupercapacitors possess two structural configurations (As shown in Figure 2.1) and different techniques are used for realization of each of these configurations. These configurations are called “planar” and “stacked”[199]. In the stacked configuration, on an insulating substrate, the current collectors are first deposited. Next, on top of the current collectors comes the first electrode, then electrolyte is added as the next layer and then the second electrode is deposited. The last layer is the second current collector. In the planar configuration, interdigitated current collectors are deposited on an insulating substrate, then the electrodes are deposited on top of the current collectors, then the electrolyte is added to cover the interdigitated layers of the electrodes and to fill the empty space between them. Between these two configurations, the planar configuration is preferred as it is believed that it could provide better electrochemical performance due to the shorter ionic diffusion distance of electrolyte and higher active surface area of the electrodes as a result of its interdigitated structure [195], [200]. Hence, we have designed our microsupercapacitors

## Chapter 2

---

fabricated and studied in this thesis in the planar configuration. In the next section of this chapter, we will focus on reporting the fabrication techniques used for realization of microsupercapacitors with an emphasis on planar microsupercapacitors. We also will discuss examples of microsupercapacitors fabricated using these fabrication techniques.

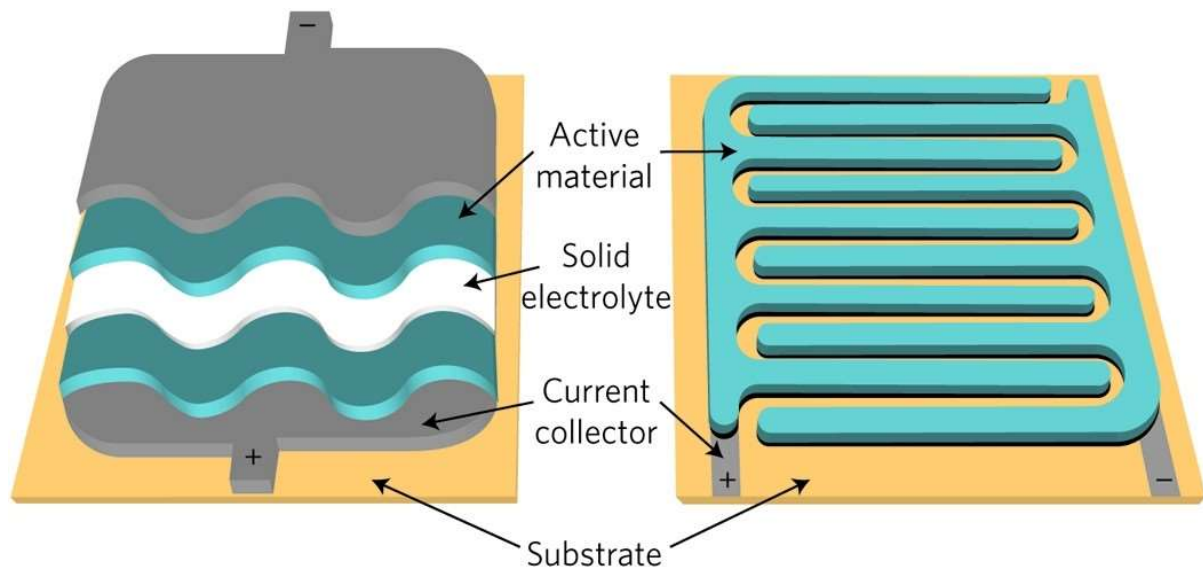


Figure 2.1. Different configurations of microsupercapacitors, left: stacked, right: planar. Adapted from [199]

### 2.2. Fabrication techniques of microsupercapacitors

In this section, we will discuss the fabrication techniques of microsupercapacitors with an emphasis on planar microsupercapacitors. We also discuss the chemistries of the components of microsupercapacitors fabricated by each of those techniques.

All the fabrication techniques used for microsupercapacitors have pros and cons and depending on the techniques used, different component materials and processing conditions are involved in realization of microsupercapacitors.

Microsupercapacitors have been mostly fabricated by photolithography techniques, laser processing (scribing), plasma jet etching, and printing techniques which are divided into two subgroups, namely, the ones requiring templates (e.g., stamping and screen printing), and the template-less ones (i.e., additive fabrication or 3D printing, such as fused deposition modeling (FDM), extrusion-based 3D printing and inkjet printing). Among printing techniques of

microsupercapacitors, the most dominant ones are inkjet printing, screen printing and extrusion-based 3D printing. Additionally, some of the less frequently used printing techniques for microsupercapacitors such as offset printing, spray printing, and gravure printing will also be discussed in this section.

Firstly, we start with discussion on photolithographic techniques used in fabrication of microsupercapacitors.

### **Photolithographic techniques**

Due to high precision that the photolithographic techniques provide, they have been widely used to fabricate microsupercapacitors. These techniques are industrially mature and are compatible with the traditional semiconductor technologies.[201] However, they usually are capable of fabricating microsupercapacitors with thin electrodes, which consequently would limit the amount of active materials used in a certain footprint[202]. These techniques usually involve using a photoresist and a mask followed by UV irradiation to realize interdigitated patterns by subsequent development steps[201], [203] (as shown in Figure 2.2). Moreover, the outlook on photolithographic techniques for the fabrication of microsupercapacitors is that these methods generally are limited by the types of materials, types of substrates, and the complexity of the involved processes as a whole. However, the feature sizes achievable by these methods are still unmatched compared to other techniques of fabrication of microsupercapacitors. Thus, there is a tradeoff between the precision and simplicity of the fabrication of microsupercapacitors using photolithographic techniques. Examples of microsupercapacitors fabricated based on photolithographic techniques include, graphene-based electrode/ $\text{H}_2\text{SO}_4$ -PVA gel electrolyte/gold current collector[204]–[206], graphene quantum dots/ $\text{H}_2\text{SO}_4$ -PVA gel electrolyte/gold current collector[207], CNT-based electrode and current collector,  $\text{H}_2\text{SO}_4$  aqueous electrolyte[208], graphene-based electrode/ $\text{H}_3\text{PO}_4$ -PVA gel electrolyte/gold current collector[209], poly(3,4-ethylenedioxythiophene) (PEDOT) electrode/  $\text{H}_2\text{SO}_4$  aqueous electrolyte/gold current collectors[210], reduced graphene oxide/manganese oxide ( $\text{MnO}_2$ ) electrodes/ $\text{Na}_2\text{SO}_4$  aqueous electrolyte/gold current

## Chapter 2

---

collector[211], graphene- $\text{Fe}_2\text{O}_3$  electrode/PVA-KOH electrolyte/nickel current collector[212], PEDOT-CNT electrode/ $\text{H}_2\text{SO}_4$ -PVA gel electrolyte/gold-chromium current collector[213], and MXene electrode/ $\text{H}_2\text{SO}_4$ -EMIMBF<sub>4</sub> electrolyte/gold-titanium current collector[214]. In order to expand the capabilities of the photolithographic techniques, the available ranges of technology-compatible materials should become wider and innovative approaches should emerge such that the involved processes become more facile and environmentally friendly.

Now, we continue with the laser processing (scribing) technique as a method for the fabrication of microsupercapacitors.

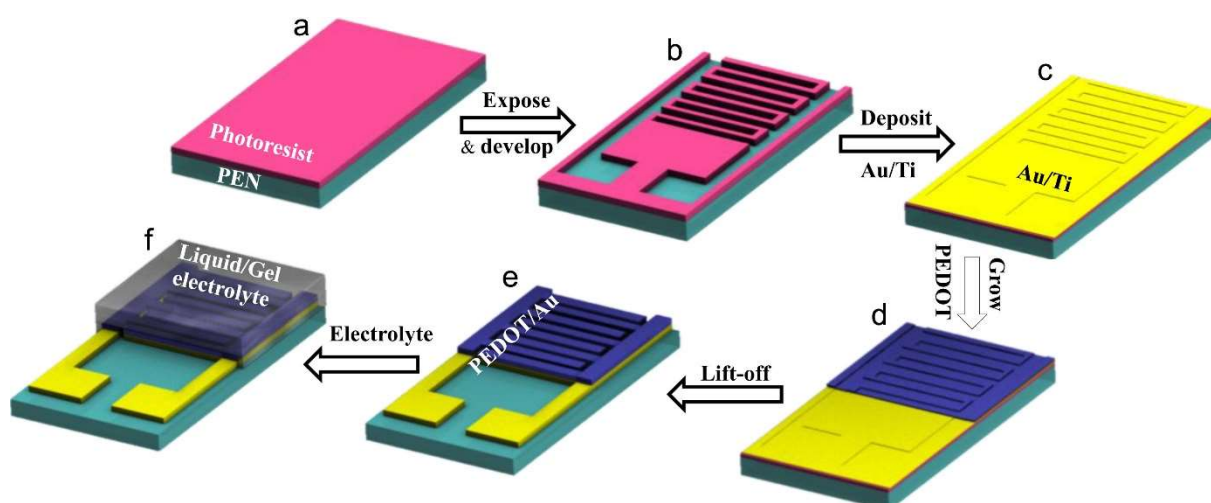


Figure 2.2. Fabrication of a microsupercapacitor through a photolithographic process. Adapted from [210]

### Laser processing (scribing)

Laser processing (scribing) of microsupercapacitors is an attractive method of fabrication which involves using a laser to create patterns (e.g., interdigitated) in a template-free fashion on a substrate covered with the a material and subsequently convert the material by photothermal/photochemical effects to a desired composition as a result of the laser irradiation[215] (An example is shown in Figure 2.3). Unlike photolithography techniques that require using sacrificial templates throughout their involved steps, laser processing (scribing) has been widely used to synthesize electrode materials with high-resolution patterns by using the heat of a laser.[216] This techniques is used both for cutting/patterning of the electrodes,

and for the chemical conversion of them. Examples of laser processed microsupercapacitors include: graphene-manganese oxide ( $\text{MnO}_2$ ) electrodes/PVA- $\text{H}_3\text{PO}_4$  gel electrolyte[217], graphene electrode (acting also as current collectors)/PVA- $\text{H}_3\text{PO}_4$  gel electrolyte and  $\text{H}_3\text{PO}_4$  aqueous electrolyte[218], graphene electrode/LiCl-PVA gel electrolyte/nickel current collector[219], reduced graphene oxide electrode (acting also as current collectors)/ $\text{Na}_2\text{SO}_4$  aqueous electrolyte[220], reduced graphene oxide electrode (acting also as current collectors)/poly(vinylidene fluoride-co-hexafluoropropylene) (PVdF-HFP) + 1-butyl-3-methylimidazolium tetrafluoroborate, (BMIM-BF<sub>4</sub>) in acetone electrolyte[221].

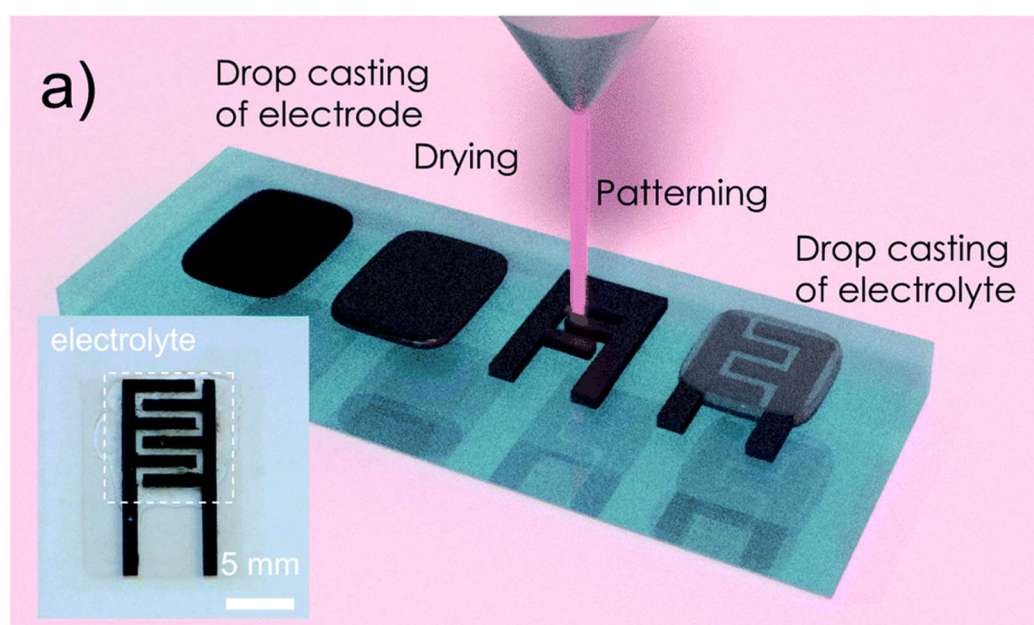


Figure 2.3. Fabrication of microsupercapacitors by laser processing. Adapted from [221]

### Plasma jet etching

Plasma jet etching uses a directed beam to scribe desired patterns with the use of a template on substrates coated with a material, except instead of a laser, it uses plasma for scribing[201]. This process is relatively fast, cost effective and simple and can also be performed in ambient conditions.[201] Compared to laser scribing, plasma jet etching is slower and it also provides lower precision. However, plasma jet etching, unlike laser processing (scribing) can operate on reflective surfaces as it does not involve a light/matter interactions. Examples of microsupercapacitors fabricated by this method include: CNT-silver nanowires



## Chapter 2

electrodes/PVA–H<sub>3</sub>PO<sub>4</sub> gel electrolyte/silver nanowires current collector[222], CNT electrodes (acting also as current collectors)/PVA–H<sub>3</sub>PO<sub>4</sub> gel electrolyte[223], reduced graphene oxide-carbon black (CB) electrodes (acting also as current collectors)/PVA–H<sub>2</sub>SO<sub>4</sub> gel electrolyte[224], reduced graphene oxide electrode/PVA–H<sub>2</sub>SO<sub>4</sub> electrolyte/gold current collector[225]. The plasma jet etching fabrication of the microsupercapacitor reported in reference[223] is shown in Figure 2.4.

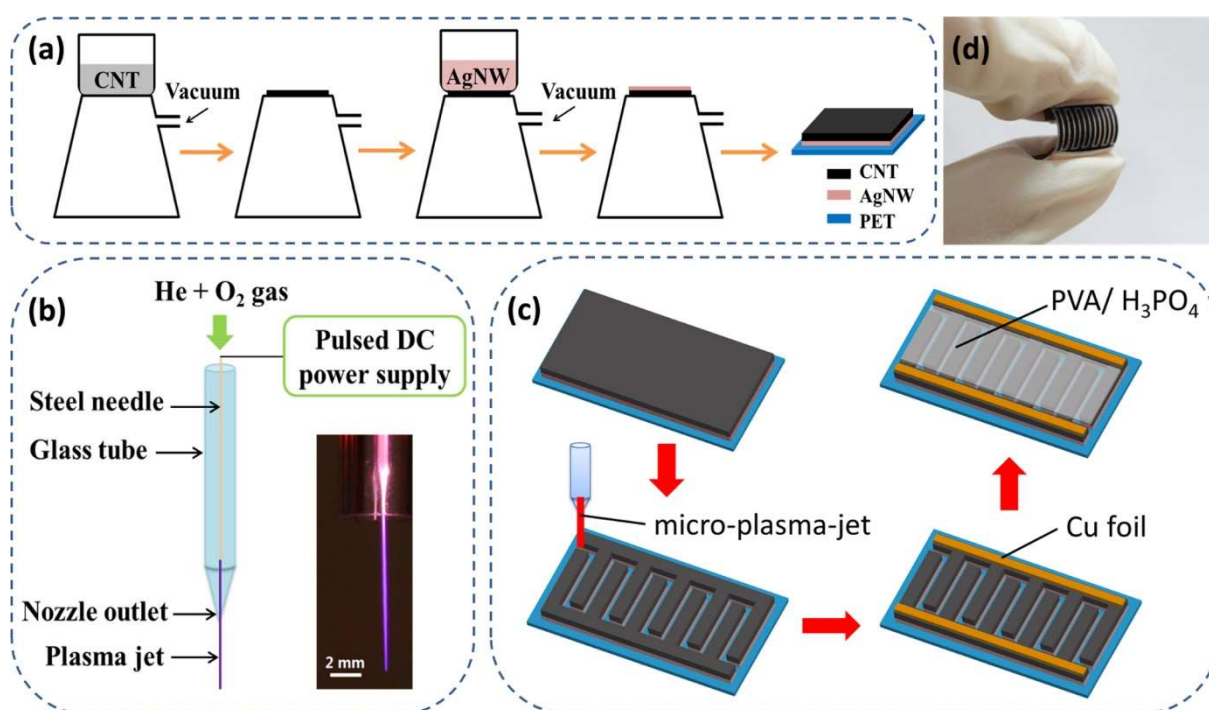


Figure 2.4. Exhibition of the plasma jet etching fabrication of a microsupercapacitor. Adapted from [222]

### Stamping

In this fabrication technique, pre-fabricated stamps (e.g., polymer-based) with desired patterns are coated with active materials (usually for electrodes and/or current collectors) and are pressed on a target substrate[226]. This fabrication technique provides a facile pathway for production of microsupercapacitors. Theoretically, the resolution of this technique is limited by the feature sizes of the patterns on the stamps and the chemical/physical properties of the active materials coated on them (i.e., surface tension, hydrophilicity/hydrophobicity, etc.). Some examples of such microsupercapacitors include:

MXene electrode (also serving as current collectors)/PVA-H<sub>2</sub>SO<sub>4</sub> gel electrolyte[226], graphene electrodes (also serving as current collectors)/PVA-KOH gel electrolyte[227], Methyl-cellulose-derived porous carbon/MnO<sub>2</sub> nanowires electrodes (also serving as current collectors)/Na<sub>2</sub>SO<sub>4</sub> aqueous electrolyte[228], Nickel-MnO<sub>2</sub> electrodes (acting also as current collectors)/CMC-Na<sub>2</sub>SO<sub>4</sub> electrolyte[229]. As shown in Figure 2.5, stamps with desired patterns are used to transfer MXenes-based inks to target substrates followed by the deposition of PVA-H<sub>2</sub>SO<sub>4</sub> gel electrolyte on the interdigitated area.

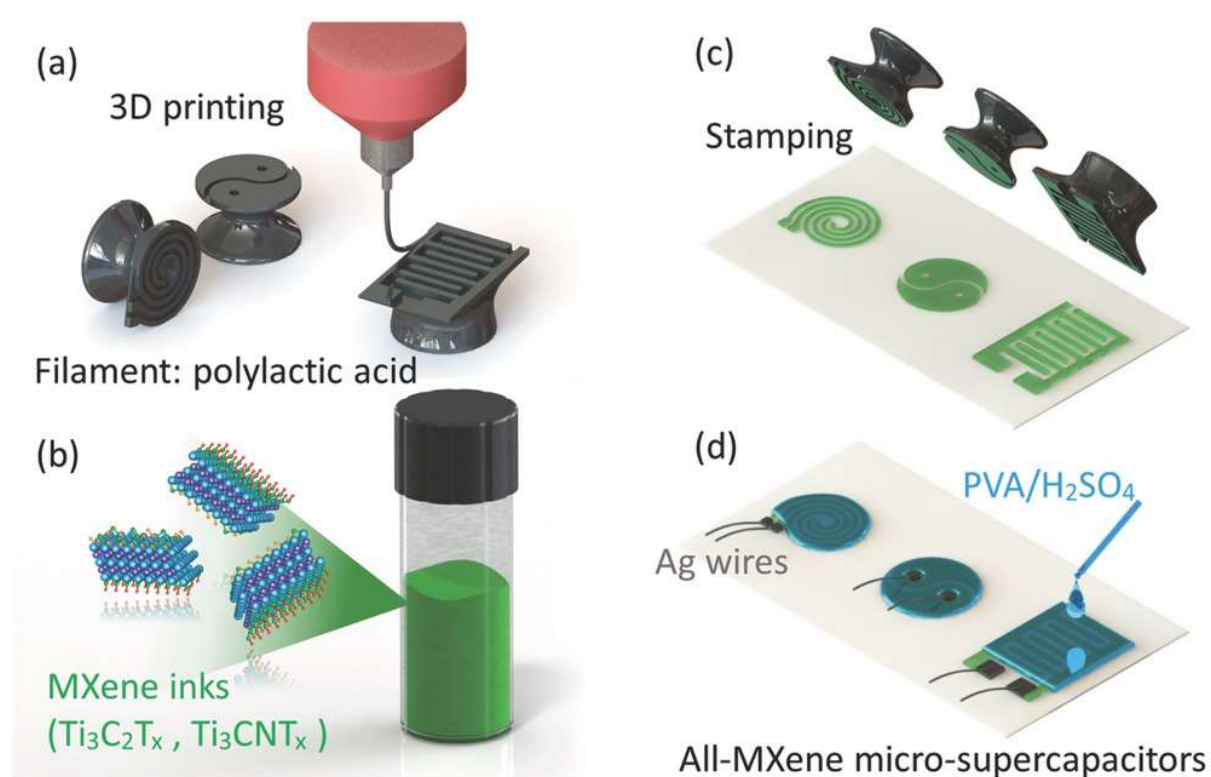


Figure 2.5. Fabrication of microsupercapacitors using the stamping technique. Adapted from [226]

## Screen printing

In screen printing, a screen stencil with the desired pattern is used to transfer an ink/slurry to a target substrate when a blade/squeegee passes across the screen to fill the open stencil apertures with the ink[230]. This technique is relatively fast and is compatible with a wide range of substrates. Screen printing offers very high deposition rates, which makes this technique suitable for fast and scalable production. This method has been successfully used

## Chapter 2

---

in fabrication of microsupercapacitors and examples of such microsupercapacitors are as follows: CNT–MnO<sub>2</sub> electrodes/PVA–LiCl gel electrolyte/silver current collector[231], CNT–graphene electrode/PVA–H<sub>3</sub>PO<sub>4</sub> gel electrolyte/pyrolytic graphite paper[232], and MXene electrodes (acting also as current collectors)/ PVA–H<sub>2</sub>SO<sub>4</sub> gel electrolyte[185]. Figure 2.6 demonstrates an example of screen printed microsupercapacitors.

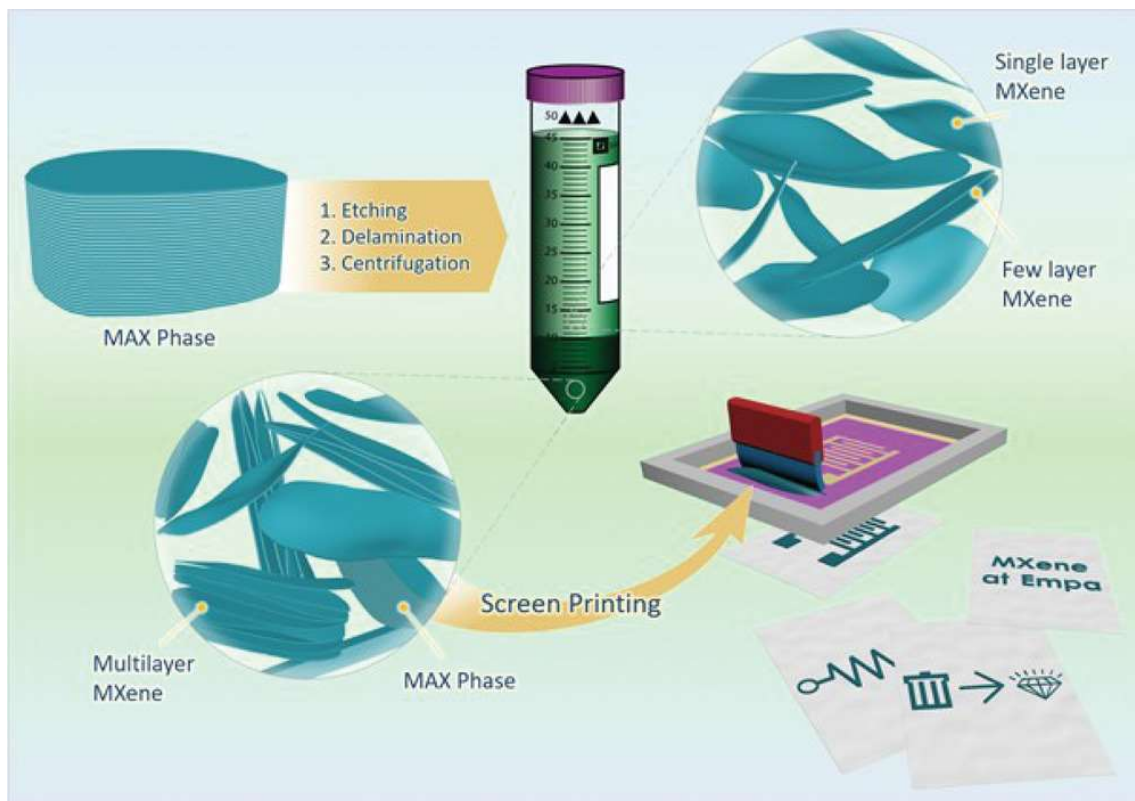


Figure 2.6. An example of screen printed microsupercapacitor. Adapted from [185]

### Gravure printing

Gravure printing is a fabrication technique that involves transfer of an ink by direct contact with a large engraved metal roll onto a target substrate[233], [234] (see Figure 2.7). Gravure printing has been historically used in newspaper and packaging printing.[235] It is relatively a fast and high-resolution printing technique and has been used in fabrication of microsupercapacitors. This method is particularly of interest for the fabrication of flexible microsupercapacitors.

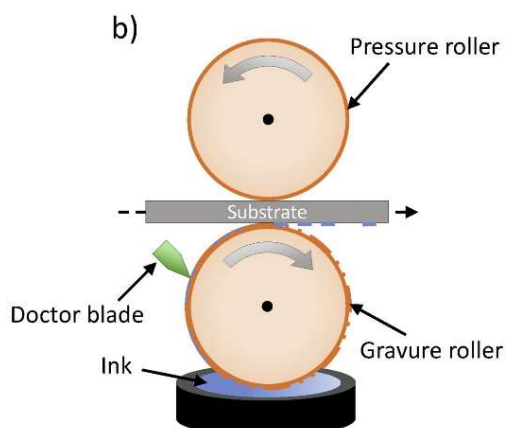


Figure 2.7. Schematics showing the gravure printing process. Adapted from [233]

Examples of microsupercapacitors fabricated with this technique include: graphene electrodes/PVA-H<sub>2</sub>SO<sub>4</sub> gel electrolyte/silver current collector[236], and sulfonated reduced graphene oxide (S-rGO)-MoS<sub>2</sub>/KOH-PVA gel electrolyte/silver current collector[237]. An example of gravure printed microsupercapacitors is illustrated in Figure 2.8.

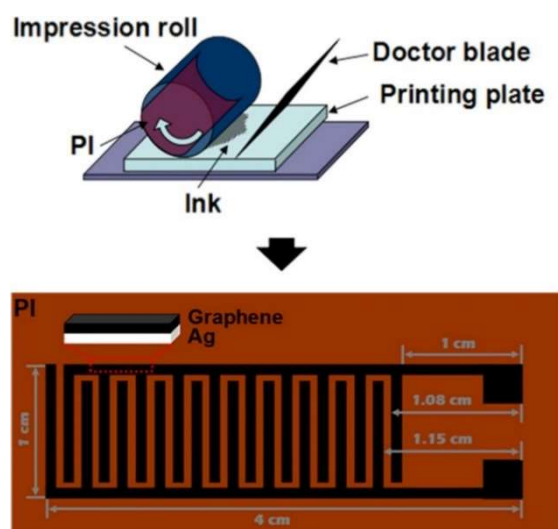


Figure 2.8. An example of gravure printed microsupercapacitors. Adapted from [236]

## Spray printing

Spray printing is a simple technique in which an ink is sprayed onto a target substrate using a spray gun[238] (An example is shown in Figure 2.9). This technique is one of the most facile

## Chapter 2

---

techniques used for the fabrication of microsupercapacitors. In practice, any mixture of active materials/solvents/dispersants that can be sprayed using a conventional spray gun might be used in this fabrication technique. It should be noted that the mixtures (i.e., inks) should be homogeneous with tuned evaporation rates of their solvents/dispersants to realize high quality patterns on any given substrates. This technique has been frequently combined with other techniques of microsupercapacitors fabrication such as laser processing (scribing) in fabrication of microsupercapacitors and some of those examples are as follows: MXene electrodes (also used as current collectors)/PVA-H<sub>2</sub>SO<sub>4</sub> gel electrolyte[239], CuFe-Prussian blue analogue (CuFe-PBA) -MXene electrodes/PVA-H<sub>2</sub>SO<sub>4</sub> gel electrolyte/graphene current collector[240], MXene electrodes (also used as current collectors)/PVA-H<sub>3</sub>PO<sub>4</sub> gel electrolyte[241], MXene-PEDOT electrodes/PVA-H<sub>2</sub>SO<sub>4</sub> gel electrolyte/MXene current collector[242], and graphene oxide-PANI electrodes/PVA-H<sub>2</sub>SO<sub>4</sub> gel electrolyte/gold current collectors[243].

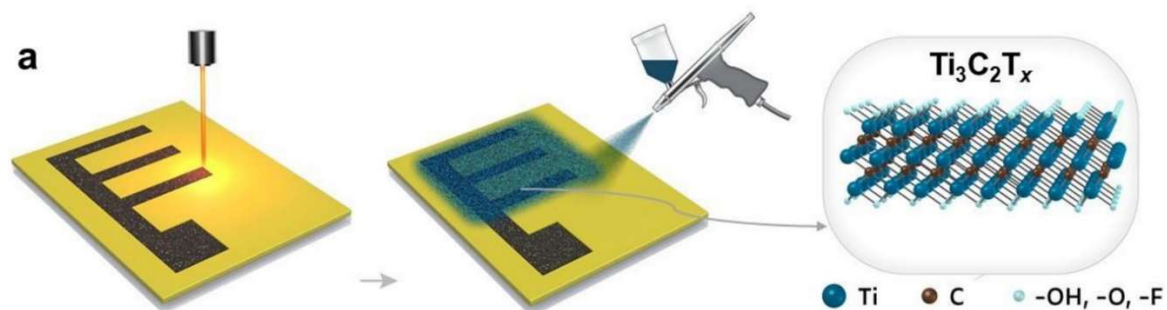


Figure 2.9. Spray printing process in combination with laser processing (scribing) for fabrication of microsupercapacitors. Adapted from [240]

### Fused deposition modeling (FDM)

Fused deposition modeling (FDM) is a printing technique which operates based feeding a thermoplastic filament to a heated printing head resulting in melting the filaments and subsequently, depositing it on a desired substrate to be solidified[244]. This technique usually involves using polymeric or polymer-based composite materials to form 3D constructs. Moreover, depending on the type of materials used as filaments, the maximum resolution of

printing will be different. For instance, if the filament is based on composites of inorganic particles dispersed in a polymeric matrix, the printing resolution is mainly limited by the size of the particle, assuming that these particles do not melt/soften at the temperature of the nozzle used for printing. Examples of FDM printed microsupercapacitors include: MXene– $\text{MoS}_{3-x}$  coated carbon framework electrodes/PVA– $\text{H}_2\text{SO}_4$  gel electrolyte/carbon cloth current collectors[245], and Graphene–PLA electrodes (acting also as current collectors)/PVA– $\text{H}_2\text{SO}_4$  gel electrolyte[246]. An example of using FDM printing in fabrication of microsupercapacitors is shown in Figure 2.10.

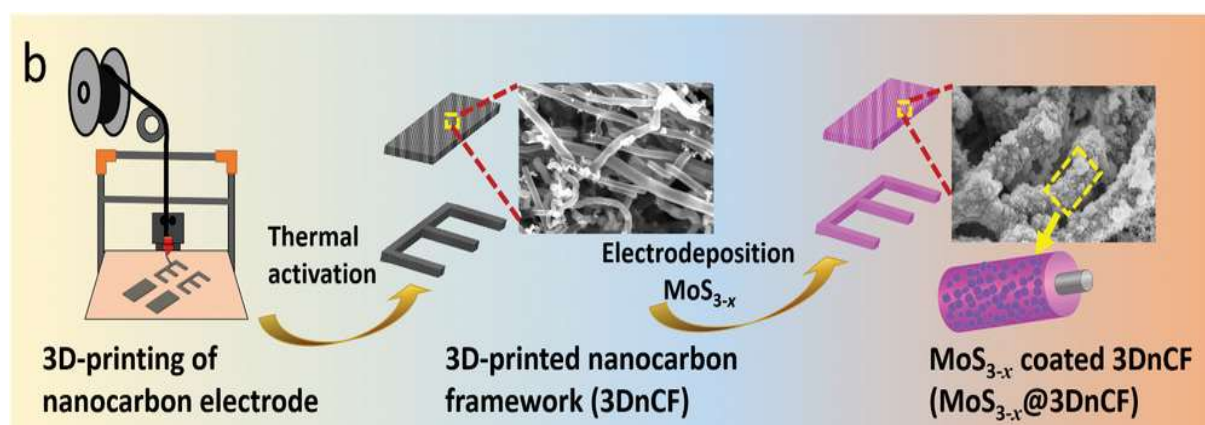


Figure 2.10. Schematic representation of FDM printed electrodes of microsupercapacitors. Adapted from [245]

## Inkjet printing

Inkjet printing is one of the fabrication techniques of microsupercapacitors that functions based on ejecting droplets of inks of active materials on a target substrate[247]. This method provides quite high levels of printing resolution and it also supports diverse ranges of ink chemistries. Since it is a low cost, fast, and scalable technique, inkjet printing has been widely used in fabrication of microsupercapacitors due to its advantages such as low-cost and fast fabrication, in addition to scalability.[248] Moreover, different types of active materials can be used by this techniques, such as polymeric, ceramic and metallic materials, dispersed in a relatively dilute suspension. Although this techniques provides one of the highest levels of printing resolution among printing techniques, this technique is not capable of printing thick (i.e., tens of microns and more) layers of materials. Some examples of microsupercapacitors

## Chapter 2

---

fabricated by inkjet printing are as follows: graphene electrodes (acting also as current collectors)/poly(4-styrenesulfonic acid) (PSSH) solid-state electrolyte[249], activated carbon electrodes/ $\text{Et}_4\text{NBF}_4$  propylene carbonate electrolyte/gold current collectors[250], PEDOT:PSS- $\text{MnO}_2$  electrodes (acting also as current collectors)/PVA-LiCl gel electrolyte [248], MXene-poly(3,4-ethylenedioxythiophene):poly(styrenesulfonic acid) electrodes (acting also as current collectors)/ $\text{H}_2\text{SO}_4$ -PVA gel electrolyte[251], graphene electrodes (acting also the current collectors)/PVA- $\text{H}_3\text{PO}_4$  gel electrolyte[252], NiO electrodes/magnesium perchlorate-PVA-ethylene glycol gel electrolyte/silver current collector[253], carbon electrodes/ PVA- $\text{H}_2\text{SO}_4$  gel electrolyte/gold current collectors[254], reduced graphene oxide electrodes/ $\text{H}_2\text{SO}_4$  aqueous electrolyte/Ti current collectors[255]. Figure 2.11 exhibits an example of an inkjet printed microsupercapacitors.

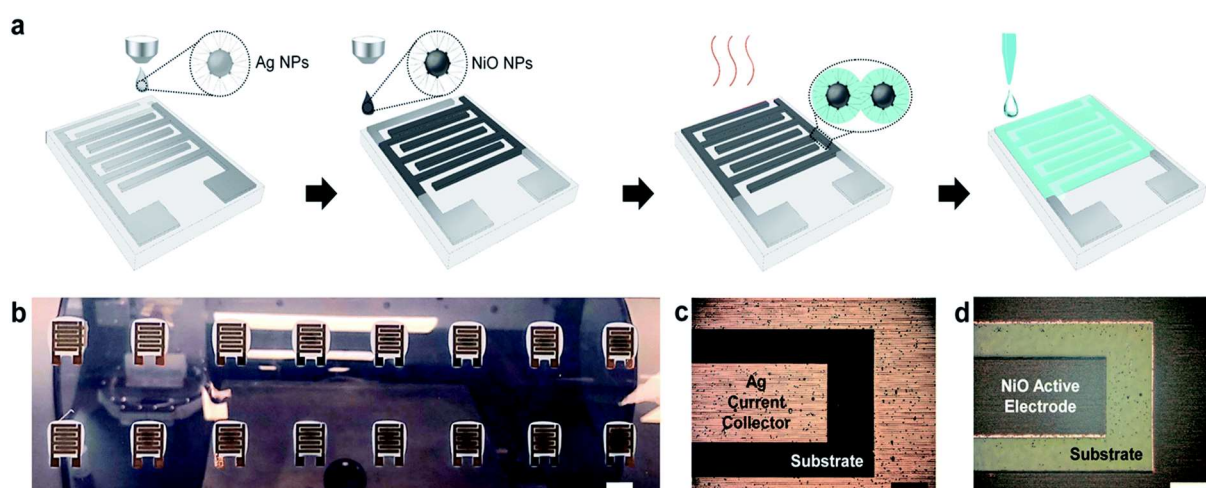


Figure 2.11. An example of inkjet printing of microsupercapacitors. Scale bars, 500 nm. Adapted from [253]

### Extrusion-based 3D printing

Extrusion-based 3D printing involves depositing a rheology-controlled paste-like ink (filled in a barrel) in form of an extrudate out of a nozzle with a specific outlet diameter in a layer-by-layer fashion[235]. Figure 2.12 demonstrates the operation principles of this fabrication technique through three different mechanisms of extrusion of the paste, i.e., pneumatic, piston-driven and screw-driven.

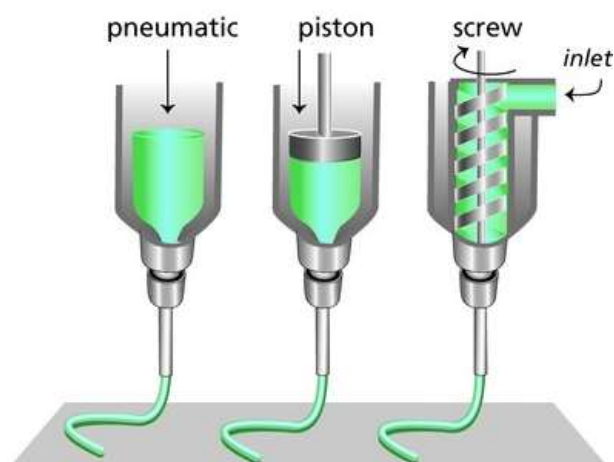


Figure 2.12. Demonstration of the principles of extrusion-based 3D printing—three different types of barrels and the mechanisms of extrusion of the inks (pastes), namely, pneumatic, piston-driven and screw-driven, and extrusion of the ink out of the nozzles, and subsequent deposition of the ink on a target substrate. Adapted from [256]

Extrusion-based 3D printing has been successfully utilized in a large number of examples in literature as a fabrication technique for microsupercapacitors (An example is shown in Figure 2.13). This technique is specifically attractive for the fabrication of thick layers of materials, which is not the case for inkjet printing. Moreover, practically, any types of materials that can be made into homogenous paste-like inks, can be extrusion printed. It is worth mentioning that some extrusion printers have the option of heating the extrusion printing nozzles, which resembles some characteristics of the FDM printing. Thus, it is possible to achieve high levels of freedom for materials selection and processing in this technique. A number of such example are as follows: vanadium nitride quantum dots (VNQDs)–graphene oxide and  $V_2O_5$  graphene electrodes/LiCl–PVA gel electrolyte/Ti–Au current collectors[181], MXene–manganese dioxide nanowires–silver nanowires–fullerene (C60) electrodes (acting also the current collector)/PVA–KOH gel electrolyte[257], ( $Fe_2O_3$ –graphene–Ag) electrodes/LiCl–PVA gel electrolyte/silver current collector[258], reduced graphene oxide electrode/PVA– $H_3PO_4$  gel electrolyte/Cr–Au current collector[259], MXene electrode/PVA– $H_2SO_4$  gel electrolyte/gold current collectors[260], polyaniline/reduced graphene oxide electrodes/ $H_2SO_4$ –PVA gel electrolyte/silver current collector[261], reduced holey graphene oxide electrodes/PVA–KOH gel electrolyte/silver electrode[262], CNT electrodes (acting also the current collector)/PVA–



## Chapter 2

---

H<sub>3</sub>PO<sub>4</sub> gel electrolyte[263], pyrrole surface-modified reduced graphene oxide electrodes (acting also the current collector)/H<sub>2</sub>SO<sub>4</sub> or Tetraethylammonium tetrafluoroborate–Acetonitrile (TEATFB/AN) electrolytes[264], and (activated carbon–graphite–nanocellulose) /nanocellulose–glycerol–NaCl electrolyte /graphite–carbon black current collectors[265].

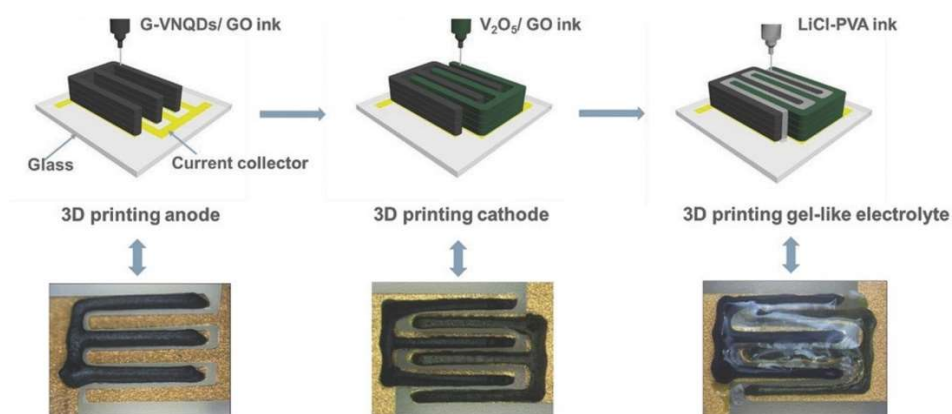


Figure 2.13. An example of a microsupercapacitor fabricated by extrusion-based 3D printing. Adapted from [181]

In the next section, we will discuss some of the fundamental definitions in rheology and also the rheological characteristics of inks used in 3D printing with special emphasis on extrusion-based 3D printing. Later, at the end of thesis chapter, we will talk about the visions and goals of this thesis and our proposals as solutions for challenges in fabrication of microsupercapacitors.

### 2.3. Rheological characteristics of the inks for 3D printing

The term “rheology” means the study of deformation and flow of matter and the goal of the rheological studies is to understand how matter deforms and flows upon exertion of force to it[266], [267]. Rheological characterization of the inks determines if they are suitable for additive fabrication and provides a guide on the restrictions involved in processing of the inks for additive fabrication. For instance, rheological characterizations determine the printing parameters, such as minimum printing resolution achievable, printing pressure and speed, and maximum solid loadings in the inks, to name a few. Thus, it is fundamentally crucial to determine the rheological characteristics of the inks for successful printing when formulating

them. There are three different techniques of rheometry, namely, i) rotational rheometry, ii) extensional rheometry, and iii) Falling/rolling ball technique[268]. As the most widely employed technique for rheometry of the inks used in additive fabrication (and more specifically in 3D printing techniques) has been rotational rheometry, we will focus on this technique in this thesis. Rotational rheometry involves measurements of rheological properties of materials through the rotation of the rheometer geometrical configuration[269]. Now, we discuss some of the most important rheological properties and definitions which are widely used in printing of inks for different realms of applications which are all also relevant to the additive fabrication (especially extrusion-based 3D printing) of energy storage systems such as microsupercapacitors.

**Viscosity:** Materials, and more specifically related to the printing techniques—inks, show resistance to flow and this resistance is defined as viscosity which is measured by calculation of the ratio of the shear stress to shear rate[235]. Viscosity of the inks are one of the main characteristics that determine the printing conditions, such as printing pressure, nozzle diameter, and ultimately printing resolution. Hence, the viscosity of the inks should be carefully tuned to fulfill the printing requirements. However, depending on the nature of the active materials in the ink (i.e., particle size, concentration, etc.), the level of fine tuning of the viscosity of the inks can be quite limited. Depending on how viscosity changes as a function of shear rate, materials are categorized into two main groups: i) Newtonian and ii) non-Newtonian materials. While Newtonian materials, such as water, show a constant viscosity as a function of shear rate, the non-Newtonian materials exhibit non-constant viscosity as a function of shear rate[270].

**Shear thinning and shear thickening behaviors:** For non-Newtonian materials, if the viscosity is reduced as a function of shear rate, they are called “shear thinning” materials and in case of increase in viscosity as a function of shear rate, they are called “shear thickening”[235]. It is favorable for printing purposes that the inks show shear thinning behavior since it facilitates extrusion of the ink out of nozzle. In case the inks are shear

## Chapter 2

---

thickening, while being extruded, their viscosity increases, which makes the deposition more difficult and less predictable.

**Viscoelastic behavior:** Viscoelastic behavior is a combination of “elastic—reversible” and “viscous—non-reversible” behaviors inks used for extrusion-based 3D printing should possess due to the nature of this technique. The elastic portion of this behavior refers to the energy stored in the system while flowing and the viscous portion refers to the energy loss incurred due to the flow[271]. Before printing constructs, the elastic behavior is dominant and as the ink is being printed, it undergoes plastic deformation— a non-reversible deformation, hence, the viscous behavior becomes more dominant at that stage. The combination of elastic and viscous behaviors is required to have a successful printing process, since it ensures the printability of the ink from the time it is at rest in the printing barrel (elastic behavior dominance) to the moment it is printed on a substrate (viscous behavior dominance).

**Storage modulus and loss modulus:** The storage and loss modulus are two parameters that demonstrate the energy storage and energy loss in viscoelastic materials, respectively, under rheological measurements. While the storage modulus (i.e.,  $G'$ ) shows the elastic properties of the materials, the loss modulus (i.e.,  $G''$ ) demonstrates their viscous characteristics. In other words, the elastic modulus is a demonstration of the solid-like behavior of the materials and the loss modulus is a demonstration of their liquid-like behavior[270]. Thus, an investigation of these parameters of the rheological properties of the ink determine whether they are suitable for printing. It should be noted that the elastic modulus becomes more dominant when the solid content of the inks is increased while the ink is homogeneous.

**Yield stress:** by definition, yield stress is defined as the critical stress below which the material does not flow, and passing this stress limit, the material enters the flow regime[272]. It is usually defined as the shear stress at which the  $G'$  and  $G''$  values are equal in viscoelastic materials[273]. We must tune the yield stress of inks such that successful printing of the inks

is ensured. In other words, too high yield stresses require very high printing pressures to extrude the ink, for instance, in the case of extrusion-based 3D printing. On the other hand, if the yield stress is too low, the material becomes too liquid, which does not retain its shape upon deposition although it can be deposited using very low pressures.

All the aforementioned rheological properties can be measured through “shear flow” and/or “oscillatory” rheological measurements.

Generally, the inks used for extrusion-based 3D printing should show shear thinning behavior (i.e., decrease in viscosity as a function of increase in shear rate), suitable range of viscosity, and relatively high values of storage modulus ( $G'$ ) at low shear stresses (i.e., usually having higher storage modulus than loss modulus at low shear stresses—more pronounced elastic behavior at low shear stresses), and good shape retention after deposition[274]. Figure 2.14 shows an example of the typical rheological properties of the inks used for extrusion-based 3D printing (this example is specifically regarding extrusion-based 3D printing of a microsupercapacitor[275]). Moreover, the inks used for extrusion-based 3D printing should demonstrate viscoelastic behavior where the yield stress should preferably not be relatively very high. When the yield stress is very high, the amount of pressure need to extrude the ink out of the nozzle becomes proportionally higher and it might cause difficulty in reliable printing of the inks. This limitation becomes more pronounced when the nozzle diameter is smaller, hence, the pressure for extrusion needs to be higher, which might ultimately make the ink enter a plug flow regime where it just is thrown out of the nozzle with minimum flow control.[276] Thus, the inks used for extrusion-based 3D printing should show all the aforementioned characteristics to realize a reliable and high-quality printing.

## Chapter 2

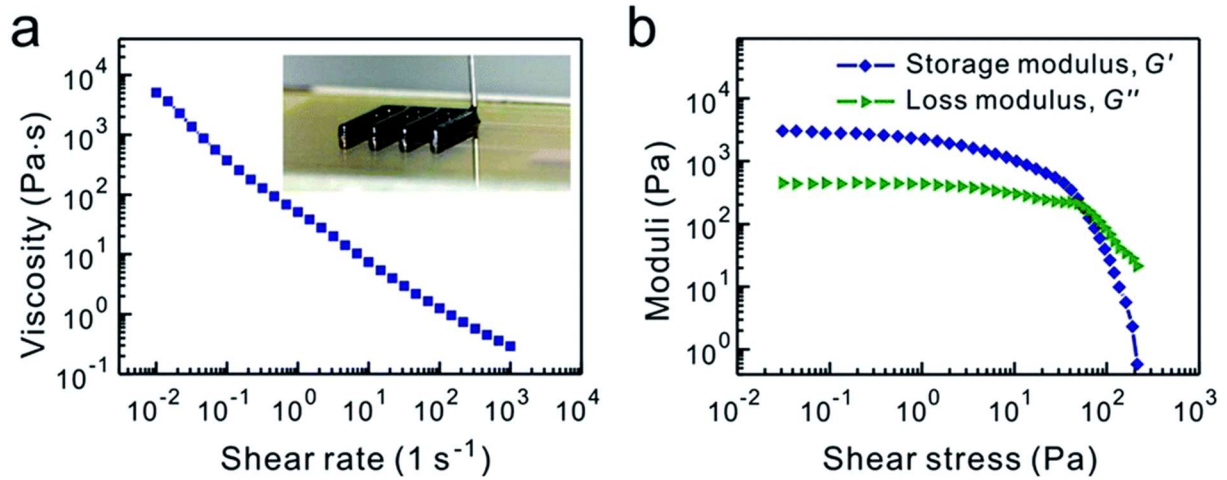


Figure 2.14. Rheological properties: a) viscosity as a function of shear rate, demonstrating shear thinning behavior, and b) oscillatory behavior of the ink showing the storage modulus ( $G'$ ) and loss modulus ( $G''$ ) of the ink and the intersection of them representing the yield stress of an ink used for extrusion-based 3D printing of microsupercapacitors. Adapted from [275]

Comparing different printing techniques, extrusion-based 3D printing enables printing very high-viscosity inks (favorable for formulation of inks with maximum solid active material content) and also it provides the opportunity to print very thick layers (e.g. few hundreds of microns) of electrodes realizing a possible solution to increasing energy density of the planar interdigitated microsupercapacitors by allowing for higher loadings of active material per area[235]. Figure 2.15 exhibits a comparison on the achievable printed layer thickness and printing resolution as a function of the compatible viscosity of the inks used in several printing techniques.

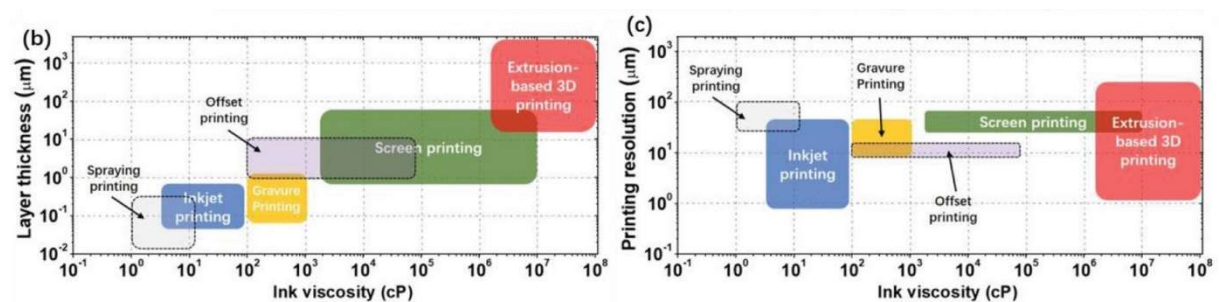


Figure 2.15. Layer thickness and printing resolution as a function of ink viscosity attained by different printing techniques. Adapted from[235]

In the next sections, we will discuss the challenges and opportunities in fabrication of microsupercapacitors in addition to the research goals of the thesis.

### **2.4. Challenges and opportunities in fabrication of microsupercapacitors**

Although significant attention has been devoted in recent years to the development of microsupercapacitors as a relatively new branch of miniaturized energy storage systems, huge opportunities are in sight for further improvements on all levels of their fabrication, namely, i) materials development and optimization for their different components, ii) their facile fabrication with high precision and high levels of integration, and iii) downsizing them without sacrificing their performance which are among the most important challenges to be tackled for microsupercapacitors.

To the best of our knowledge, there is no example of a fully additively fabricated microsupercapacitor—by printing all the components, i.e., current collectors, electrodes, electrolytes, packaging/encapsulation, and more specifically, at footprints below 1 cm<sup>2</sup>. Moreover, fully printed microsupercapacitors should possess excellent performance; such as outstanding areal/volumetric capacitance, energy density, power density, and cyclic stability at as small as possible footprints. These requirements will be fulfilled by careful design, synthesis, and optimization of active materials and formulating rheology-controlled inks based on these active materials for realization of the components of microsupercapacitors in addition to fabrication process optimization for full integration of all the components.

Another important missing knowledge, hence, would be understanding the effect of dimensional scaling of fully additively fabricated microsupercapacitors. Coupled with downsizing them, we need to systematically investigate how their performance changes as a function of their component and subsequently overall sizes.

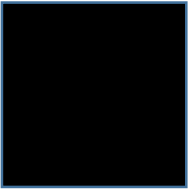
Meeting all the above-mentioned requirements results in high-performance and ultra-small microsupercapacitors which will be great candidates as energy storage systems in

## Chapter 2

---

microelectronics, internet of things (IoT), and other microsystems. In summary, in this chapter, we discussed the background on microsupercapacitors, fabrication techniques of microsupercapacitors, rheological characteristics of the inks used for 3D printing, and challenges and opportunities in fabrication of microsupercapacitors.

In the next chapter, we will discuss the details on the selection and optimization of the materials for each component of the microsupercapacitors, in addition to the designed additive fabrication process and detailed compositional, structural and electrochemical characterizations of the fully additively-fabricated microsupercapacitors.



### **3. Additive Fabrication of High Performance Millimeter-Scale Microsupercapacitors: Fine-Tuning Chemistry to Maximize Performance**

In this chapter, we will discuss the optimization of the performance of microsupercapacitors as a function of the chemistries of their components. We systematically investigate how the optimized chemistries can realize the maximized performance of the microsupercapacitors.

Amin Hodaei designed the experiments and synthesized the active materials of the electrodes and formulated the electrolytes. Amin Hodaei performed the rheological characterizations, 3D printing of the microsupercapacitors and also the electrochemical characterizations of the microsupercapacitors. Amin Hodaei and Vivek Subramanian conceptualized the research, analyzed the data and wrote the manuscript.

The contents of this chapter are parts of a manuscript that is under review in the “Journal of Power Sources” as a journal article



## Chapter 3

---

### 3.1. Introduction

In this chapter, we show full additive fabrication of microsupercapacitors and we also investigate the optimization of the performance of microsupercapacitors as a function of the chemistries of their components. Through systematic investigation, optimized chemistries can realize maximized performance of the microsupercapacitors. The optimization is done on both levels of materials chemistry of the components and their processing conditions. In a step-by-step fashion, we will show how we could reach the maximized performance of our fully additively-fabricated microsupercapacitors.

### 3.2. Fabrication and Characterization of microsupercapacitors

In this part, we will discuss i) fabrication of microsupercapacitors in full detail, ii) component structures of the microsupercapacitors, iii) selection of the electrolyte, the encapsulant and their UV curing conditions, iv) optimization of electrode active materials, and, finally, v) realization of microsupercapacitors with optimal performance.

#### 3.2.1. Fabrication of the microsupercapacitors

In this sub-section, we discuss the additive fabrication of the microsupercapacitors in detail. We additively fabricated the microsupercapacitors by a sequence of additive printing steps. First, we fabricated the interdigitated current collectors by extrusion-based 3D printing of a commercial silver paste on a wet-oxidized silicon wafer (with a 200 nm oxide layer) and subsequently, the printed current collectors were heat-treated (Figure 3.1A). Then, the package walls were printed using polycaprolactone (PCL) surrounding the interdigitated fingers of the current collectors through fused deposition modeling (FDM) (Figure 3.1B). Next, we deposited the electrode aqueous ink (edge-oxidized graphite oxide (EOGO)/ceria nanoparticles (NPs) nanocomposites + water) on the interdigitated fingers of the current collectors through extrusion-based 3D printing (Figure 3.1C). In the next step, we deposited a UV-curable electrolyte (poly (ethylene glycol) diacrylate (PEGDA) + LiCl + lithium phenyl-2,4,6-

trimethylbenzoylphosphinate (LAP) + water) in the interior space of the package walls to immerse the electrodes and subsequently UV cured the electrolyte to consolidate the components (Figure 3.1D). This provided the necessary mechanical stability for subsequent sealing. In the next step, we deposited a UV-curable encapsulant on top of the cured electrolyte and around the exteriors of the package walls, followed by a UV curing step to seal the system completely (Figure 3.1E). Figures 3.1F and 3.1G exhibit the top and the side views of a fully additively fabricated MSC, respectively.

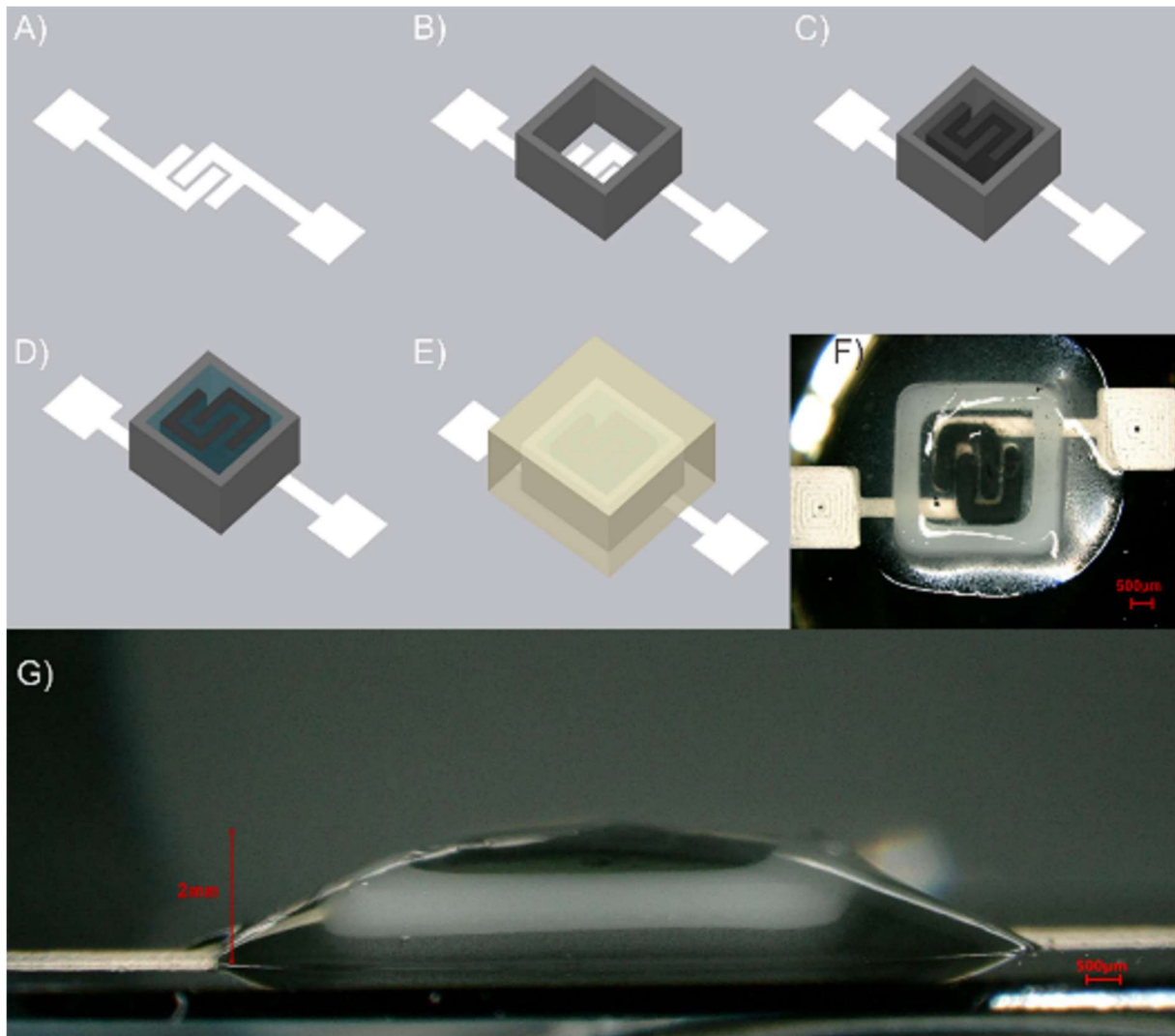


Figure 3.1. Schematic of the fabrication procedure of the microsupercapacitors, A) 3D printing (extrusion-based) of the silver current collectors on a wet-oxidized silicon wafer and heat treatment of the current collectors, B) 3D printing of the package using PCL through fused deposition modeling (FDM) printing, C) 3D printing (extrusion-based) the electrodes on the current collectors (inside the package), D) Deposition of UV-curable electrolytes inside the package and immersing the electrodes and UV curing the electrolyte, E) Deposition of an encapsulant on top of the UV-cured electrolyte and subsequently UV curing it, F) An image of one of our fully-fabricated microsupercapacitors (top view), G) An image of a fully-fabricated microsupercapacitor (the same as in (F)) (side view).

### 3.2.2. Component Structures of the Microsupercapacitors

In this sub-section, we discuss what optimization procedures are followed, which resulted in realization of the fabrication of microsupercapacitors with maximized performance. In order to optimize and maximize the performance of the MSCs, the properties of each of their component structures (i.e., current collectors, electrodes, electrolyte, and encapsulant) need to be optimized. Hence, we optimized i) the electrical conductivity of the current collectors by tuning the heat treatment used to convert the printed current collectors into conductive contacts, ii) package walls using PCL were FDM printed around the fingers of the current collectors to as a container for the electrolyte when deposited to immerse the electrodes and investigating whether the electrolyte leaks from these walls to outside, iii) loading of ceria NPs in the electrode to maximize capacitor performance, iv) UV curing condition of the electrolyte and the concentration of LiCl in it to maximize ionic conductivity and limit series resistance contributions of the electrolyte while delivering suitable mechanical stability, and v) UV curing condition of the encapsulant to ensure proper sealing performance and mechanical stability.

### 3.2.3. Fabrication of the current collector

Current collectors should provide sufficient electrical conductivity to pass the stored charges to/from the system without adding excessive series resistance. We optimized the electrical conductivity of the current collector through systematic investigation of its change as a function of curing temperature. To fabricate the current collectors through extrusion-based 3D printing, we selected a commercial silver paste (DELO-DUALBOND IC343) that is light-fixable and heat curable and is composed of silver particles and a modified polycarbamin acid derivative as an organic additive. We heat treated the printed current collectors to optimize their electrical conductivity; this facilitates the removal of solvent and aids in the consolidation of the particulate conductive materials. Chemical stability of the current collectors is also another important factor to determine their suitability for use in an energy storage system. We did not observe any chemical instability, such as change in color and decomposition-driven release of materials from the current collectors in the fully fabricated MSCs before and after electrochemical tests. Figure 3.3A illustrates the sheet resistance of the silver paste used for

## Chapter 3

the current collector fabrication as a function of heat treatment conditions (all heat treatment was performed in air). We measured the sheet resistance values using four-point probe measurements and repeated the measurements on 6 different square patterns (8 mm × 8 mm) at each heat treatment condition (inset of Figure 3.2A). The square structures were heat treated at temperatures ranging from 400 °C to 550 °C for 5 to 30 minutes. We selected this heat treatment regime based on the TGA curve of the silver paste (Figure 3.10 – in Materials and Methods section). The optimal condition was found to be 450°C for 10 minutes; this was therefore used for heat treatment of the electrodes. Figure 3.2B shows current collectors fabricated via extrusion-based 3D printing of the silver paste; these were subsequently heat treated at 450 °C for 10 minutes. We used this optimized processing condition of current collectors for all the microsupercapacitors that we fabricated.

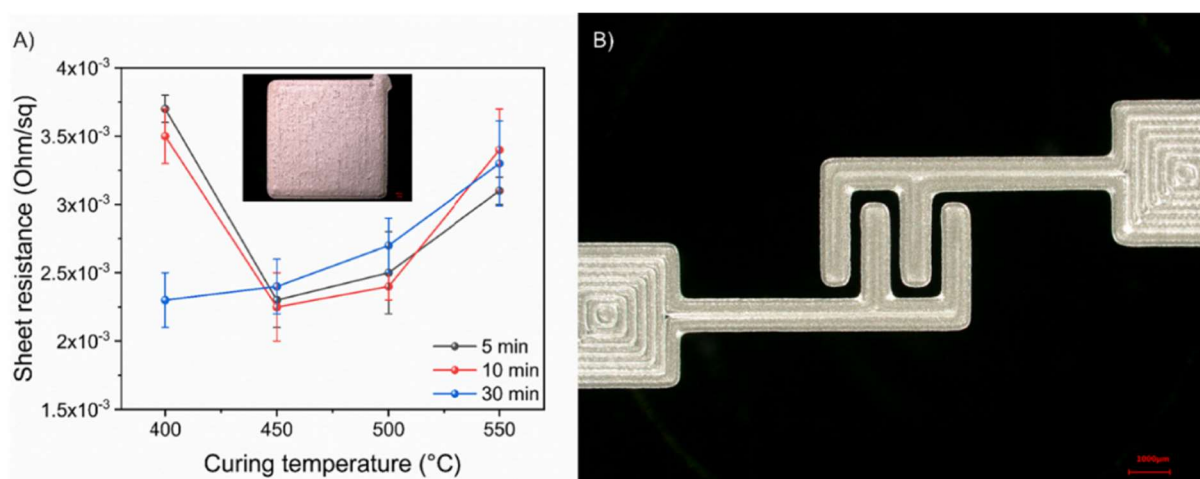


Figure 3.2. A) Sheet resistance of the silver paste used for the current collector fabrication as a function of heat treatment temperature and duration in air, B) current collectors fabricated via extrusion-based 3D printing of the silver paste; these were subsequently heat treated at 450 °C for 10 minutes.

### 3.2.4. Fabrication of the package walls

For FDM printing the package walls, we used polycaprolactone (PCL). PCL is a biocompatible polymer with low melting temperature and a hydrophobic nature.[277] The main reason behind printing the package walls is that it acts as a container for the electrolyte before it is UV-cured when immersing the electrodes in the sequence of MSCs fabrication. Without the

presence of the package walls, the electrolyte spreads and as a result, shape integrity of the MSCs will not be fulfilled. We observed that no leakage of electrolyte from the package walls to the outside occurred over time (Figures 3.3A and 3.3B). However, as the top side of the package walls is open, the solvent of the electrolyte (i.e., water) evaporated over time seriously questioning the stability of the non-encapsulated MSCs over time. As seen in Figure 4B, the electrolyte started to being evaporated and as a result, some parts of the electrodes surfaced out of the electrolyte. Hence, this observation further emphasized that presence of a proper encapsulation for structural stability of the MSCs is vital.

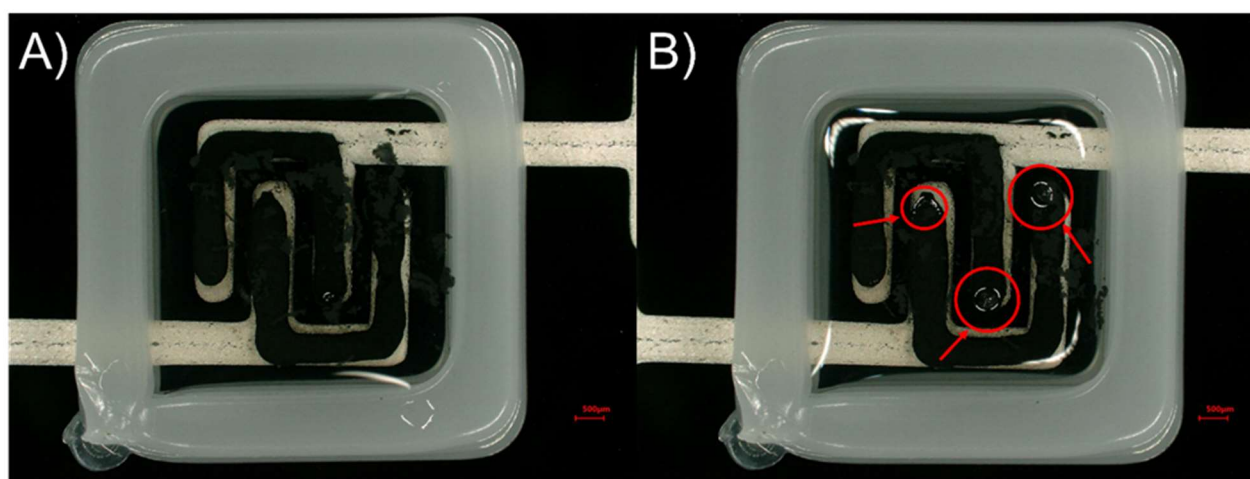


Figure 3.3. MSCs before encapsulation, A) A fabricated MSC only waiting for the encapsulation step, B) the same MSC after 1 hour resting in ambient conditions. As it can be seen, there is no leakage of the electrolyte to outside over time, however, the electrolyte started to face evaporation and shrinkage although being UV-cured (the red arrows show surfacing of the electrodes due to evaporation of the electrolyte solvent (see the red circles).

### 3.2.5. Selection of the electrolyte, the encapsulant and their UV curing conditions

The electrolyte systems that we have used in this study are aqueous UV-curable electrolytes based on (poly (ethylene glycol) diacrylate (PEGDA) + LiCl + lithium phenyl-2,4,6-trimethylbenzoylphosphinate (LAP) + water). PEGDA has been widely used in the formulation of hydrogels for 3D bioprinting[278], [279]. In addition, LAP is one of the most widely used water-soluble photo-initiators used in 3D printing of hydrogels.[280], [281] We were inspired by the usage of 3D printable UV-curable hydrogels comprising PEGDA and LAP to formulate

## Chapter 3

---

our UV-curable hydrogel electrolytes. We tuned the ionic conductivity of the electrolyte through addition of lithium precursors. We investigated the performance of the MSCs as a function of different electrolyte compositions, electrode compositions (varying ceria NPs concentrations), electrolyte UV curing duration, and the encapsulant UV curing time. For the encapsulant, we used a UV-curable modified epoxy resin (DELO Dualbond AD 761). As the combined thickness of the electrolyte and the encapsulant layers is relatively small (~2 mm) and the UV curing step of the encapsulant was expected to penetrate to and thus at least partially cure the underlying electrolyte layer, we decided to optimize the UV curing conditions for both these components concurrently (details of the UV curing steps are provided in the Experimental section). Hence, we optimized the UV curing condition of the electrolyte as a function of LiCl concentration and also of the UV curing condition of the encapsulant. Since electrolyte performance is expected to interact strongly with the electrode electrochemistry, we simultaneously varied the ceria NPs loading in the electrode. Figures 3.4A–C show the change in areal capacitance of the MSCs as a function of UV curing duration of the electrolyte, LiCl concentration, and UV curing duration of the encapsulant, all as a function of the loading of ceria NPs in the electrode.

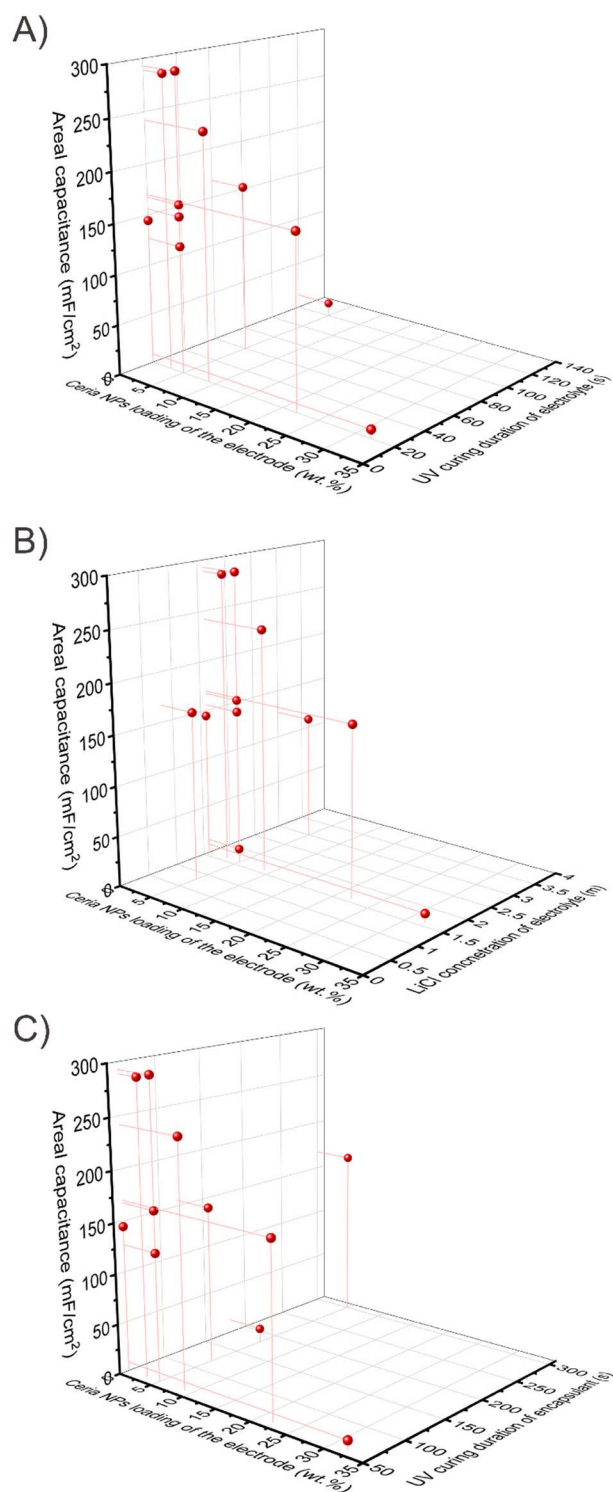


Figure 3.4. Effect of A) UV curing duration of the electrolyte and B) Electrolyte LiCl concentration, and C) the UV curing duration of the encapsulant on the areal capacitance of the MSCs all as a function loading of ceria NPs in the electrode.



## Chapter 3

---

Summarizing the data depicted in Figure 3.4, the optimum chemical composition and processing condition was thus found to be as follows: i) 5 wt.% ceria NPs loading in the electrode, ii) the electrolyte composition (1.6 m LiCl) cured for 20 seconds, and iii) the encapsulant UV curing of 60 seconds. The concentration of the PEGDA was set to 0.08 g.ml<sup>-1</sup> and the concentration of LAP was 0.16 wt.% (by weight of PEGDA). This optimized processing condition and chemistry resulted in the maximized performance of microsupercapacitors.

### 3.2.6. Optimization of electrode active materials

We performed various microstructural characterization on EOGO, including X-ray diffraction (XRD), Raman spectroscopy, X-ray photoelectron spectroscopy (XPS), and transmission electron microscopy (TEM) micrographs, which are shown in Figure 3.5A–F. The simultaneous presence of the sharp peak at  $\sim 26^\circ$  and the wide peak at  $\sim 13^\circ$  in the XRD pattern is attributed to the almost intact graphitic basal plane and the presence of oxygen-containing functional groups on the edges of the planes of EOGO, respectively[282] (Figure 3.5A). Based on the Raman spectroscopy data (Figure 3.5B), the ratio of the intensity of the D band to that of the G band ( $I_D/I_G$ ) is equal to ( $\sim 0.26$ ) which demonstrates relatively low population of defects on the basal plane (i.e., almost intact  $sp^2$  lattice structure) of the EOGO[283], [284]. The peak intensity ratio of the G band to the 2D band ( $I_G/I_{2D}$ ) is a good indication of the number of layers of graphene.[285] We obtained a value of  $I_G/I_{2D}$  equal to  $\sim 2.02$  which reveals the few-layer nature of the EOGO representing a graphitic structure.[286] The deconvolution of the XPS peaks at the C1s region shows that there are five main peaks (Figure 3.5C). These peaks correspond to  $sp^2$  carbon (i.e., C=C bond) at 284.15 eV,  $sp^3$  carbon (i.e., C–C bond) at 284.78 eV, C–O bond at 286.65 eV, C=O bond centered at 288.57 eV, and the shake-up satellite of the  $sp^2$  band at 290.7 eV ( $\pi \rightarrow \pi^*$  transition). The contribution percentage of these peaks as shown in Figure 3.5D, obtained by calculating the area under the peaks, implies that the oxygen-containing functional groups are relatively low in amount and the C–C and C=C carbon bonds make up  $\sim 86\%$  of the bonds. The peak corresponding to the  $\pi \rightarrow \pi^*$  transition of the carbon atoms at 290.7 eV (contributing  $\sim 4.14\%$ ) stems from the  $sp^2$  carbon bonds on the basal plane of the EOGO sheets[287], [288]. This observation further suggests that the basal planes of the

EOGO sheets are almost pristine with very low population of functional groups. Moreover, the C=O bonds are usually present through carboxyl/carbonyl functional groups which are located at the edge of the graphitic sheets, whereas the C–O bonds are formed by the hydroxyl/epoxy groups that appear on the basal plane of the graphitic sheets[289]. Considering the population of the C=O bonds (5.54%) and the C–O bonds (4.59%) (Figure 3.5D), the concentration of the functional groups on the edges are higher than on the basal planes, noting the significant difference in the number of sites on the perimeter and the area of a given graphitic sheet (i.e., perimeter contribution being significantly smaller than the area of the sheets). TEM images of EOGO show their lateral sizes (Figure 3.5E) and their edges (Figure 3.5F). The EOGO sheets on average possess lateral sizes of ~500 nm and they are composed of few stacked layers (up to ~10 layers) of graphene (Figure 3.5F).

## Chapter 3

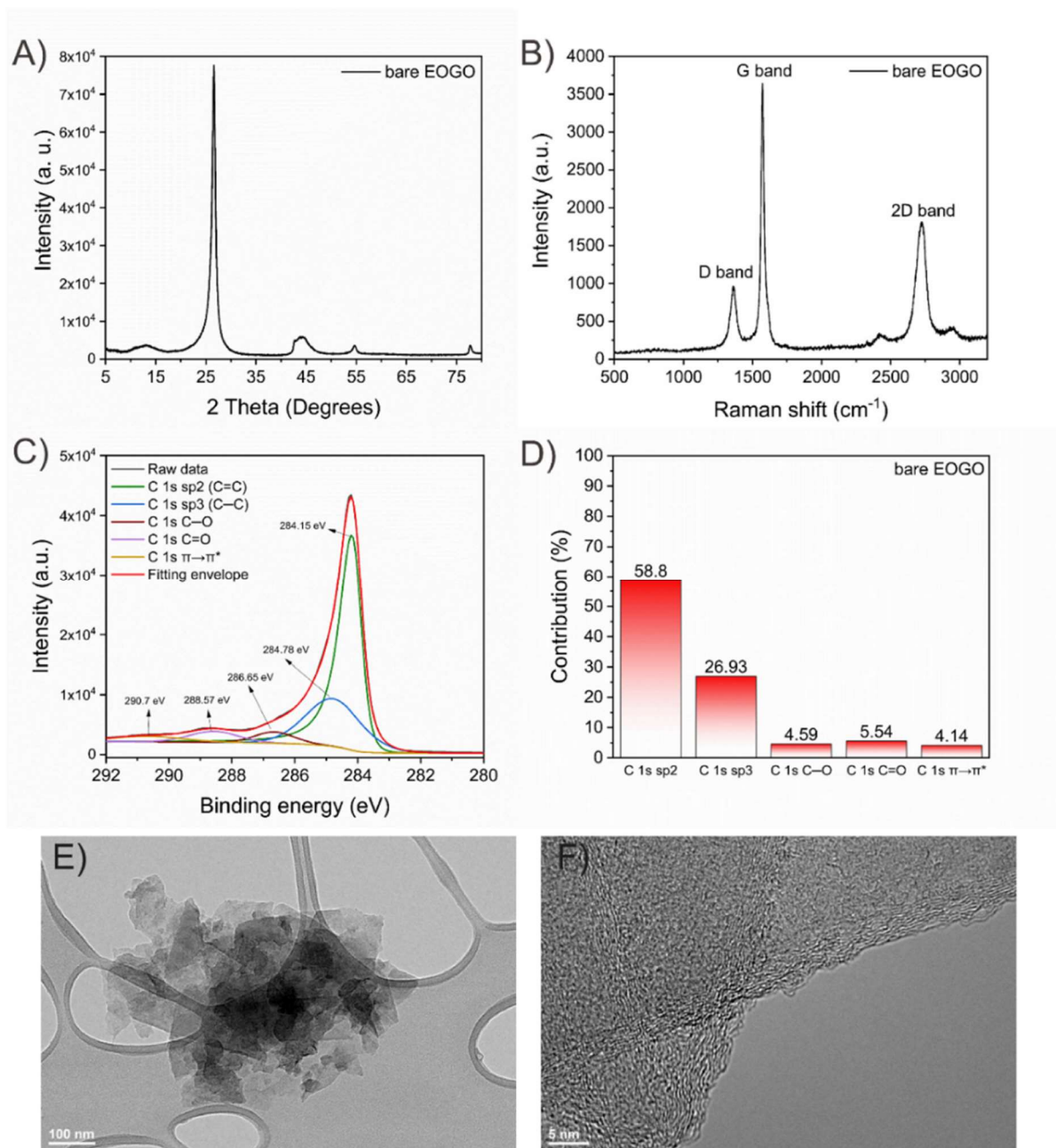


Figure 3.5. Microstructural characterization of EGO precursor the we used as one of the components in formulating the electrode inks, A) XRD pattern, B) Raman spectroscopy data, C) XPS results showing the c1s region and the deconvoluted peaks after fitting, D) contribution of different bonds that the carbon atoms form in EGO, TEM images of the EGO E) showing their size and morphology, and F) the edges of the stacked graphene layers.

As the next step, we continued with the synthesis of the EGO/ceria nanocomposites for use as active materials (varying the ceria nanoparticles loadings). Cerium oxide is one of the most

abundant and least expensive rare metal oxides and it has shown promising redox reactivity as electrode material for supercapacitors.[77], [290]–[292] The redox properties of cerium oxide stem from the presence of binary oxidation states of  $\text{Ce}^{3+}/\text{Ce}^{4+}$  which results in rapid redox reactions.[293]. We also characterized the electrode nanocomposites using XRD, XPS, TEM, and nitrogen surface adsorption/desorption. All the characterization on the electrode inks reported throughout this work, except for the rheological characterization, have been performed on electrode inks dried at room temperature in air. The rheological characterization was performed on liquid electrode inks in the same formulation as was used for 3D printing. The formation of  $\text{CeO}_2$  crystalline phase in the EOGO/ceria nanocomposites was confirmed by XRD (Figure 3.6A). The XRD patterns of all the electrode compositions confirmed the formation of a  $\text{CeO}_2$  crystalline phase[290], [294]. In addition, the TEM images of these samples show that sub-10 nm crystalline nanoparticles of ceria have been formed (Figure 3.6B and 3.6C). The crystalline nature of metal oxides nanoparticles have been shown to improve their pseudocapacitive performance[295], [296]. Based on these TEM images, the nanoparticles in the sample containing 3 wt.% ceria are better dispersed and are relatively smaller (on average smaller than  $\sim 5$  nm), while the ceria nanoparticles in the sample with 32 wt.% ceria loading are clustered, hence they are effectively larger ( $5\text{nm} < X < 10\text{nm}$  in diameter). We also investigated the rheological properties of the electrode inks (Figures 3.6D and 3.6E). The electrode inks showed a shear-thinning behavior, which is preferred for extrusion-based 3D printing[297]. In addition, oscillation amplitude measurements of both inks showed a viscoelastic behavior and  $G'$  (storage modulus, i.e., elastic behavior) values larger than  $G''$  (loss modulus, i.e., viscous behavior) (Figure 3.6E). This observation display a more dominantly elastic behavior of the inks ( $G' > G''$ ) below the flow stress point (i.e., where  $G'$  and  $G''$  intercept); this is favorable for providing shape retention of the inks after printing[298]. Increasing the loading of ceria resulted in an increase in the viscosity and in the storage and loss moduli values of the inks. This is likely due to the effect of the NPs loading on the filling factor of the inks[299].

## Chapter 3

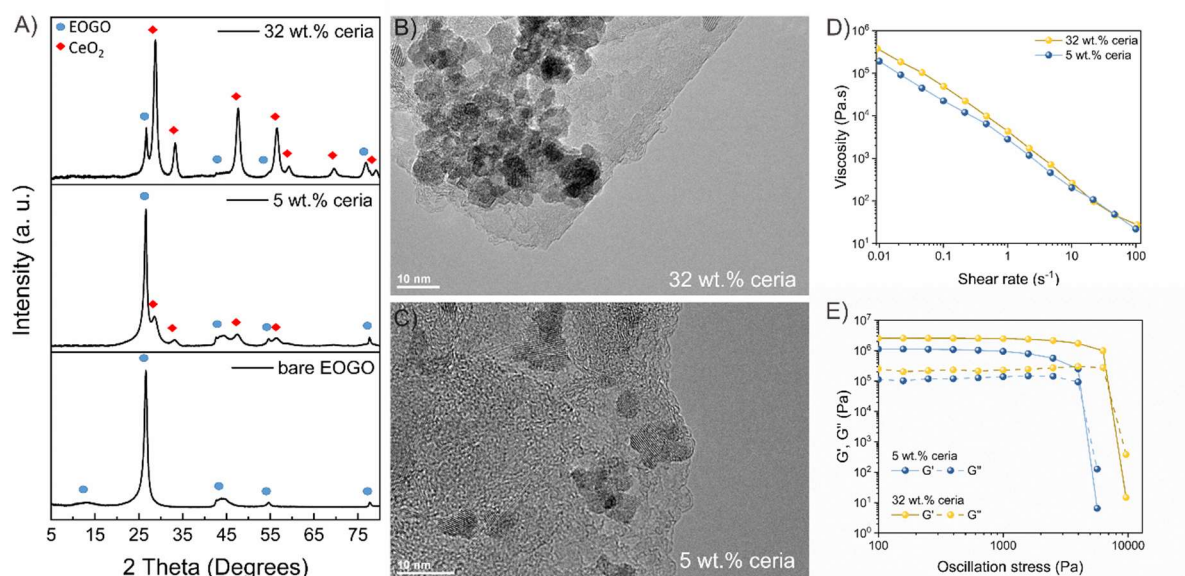


Figure 3.6. A) XRD patterns of the bare EOGO, 5 wt.% ceria loaded electrode, and 32 wt.% ceria loaded electrode (the ceria containing electrodes were dried in air at room temperature), TEM images of B) 32 wt.% ceria loaded electrode, and C) 5 wt.% ceria loaded electrode; rheological characterizations of 5 wt.% ceria loaded, and 32 wt.% ceria loaded electrode inks, D) viscosity as a function of shear rate, and E) oscillation amplitude measurements determining the storage ( $G'$ ) and loss ( $G''$ ) moduli of the inks.

After additive fabrication of microsupercapacitors, we investigated their electrochemical performance as a function of the chemistry and microstructure of their components. It is worth mentioning that we maximized the performance of microsupercapacitors by simultaneous optimization of the processing conditions and chemistries for the electrodes, the electrolyte, and the encapsulant through full fabrication of microsupercapacitors, as described in section 3.2.5., (Selection of the electrolyte, the encapsulant and their UV curing conditions). Here, we present more details on this optimization process, with an emphasis on the electrodes' chemistries. By varying the ceria NPs concentration in the electrodes, we investigated how the electrochemical performance of the MSCs are affected. The concentration of ceria NPs in the electrodes were determined by thermogravimetric analysis (TGA). The corresponding electrochemical characterization results from the cyclic voltammetry (CV), and galvanostatic charge-discharge (GCD) measurements are shown in Figures 3.7A–H. The CV curves (scan rate of 5 mV/s) of all the electrode compositions with

varying concentrations of ceria NPs are presented in Figure 3.7A. Addition of ceria NPs to the electrode nanocomposites up to ~3-5 wt.% ceria enlarged the CV curves, while higher concentrations of ceria NPs significantly narrowed the curves. This result illustrates that there is an optimum range of ceria NPs concentration to maximize the capacitance of the MSCs. Figure 3.7B shows the change in the aerial capacitance of the MSCs fabricated as a function of ceria NPs concentration in their electrodes. Compared to the MSCs constructed with EOGO electrode (i.e., no ceria), the MSCs with electrode compositions of ~3–5 wt.% ceria showed 104–106% increase in their aerial capacitance. Higher concentrations of ceria in the electrodes, however, resulted in a decrease in the areal capacitance. For instance, MSCs fabricated with electrodes composed of ~32 wt.% ceria showed ~97% lower capacitance compared to ceria-free MSCs. The GCD curves also exhibited a similar trend as the electrodes with 3–5 wt.% ceria showed a longer charge/discharge cycle at the same current density (1.42 mA/cm<sup>2</sup>) which confirms a better capacitive behavior (Figure 3.7C). This observation further emphasizes that there is an optimum loading of ceria NPs in the EOGO/ceria NPs nanocomposites to maximize the capacitance.

We correlated the change in the capacitances of the MSCs as a function of the chemistry and the microstructure of their electrodes to: i) size and distribution of the ceria nanoparticles on the surface of EOGO, ii) the specific area of the electrodes, iii) the ratio of the oxidation states of cerium ( $\text{Ce}^{3+}/\text{Ce}^{4+}$ ) in each electrode (implying the presence of oxygen vacancies in the structure of ceria ( $\text{CeO}_2$ )). TEM images of 5 wt.% and 32 wt.% ceria loaded samples (Figures 3.7D and 3.7E, respectively) clearly show the dispersion of the ceria nanoparticles on the EOGO sheets in these nanocomposites. The sample with 5 wt.% ceria loading exhibits better dispersion of nanoparticles and these nanoparticles are smaller compared to the ones in the 32 wt.% ceria containing electrode (insets of Figures 3.7D and 3.7E). Smaller metal oxide nanoparticles that are well dispersed have been shown to significantly increase the capacitance of supercapacitors[300]. Furthermore, loading, size and dispersion of ceria nanoparticles strongly affected the specific surface areas of the electrodes (Figure 3.7F). Increasing the ceria nanoparticles loading decreased the specific surface area of the electrodes, likely due to the clustering of nanoparticles and heavier coverage of the EOGO

## Chapter 3

---

sheets by them. Although presence of even low loadings of ceria nanoparticles (i.e., 3–5 wt.%) significantly decreased the specific surface of the electrodes from 368 m<sup>2</sup>/g in EOGO to 286 m<sup>2</sup>/g and 284 m<sup>2</sup>/g in 3 wt.% and 5 wt.% ceria loaded electrodes, respectively, the capacitance values increased by ~106% (Figure 3.7B). This result further emphasizes that the specific surface area of the electrodes is not the dominant factor determining their capacitance[301]. The ratio of Ce<sup>3+</sup>/Ce<sup>4+</sup> oxidation states in the electrodes as a function of varying concentrations of ceria NPs is shown in Figure 3.7G. The concentration of the Ce<sup>3+</sup> oxidation state is an indication of oxygen vacancies in the structure of NPs[302]. Higher oxygen vacancy concentration facilitates the change in oxidation states of ceria (between Ce<sup>3+</sup> and Ce<sup>4+</sup>), which is crucial for enhanced surface reactivity[303]. The concentration of Ce<sup>3+</sup> oxidation states is higher in the electrodes with loading of ceria NPs up to 5 wt.%. Further increase in the loading of ceria NPs decreased the Ce<sup>3+</sup> oxidation state in the electrodes. This might be due to the clustering of the ceria NPs in the electrodes with higher loadings of ceria. As the size of ceria NPs increases, the contribution from oxygen vacancies population is decreased[303].

As shown in Figure 3.7H, we also performed a kinetic analysis on the charge storage of the MSCs as a function of electrode ceria NP concentration to investigate the contribution of electrical double layer capacitance (EDLC), pseudocapacitance stemming from the faradaic reactions, and diffusive contribution based on ion insertion. While EDLC and faradaic reactions are fast kinetic processes, the ion insertion process is limited by ion diffusion.[304], [305] With the addition of ceria NPs up to 5 wt.%, the diffusive contribution is increased by 3%, though the EDLC contribution is dominant in these electrodes. The diffusive contribution can occur in two possible ways: i) through the insertion of the ions into the surface of ceria NPs and ii) through the insertion of ions between the EOGO stacked layers. Further addition of ceria NPs, flipped the ratio of the EDLC and diffusive contributions and the diffusive contribution became more dominant. These results can be further explained by considering the capacitance values of the electrodes and their specific surface area values (Figures 3.7B and 3.7F respectively). Addition of up to 5 wt.% ceria NPs resulted in the maximum capacitance obtained, which also correlates with the highest values of specific surface area among the ceria-containing electrodes. These results demonstrate that at this critical concentration of ceria NPs, the

specific surface areas of the samples are still high enough and the ceria NPs can more effectively contribute to the charge storage. Ceria NPs contribution at this critical loading can be attributed to their smaller size (on average <5 nm) and homogeneous dispersion on the EOGO sheets when compared to the samples with higher loadings (Figures 3.7D and 3.7E).

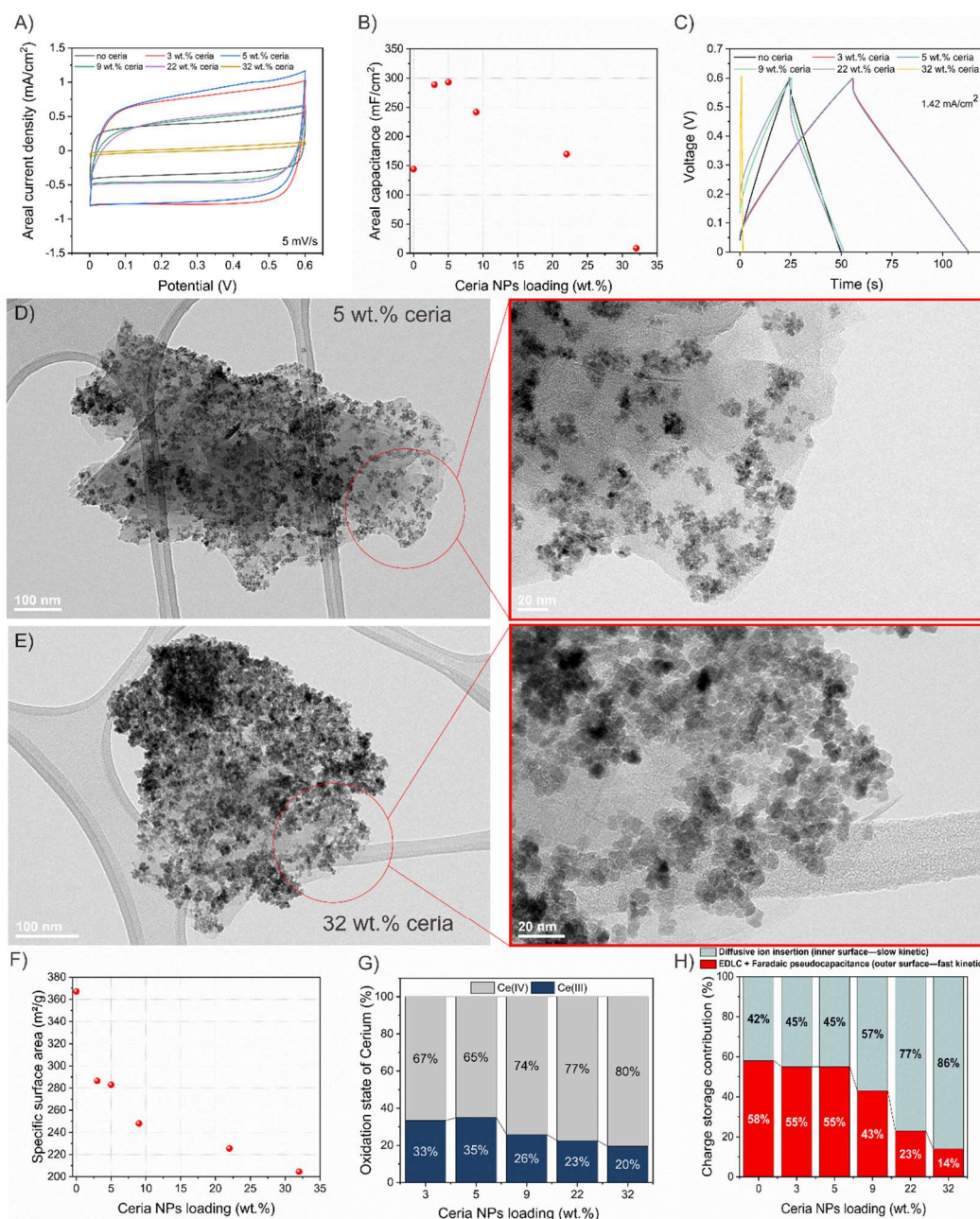


Figure 3.7. Electrochemical characterization of the microsupercapacitors: A) CV curves at the scan rate 5 mV/s, B) areal capacitances of the microsupercapacitors as a function of ceria NPs loading at the scan rate of 5 mV/s, C) GCD curves of the microsupercapacitors at a current density of 1.42 mA/cm<sup>2</sup>, TEM images of D) 5 wt.% ceria-



containing electrodes—inset shows higher magnification of the same image, and E) 32 wt.% ceria-containing electrode—inset exhibits higher magnification of the same image, F) Specific surface area measurements as a function ceria NPs loading, G) The ratio of  $\text{Ce}^{3+}/\text{Ce}^{4+}$  oxidation states in the electrodes with varying concentrations of ceria NPs, H) kinetic analysis on the charge storage of the MSCs comprising electrodes with varying amounts of ceria NPs to investigate the contributions of electrical double layer capacitance (EDLC), diffusive mechanisms.

### 3.2.7. Realization of microsupercapacitors with optimal performance

Now, we discuss the optimization procedure that we followed in order to maximize the performance of microsupercapacitors. Figures 3.8A–C show the corresponding electrochemical characterization results from cyclic voltammetry (CV), galvanostatic charge-discharge (GCD), and electrochemical impedance spectroscopy (EIS) measurements of MSCs fabricated with optimized chemistries and processing conditions, as will be discussed further below. As a reminder, the optimum chemical composition and processing condition was found to be as follows: i) 5 wt.% ceria NPs loading in the electrode, ii) the electrolyte composition (1.6 m LiCl) cured for 20 seconds, and iii) the encapsulant UV curing of 60 seconds. The concentration of the PEGDA was set to 0.08 g.ml<sup>-1</sup> and the concentration of LAP was 0.16 wt.% (by weight of PEGDA). Figure 3.8A demonstrates the CV curves at different scan rates ranging from 2 mVs<sup>-1</sup> to 100 mVs<sup>-1</sup>. The increase in the scan rate resulted in enlarging the area under the CV curves. Figure 3.8B shows the GCD curves at different current densities (from 1.42 mAcm<sup>-2</sup> up to 5.72 mAcm<sup>-2</sup>). As expected, with increasing current density, the full cycle of charge and discharge became shorter. Figure 3.8C, exhibits the change in areal and volumetric capacitances as a function of scan rate (from 2 mVs<sup>-1</sup> to 100 mVs<sup>-1</sup>). While the areal capacitance decreased from 323 mFcm<sup>-2</sup> at 2 mVs<sup>-1</sup> to 100.9 mFcm<sup>-2</sup> at 100 mVs<sup>-1</sup>, the volumetric capacitance decreased from 10.8 Fcm<sup>-3</sup> to 3.36 Fcm<sup>-3</sup>. The results of EIS analysis are shown in Figure 3.8D. There is a relatively small semicircle moving from the high-frequency region towards the low-frequency region, which demonstrates a relatively low charge transfer resistance in the system. In addition, the linear region exhibits a relatively steep slope at low frequencies, indicative of a desirable capacitive behavior. The inset highlights the high frequency region of the plot in more detail. We compared the reported cyclic life and areal capacitance of various microsupercapacitors in the literature with respect to their active

charge storage area (i.e., electrode) to our system (Figure 3.8E). The comparison systems include graphene-vanadium quantum dots/reduced graphene oxide (G–VNQDs/rGO) (207.9 mFcm<sup>-2</sup>—8000 cycles—0.16 cm<sup>2</sup>),[181] Graphene-CNT (9.81 mFcm<sup>-2</sup>—10000 cycles—0.3 cm<sup>2</sup>),[306] Boron-Doped Graphene (16.5 mFcm<sup>-2</sup>—12000 cycles—0.6 cm<sup>2</sup>)[307], Ag@polypyrrole (47.5 mFcm<sup>-2</sup>—10000 cycles—4 cm<sup>2</sup>),[308] MXene (158 mFcm<sup>-2</sup>—17000 cycles—1 cm<sup>2</sup>,[185] 2100 mFcm<sup>-2</sup>—10000 cycles—1.25 cm<sup>2</sup>,[178] 1035 mFcm<sup>-2</sup>—1200 cycles—0.48 cm<sup>2</sup>[260]), MnO<sub>2</sub>/graphite (40.2 mFcm<sup>-2</sup>—2000 cycles—6 cm<sup>2</sup>),[309] and also our optimized result (323 mFcm<sup>-2</sup>—21000 cycles—0.14 cm<sup>2</sup>). Although there are a few reported examples of microsupercapacitors with higher capacitance values compared to our best results (for instance, two MXene-based microsupercapacitors with performance levels as high as 2100 mFcm<sup>-2</sup>—10000 cycles—1.25 cm<sup>2</sup>,[178] 1035 mFcm<sup>-2</sup>—1200 cycles—0.48 cm<sup>2</sup>[260]), these systems utilized larger active areas and also showed shorter cyclic life. While our system achieved at least 21000 cycles of charge-discharge with over 91% capacitance retention, these systems delivered 10000 cycles at a ×8.93 larger footprint,[178] and 1200 cycles at a ×3.43 larger footprint[260], respectively. The energy density and power density values obtained in our system are 16.1 μWhcm<sup>-2</sup> and 3052 mWcm<sup>-2</sup> respectively, which are significantly higher than the other systems as shown in Figure 3.8F. To the best of our knowledge, our results thus introduce the smallest fully 3D printed microsupercapacitor with an outstanding combination of performance (i.e., capacitance, cyclic life, energy density and power density) at such a small footprint. In addition, Figure 3.8G exhibits the cyclic life results of our optimal system in more detail. After 21000 cycles at a current density of 5 mAcm<sup>-2</sup>, ~91.3% of capacitance of the system was retained. The inset shows the GCD curve of the first and the last (21000<sup>th</sup>) cycles. As expected, the duration of the charge-discharge process is increased in the last cycle compared to the first one. However, the discharging time of the last cycle became shorter which may be due to the aging of the electrode over the large number of cycles. According to X-ray tomographic scans (Figure 3.8H), the electrodes are relatively homogenous in dimension —thickness of ~500 μm and height of ~300 μm. We used the height values obtained by X-ray tomography to calculate the volumetric capacitance of our system.

## Chapter 3

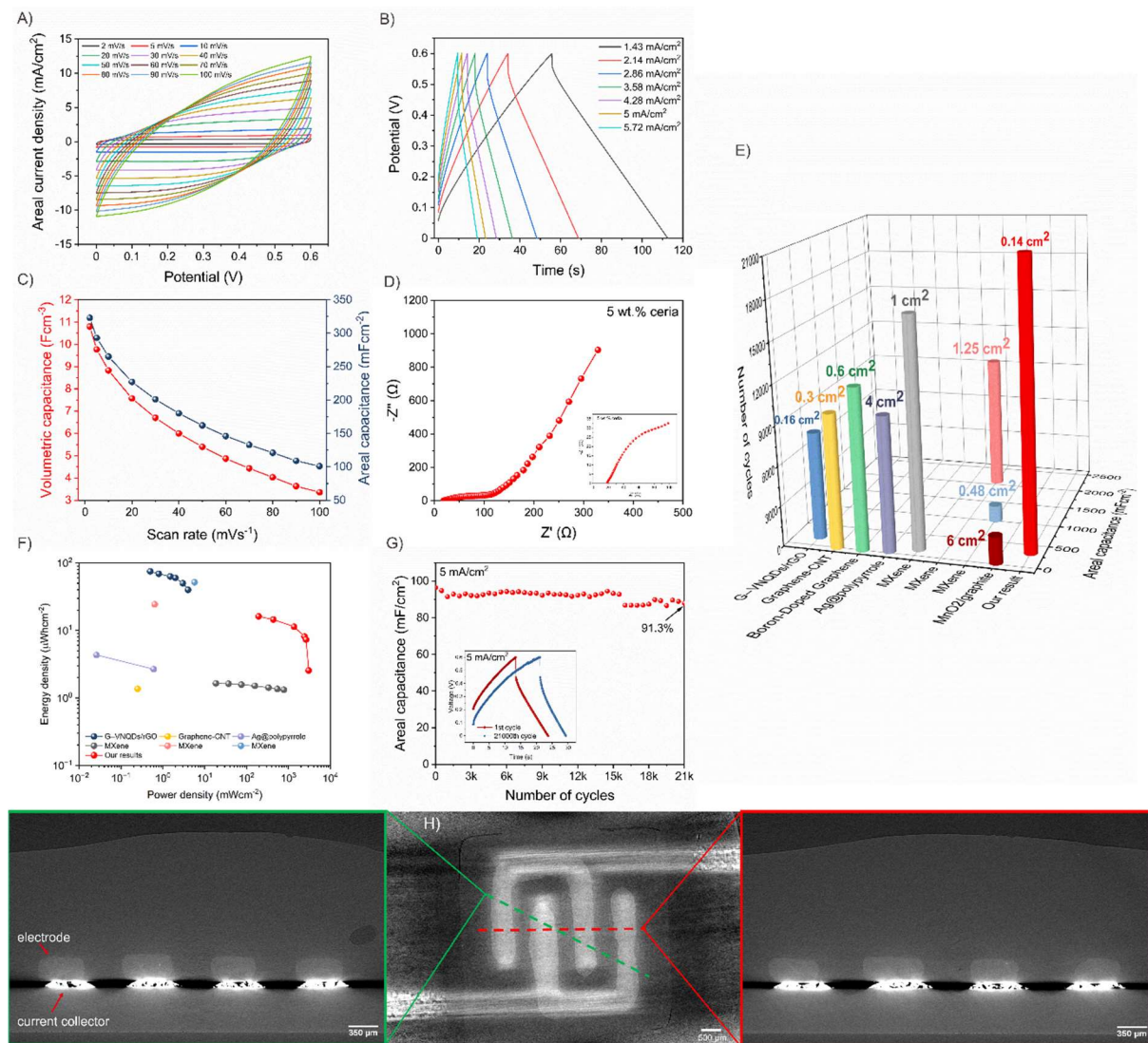


Figure 3.8. Electrochemical characterization of the best performing microsupercapacitor (5 wt.% ceria-containing electrode), A) CV curves at different scan rates (2 mVs<sup>-1</sup> to 100 mVs<sup>-1</sup>), B) GCD curves at different current densities (1.43 mAcm<sup>-2</sup> to 5.72 mAcm<sup>-2</sup>), C) areal and volumetric capacitance values as a function of scan rate (2 mVs<sup>-1</sup> to 100 mVs<sup>-1</sup>), D) EIS data—the inset shows the high-frequency region in more details, E) comparison of the cyclic life and areal capacitance values of a selected number of microsupercapacitors with respect to their active charge storage area (i.e., electrode) and our system, F) the Ragone plot showing the energy and power densities of some of the selected system as shown in part (E) including our result, G) cyclic life of our system—the inset demonstrates the GCD curves of the first and the last cycles, H) X-ray tomography images of the fully-fabricated microsupercapacitor—the insets are two cross-section images showing the different components of the system with their geometrical dimensions.

### 3.3. Materials and Methods

In this section, we list all the chemicals, synthesis procedures, and characterizations that we have used/performed in this chapter.

#### 3.3.1. Chemicals

Edge-oxidized graphite oxide (EOGO) was purchased from Garmor Inc. and cerium nitrate hexahydrate (99% trace metals basis), sodium hydroxide (anhydrous, reagent grade,  $\geq 98\%$ ), lithium chloride (ACS reagent,  $\geq 99\%$ ), poly(ethylene glycol) diacrylate (average Mn 700) were purchased from Sigma Aldrich. Lithium phenyl-2,4,6-trimethylbenzoylphosphinate (LAP) (99%) was purchased from Apollo scientific. All chemicals were used as received without further modifications. We purchased a commercial silver paste (DELO-DUALBOND IC343) from DELO and used it for the fabrication of the current collectors. We used a commercial UV-curable encapsulant (DELO Dualbond AD 761) for encapsulation of the MSCs.

#### 3.3.2. Synthesis of edge-oxidized graphite oxide (EOGO)/ceria nanocomposites

We synthesized the edge-oxidized graphite oxide (EOGO)/ceria nanocomposites by a facile sonochemical method. As an example, for the synthesis of the EOGO/ceria nanocomposite with 22 wt.% ceria, we dispersed EOGO (2.5 g) in deionized water (50 ml). We sonicated this suspension in a sonication bath for 15 min (mixture I). After this step and while sonication was continued, an aqueous solution of cerium nitrate hexahydrate (25 ml of 0.5 M) was added (increments of 500  $\mu\text{l}$ ) to the EOGO suspension within 15 min (mixture II). Then, we continued the sonication for another 15 min while adding an aqueous solution of sodium hydroxide (25 ml of 0.5 M) to this mixture (increments of 250  $\mu\text{l}$ ) (mixture III). Afterwards, we continued the sonication of the mixture III for 2 hours (mixture IV). At the end of the sonication procedure, the mixture IV was poured into 50 ml centrifuge tubes to be centrifuged at 10000 rpm for 15 minutes at 4 °C. The centrifugation of the mixture IV was repeated three more times under the same conditions, with intermediate disposal the supernatant and redispersion of the solid between centrifugation steps, so that the pH of the supernatant went above  $\sim 6$ . We followed a similar procedure for the preparation of the EOGO ink, EOGO was added (2.5 g) to deionized

## Chapter 3

---

water (50 mL) and the sonication was continued for 2 hours (no other solutions were added). We similarly performed the centrifugation process four times until the pH of the supernatant reached above ~6. At the end of the last centrifugation step, we collected the pastes at the bottom of the centrifuge tubes and transferred them to 3 ml barrels without further modifications. The barrels were mounted on the 3D printer for printing the electrodes. Table 3.1 summarizes the proportion of the precursors used in the synthesis of electrode materials with varying ceria NPs concentrations.

Table 3.1. Proportion of the precursors used in the synthesis of electrode materials with varying Ceria NPs concentrations.

| Sample ID | Ceria NPs concentration (wt.%) <sup>*</sup> | Cerium nitrate hexahydrate concentration (25 ml) | Sodium hydroxide concentration (25 ml) |
|-----------|---|--|--|
| S0        | 0   | 0  | 0                                      |
| S1        | 3   | 0.03125 m  | 0.03125 m                              |
| S2        | 5   | 0.0625 m   | 0.0625 m                               |
| S3        | 9   | 0.25 m   | 0.25 m                                 |
| S4        | 22  | 0.5 m  | 0.5 m                                  |
| S5        | 32  | 1 m  | 1 m                                    |

<sup>\*</sup>determined by thermogravimetric analysis (TGA)

### 3.3.3. Preparation of the UV-curable electrolytes

In a typical procedure, 10 ml solutions of poly (ethylene glycol) diacrylate (PEGDA) with a concentration of 0.2 g.ml<sup>-1</sup> were prepared. Then, 10 ml solutions of LiCl at varying concentrations (2m to 7.5m) were prepared. The LiCl solution was added at once to the PGDA solution and stirring was continued for 30 min at 50 °C (mixture I). Then, 5 ml solutions of lithium phenyl-2,4,6-trimethylbenzoylphosphinate (LAP) (0.8 wt.% by weight of PEGDA) were prepared and this solution was added to mixture I to make the UV-curable electrolyte (total volume of 25 ml).

### 3.3.4. 3D printing of the Microsupercapacitors

We printed the MSCs by a combination of extrusion-based 3D printing and fused deposition modeling (FDM) printing on a multi-head 3D printer (BioX6-Cellink) equipped with six different

heads. We started 3D printing of the MSCs first by printing the current collectors on a wet-oxidized silicon wafer using a pneumatically pressurized head on the 3D printer. We used a commercial silver paste (DELO-DUALBOND IC343). The current collector was printed at room temperature using a nozzle with an inner diameter of 100  $\mu\text{m}$  (6.35 mm nozzle length). The printing pressure and printing speed were 5.4 bar and 2  $\text{mm}\cdot\text{s}^{-1}$ , respectively. After the printing of the current collectors, the printed patterns were heat treated at temperatures ranging from 400  $^{\circ}\text{C}$  to 550  $^{\circ}\text{C}$  for 10 to 30 min in air in a muffle furnace (Thermo SCIENTIFIC F6020C-33-80). Next, the package walls were printed using polycaprolactone (PCL) surrounding the interdigitated fingers of the current collectors through FDM. The nozzle inner diameter, nozzle temperature, printing pressure and printing speed were set to 410  $\mu\text{m}$ , 140  $^{\circ}\text{C}$ , 5.7 bar, and 1  $\text{mm}\cdot\text{s}^{-1}$ , respectively. Next, we deposited the electrode aqueous inks (edge-oxidized graphite oxide (EOGO)/ceria NPs nanocomposites + water) on the interdigitated fingers of the current collectors through extrusion-based 3D printing at room temperature. We used a nozzle with an inner diameter of 330  $\mu\text{m}$  (6.35 mm nozzle length), and we set the printing pressure and speed to 2–2.2 bar, and 3  $\text{mm}\cdot\text{s}^{-1}$ , respectively. Then, we deposited a UV-curable electrolyte (poly (ethylene glycol) diacrylate (PEGDA) + LiCl + lithium phenyl-2,4,6-trimethylbenzoylphosphinate (LAP) + water) through a nozzle with inner diameter of 1 mm in the interior space inside the package walls to immerse the electrodes. Subsequently, we UV cured the electrolyte for various time intervals using a UV curing head on the 3D printer (UV wavelength of 365 nm) from a 1.5 cm distance to cross-link and mechanically stabilize the structure. Afterwards, we deposited a UV-curable encapsulant (DELO Dualbond AD 761—a modified epoxy resin) on top of the cured electrolyte and around the exteriors of the package walls using a nozzle with an inner diameter of 1 mm. We then UV cured the encapsulant using another UV curing head on the 3D printer (UV wavelength of 405 nm) from a 3 cm distance for different time intervals to realize the fully integrated MSCs.

### 3.3.5. Characterization Methods

#### **Thermogravimetric analysis (TGA) and dynamic scanning calorimetry (DSC) measurements**

TGA analyses were performed on dried electrode inks using a LINSEIS STA 1600 in air with a heating rate of 10 °C/min from room temperature up to 750 °C. We dried all the electrode inks at room temperature under ambient conditions for 2 days and then obtained these samples in powder form and used them for the measurements. As the EOGO electrode without ceria showed a residue of around 4 wt.% at the end of the TGA measurement, we assumed this amount of EOGO to be present in all the ceria-containing electrodes, as well. Hence, we subtracted this value (4 wt.%) from the residual values obtained for the TGA measurements of the other electrode materials to calculate the weight percentage of ceria NPs in these electrode materials. Figure 3.9 shows the TGA curves of the electrode materials and table 3.2 summarizes the calculated ceria NPs loading of each electrode material derived from the TGA measurements.

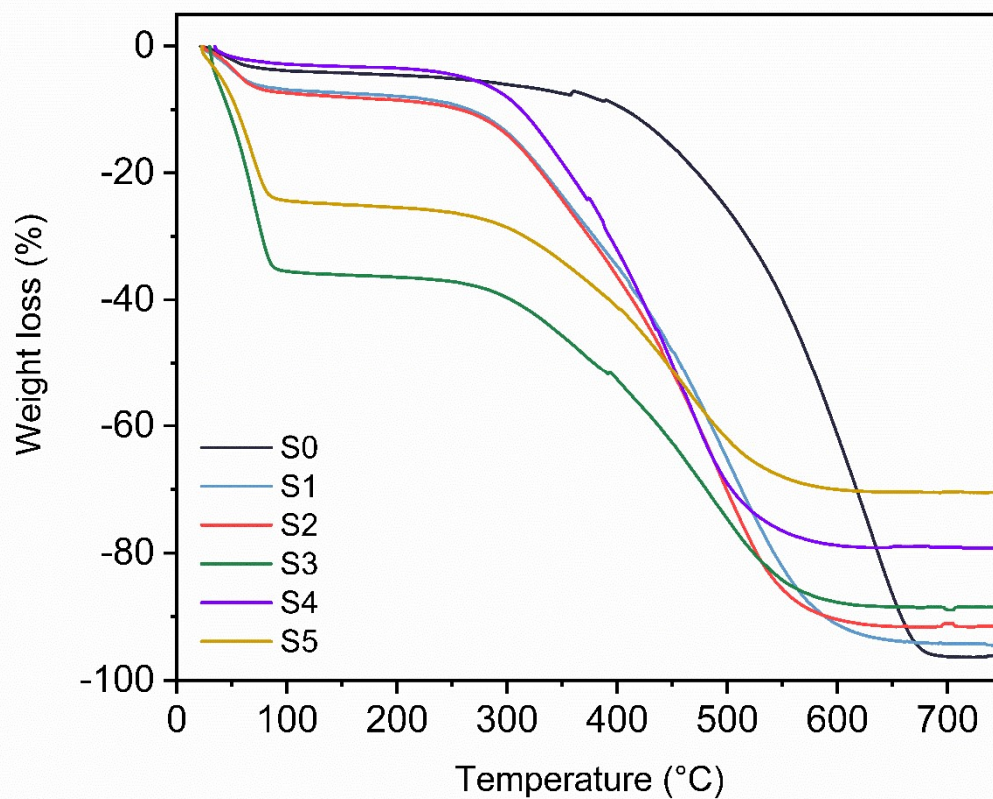


Figure 3.9. Thermogravimetric analysis (TGA) plots of all the electrode active materials.

Table 3.2. Ceria NPs concentrations of different electrode materials determined by TGA.

| Sample ID | Ceria NPs concentration (wt.%) |
|-----------|--------------------------------|
| S0        | 0                              |
| S1        | 3                              |
| S2        | 5                              |
| S3        | 9                              |
| S4        | 22                             |
| S5        | 32                             |

We also performed TGA and DCS analysis on the silver paste used for printing the current collectors to find out the most suitable heat treatment condition to achieve the maximum



## Chapter 3

---

conductivity of the printed paste. We printed squares of 8 mm × 8 mm and heat treated them at temperatures ranging from 400 °C to 550 °C for 5 to 30 minutes. We selected this heat treatment regime based on the TGA and DSC curves of the silver paste as shown in Figure 3.10.

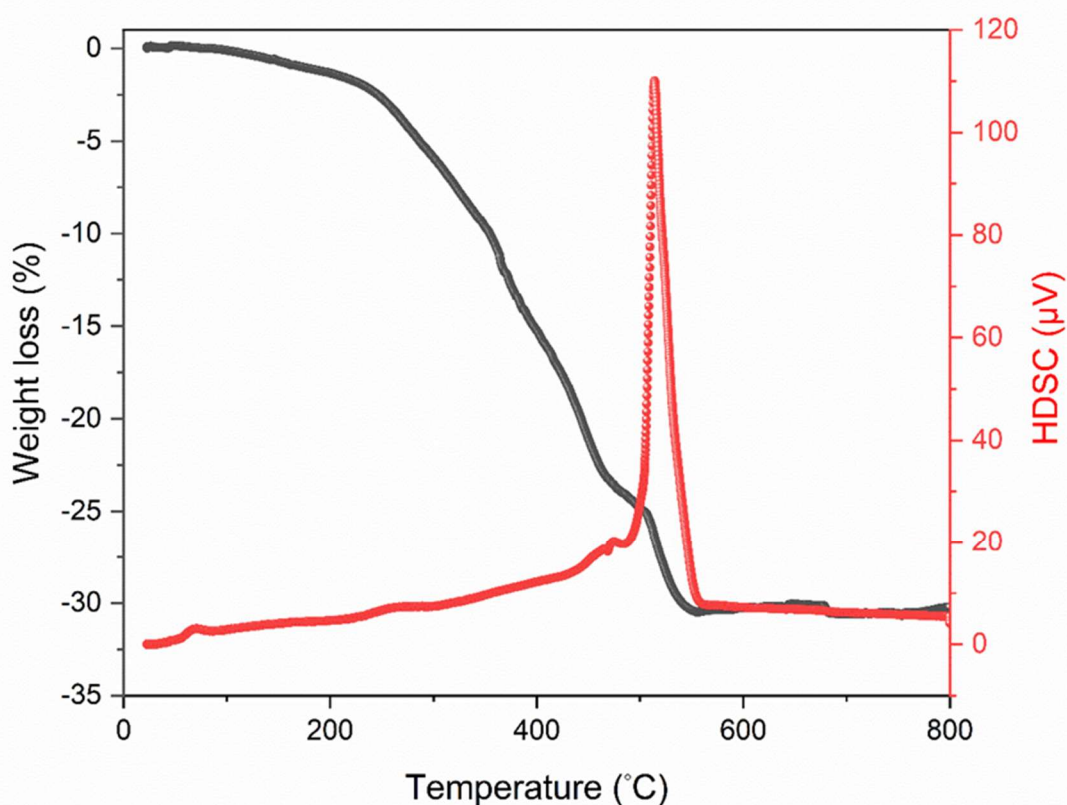


Figure 3.10. TGA and DSC curves of the silver paste used for 3D printing of the current collector. A peak in the DSC plot is gradually formed from temperatures around 300 °C that extends up to 570 °C.

### TEM imaging and energy dispersive X-ray spectroscopy (EDX)

TEM imaging and EDX analysis were performed on an analytical TEM instrument (FEI Tecnai Osiris). We used Lacey/Carbon TEM grids (200 Mesh, Cu, LC200-Cu-25-Electron Microscopy Sciences) for the observations. For the imaging conditions, we set the acceleration voltage to 200kV and the vacuum level in the column was 8.8e-008 Torr (1.18e-005 Pascal). Figures

3.11–3.15 show the TEM images, EDX elemental maps, and EDX spectra of the ceria NPs-containing electrode materials. These images show the formation of sub-10 nm cerium oxide NPs on the EOGO sheets. This is also confirmed by the EDX elemental maps and spectra. It can be seen that by the increase in loading of cerium oxide NPs, they started to agglomerate as can reasonably be expected, and also they heavily covered the surface of EOGO.

## 3 wt.% ceria-containing electrode

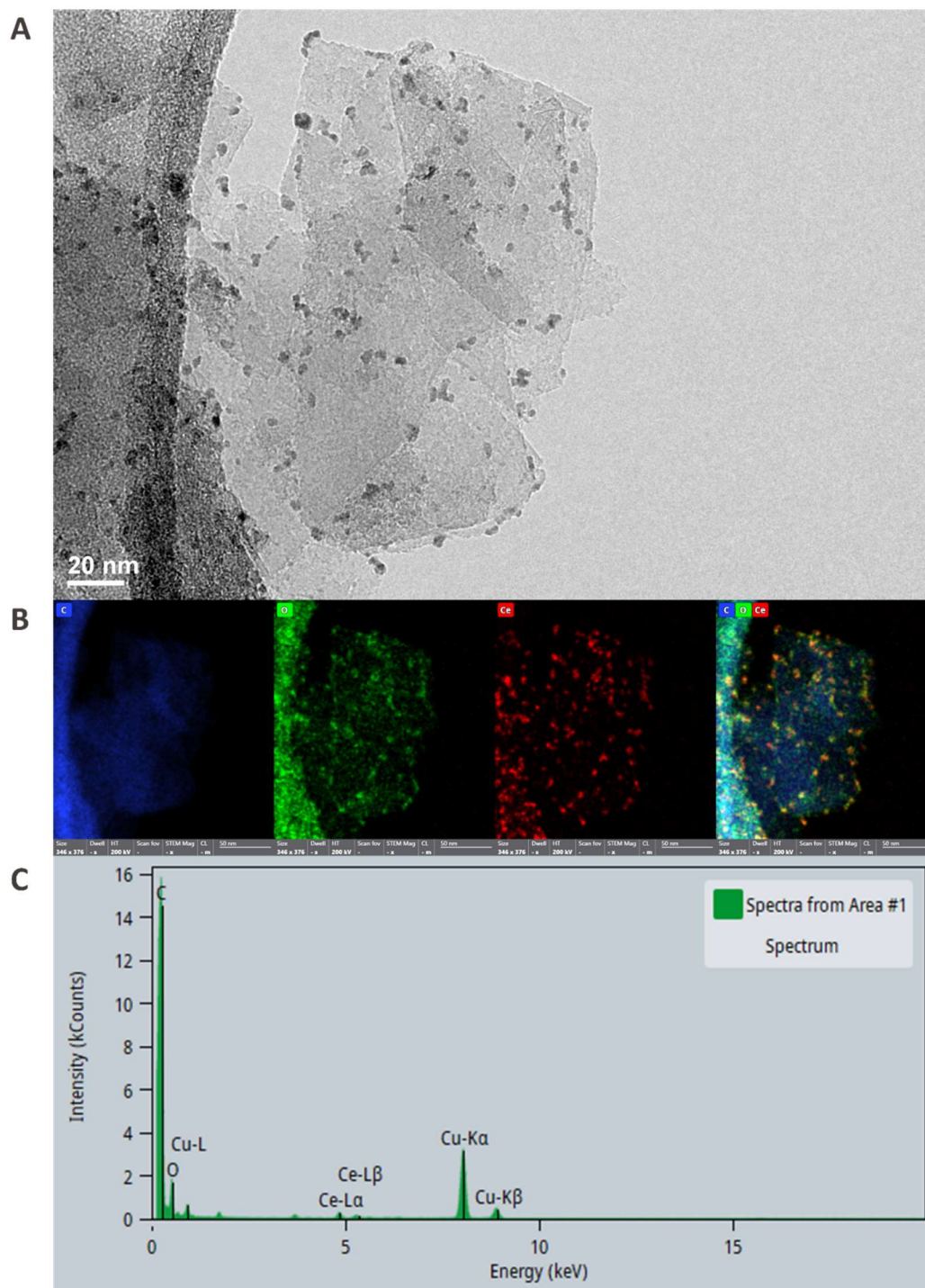


Figure 3.11. A) a TEM image, B) EDX elemental maps, and C) EDX spectrum of the electrode containing 3 wt.% ceria NPs.

## 5 wt.% ceria-containing electrode

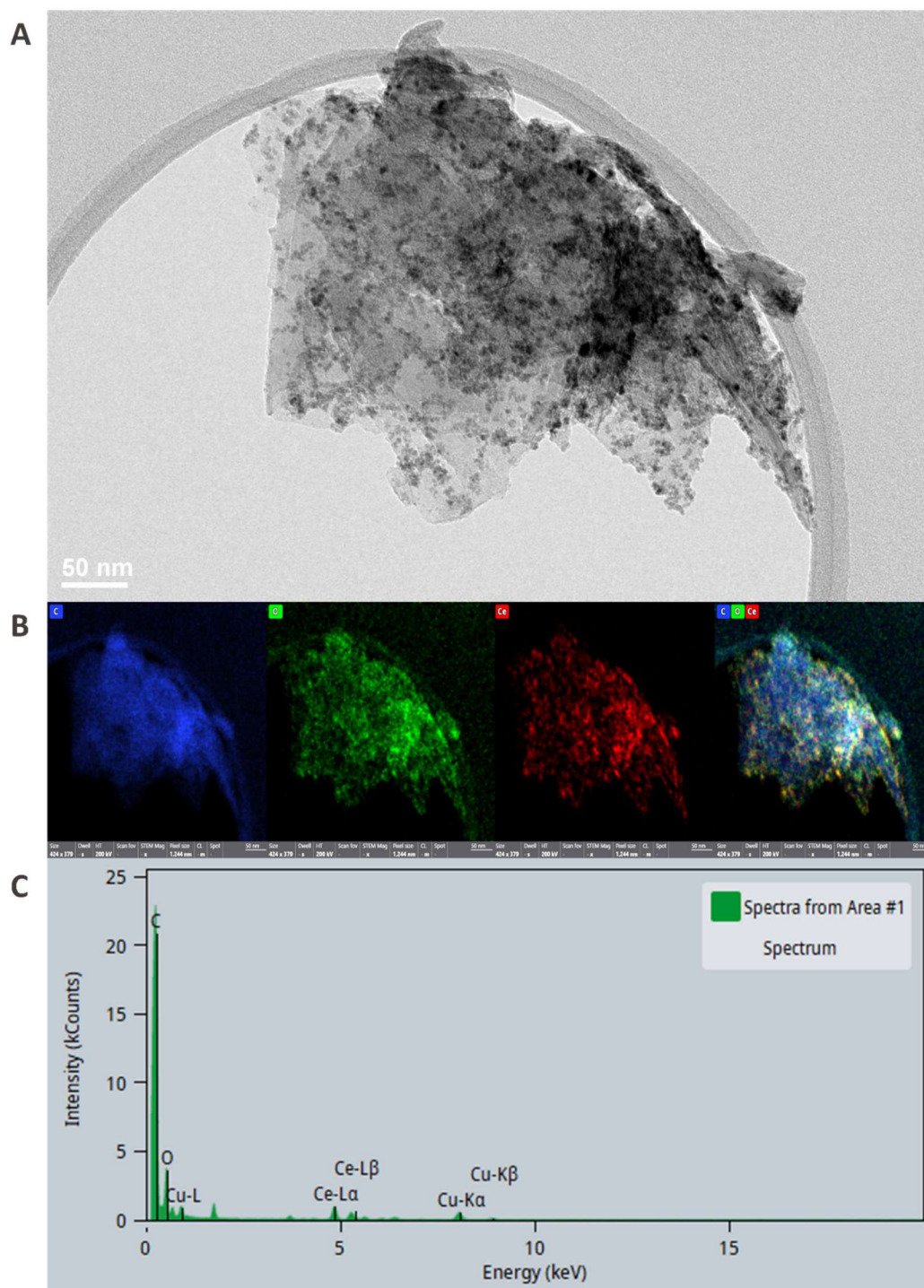


Figure 3.12. A) a TEM image, B) EDX elemental maps, and C) EDX spectrum of the electrode containing 5 wt.% ceria NPs.

## 9 wt.% ceria-containing electrode

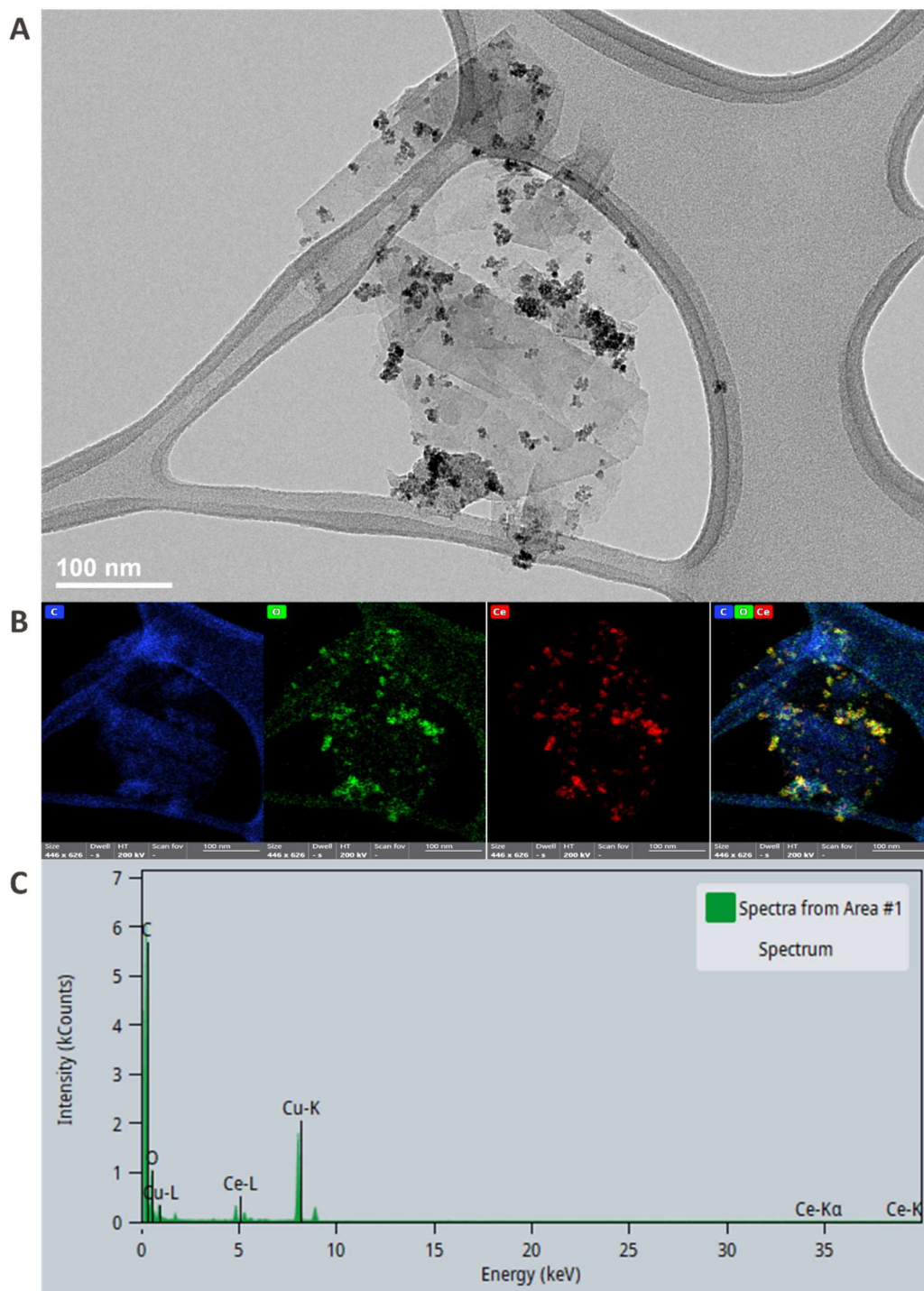


Figure 3.13. A) a TEM image, B) EDX elemental maps, and C) EDX spectrum of the electrode containing 9 wt.% ceria NPs.

## 22 wt.% ceria-containing electrode

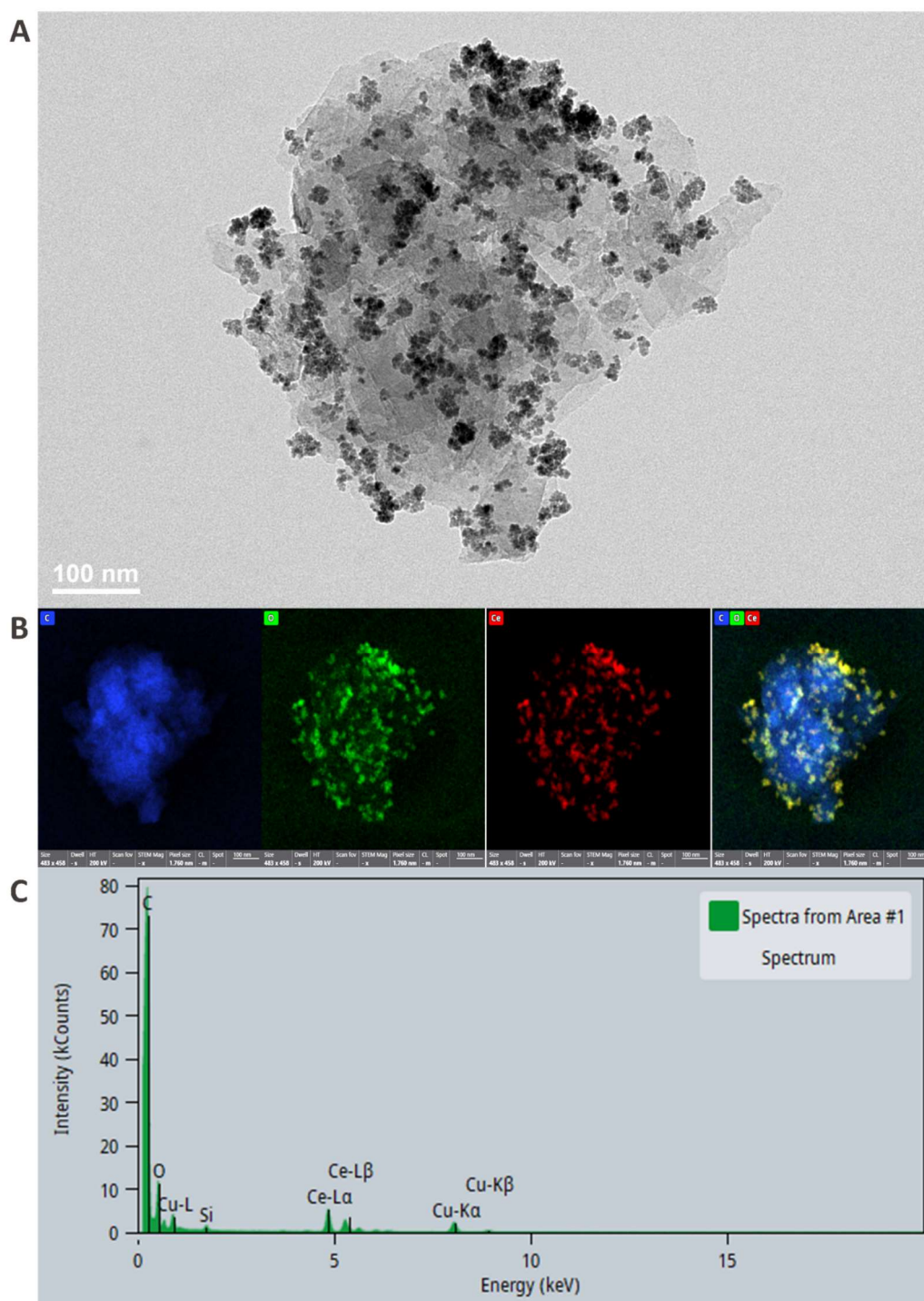


Figure 3.14. A) a TEM image, B) EDX elemental maps, and C) EDX spectrum of the electrode containing 22 wt.% ceria NPs.

## Chapter 3

### 32 wt.% ceria-containing electrode

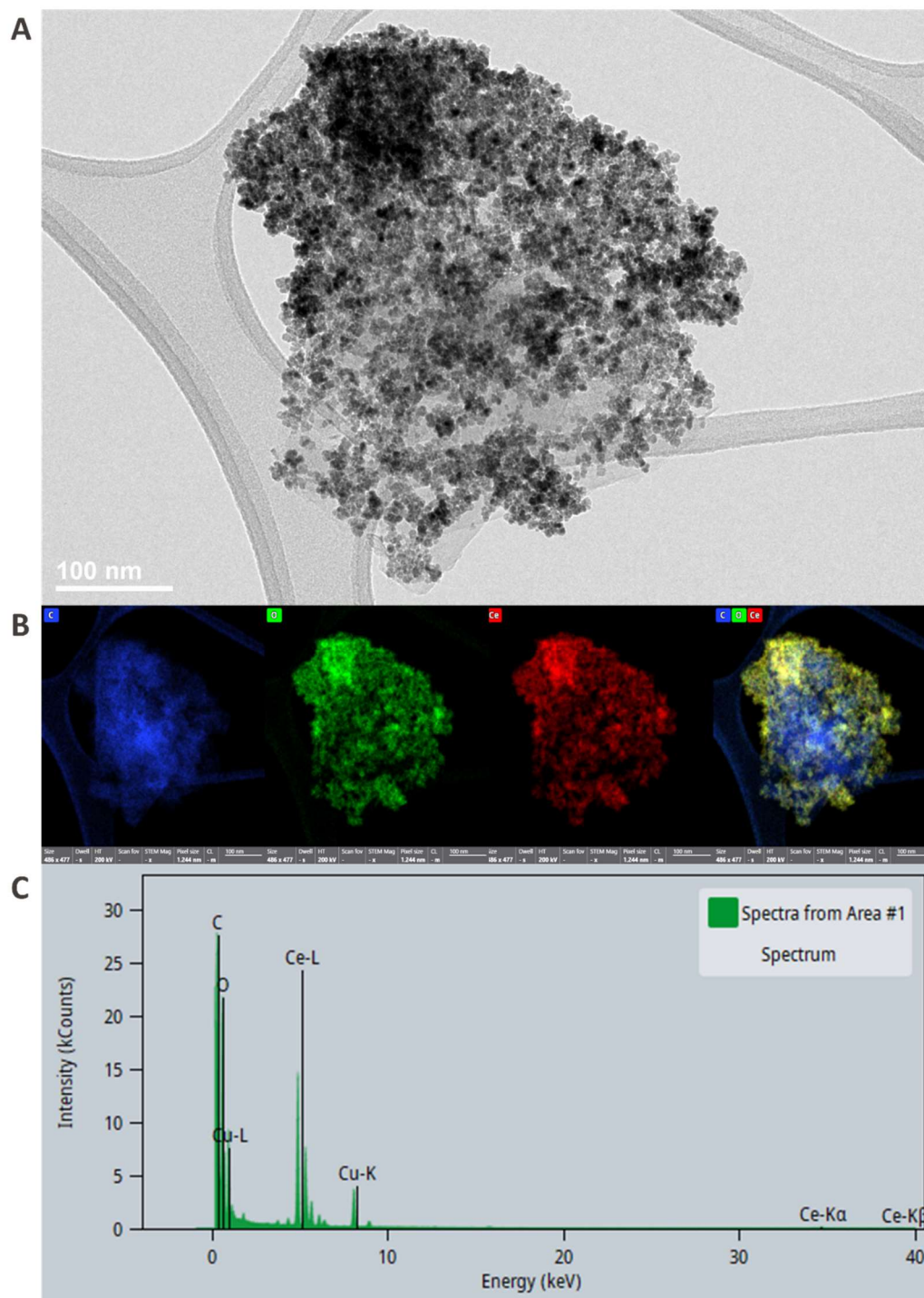


Figure 3.15. A) a TEM image, B) EDX elemental maps, and C) EDX spectrum of the electrode containing 32 wt.% ceria NPs.

### **Four-Point-Probe measurements**

Electrical resistivity of the current collector was measured using a four-point probe (LUCAS LABS 302) with a KEITHLEY 2601 SYSTEM Source Meter. We used this tool to investigate the electrical resistivity of the heat-treated current collectors to understand what heat treatment regime results in the lowest resistivity.

### **Nitrogen gas adsorption/desorption measurements**

Specific surface area measurements were conducted on the dried electrode inks using a surface area analyzer (Anton-paar, autosorb iQ-adsorption analyzer) applying the Brunauer–Emmett–Teller (BET) method. We dried all the electrode inks at room temperature under ambient conditions for 2 days and then obtained these samples in powder form and used them for the measurements. These samples were first degassed under vacuum for 4 hours at a temperature of 200 °C. Then, Nitrogen gas adsorption/desorption measurements were performed to find the values of specific surface area of the electrode materials. We dried all the electrode inks at room temperature under ambient conditions for 2 days and then obtained these samples in powder form and used them for the measurements. Figure 3.16 demonstrates the Nitrogen gas adsorption/desorption isotherms of all the electrode materials.



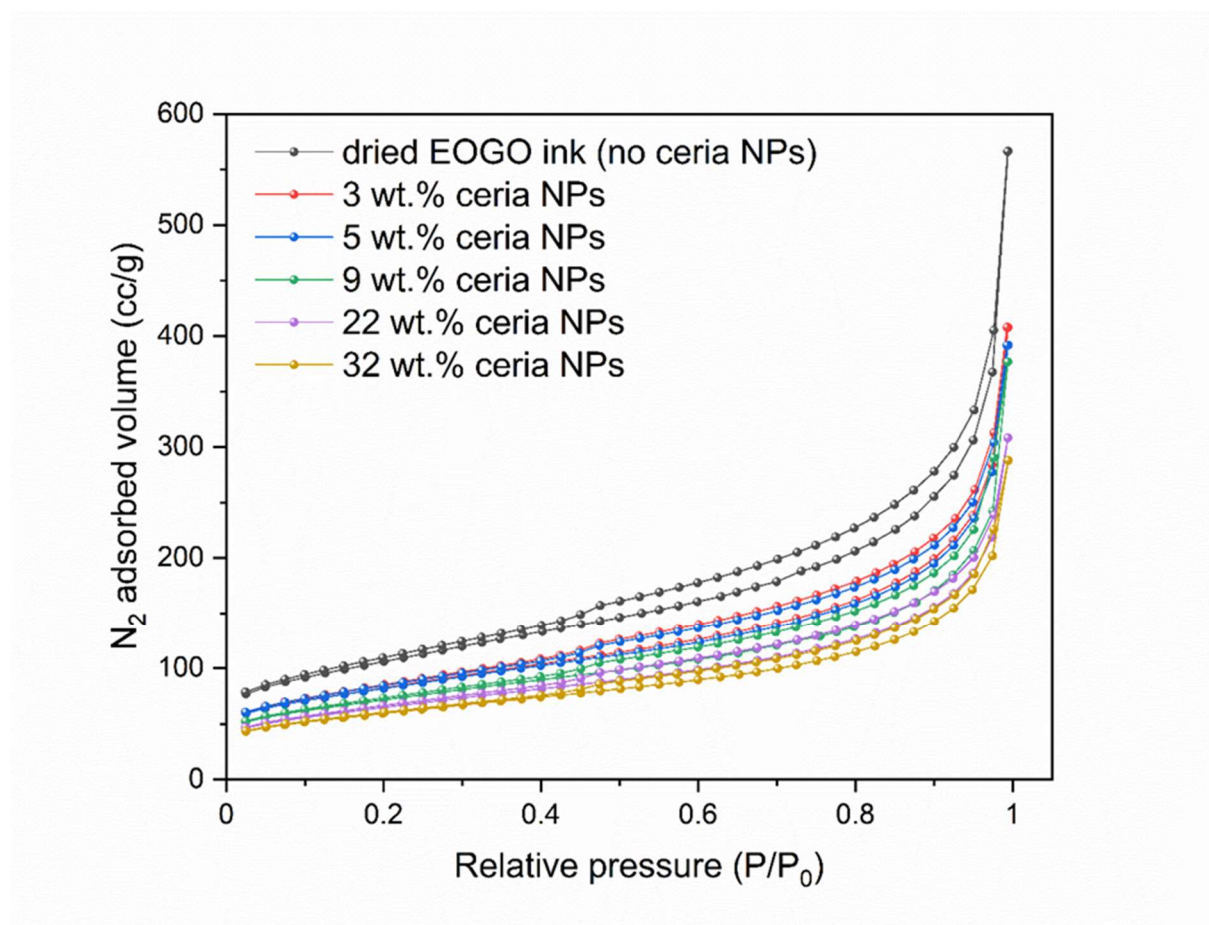


Figure 3.16.  $N_2$  adsorption isotherms of all the electrode materials.

## Rheological measurements

We carried out rheological measurements on a rotational rheometer (DHR2-TA Instruments) using aluminum disposable parallel plates of diameter of 25 mm at a gap size of 1000  $\mu\text{m}$ . For the oscillation measurements, the frequency was set to 10  $\text{rad}\cdot\text{s}^{-1}$ , and the stress was altered from 0.01 up to a maximum of 3000 Pa. for the flow stress measurements, the shear rate ranged from 0.01  $\text{s}^{-1}$  to 100  $\text{s}^{-1}$ .

### **Raman spectroscopy**

Raman spectroscopy was performed on dried electrode inks using a Renishaw inVia Raman microscope using a 457 nm excitation laser, and a 100X, 0.82NA microscope objective. Laser power and exposure time were adjusted in order not to burn the material. We dried all the electrode inks at room temperature under ambient conditions for 2 days and then obtained these samples in powder form and used them for the measurements.

### **X-ray photoelectron spectroscopy (XPS)**

XPS measurements were carried out on the dried electrode inks on an Axis Supra (Kratos Analytical) using the monochromated  $K_{\alpha}$  X-ray line of an Aluminium anode. We dried all the electrode inks at room temperature under ambient conditions for 2 days and then obtained these samples in powder form and used them for the measurements. The pass energy of the XPS measurements was set to 40 eV with a step size of 0.15 eV. The samples were insulated from the sample holder and an electron flood gun was used to limit charging effects. Data were subsequently referenced at 284.2 eV using the  $sp^2$  component of the C1s orbital. Peaks were fitted using CasaXPS. Cerium peaks were fitted using CasaXPS according to E. Paparazzo.[310] Figure 3.17 shows the deconvoluted Ce 3d region of XPS spectra of the electrode materials. Table 3.3 summarizes the list of binding energies of the peaks and what oxidation states those cerium related peaks are related to.

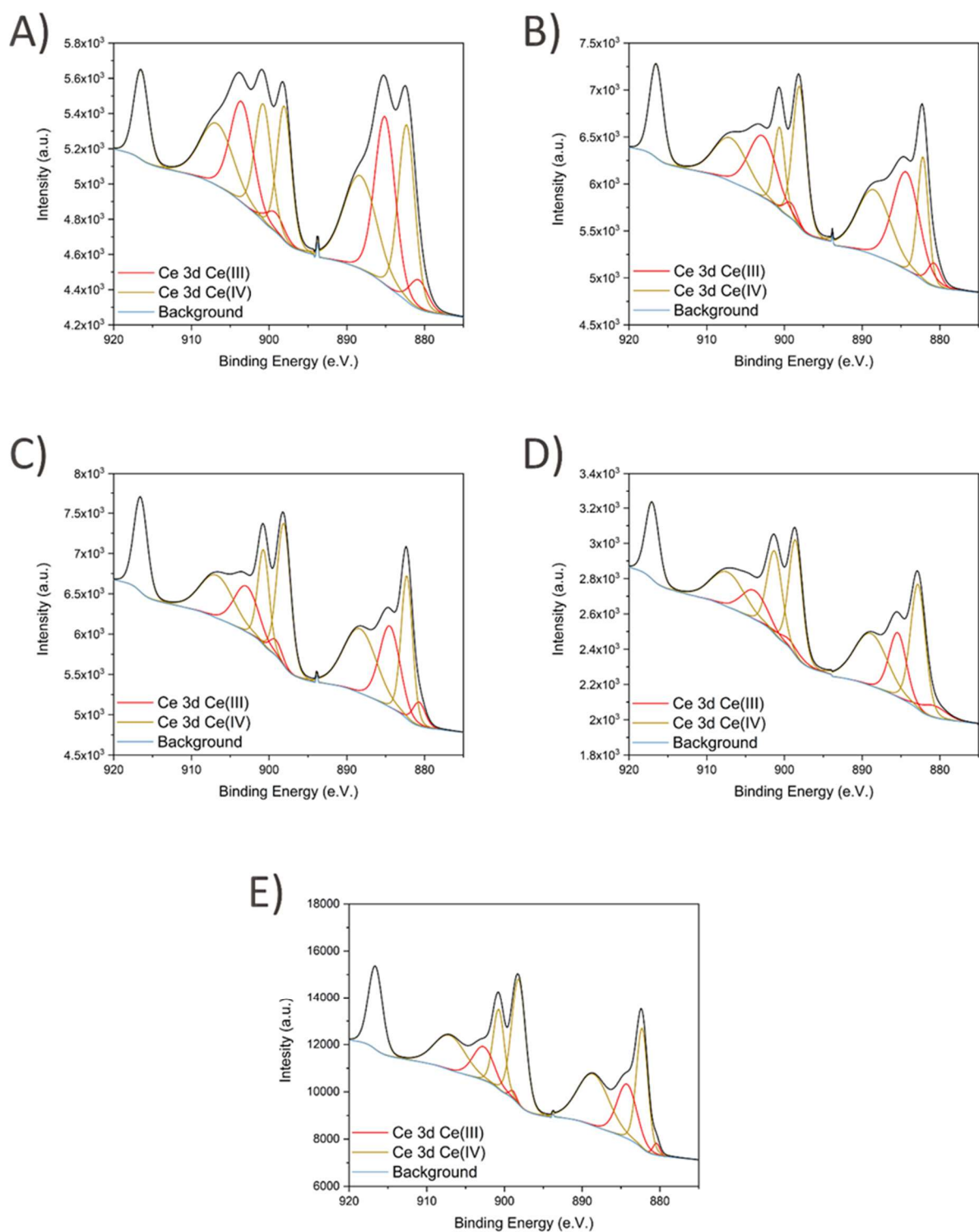


Figure 3.17. Deconvoluted Ce 3d region of XPS spectra of the electrode materials in high resolution, A) 3 wt.% ceria NPs, B) 5 wt.% ceria NPs, C) 9 wt.% ceria NPs, D) 22 wt.% ceria NPs, E) 32 wt.% ceria NPs.

Table 3.3. Assignment of Ce oxidation state associated with deconvoluted peaks in the Ce 3d region of XPS spectra of the electrode materials.

| Deconvoluted peak binding energy (e.V.) | Oxidation state of Ce associated with the deconvoluted peak |
|---|---|
| 880.45-880.77                           | Ce(III)   |
| 882.28-882.3                            | Ce(IV)  |
| 884.24-885.1                            | Ce(III)   |
| 888.29-888.58                           | Ce(IV)  |
| 898.05-898.9                            | Ce(IV)  |
| 898.9-899.22                            | Ce(III)   |
| 900.73-900.75                           | Ce(IV)  |
| 902.69-903.55                           | Ce(III)   |
| 906.74-907.03                           | Ce(IV)  |
| 916.5-916.62                            | Ce(IV)  |

### X-ray Diffraction (XRD)

XRD patterns of the dried electrode inks and the bare EOGO powder were acquired using an Empyrean diffractometer (Malvern Panalytical) with a Cu K $\alpha$  radiation ( $\lambda = 1.5406 \text{ \AA}$ ). The electrode samples (dried powder) were deposited and spread over single crystalline silicon substrates. The diffraction patterns were collected within a  $2\theta$  range of  $5^\circ$  to  $80^\circ$  at a scanning step size of  $0.1^\circ \cdot \text{s}^{-1}$ . We dried all the electrode inks at room temperature under ambient conditions for 2 days and then obtained these samples in powder form and used them for the measurements. Figure 3.18 demonstrates the XRD patterns of the air-dried powders of all the electrode materials.

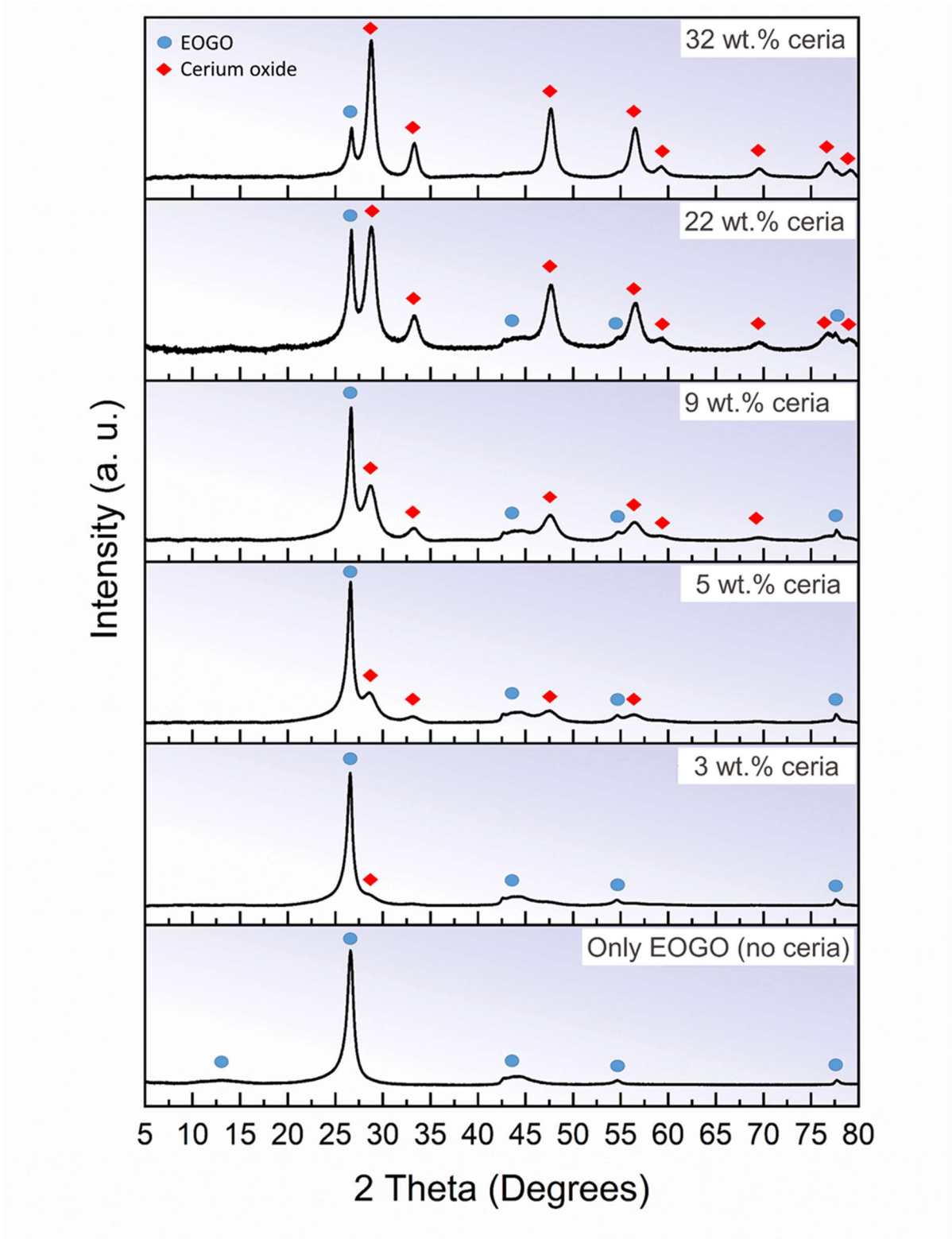


Figure 3.18. XRD patterns of all the electrode materials showing the assigned peaks of EOGO and ceria.

## Electrochemical measurements

On the fully fabricated MSCs, we performed electrochemical characterizations. We measured the electrochemical performance of the fully 3D printed MSCs (CV, GCD, and EIS measurements) in a two-electrode setup using an electrochemical working station (Autolab PGSTAT 302, Metrohm) equipped with an impedance module (FRA32M). The CV measurements were performed at varying scan rates (2 to 100 mVs<sup>-1</sup>) within a 0.6 V (from 0 V to +0.6 V) potential window. The GCD curves were collected at different current densities (1.43 to 5.72 mAcm<sup>-2</sup>). The EIS measurements were carried out at a range of frequencies from 100 mHz to 100 kHz, and at an amplitude of 10 mV.

## X-ray tomography

X-ray tomography imaging was done using a RX-SOLUTIONS Ultratom micro CT system. The X-ray source voltage and current were 80 kV and 101  $\mu$ A, respectively. The frame rate and frame averaging were set to 2 s<sup>-1</sup> and 6, respectively (2 frames were taken every second (0.5 s exposure time) and a single image was saved for every 6 frames).

### 3.3.6. Electrochemical performance calculations

In this sub-section, we discuss how some of the microsupercapacitors' performance metrics (namely, areal capacitance, areal energy density and areal power density) were calculated in this thesis. The areal capacitance, the energy density and the power density of the fully 3D printed MSCs were calculated based on the equations below using the CV curves[185], [260]:

$$C_A = \frac{\int_0^{0.6} j dV}{A \times \Delta V \times v} \quad (3.1)$$

$$E_A = \frac{C_A \times V^2}{2 \times 3.6} \quad (3.2)$$

## Chapter 3

---

$$P_A = \frac{E_A \times v \times 3600}{\Delta V} \quad (3.3)$$

Where  $C_A$  ( $\text{mF}/\text{cm}^2$ ) is the areal capacitance of the device,  $A$  ( $\text{cm}^2$ ) is the geometric area of the MSC considering,  $E_A$  is the areal energy density ( $\mu\text{Wh}/\text{cm}^2$ ),  $P_A$  is the areal power density ( $\mu\text{W}/\text{cm}^2$ ),  $j$  is the current (mA),  $\Delta V$  is the voltage window (0.6 V), and  $v$  is the scan rate (mV/s). The image below (Figure 3.19) shows the active area ( $A$ ) used for the calculations in the abovementioned equations. The area we used in all our calculations is  $0.14 \text{ cm}^2$  ( $4 \text{ mm} \times 3.5 \text{ mm}$ ).

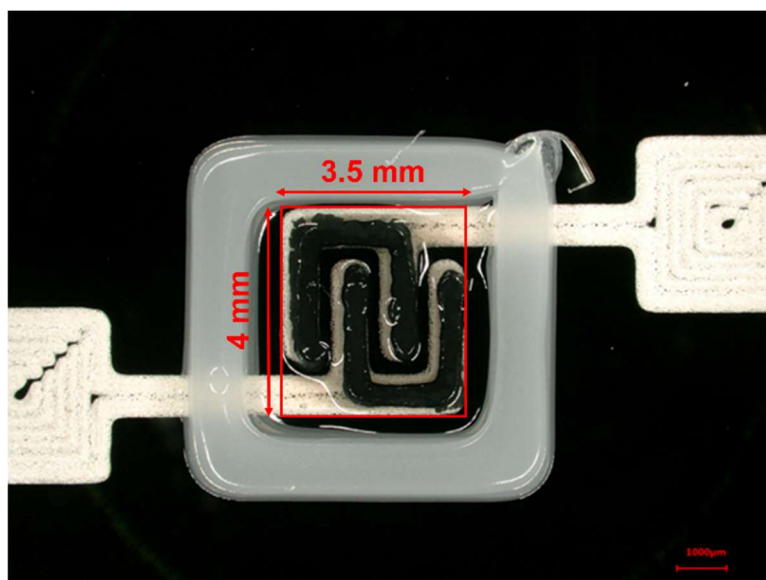


Figure 3.19. Determination of the active area of the MSCs used in the calculations of areal capacitance, area energy density and areal power density. The image shows a fully 3D printed MSC just before the deposition and subsequent UV curing of the encapsulant.

### 3.3.7. Kinetic study of charge storage mechanisms

We performed a kinetic study of charge storage mechanisms of microsupercapacitors. Through this study, we were able to understand how the chemistry of the electrodes affect the kinetics of charge storage in the microsupercapacitors. The ratio of (EDLC + Faradaic pseudocapacitance) (fast kinetic—outer surface)/diffusive ion insertion (diffusive pseudocapacitance—inner surface) (slow kinetic) charge storage contributions of the MSCs was

calculated as a function of the sweep rates ( $\nu$ ) according to a method introduced by Trasatti.[311]

These calculations differentiate the fast-kinetic charge storage (EDLC + Faradaic pseudocapacitance—outer surface) and the slow-kinetic charge storage (diffusive ion insertion—diffusive pseudocapacitance—inner surface) mechanisms. The value of the fast-kinetic (outer surface) areal capacitance  $(C_A)_o$  is obtained from the extrapolation of areal capacitance  $(C_A)$  to  $\nu=\infty$  derived from the plot of areal capacitance  $(C_A)$  vs.  $\nu^{-0.5}$ . And, the value of the total areal capacitance  $(C_A)_t$  is obtained from the extrapolation of inverse of areal capacitance  $(C_A^{-1})$  to  $\nu=0$  from the plot of inverse of areal capacitance  $(C_A^{-1})$  vs.  $\nu^{0.5}$ . By calculating the  $C_o$  and  $C_t$ , one can calculate the  $C_i$  (inner surface capacitance—diffusive ion insertion—diffusive pseudocapacitance) using equation 3.4.

$$(C_A)_t = (C_A)_i + (C_A)_o \quad (3.4)$$

Where  $(C_A)_t$  is the total areal capacitance ( $\text{mF}\cdot\text{cm}^{-2}$ ),  $(C_A)_i$  is the inner surface areal capacitance stemming from the slow-kinetic charge storage (diffusive ion insertion—diffusive pseudocapacitance—inner surface) ( $\text{mF}\cdot\text{cm}^{-2}$ ), and  $(C_A)_o$  is the outer surface areal capacitance caused by the fast-kinetic charge storage (EDLC + Faradaic pseudocapacitance—outer surface) ( $\text{mF}\cdot\text{cm}^{-2}$ ). Figures 3.20–3.25 exhibit the fittings done on the related plots for all the ceria-NPs containing electrodes materials. Table 3.4 summarizes the contribution of the fast-kinetic and slow-kinetic processes involved in the charge storage of the electrodes as a function their ceria NPs loading.



## Chapter 3

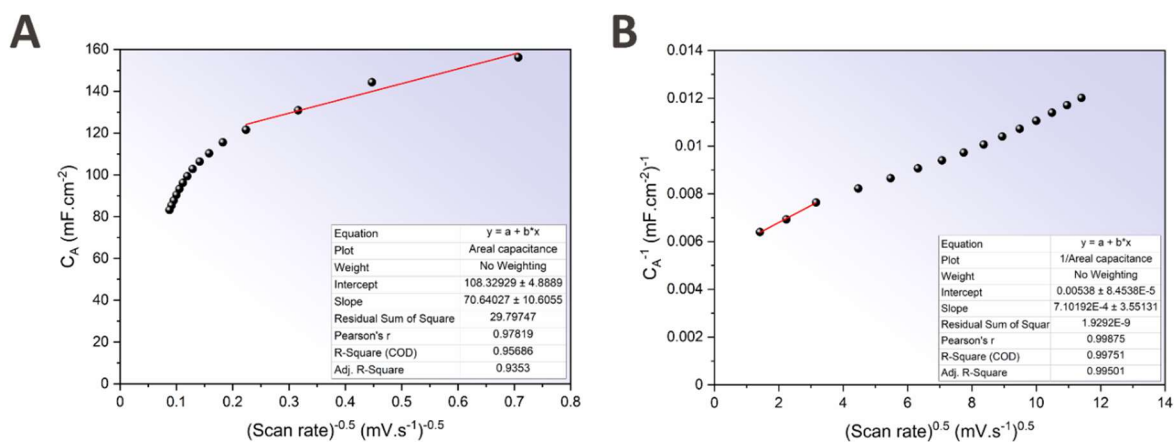


Figure 3.20. The plots of A)  $C_A$  vs.  $u^{-0.5}$  and B)  $C_A^{-1}$  vs.  $u^{0.5}$  of the MSC constructed by the electrode containing no ceria and the optimum electrolyte composition.

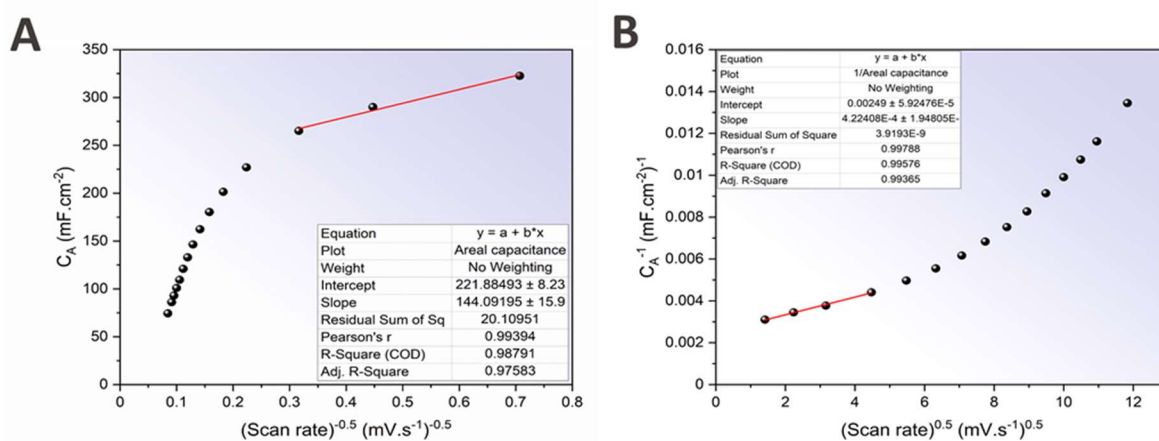


Figure 3.21. The plots of A)  $C_A$  vs.  $u^{-0.5}$  and B)  $C_A^{-1}$  vs.  $u^{0.5}$  of the MSC constructed by the electrode containing 3 wt.% ceria and the optimum electrolyte composition.

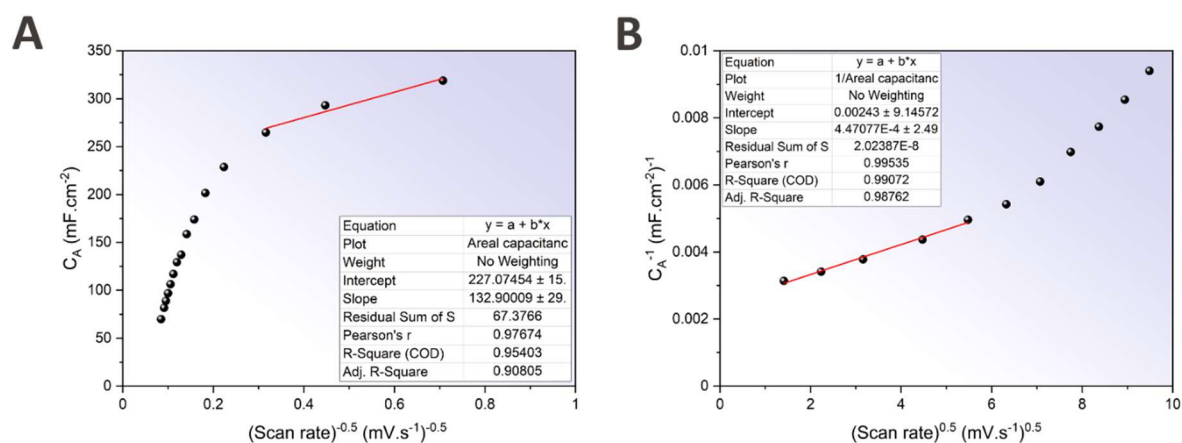


Figure 3.22. The plots of A)  $C_A$  vs.  $u^{-0.5}$  and B)  $C_A^{-1}$  vs.  $u^{0.5}$  of the MSC constructed by the electrode containing 5 wt.% ceria and the optimum electrolyte composition.

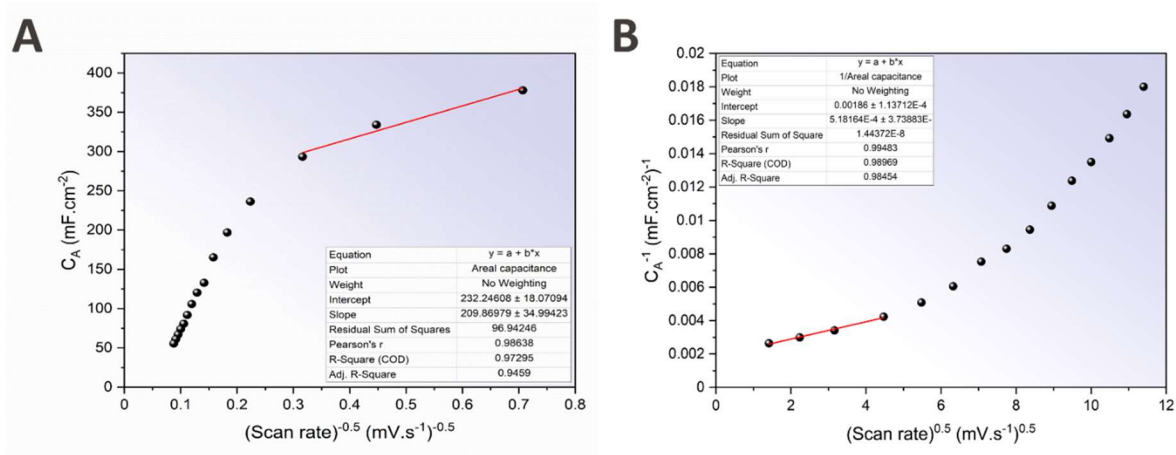


Figure 3.23. The plots of A)  $C_A$  vs.  $u^{-0.5}$  and B)  $C_A^{-1}$  vs.  $u^{0.5}$  of the MSC constructed by the electrode containing 9 wt.% ceria and the optimum electrolyte composition.

## Chapter 3

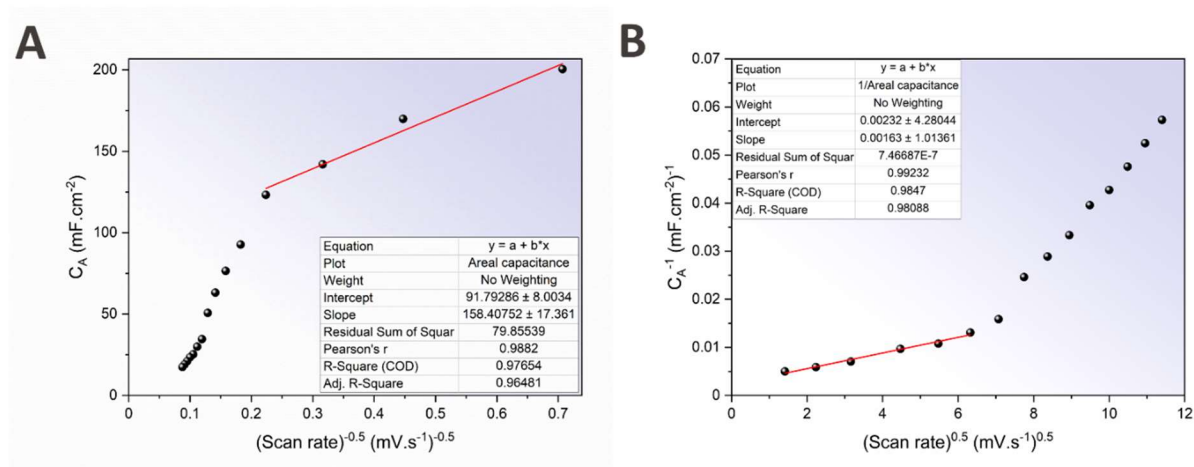


Figure 3.24. The plots of A)  $C_A$  vs.  $u^{-0.5}$  and B)  $C_A^{-1}$  vs.  $u^{0.5}$  of the MSC constructed by the electrode containing 22 wt.% ceria and the optimum electrolyte composition.

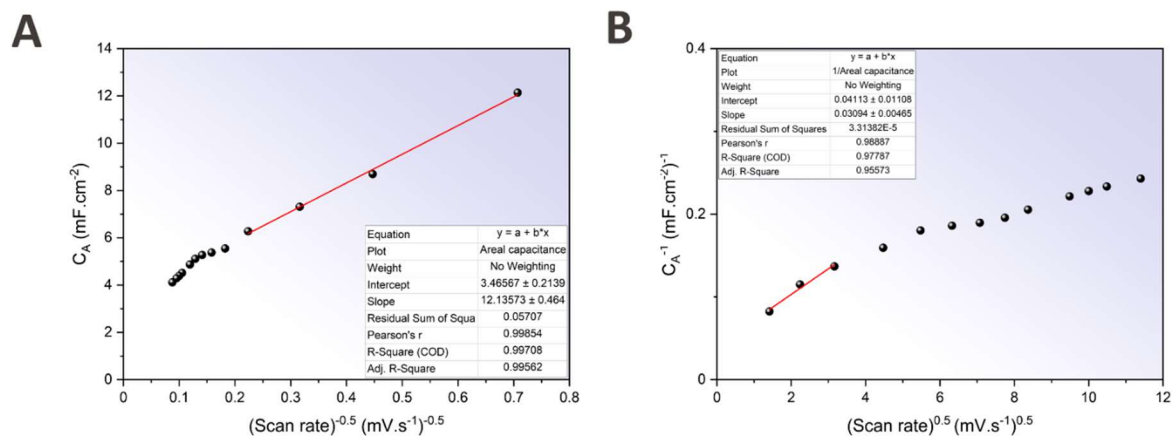


Figure 3.25. The plots of A)  $C_A$  vs.  $u^{-0.5}$  and B)  $C_A^{-1}$  vs.  $u^{0.5}$  of the MSC constructed by the electrode containing 32 wt.% ceria and the optimum electrolyte composition.

Table 3.4. The contribution of fast-kinetic and slow-kinetic processes involved in the charge storage of the electrodes as a function their ceria NPs loading.

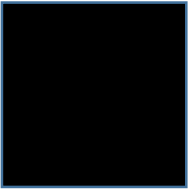
| Ceria NPs concentration (wt.%) | Total areal capacitance ( $C_A$ ) <sub>t</sub> (mF.cm <sup>-2</sup> ) | Fast-kinetic areal capacitance ( $C_A$ ) <sub>o</sub> (mF.cm <sup>-2</sup> ) | Slow-kinetic areal capacitance ( $C_A$ ) <sub>i</sub> (mF.cm <sup>-2</sup> ) |
|--------------------------------|---|--|--|
| 0                              | 185.87  | 108.33   | 77.54  |
| 3                              | 401.61  | 221.88   | 179.73   |
| 5                              | 411.52  | 227.07   | 184.45   |
| 9                              | 537.63  | 232.25   | 305.38   |
| 22                             | 431.03  | 91.79  | 339.24   |
| 32                             | 24.31   | 3.47   | 20.84  |

### 3.4. Conclusions

In summary, we demonstrate additively fabricated mm-scale microsupercapacitors with lateral sizes  $< 0.5 \text{ cm}^2$  (full package:  $7 \text{ mm} \times 7 \text{ mm}$  and charge storage active area:  $4 \text{ mm} \times 3.5 \text{ mm}$ ) and total height of  $\sim 2 \text{ mm}$  with outstanding electrochemical performance. By fine-tuning the chemistries of the components of the microsupercapacitors, we achieve a high areal capacitance of  $\sim 323 \text{ mFcm}^{-2}$ , energy density of  $16.1 \mu\text{Whcm}^{-2}$ , power density of  $\sim 3028 \text{ mWcm}^{-2}$ , and  $\sim 91.3\%$  capacitance retention after 21000 cycles. To the best of our knowledge, our results display the smallest fully 3D printed microsupercapacitors delivering excellent performance, including outstanding capacitance, cyclic life, energy density and power density at such a small footprint. This was achieved through optimization of all component structures within the capacitor. These microsupercapacitors are thus promising for use as integrated energy sources for powering microsystems, wearables, and IoT.

In the next chapter, we will focus on the dimensional scaling study of the microsupercapacitors using the optimized processing conditions and chemistries of the component selected in this chapter.





## **4. Sub-mm<sup>3</sup> Dimensional Scaling of High-Performance Additively-Fabricated Microsupercapacitors for Embedded Energy Applications**

In this chapter, we systematically investigate the effects of dimensional scaling of these fully-additively fabricated microsupercapacitors on their performance using the optimized chemistries of the components as determined in chapter 3.

Amin Hodaei designed the experiments and synthesized the active materials of the electrodes and formulated the electrolytes. Amin Hodaei performed the rheological characterizations of the inks, 3D printing of the microsupercapacitors and also the electrochemical characterizations of the microsupercapacitors. Amin Hodaei and Vivek Subramanian conceptualized the research and they analyzed the data and wrote the manuscript.

The contents of this chapter are parts of a manuscript that is going to be submitted as a journal article.

## Chapter 4

---

### **4.1. Introduction**

In this chapter, we will discuss a systematic study on the effects of sub-mm<sup>3</sup> dimensional scaling on the performance of fully additively-fabricated microsupercapacitors. We used the optimized chemistries of the components of microsupercapacitors as determined in chapter 3 of this thesis. We will start with discussions on the fabrication of microsupercapacitors and introduce their dimensional scaling, chemistries of the components of the microsupercapacitors, and performance evaluation of the fabricated microsupercapacitors. We will next discuss the details of the dimensional scaling of the microsupercapacitors.

### **4.2. Fabrication, scaling procedures, and characterization**

#### **4.2.1. Fabrication of microsupercapacitors and designing their dimensional scaling**

We additively fabricated the microsupercapacitors via a combination of fused deposition modeling (FDM) and extrusion-based 3D printing as described in chapter 3. Figure 4.1 exhibits the printing procedure of the MSCs and their plan of dimensional scaling. The main difference between the designs of microsupercapacitors in this chapter and chapter 3 is that here, instead of interdigitated fingers, we focused on parallel fingers configuration. This has been done as this configuration is the most typical configuration of capacitors (i.e., parallel plate), hence, it can be used to generate the basis for understanding of the effects of dimensional scaling on microsupercapacitors as well. We first started with extrusion-based 3D printing of the current collectors using a silver paste (DELO-Dualbond IC343) on wet-oxidized silicon wafer (Figure 4.1A). The current collector patterns resemble a parallel plates configuration such that two fingers (i.e., plates) are located at a certain distance from each other (750  $\mu\text{m}$  for all our MSCs). After printing, the current collectors were heat treated in air at 450 °C for 10 min. Then, we FDM printed the package walls around the fingers of the current collectors using polycaprolactone (PCL) (Figure 4.1B). We then extrusion 3D printed the electrodes on the fingers of the heat treated current collectors without any following post treatments (Figure

4.1C). Next, a UV-curable electrolyte based on (poly (ethylene glycol) diacrylate (PEGDA) + LiCl + lithium phenyl-2,4,6-trimethylbenzoylphosphinate (LAP) + water) was deposited in the interior space of the package walls to fully immerse the electrodes, which was followed by UV curing to realize a hydrogel electrolyte and subsequently to consolidate the components (Figure 4.1D). Finally, we deposited a UV-curable resin-based encapsulant (DELO Dualbond AD 761- a modified epoxy resin) on top of the UV cured electrolyte, which was also followed by a UV curing step to fully seal the MSCs (Figure 4.1E). As shown in Figure 4.1F, we designed the dimensional scaling study in such a way that the performance of the MSCs are evaluated as a function of change in the length of the electrodes and also the inner diameter of the nozzles with which the electrodes are 3D printed. The electrodes are 3D printed at three levels: 2.5 mm, 3.75 mm, and 5 mm (a variation of 2.5 mm). The inner diameters of the nozzles used to 3D print these electrodes are 250  $\mu\text{m}$ , 330  $\mu\text{m}$ , 510  $\mu\text{m}$ , and 840  $\mu\text{m}$  (with a maximum variation of 590  $\mu\text{m}$ ). Thus, a total dimensional variation of 0.87025  $\text{mm}^3$  (i.e., sub- $\text{mm}^3$  range) ( $\Delta L$  (length) = 2.5mm,  $\Delta W$  (width) = 0.59  $\mu\text{m}$  (i.e., the difference of the Max and Min of the nozzle diameters),  $\Delta H$  (Height) = 0.59  $\mu\text{m}$  (i.e., the difference of the Max and Min of the nozzle diameters)). Hence, we describe this study as a sub- $\text{mm}^3$  dimensional scaling considering the scaling ranges of the electrode length and the nozzle diameters with which they are 3D printed. A more detailed description of the dimensional scaling of the MSCs is provided in Table 4.1.



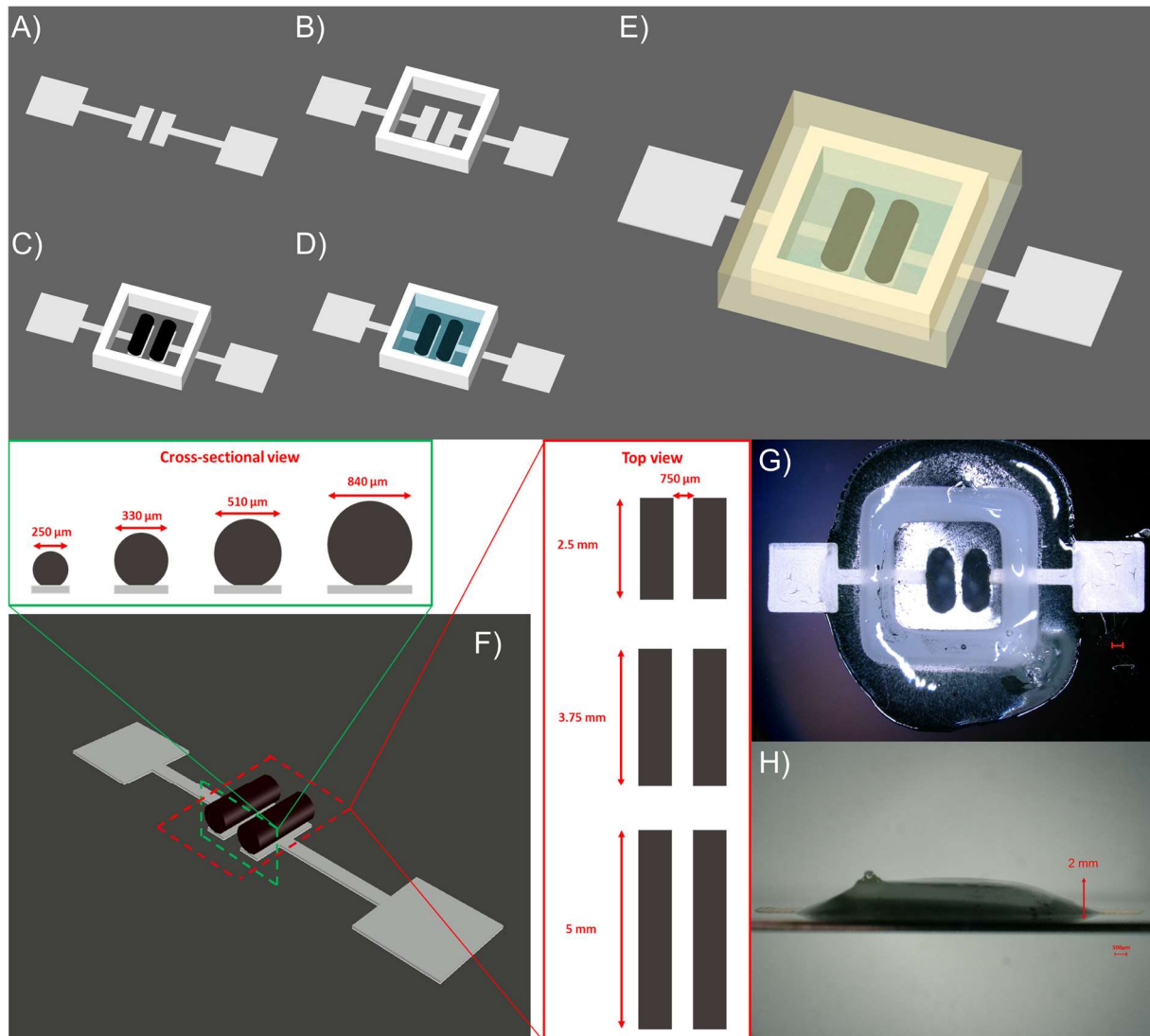


Figure 4.1. The Schematics of the fabrication steps of the microsupercapacitors, A) Extrusion-based 3D printing the current collectors on a wet-oxidized silicon wafer using a silver paste and subsequently, heat treating the current collectors, B) FDM printing of the package using PCL, C) Extrusion-based 3D printing of the electrodes on the current collectors (inside the package space), D) Deposition of UV-curable electrolytes inside the package to immerse the electrodes and subsequently, UV curing the electrolyte, E) Deposition of an encapsulant on top of the UV-cured electrolyte and subsequently UV curing it, F) Illustration of the design of dimensional scaling of the microsupercapacitors by changing the diameter of the nozzles used to 3D print the electrodes with different lengths, G) A top view image of one of the fully 3D printed microsupercapacitors (nozzle diameter of 510  $\mu\text{m}$  and electrode length of 2.5 mm), and H) A side view image the same fully 3D printed microsupercapacitor as in (G) scale bars are 500  $\mu\text{m}$ .

### 4.2.2. Chemistries of the components of the microsupercapacitors

We formulated the electrode inks using a nanocomposite of EOGO/ceria NPs (~95 wt. % EOGO — ~5 wt. % ceria NPs) dispersed in water without using any organic additives, binders, or rheology modifiers. The novel chemistry of our electrode inks provides a green formulation of a hybrid system delivering both electrical double-layer capacitance (EDLC) stemming mostly from EOGO sheets and pseudocapacitance originating mostly from ceria NPs. Figure 4.2A shows the XRD patterns of the bare EOGO powder and the air-dried electrode ink. The concurrent presence of the sharp peak at  $\sim 26^\circ$  and the wide and less intense peak at  $\sim 13^\circ$  in the XRD pattern of the bare EOGO corresponds to its almost intact  $sp^2$  graphitic basal plane and the presence of oxygen-containing functional groups on its edges.[282] The XRD pattern of the air-dried electrode ink shows the formation of  $CeO_2$  crystalline phase.[290], [294]

We investigated the rheological characterizations of the aqueous electrode ink as shown in Figures 4.2B and 4.2C. The aqueous electrode ink demonstrated a shear-thinning behavior—decrease in the viscosity as a function of the increase in shear rate (Figure 4.2B), and a viscoelastic behavior with a more dominant  $G'$  (storage modulus, i.e., elastic behavior) values than  $G''$  (loss modulus, i.e., viscous behavior) before their intersection point (known as the flow point), which are all indicators of the suitability of the ink for extrusion-based 3D printing.[274] Changing the shear rate from 0.01 Pa.s to 100 Pa.s, the viscosity of the ink significantly dropped (by almost four orders of magnitude). The oscillation rheometry showed that the  $G'$  of the electrode ink in the linear viscoelastic region is almost one order of magnitude larger than its  $G''$ . We also investigated the morphological details of the EOGO/ceria NPs nanocomposite using TEM imaging as shown in Figure 2D. The crystalline ceria NPs with sizes of less than 5-10 nm are anchored onto the EOGO sheets and they quite fairly distributed on the surface EOGO sheets.

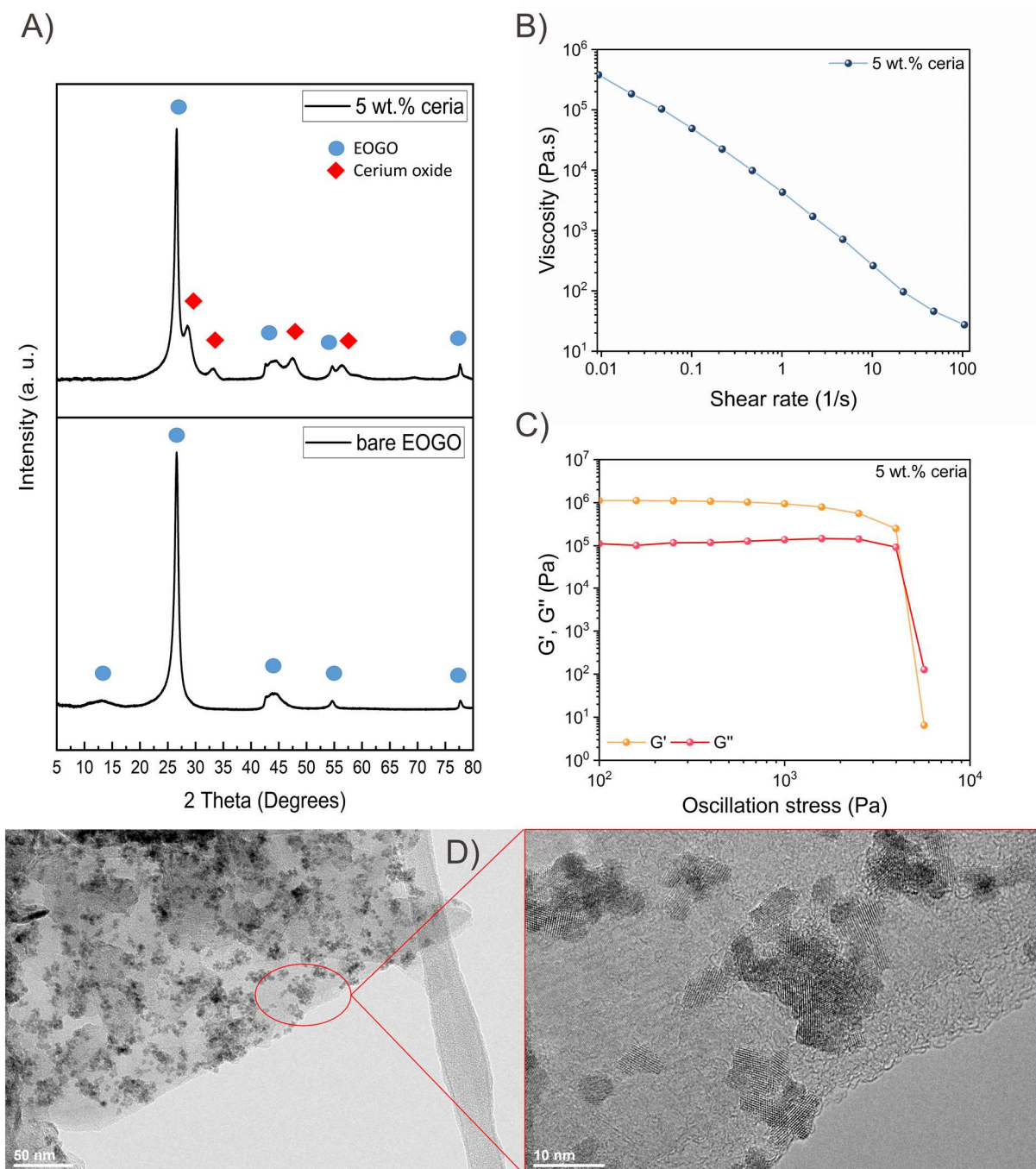


Figure 4.2. A) XRD characterization of the bare EOGO powder and the air-dried electrode ink comprising 5 wt.% ceria nanoparticles, rheological characterizations of the aqueous electrodes ink (EOGO/ceria nanocomposite — 5 wt.% ceria nanoparticles) B) viscosity as a function of shear rate, C) oscillation measurement demonstrating the storage modulus ( $G'$ ) and the loss modulus ( $G''$ ) of the same ink as a function of oscillation stress, and D) TEM images of the air-dried electrodes, the same used for XRD characterization as shown in (A).

As a reminder from chapter 3, we formulated a UV-curable hydrogel electrolyte based on (poly (ethylene glycol) diacrylate (PEGDA) + LiCl + lithium phenyl-2,4,6-trimethylbenzoylphosphinate (LAP) + water). LiCl has been widely employed in electrolytes of printed microsupercapacitors.[181], [231], [248], [258] On the other hand, PEGDA[278], [279], [312] and LAP (a water-soluble photo-initiator)[280], [281], [313] have been commonly utilized in 3D printing of hydrogels. The resultant electrolyte after UV curing, showed a gel structure providing suitable mechanical stability in the MSCs eliminating the need for a separator between the electrodes.[151] As a reminder from chapter 3, the optimized chemical composition and processing condition for the electrolyte was set to a LiCl concentration of (1.6 M), while the concentration of the PEGDA was set to  $0.08 \text{ g.ml}^{-1}$  and the concentration of LAP was 0.16 wt.% (by weight of PEGDA) that was cured for 20 seconds by a 365 nm UV lamp. For FDM printing the package walls, we used polycaprolactone (PCL). PCL is a biocompatible polymer with low melting temperature and a hydrophobic nature.[277] The main reason behind printing the package walls is that it acts as a container for the electrolyte before it is UV-cured when immersing the electrodes in the sequence of microsupercapacitors fabrication. Similar to the procedure followed in chapter 3, we encapsulated the microsupercapacitors in order to enhance their stability by making sure that the electrolyte does not get evaporated over time. We used a modified epoxy-based resin which is UV-curable. The encapsulant was UV cured using a 405 nm UV lamp for 60 seconds.

### 4.2.3. Performance evaluation of the fabricated microsupercapacitors

We systematically investigated the electrochemical performance of the microsupercapacitors as a function of their dimensions (i.e., length of the electrodes, and the diameter of the nozzle with which they are printed). This has been done in order to elucidate the effects of scaling on the performance of the microsupercapacitors. In order to investigate how changing the dimensions influences the charge-discharge behavior of the microsupercapacitors, we performed galvanostatic charge-discharge (GCD) measurements on microsupercapacitors with varying dimensions. As shown in Figures 4.3A-D, by a simultaneous increase of the length of the electrodes, and the nozzle size used for printing the electrodes, the duration of full cycle

## Chapter 4

of charge-discharge was increased. For example, a full charge-discharge cycle at a current of  $50\ \mu\text{A}$  took  $\sim 175\ \text{s}$  for an MSC printed  $250\ \mu\text{m}$  nozzle and electrode length of  $5\ \text{mm}$ , while for the microsupercapacitor comprising a  $5\ \text{mm}$  long electrode printed with a  $840\ \mu\text{m}$  nozzle, a full cycle takes  $\sim 1140\ \text{s}$ . These results demonstrate that longer electrodes printed with larger nozzle diameters realize higher capacitance levels is expected due to the larger volumes and larger outmost surface of the active materials available in these electrodes.

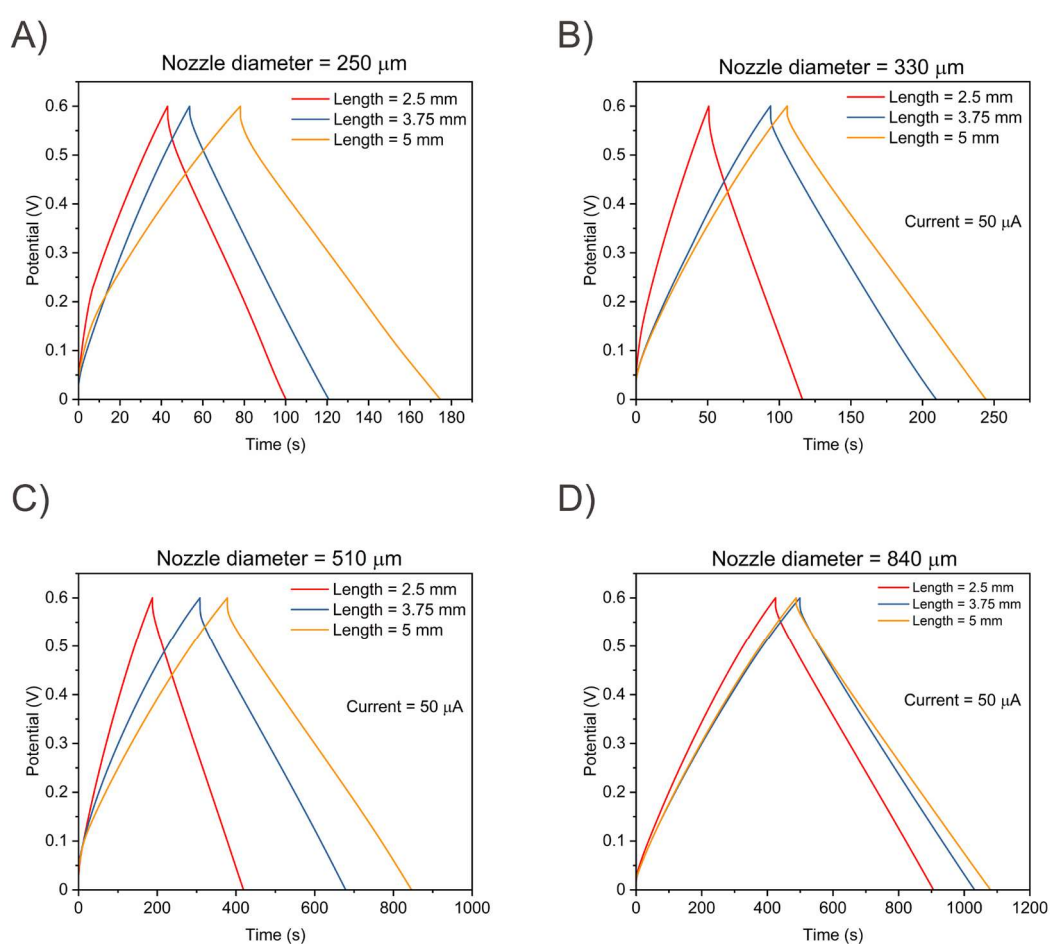


Figure 4.3. Galvanostatic charge discharge diagrams of the additively fabricated MSCs as a function of electrode length and the nozzle diameter with which the electrodes are printed, A) nozzle diameter:  $250\ \mu\text{m}$ , B) nozzle diameter:  $330\ \mu\text{m}$ , C) nozzle diameter:  $510\ \mu\text{m}$ , D) nozzle diameter:  $840\ \mu\text{m}$ .

We further investigated the electrochemical properties of the microsupercapacitors by cyclic voltammetry (CV). This has been done in order to investigate different electrochemical characterization methods to ensure that the results obtained from them are in agreement with each other. As shown in Figure 4.4, capacitance (not normalized per area or volume) of the microsupercapacitors scales with the length of the electrodes and the diameters of the nozzle with which they are printed. The slope of the change in the capacitance of the microsupercapacitors is steeper for 5mm long electrodes compared to 3.75 mm, and 2.5 mm long ones. At each nozzle diameter level, increase in the length of the electrode, also resulted in an increase in the capacitance of the microsupercapacitors. This can be due to the greater increase in the active surface area when electrodes become thicker and longer. This observation is in agreement with the result from GCD measurements discussed earlier.

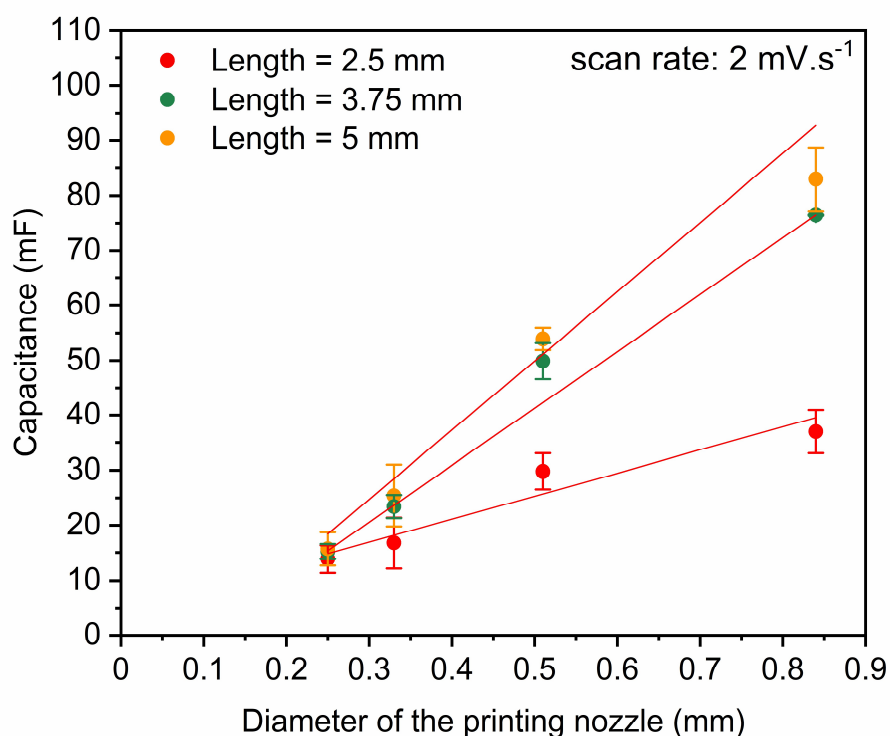


Figure 4.4. Capacitance (non-normalized per area or volume) of all the MSCs as a function of their electrode length and the diameter of the nozzle used for printing them.

## Chapter 4

---

We used electrochemical impedance spectroscopy (EIS) measurements to calculate the equivalent series resistance (ESR) of the microsupercapacitors. Figure 4.5A illustrates the ESR of the microsupercapacitors as a function of the length of the electrodes and the printing nozzle diameter used for them. ESR also known as the internal resistance, is an indication of the total resistance of the system—defined as the sum of the bulk electrolyte resistance, the resistance of the electrode, and the contact resistance between the electrode and the current collector.[192] It is one of the important performance metrics of microsupercapacitors since it correlates to how much energy loss a system has. We observed that at each nozzle diameter, increasing the length decreased the ESR of the microsupercapacitors. We also observed that electrodes printed with larger nozzle diameters showed smaller ESR values. The reason behind these observations might be that by increasing the length and the thickness of the electrodes, more available surface for the passage of electron is provided. Hence, lower values of ESR is obtained for longer and thicker electrodes (since the low-resistance current collector acts as a strap for the entire length of the electrodes, the increased length of the electrodes is unsurprisingly not found to cause an increase in ESR). All the ESR values obtained for the microsupercapacitors are less than  $\sim 90 \Omega$ .

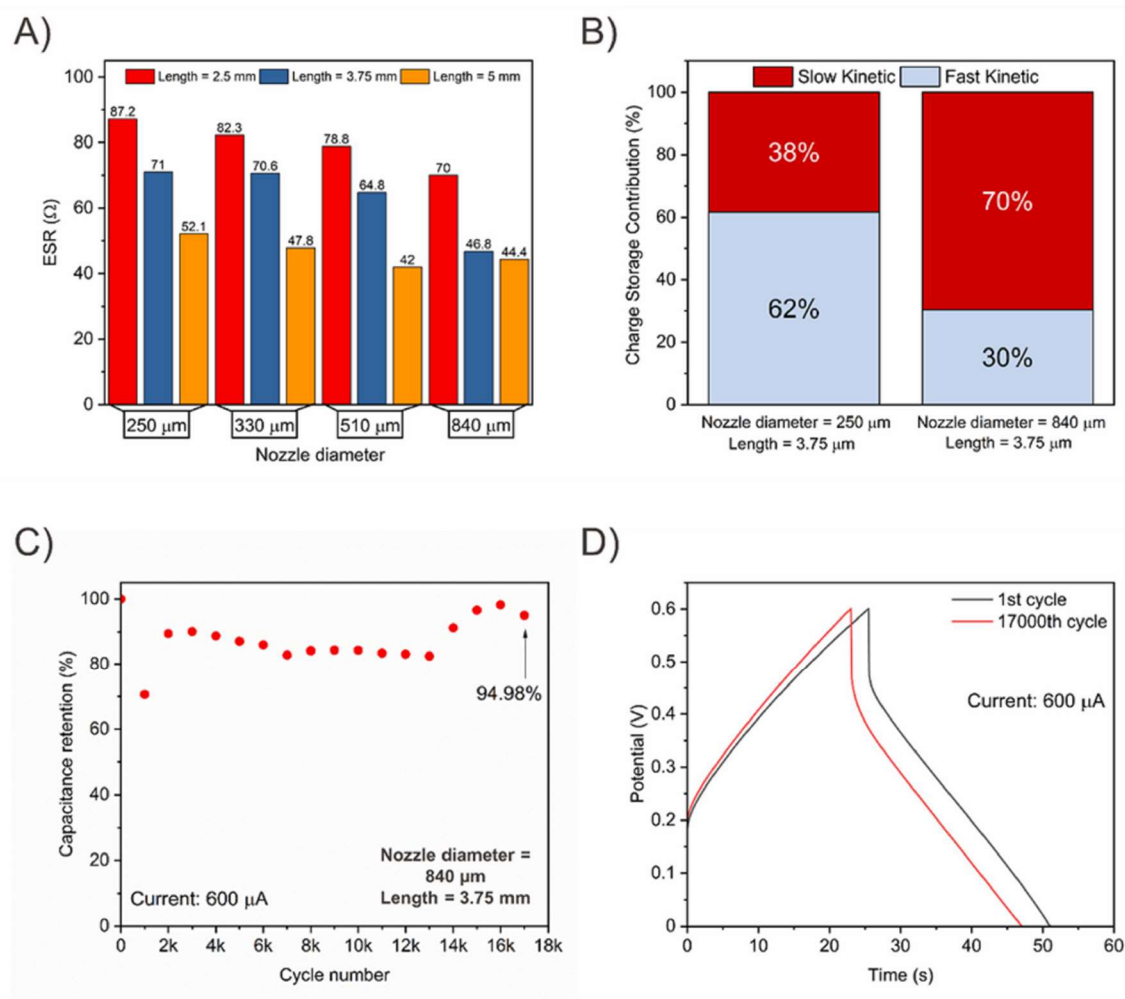


Figure 4.5. A) Capacitance (non-normalized per area or volume) of the MSCs as a function of the electrode length and thickness, B) the ESR values of the MSCs, C) kinetic study of charge storage of two of the fabricated MSCs with 2.5 mm long electrodes printed with the smallest (i.e.,  $250 \mu\text{m}$ ) and the largest (i.e.,  $840 \mu\text{m}$ ) nozzles, D) cyclic life the MSC possessing 3.75 mm long electrodes printed with a  $840 \mu\text{m}$  nozzle.

We further studied the dependence of the kinetics of charge storage of the microsupercapacitors on their dimensions. As shown in Figure 4.5B, we compared the MSCs with 3.75 mm long electrodes printed with the smallest (i.e.,  $250 \mu\text{m}$ ) and largest (i.e.,  $840 \mu\text{m}$ ) nozzles. The inks that are extrusion 3D printed experience substantial shear stresses at the wall of the printing nozzles and these shear stresses are increased by decreasing the nozzle diameter.[314] In our study, the shear stress at the wall of the nozzle of  $250 \mu\text{m}$  diameter was the highest, and in case of printing the electrodes with the printing nozzle of diameter  $840 \mu\text{m}$ ,



## Chapter 4

---

the shear stress at the wall of the nozzle was the lowest. It has been shown that the shear stress at the wall of the printing nozzle causes the graphitic sheets to align along the printing direction.[315], [316] Using smaller nozzles produces higher shear stress at the wall of the nozzles while larger nozzles generate smaller shear stresses at their wall. Thus, due to higher shear stresses at the walls of the nozzles with smaller diameters, the graphitic sheets align more strongly along the printing direction resulting in lower surface roughness/porosity at the outmost surface of the printed electrodes.[317] For the same reason, lower shear stresses are experienced by the graphitic sheets during printing with larger nozzles, hence, these printed electrodes could possess higher surface roughness/porosity at their outmost surface as the graphitic sheets experience less alignment. The kinetic study of the charge storage also demonstrates the increase in the diffusion-controlled charge storage (i.e., slow kinetic charge storage mechanism) in thicker electrodes possibly due to more available diffusion pathways, which might be due to higher surface roughness/porosity at the outmost surface of these electrodes. This observation further emphasizes that even with the same chemistry of electrodes, the printing conditions (such as nozzle diameter) can significantly affect the charging kinetics of the resultant 3D printed microsupercapacitors.

Figure 4.5C exhibits the cyclic life of the microsupercapacitors with 3.75 mm long electrodes printed with the 840  $\mu\text{m}$  nozzle achieved by GCD measurements. A remarkable cyclic life—94.98% capacitance retention after 17000 cycles at a current of 600  $\mu\text{A}$  was realized. Each cycle took almost 50 seconds and in total the cyclic life test was going nonstop for  $\sim$ 230 hours. Figure 4.5D shows the GCD diagrams of the 1<sup>st</sup> and the 17000<sup>th</sup> cycles and as it can be noticed, there is not a significant change in the shape of the diagrams.

We continued with performing CV and GCD measurements at different scan rates and currents, respectively, on the microsupercapacitors possessing 3.75 mm long electrodes printed with 250  $\mu\text{m}$  and 840  $\mu\text{m}$  nozzles (Figures 4.6A-D). As shown in Figures 4.6A and 4.6B, the CV curves were collected at scan rates ranging from 2  $\text{mV}\cdot\text{cm}^{-2}$  to 250  $\text{mV}\cdot\text{cm}^{-2}$ . Unlike the microsupercapacitor printed with the 840  $\mu\text{m}$  nozzle, the microsupercapacitor printed with the 250  $\mu\text{m}$  nozzle

---

showed a better scan rate ability—the CV curves continued to get larger by increasing the scan rate. It could be inferred from this result that the microsupercapacitor printed with the 250  $\mu\text{m}$  nozzle could facilitate faster charge storage at its outmost electrode layer. This observation is also in agreement with the results of the kinetic study of charge storage where the MSC printed with the larger nozzle showed more pronounced slow kinetic charge storage.

Figures 4.6C and 6D show GCD curves at different currents ranging from 50  $\mu\text{A}$  to 500  $\mu\text{A}$ . For both MSCs, by increasing the currents, the duration of the full charge-discharge cycle was decreased. The GCD curves of the MSC printed with the 840  $\mu\text{m}$  nozzle show longer durations at each given current. In agreement with the CV curves, this observation is also an indication that the capacitance values of the MSC printed with the 840  $\mu\text{m}$  nozzle is larger than those of the MSC printed with the 250  $\mu\text{m}$  nozzle. The areal and volumetric capacitance of these MSCs which were calculated by using their CV curves are depicted in Figures 4.6E and 4.6F. While the areal and volumetric capacitances (scan rates of 2  $\text{mV}\cdot\text{s}^{-1}$  to 250  $\text{mV}\cdot\text{s}^{-1}$ ) of the microsupercapacitors printed with the 840  $\mu\text{m}$  nozzle ranged between 731.7  $\text{mF}\cdot\text{cm}^{-2}$ —25.7  $\text{mF}\cdot\text{cm}^{-2}$ , and 8.7  $\text{F}\cdot\text{cm}^{-3}$ —0.31  $\text{F}\cdot\text{cm}^{-3}$ , respectively, the microsupercapacitors printed with the

## Chapter 4

250  $\mu\text{m}$  nozzle showed areal and volumetric capacitances of  $194.68 \text{ mF}\cdot\text{cm}^{-2}$ — $40.94 \text{ mF}\cdot\text{cm}^{-2}$ , and  $7.79 \text{ F}\cdot\text{cm}^{-3}$ — $1.64 \text{ F}\cdot\text{cm}^{-3}$ , respectively.

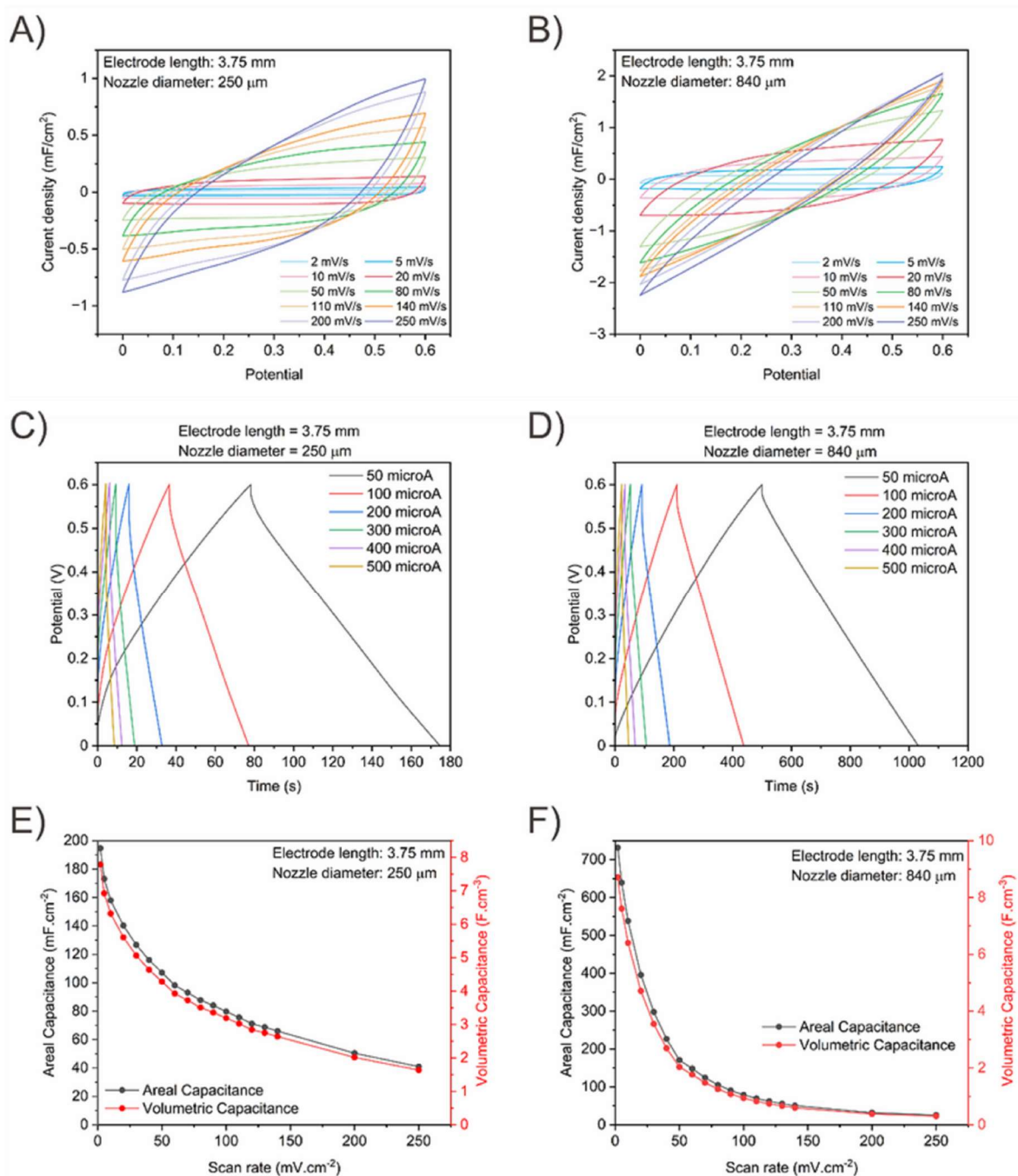


Figure 4.6. CV curves of the MSCs with an electrode length of 3.75 mm and printed with a nozzle diameter of A) 250  $\mu\text{m}$ , and B) 840  $\mu\text{m}$ , and GCD curves with an electrode length of 3.75 mm and printed with a nozzle diameter of C) 250  $\mu\text{m}$ , and D) 840  $\mu\text{m}$ , and areal and volumetric capacitance values of the MSCS (as a function of scan

---

rates used in CV measurements) with an electrode length of 3.75 mm and printed with a nozzle diameter of E) 250  $\mu\text{m}$ , and F) 840  $\mu\text{m}$ .

Next, we compared the energy density and power density values of these microsupercapacitors with some of the examples of printed microsupercapacitors from literature as shown by the Ragone plot in Figure 4.7. We used CV curves at different scan rates to calculate these performance metrics. These examples include microsupercapacitors with electrodes of graphene-vanadium quantum dots/reduced graphene oxide (G-VNQDs/rGO),[181] Ag-polypyrrole,[308] MXene,[185], [318] and graphene oxide/Ag NPs/CNT/MoS<sub>2</sub>. [319] Our MSCs with electrodes of 3.75 mm of length which were printed with an 840  $\mu\text{m}$  nozzle (microsupercapacitor ID: L2) or a 250  $\mu\text{m}$  nozzle (microsupercapacitor ID: XS2) (more details on the microsupercapacitors' IDs is provided in table 4.1) both showed a combination of high areal energy and power densities. The MSC printed with an 840  $\mu\text{m}$  nozzle generally showed higher areal energy density values with a maximum areal energy density of 36.59  $\mu\text{Wh.cm}^{-2}$ , however, it showed a sharp decrease in its energy density at higher scan rates (points that are more on the right side of the plot correspond to higher scan rates). On the other hand, the microsupercapacitors printed with the 250  $\mu\text{m}$  nozzle showed higher power density values at higher scan rates, with a maximum value of 3070.77  $\text{mW.cm}^{-2}$ . Such high levels of energy and power densities demonstrate remarkable combination of performance of our microsupercapacitors compared to examples of microsupercapacitors from literature. These results are particularly attractive as even for a microsupercapacitors printed with a nozzle of 840  $\mu\text{m}$ , an excellent performance level of energy and power density is achieved.

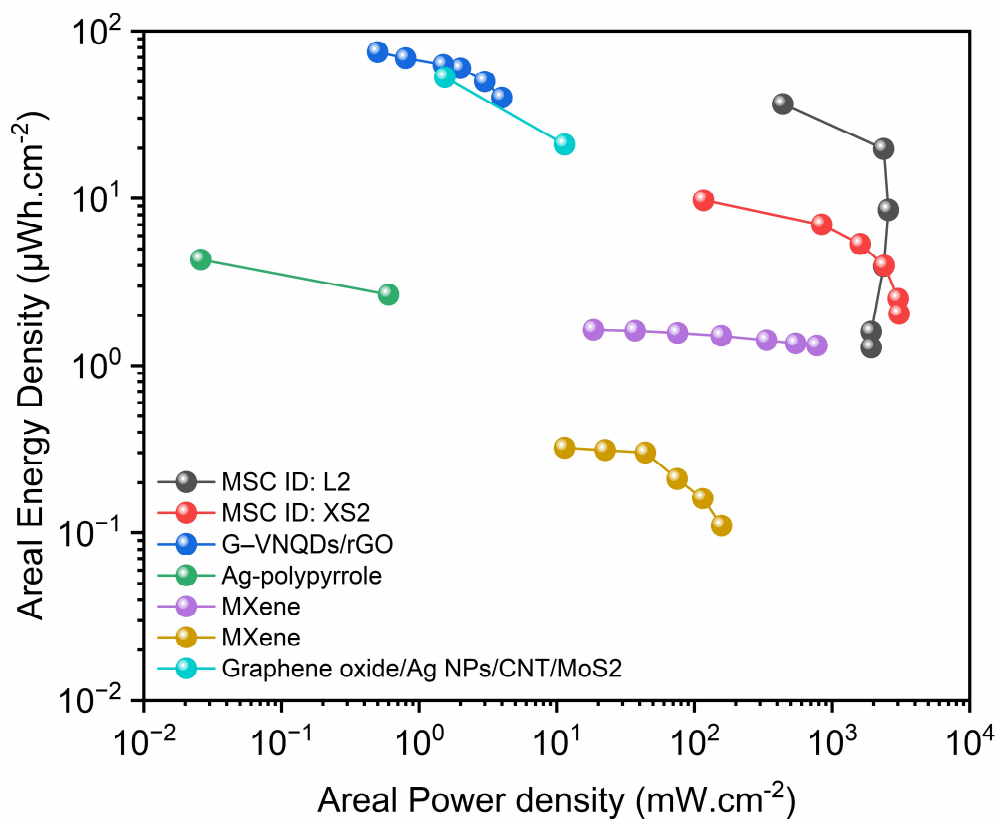


Figure 4.7. Ragone plot exhibiting areal energy and power densities of our microsupercapacitors possessing an electrode length of 3.75 and printed with a nozzle diameter of 250  $\mu\text{m}$  and 840  $\mu\text{m}$  in comparison with some of the selected examples of printed MSCs from literature.

We also compared the volumetric energy and power densities of our microsupercapacitors with results from the literature. The comparison set encompasses microsupercapacitors with electrode thicknesses ranging from nm-scale up to  $\mu\text{m}$ -scale. It should be noted that when comparisons of the performance of microsupercapacitors are made, their geometrical features (e.g., electrode thickness) should be mentioned. While the thickness of the electrodes in our microsupercapacitors range between 250  $\mu\text{m}$  and 840  $\mu\text{m}$ , the thickness of the electrodes in the selected examples from the literature are as follows: 412  $\mu\text{m}$ [181], 3.97  $\mu\text{m}$ [308], 1.4-18  $\mu\text{m}$ [185],  $530 \pm 120$  nm[318], and 500-2000  $\mu\text{m}$ [319].

We could realize microsupercapacitors with ESR values on the order of tens of ohms, areal and volumetric capacitance values on the order of hundreds of  $\text{mF}/\text{cm}^2$  and couple of  $\text{F}/\text{cm}^3$ , respectively. The energy and power densities of our microsupercapacitors are on the order of tens of  $\mu\text{Wh}/\text{cm}^2$  and thousands of  $\text{mW}/\text{cm}^2$ , respectively. Additionally, these microsupercapacitors showed cyclic stability of 95% capacitance retention after 17000 cycles of charge/discharge. The operating potential window of these microsupercapacitors is 0.6 V (0 to +0.6 V).

### **4.3. Materials and Methods**

We used the same chemicals and followed the same synthesis procedure for the electrode active materials as described in chapter 3. All the characterization techniques performed and reported in this chapter have been discussed in the “Materials and Methods” of chapter 3.

#### **4.3.1. Details of dimensional scaling of the microsupercapacitors**

Table 4.1 summarizes the details of dimensional scaling of the microsupercapacitors. Figures 4.8–4.19 show how the active areas of the microsupercapacitors were calculated. We considered the maximum rectangular areas encompassing both fingers of the current collectors in order to calculate the active areas of the microsupercapacitors. The reason behind this method is that the electrodes must be placed by printing within these areas.

## Chapter 4

---

Table 4.1. The IDs of the 3D printed microsupercapacitors and their related geometrical feature dimensions.

| MSC ID | Width of the fingers (W) (mm) | Length of the fingers (L) (mm) | Gap between the fingers (G) (mm) | Active Area's Lateral dimensions ((W+G) × L) (mm × mm) | Active area (cm <sup>2</sup> )* |
|--------|-------------------------------|--------------------------------|----------------------------------|--|---------------------------------|
| XS1    | 0.35                          | 2.5                            | 0.75                             | 1.45 × 2.5   | 0.04375                         |
| XS2    | 0.35                          | 3.75                           | 0.75                             | 1.45 × 3.75  | 0.065625                        |
| XS3    | 0.35                          | 5                              | 0.75                             | 1.45 × 5   | 0.0875                          |
| S1     | 0.5                           | 2.5                            | 0.75                             | 1.75 × 2.5   | 0.04375                         |
| S2     | 0.5                           | 3.75                           | 0.75                             | 1.75 × 3.75  | 0.065625                        |
| S3     | 0.5                           | 5                              | 0.75                             | 1.75 × 5   | 0.0875                          |
| M1     | 0.75                          | 2.5                            | 0.75                             | 2.25 × 2.5   | 0.05625                         |
| M2     | 0.75                          | 3.75                           | 0.75                             | 2.25 × 3.75  | 0.084375                        |
| M3     | 0.75                          | 5                              | 0.75                             | 2.25 × 5   | 0.1125                          |
| L1     | 1                             | 2.5                            | 0.75                             | 2.75 × 2.5   | 0.06875                         |
| L2     | 1                             | 3.75                           | 0.75                             | 2.75 × 3.75  | 0.103125                        |
| L3     | 1                             | 5                              | 0.75                             | 2.75 × 5   | 0.1375                          |

(\*) calculations of the active area is based on the rectangular area (i.e., the dashed yellow rectangles as shown in Figures 4.8-4.19) surrounding the current collector fingers which is theoretically the maximum area that the electrodes can take up after printing.

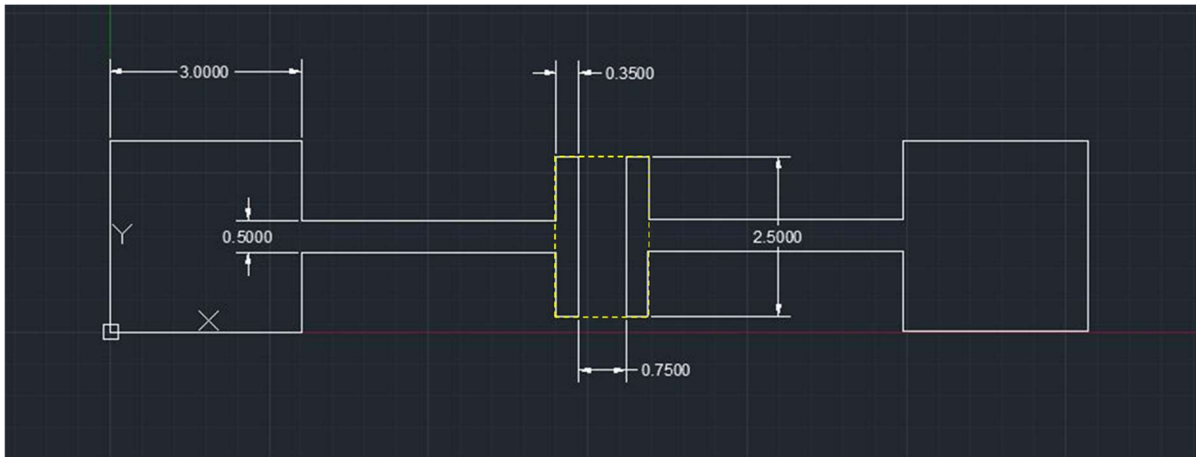


Figure 4.8. The geometrical details of the design of the current collectors of the MSC with the sample ID XS1.

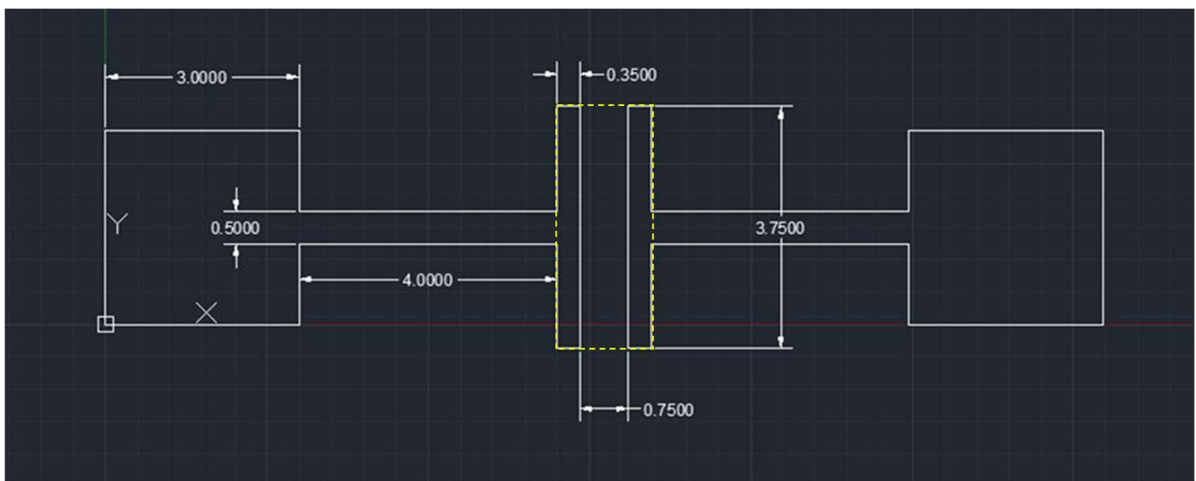


Figure 4.9. The geometrical details of the design of the current collectors of the MSC with the sample ID XS2.



# Chapter 4

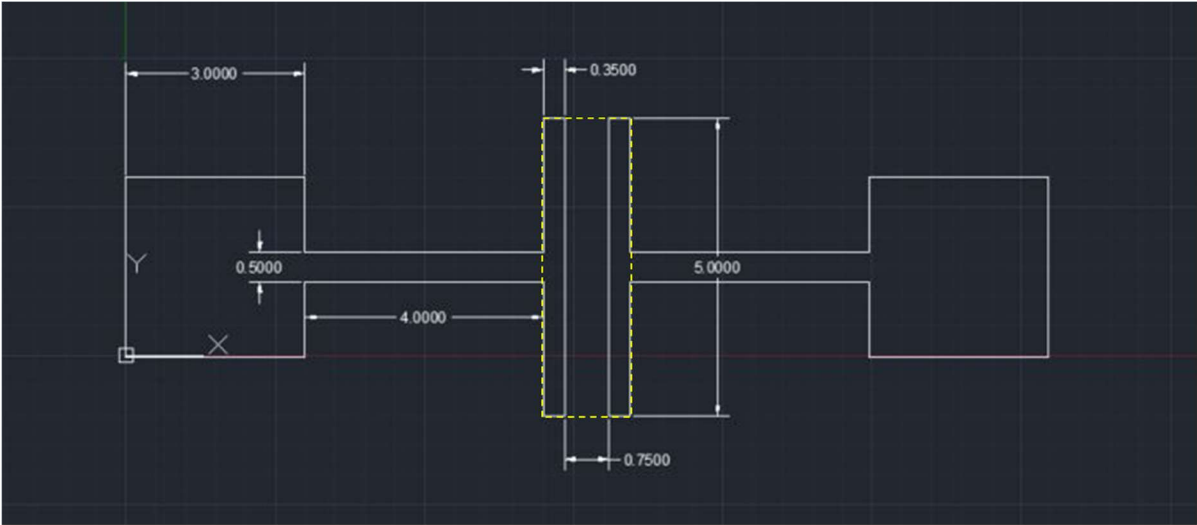


Figure 4.10. The geometrical details of the design of the current collectors of the MSC with the sample ID XS3.

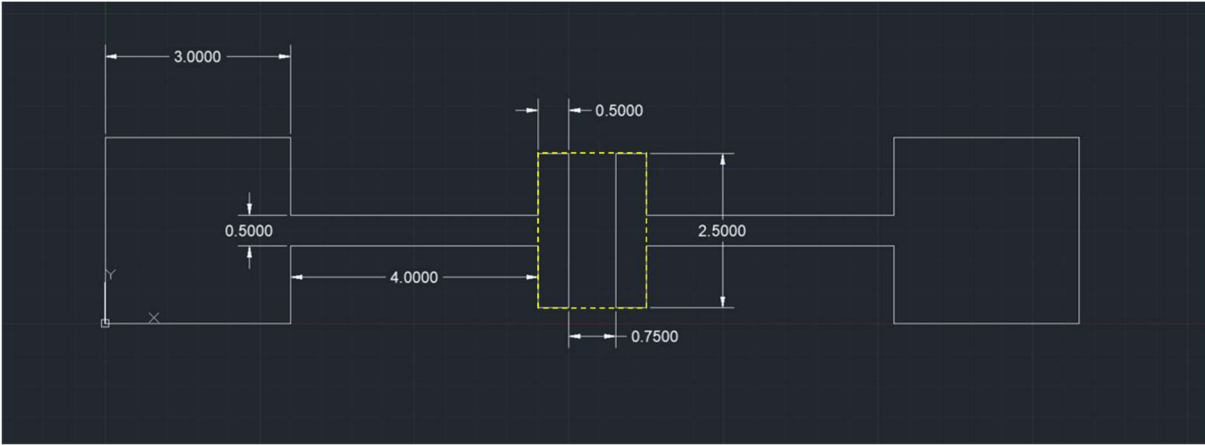


Figure 4.11. The geometrical details of the design of the current collectors of the MSC with the sample ID S1.

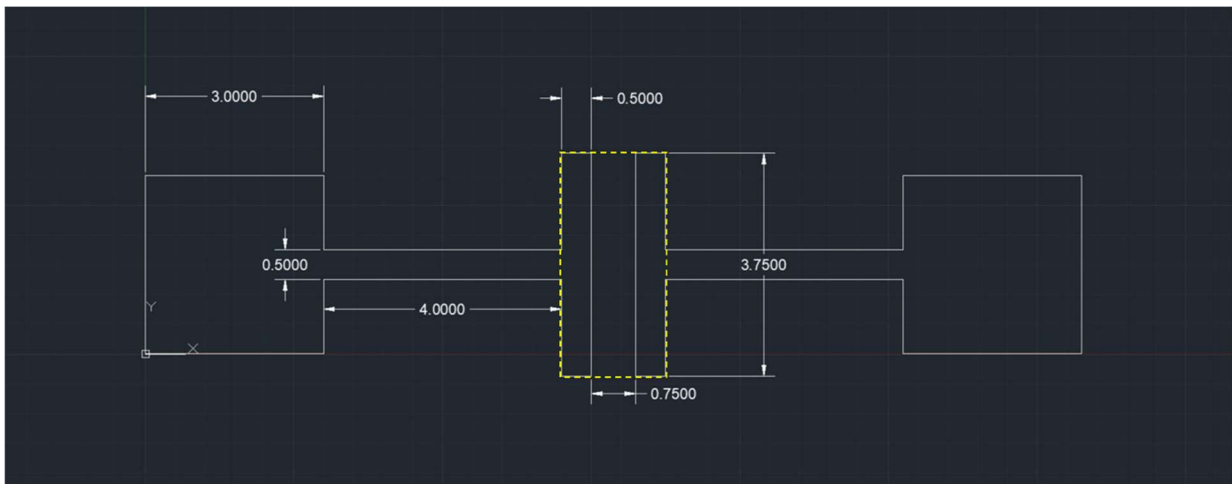


Figure 4.12. The geometrical details of the design of the current collectors of the MSC with the sample ID S2.

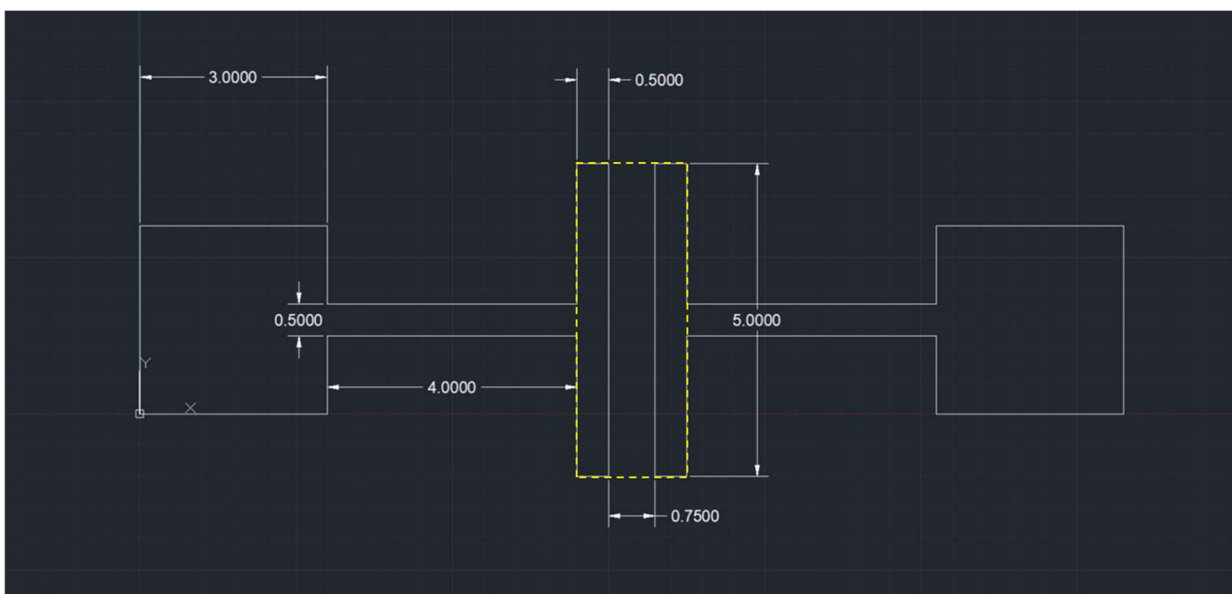


Figure 4.13. The geometrical details of the design of the current collectors of the MSC with the sample ID S3.

# Chapter 4

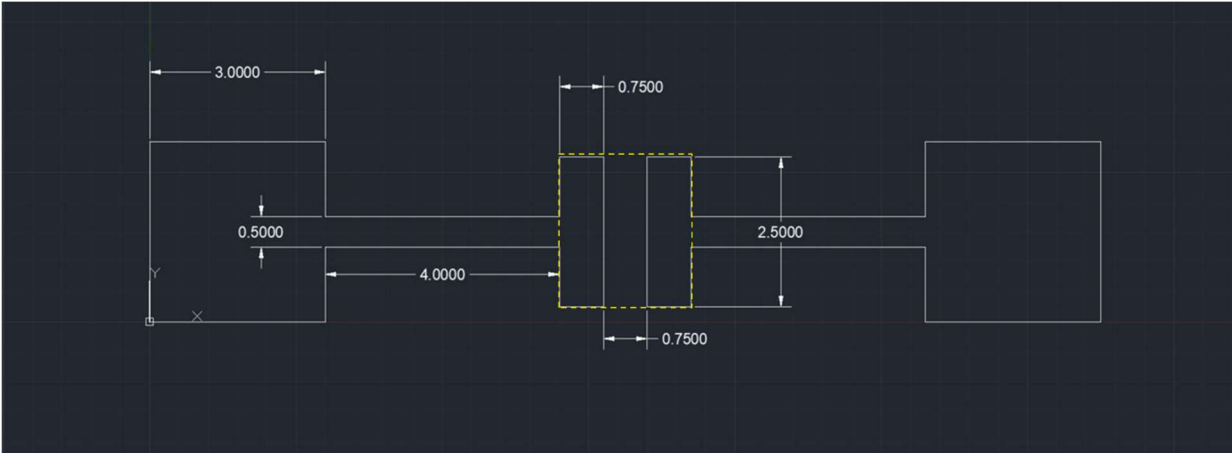


Figure 4.14. The geometrical details of the design of the current collectors of the MSC with the sample ID M1.

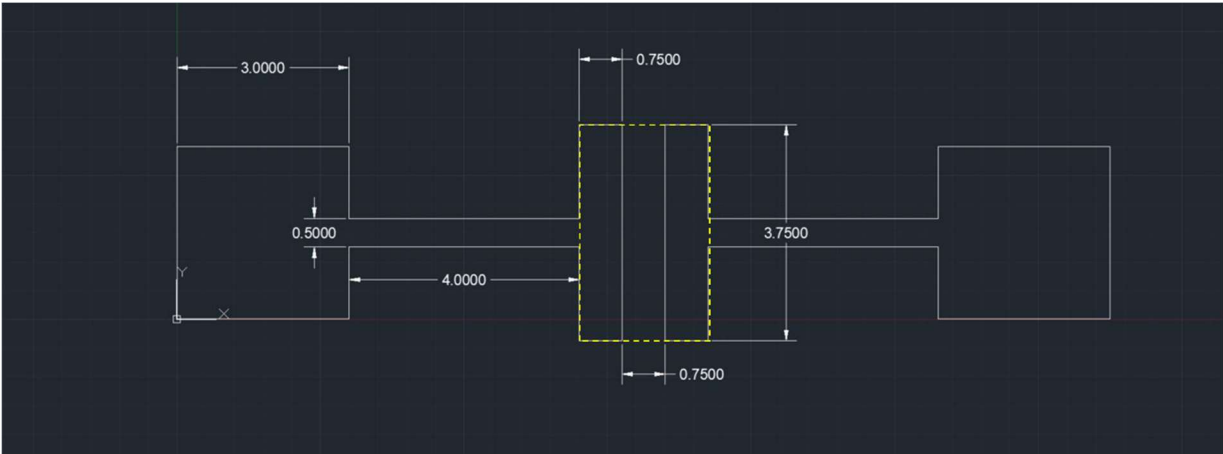


Figure 4.15. The geometrical details of the design of the current collectors of the MSC with the sample ID M2.

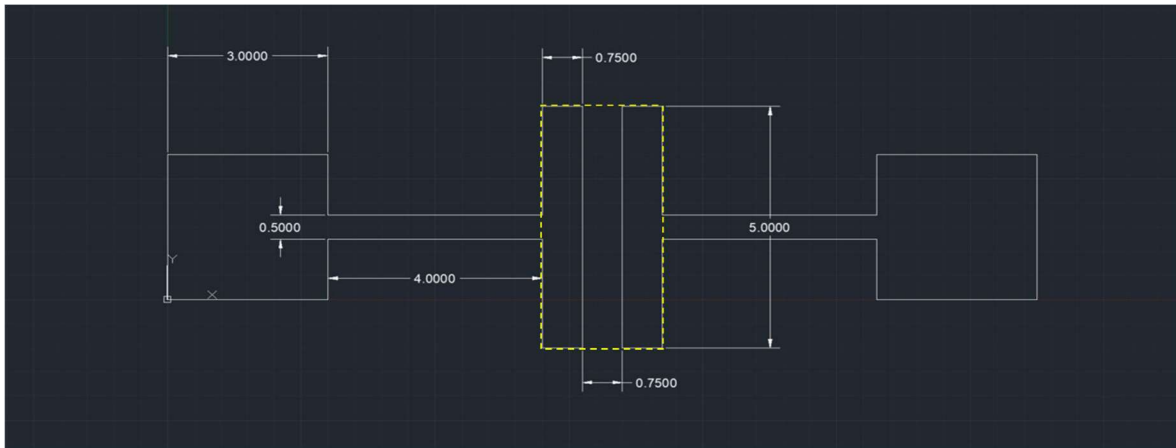


Figure 4.16. The geometrical details of the design of the current collectors of the MSC with the sample ID M3.

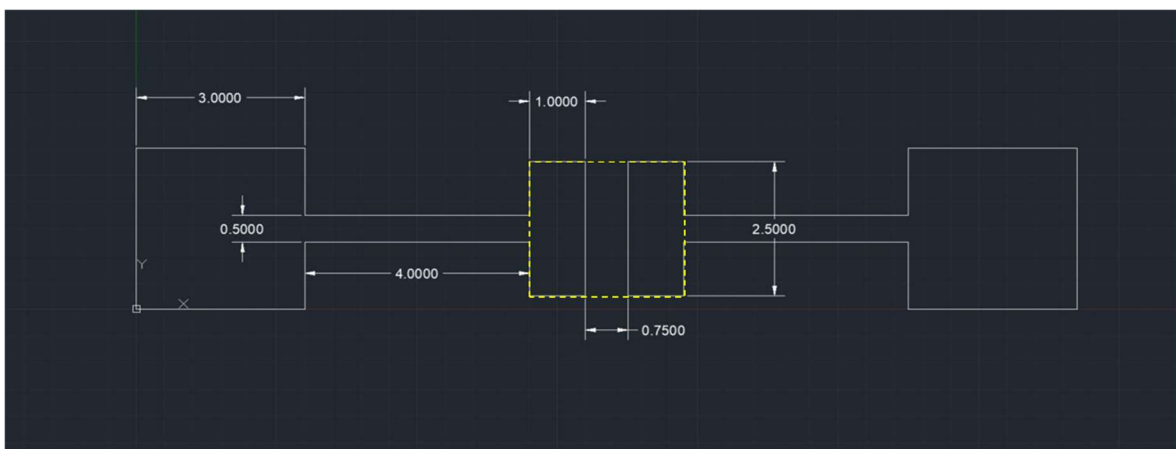


Figure 4.17. The geometrical details of the design of the current collectors of the MSC with the sample ID L1.

# Chapter 4

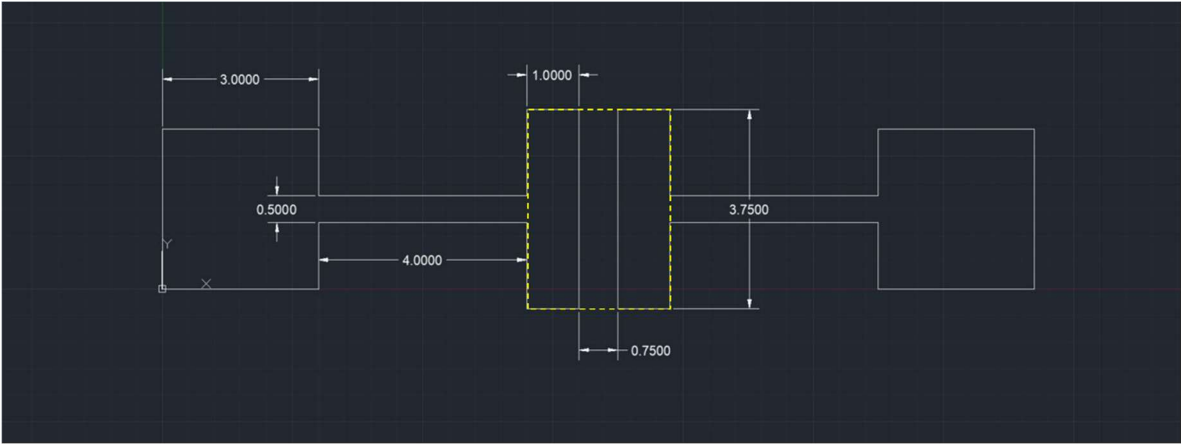


Figure 4.18. The geometrical details of the design of the current collectors of the MSC with the sample ID L2.

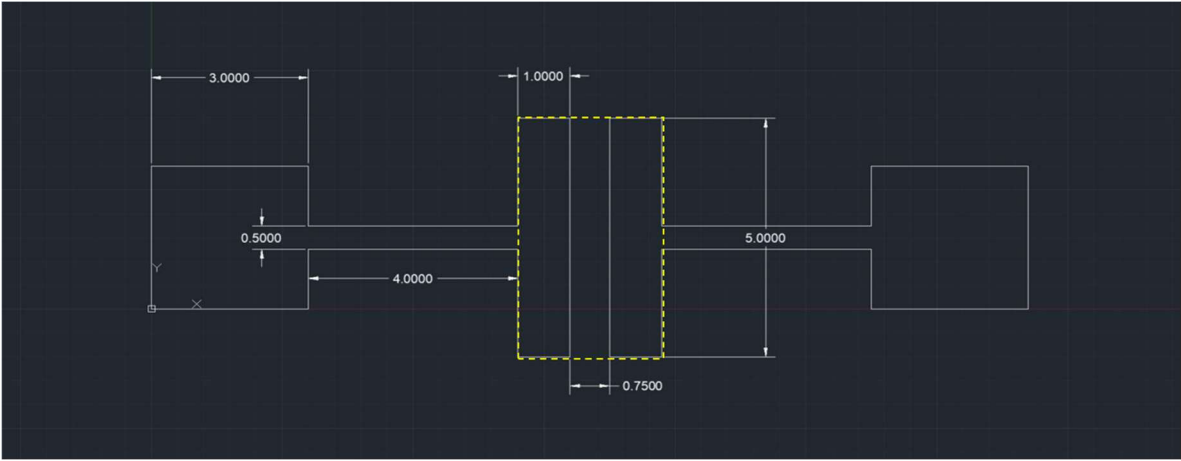


Figure 4.19. The geometrical details of the design of the current collectors of the MSC with the sample ID L3.

### 4.3.2. Electrochemical performance calculations

We used the same equations as provided in chapter 3, for electrochemical performance evaluation of the microsupercapacitors (as listed below).

$$C_A = \frac{\int_0^{0.6} j dV}{A \times \Delta V \times \nu} \quad (4.1)$$

$$E_A = \frac{C_A \times V^2}{2 \times 3.6} \quad (4.2)$$

$$P_A = \frac{E_A \times \nu \times 3600}{\Delta V} \quad (4.3)$$

Where  $C_A$  (mF/cm<sup>2</sup>) is the areal capacitance of the device,  $A$  (cm<sup>2</sup>) is the active area of the microsupercapacitors,  $E_A$  is the areal energy density (μWh/cm<sup>2</sup>),  $P_A$  is the areal power density (μW/cm<sup>2</sup>),  $j$  is the current (mA),  $\Delta V$  is the voltage window (0.6 V), and  $\nu$  is the scan rate (mV/s).

### 4.3.3. Kinetic study of charge storage mechanisms

Similar to the procedure followed in chapter 3, we calculated the ratio of (EDLC + Faradaic pseudocapacitance) (fast kinetic)/diffusive ion insertion (diffusive pseudocapacitance) (slow kinetic) charge storage contributions of the MSCs comprising 3.75 mm electrodes printed with the smallest nozzle (i.e., 250 μm) and the largest nozzle (i.e., 840 μm). We followed the same calculations as mentioned in chapter 3. Figures 4.20 and 4.21 demonstrate the microsupercapacitors constructed by the electrode with the length of 3.75 mm, which are printed with a nozzle of diameter 250 μm and 840 μm, respectively.

## Chapter 4

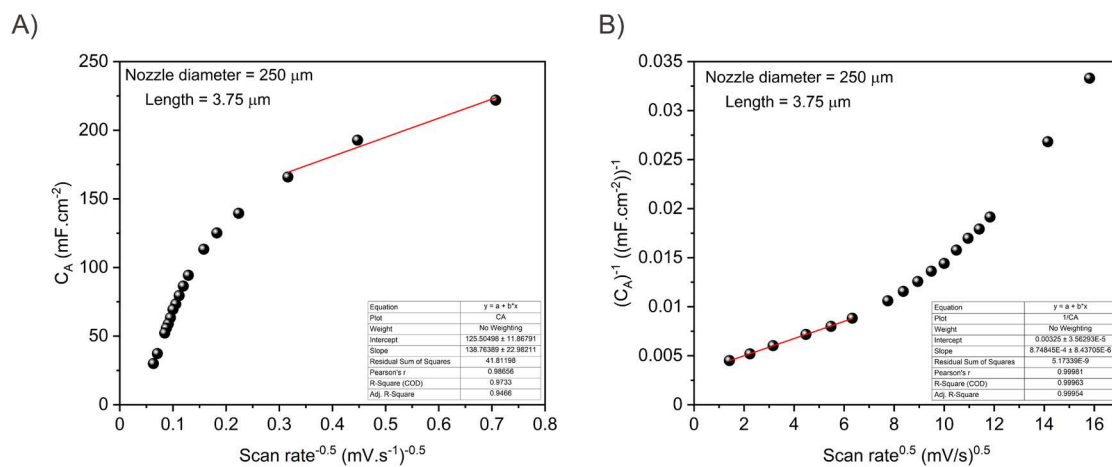


Figure 4.20. The plots of A)  $C_A$  vs.  $u^{-0.5}$  and B)  $C_A^{-1}$  vs.  $u^{0.5}$  of the microsupercapacitor constructed by the electrode with the length of 3.75 mm, which is printed with a nozzle of diameter 250 μm.

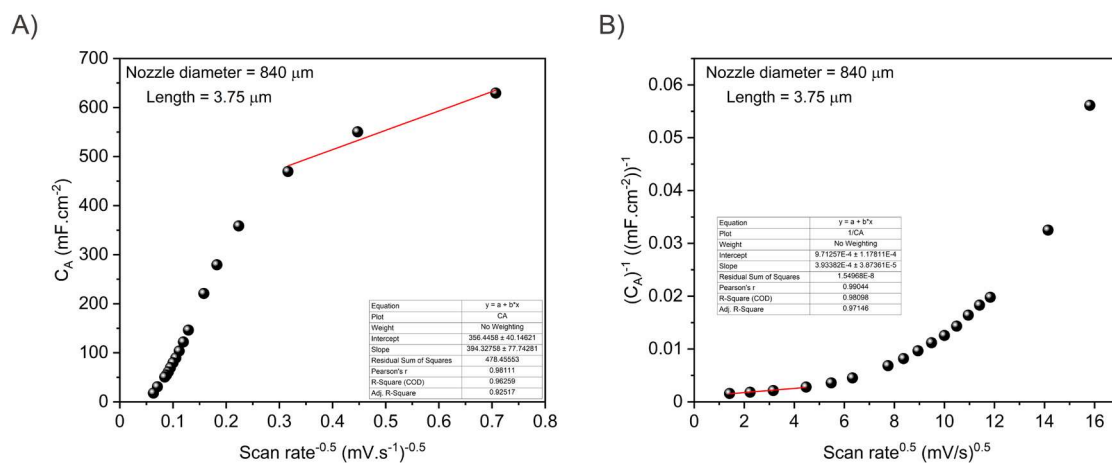


Figure 4.21. The plots of A)  $C_A$  vs.  $u^{-0.5}$  and B)  $C_A^{-1}$  vs.  $u^{0.5}$  of the microsupercapacitor constructed by the electrode with the length of 3.75 mm, which is printed with a nozzle of diameter 840 μm.

#### 4.4. Conclusions

In summary, we systematically studied the effects of sub-mm<sup>3</sup> dimensional scaling on the performance of all-additively fabricated encapsulated hybrid microsupercapacitors (i.e., modifying their electrode lengths and the nozzle diameter with which they are printed) comprising a nanocomposite electrode (i.e., edge-oxidized graphite oxide (EOGO) (~95 wt.)/cerium oxide NPs (~5 wt.%)), a UV-curable hydrogel electrolyte based on (poly (ethylene glycol) diacrylate (PEGDA) + LiCl + lithium phenyl-2,4,6-trimethylbenzoylphosphinate (LAP) + water), a silver current collector, a polycaprolactone (PCL) packaging and a UV-curable resin-based encapsulant. We observed that capacitance scales with dimensions, as expected. Moreover, we achieved remarkable combinations of performance levels such as a areal capacitance of ~731.7 mF/cm<sup>2</sup>, energy density of ~ 36.59 μWh/cm<sup>2</sup>, power density of ~ 2,669.8 mW/cm<sup>2</sup>, and ~95% capacitance retention after 17000 cycles (at the electrode length of 3.75 mm printed with a nozzle diameter of 840 μm). We have thus shown that dimensional scaling to sub-mm<sup>3</sup> of these microsupercapacitors is possible, which is obviously attractive for these use in small microsystems. We have further shown how the performance of the supercapacitors is altered during dimensional scaling. As such, therefore, through this chapter, we have provided a comprehensive understanding of the scaling of additively fabricated microsupercapacitors.

In the next chapter, we will discuss the key outcomes of the thesis, why these outcomes are important, in addition to specific and detailed discussion of future work that can be potentially pursued on fully-additively fabricated microsupercapacitors.





## 5. Conclusions and Outlook

Fabrication of miniaturized energy storage systems, such as microsupercapacitors, entails challenges and great potential for development of high-efficiency energy systems. These systems find applications in versatile fields of microelectronics, IoT, and other microsystems, hence, there is a significant demand on realization of simultaneously small-scale and high-performance energy storage system, such as microsupercapacitors. Among many fabrication techniques, 3D printing provides unrivaled benefits such as compatibility with diverse chemistries, realization of geometries fine structure with complex geometries for on-chip or wafer-scale integration. Hence, we aimed at full 3D printing (additive fabrication) of microsupercapacitors for all their components, namely, current collectors, electrodes, electrolyte, packaging, and encapsulation.

### 5.1. Key outcomes of the thesis

It was demonstrated in this thesis that by fine tuning the chemistries of the components of microsupercapacitors, it is possible to maximize their performance. We reached a combination of record levels of performance for microsupercapacitors at mm-scale active area level through a fully additive fabrication procedure. Special emphasis is placed on design, synthesis, characterization and optimization of novel chemistries for the electrodes and the electrolytes. The electrode of the microsupercapacitors is a nanocomposite of edge-oxidized graphite oxide (EOGO)/cerium oxide nanoparticles. This electrode system allows us to exploit both EDLC and pseudocapacitance charge storage mechanisms. We showed that the loading of cerium oxide NPs in the electrode nanocomposite alters the EDLC/pseudocapacitance charge storage mechanism ratio. Besides, we demonstrated that even by the addition of relatively low concentrations ( $\sim 3\text{-}5$  wt.%) of cerium oxide NPs to composite with pure EOGO, the capacitance of the microsupercapacitors almost doubled. The electrolyte is a UV- curable hydrogel based on (poly (ethylene glycol) diacrylate (PEGDA) + LiCl + lithium phenyl-2,4,6-trimethylbenzoylphosphinate (LAP) + water). Using this electrolyte enabled us to consolidate

## Chapter 5

---

the structure of the microsupercapacitors as a result of its UV curing and also eliminated the need for having a separator. The current collector is a silver paste, which provides with relatively high electrical conductivity. We extrusion printed the current collectors to construct thick layers (~100  $\mu\text{m}$ ). Printing thick current collectors is advantageous for microsupercapacitors as the conductance of the current collector increases with thickness, reducing the series resistance contribution of the same. These microsupercapacitors are fully packaged and sealed by printing a package using polycaprolactone (PCL) and depositing a UV-curable resin-based encapsulant. Using the packaging is crucial to act as a container to keep the electrolyte inside its inner space before its UV curing. Moreover, using the encapsulant is beneficial for stability and increasing the service life of the microsupercapacitors. We demonstrated that without encapsulation, the electrolytes started to be evaporated and presence of the encapsulation eliminated this problem from the system.

Moreover, we could realize the smallest microsupercapacitors with the highest levels of performance that are fully additively fabricated. This achievement is significant as it is a step towards realization of fully additive fabrication of high-performance microsupercapacitors for embedded energy applications. One of the biggest challenges in downsizing microelectronic systems is to downsize their components, and more specifically their energy systems, such as microsupercapacitors. Thus, realization of such high levels of performance for microsupercapacitors at the smallest footprints to date, as demonstrated in this thesis, is a promising achievement which could potentially lead to faster, more efficient and smaller microelectronic systems.

We also demonstrated that the chemistry of the components is not the only factor determining the performance of the microsupercapacitors. A dimensional scaling study of microsupercapacitors showed that changing the dimensions of the microsupercapacitors (e.g., the length and thickness of the electrodes) significantly alters the performance of the fully additively fabricated microsupercapacitors even when the chemistries of their components are unchanged. The significance of this study is revealed when considering hybrid

microsupercapacitors are used in energy applications with the aim to benefit from their synergy of EDLC and pseudocapacitance charge storage mechanisms to reach higher energy and power densities. It is crucial to investigate what effects the dimensional scaling of these systems have on their performance so that these systems can be designed on demand and with an application-oriented approach. Such an understanding is missing in the literature.

Scaling energy storage systems such as microbatteries and microsupercapacitors, is required to ensure suitability of them for typical IoT system requirements. In other words, the energy storage systems must scale to the device sizes and geometries in order to realize chip-scale and wafer-scale fabrication and integration. As an outcome of this thesis, we could systematically perform sub-mm<sup>3</sup> dimension scaling of additively-fabricated microsupercapacitors, which is being reported in this thesis, for the first time in literature, to the best of our knowledge. Moreover, our results demonstrated that we would design microsupercapacitors with different performance levels at various footprints, which would potentially realize selection of microsupercapacitors at a desired footprint for integration in a specific IoT application. For instance, we showed that microsupercapacitors printed with thicker electrodes show pseudocapacitance more dominantly and also reach higher levels of energy density, while microsupercapacitors possessing thinner electrodes exhibited relatively higher power density and an EDLC dominant charge storage. This range of different electrochemical performance enable us to select a microsupercapacitor according to its geometrical features to fulfill the performance requirements of an IoT application. Dimensional scaling study performed in this thesis emphasizes that the chemistries of the components are not the sole factors determining the overall performance of microsupercapacitors. In addition to chemistries of these systems, we realized that their dimensional scaling also needs to be studied in order to maximize their performance.

### 5.2. Discussion of future work

Future research directions in continuation of this thesis encompasses i) materials development for the components of the microsupercapacitors, ii) operando characterization of the fabricated microsupercapacitors (to elucidate at atomic level how these devices operate with respect to charge storage), iii) realization of high-performance flexible microsupercapacitors using the novel chemistries and fabrication techniques, and v) device integration for different energy applications.

New chemistries for the components of the microsupercapacitors need to be designed, characterized and optimized for future studies on microsupercapacitors. More emphasis is placed on electrodes and electrolytes. For instance, for the electrodes, novel nanocomposites based on EOGO with other metal oxides (e.g., vanadium oxide, manganese oxide, etc.) are worthwhile of future study. To the best of our knowledge, our results are the first examples of using EOGO in electrodes of microsupercapacitors, thus, there is huge potential for development of nanocomposite electrode based on EOGO which exhibit both EDLC and pseudocapacitance. EOGO is water dispersible and unlike conventionally synthesized graphene oxide has most of its oxygen containing functional groups on its edges—keeping its basal plane almost intact, and does not necessarily require chemical/thermal reduction to eliminate its oxygen functional groups to obtain better electrical conductivity. Thus, using EOGO in electrodes of microsupercapacitors is an aqueous-based and facile way to benefit from its fascinating properties resembling those of pristine graphene. As we could have realized high levels of performance using EOGO/cerium oxide NPs nanocomposite electrodes, we believe there is a great opportunity to develop new nanocomposite electrodes based on EOGO.

Moreover, new UV-curable gel electrolytes with acidic or basic natures or containing other ionic species (e.g., divalent and/or trivalent ionic species) should be designed to provide higher ionic conduction and redox capabilities. This is specifically important as the examples of gel

electrolytes used in microsupercapacitors are quite limited. To the best of our knowledge, systematic studies on the effects of gel electrolyte chemistries on the performance of additively fabricated microsupercapacitors are missing in the literature. The main goal in these studies should be to formulate gel electrolytes that provide high ionic conduction, good mechanical stability, wide operation voltage window, and chemical compatibility with the other components in the system.

Operando characterizations can be performed on the fabricated microsupercapacitors to unravel the atomic-scale phenomena in these systems at their electrode/electrolyte interface which determines the charge storage mechanism of the system. Moreover, these studies will also be helpful to shed light on the effects of chemistries of the components and also their dimensional scaling on cyclic life prediction of the microsupercapacitors.

Another direction for future work in continuation of the research pursued in this thesis is to realize high-performance flexible microsupercapacitors using the aforementioned novel chemistries and fabrication techniques. Fabrication of flexible microsupercapacitors is even more challenging when using thick electrodes. One possible approach in that regard would be to fabricate flexible electrodes and electrolytes by developing new chemistries fulfilling this requirement. More emphasis is placed on these two components since the current collectors can always be thinner, and the flexible packaging materials are already available for use. Thus, the main goal should be set to formulate/fabricate electrodes and electrolytes with flexible nature and high electrochemical performance.

All these efforts should be followed by device integration into different circuits to fulfill requirements of different energy applications, for both flexible and rigid microsupercapacitors. As an example, the fabricated microsupercapacitors should be incorporated into other microelectronics or IoT systems to understand how these devices perform in their final applications. Ultimately, all the research and development studies on microsupercapacitors should lead to integration of these devices into microelectronic systems, however, such examples are quite rare in the literature. As a result, there are great

## Chapter 5

---

opportunities for further research in this direction. For instance, integration of microsupercapacitors with desired performance levels in IoT-based devices could be one of ultimate applications for integrated microsupercapacitors. Moreover, these microsupercapacitors might need to be coupled with other energy storage devices, in particular, microbatteries, so that these devices can cooperate and complement each other in such applications. It is worth mentioning that by realization of microsupercapacitors with high energy densities (i.e., reaching to the levels of microbatteries), we ultimately can replace microbatteries with microsupercapacitors. This will be particularly attractive as it can lead to reduction of number of components used in microelectronics applications where both microbatteries and microsupercapacitors used to be required.





### Bibliography

- [1] C. Lethien, J. Le Bideau, and T. Brousse, "Challenges and prospects of 3D micro-supercapacitors for powering the internet of things," *Energy Environ. Sci.*, vol. 12, no. 1, pp. 96–115, 2019, doi: 10.1039/C8EE02029A.
- [2] Y. Wang *et al.*, "Supercapacitor Devices Based on Graphene Materials," *J. Phys. Chem. C*, vol. 113, no. 30, pp. 13103–13107, Jul. 2009, doi: 10.1021/jp902214f.
- [3] Y. Shao *et al.*, "Design and Mechanisms of Asymmetric Supercapacitors," *Chem. Rev.*, vol. 118, no. 18, pp. 9233–9280, Sep. 2018, doi: 10.1021/acs.chemrev.8b00252.
- [4] Helmholtz H. V., "On the Conservation of Force," *Ann. Phys.*, vol. 165, p. 211, 1853, doi: <https://doi.org/10.1002/andp.18531650603>.
- [5] M. Gouy, "Constitution of the Electric Charge at The Surface of an Electrolyte," *J. Phys. Theor. Appl.*, vol. 9, no. 1, pp. 457–468, 1910, doi: 10.1051/jphysap:019100090045700.
- [6] D. L. Chapman, "LI. A contribution to the theory of electrocapillarity," *The London, Edinburgh, and Dublin Philosophical Magazine and Journal of Science*, vol. 25, no. 148, pp. 475–481, Apr. 1913, doi: 10.1080/14786440408634187.
- [7] O. Z. Stern, "Theory of The Electrical Double Layer," *Elektrochem*, vol. 30, p. 508, 1924.
- [8] D. C. Grahame, "The Electrical Double Layer and the Theory of Electrocapillarity.," *Chem. Rev.*, vol. 41, no. 3, pp. 441–501, Dec. 1947, doi: 10.1021/cr60130a002.
- [9] P. Simon and Y. Gogotsi, "Perspectives for electrochemical capacitors and related devices," *Nat. Mater.*, Aug. 2020, doi: 10.1038/s41563-020-0747-z.
- [10] P. Simon and Y. Gogotsi, "Materials for electrochemical capacitors," *Nature Materials*, vol. 7, pp. 845–854, 2008, doi: <https://doi.org/10.1038/nmat2297>.
- [11] J. W. Long, D. Bélanger, T. Brousse, W. Sugimoto, M. B. Sassin, and O. Crosnier, "Asymmetric electrochemical capacitors—Stretching the limits of aqueous electrolytes," *MRS Bull.*, vol. 36, no. 7, pp. 513–522, Jul. 2011, doi: 10.1557/mrs.2011.137.
- [12] A. K. Samantara and S. Ratha, *Materials Development for Active/Passive Components of a Supercapacitor*. in SpringerBriefs in Materials. Singapore: Springer Singapore, 2018. doi: 10.1007/978-981-10-7263-5.
- [13] G. Yu, X. Xie, L. Pan, Z. Bao, and Y. Cui, "Hybrid nanostructured materials for high-performance electrochemical capacitors," *Nano Energy*, vol. 2, no. 2, pp. 213–234, Mar. 2013, doi: 10.1016/j.nanoen.2012.10.006.
- [14] M. R. Lukatskaya, B. Dunn, and Y. Gogotsi, "Multidimensional materials and device architectures for future hybrid energy storage," *Nat Commun*, vol. 7, no. 1, p. 12647, Sep. 2016, doi: 10.1038/ncomms12647.
- [15] C. Liu, Z. Yu, D. Neff, A. Zhamu, and B. Z. Jang, "Graphene-Based Supercapacitor with an Ultrahigh Energy Density," *Nano Lett.*, vol. 10, no. 12, pp. 4863–4868, Dec. 2010, doi: 10.1021/nl102661q.
- [16] M. D. Stoller, S. Park, Y. Zhu, J. An, and R. S. Ruoff, "Graphene-Based Ultracapacitors," *Nano Lett.*, vol. 8, no. 10, pp. 3498–3502, Oct. 2008, doi: 10.1021/nl802558y.
- [17] X. Yang, C. Cheng, Y. Wang, L. Qiu, and D. Li, "Liquid-Mediated Dense Integration of Graphene Materials for Compact Capacitive Energy Storage," *Science*, vol. 341, no. 6145, pp. 534–537, Aug. 2013, doi: 10.1126/science.1239089.
- [18] W. Yang *et al.*, "Graphene in Supercapacitor Applications," *Current Opinion in Colloid & Interface Science*, vol. 20, no. 5–6, pp. 416–428, Oct. 2015, doi: 10.1016/j.cocis.2015.10.009.

- [19] W.-W. Liu, Y.-Q. Feng, X.-B. Yan, J.-T. Chen, and Q.-J. Xue, "Superior Micro-Supercapacitors Based on Graphene Quantum Dots," *Adv. Funct. Mater.*, vol. 23, no. 33, pp. 4111–4122, Sep. 2013, doi: 10.1002/adfm.201203771.
- [20] B. Xu *et al.*, "What is the choice for supercapacitors: graphene or graphene oxide?," *Energy Environ. Sci.*, vol. 4, no. 8, p. 2826, 2011, doi: 10.1039/c1ee01198g.
- [21] S. Zhang, L. Sui, H. Dong, W. He, L. Dong, and L. Yu, "High-Performance Supercapacitor of Graphene Quantum Dots with Uniform Sizes," *ACS Appl. Mater. Interfaces*, vol. 10, no. 15, pp. 12983–12991, Apr. 2018, doi: 10.1021/acsami.8b00323.
- [22] F. Barzegar, A. Bello, D. Momodu, M. J. Madito, J. Dangbegnon, and N. Manyala, "Preparation and characterization of porous carbon from expanded graphite for high energy density supercapacitor in aqueous electrolyte," *Journal of Power Sources*, vol. 309, pp. 245–253, Mar. 2016, doi: 10.1016/j.jpowsour.2016.01.097.
- [23] E. C. Vermisoglou *et al.*, "Non-activated high surface area expanded graphite oxide for supercapacitors," *Applied Surface Science*, vol. 358, pp. 110–121, Dec. 2015, doi: 10.1016/j.apsusc.2015.08.123.
- [24] H. Li *et al.*, "Ultra-thick graphene bulk supercapacitor electrodes for compact energy storage," *Energy Environ. Sci.*, vol. 9, no. 10, pp. 3135–3142, 2016, doi: 10.1039/C6EE00941G.
- [25] Y. Zhang *et al.*, "Morphology Effect of Vertical Graphene on the High Performance of Supercapacitor Electrode," *ACS Appl. Mater. Interfaces*, vol. 8, no. 11, pp. 7363–7369, Mar. 2016, doi: 10.1021/acsami.5b12652.
- [26] B. Xie *et al.*, "Shape-Tailorable Graphene-Based Ultra-High-Rate Supercapacitor for Wearable Electronics," *ACS Nano*, vol. 9, no. 6, pp. 5636–5645, Jun. 2015, doi: 10.1021/acsnano.5b00899.
- [27] U. Fischer, R. Saliger, V. Bock, R. Petricevic, and J. Fricke, "Carbon Aerogels as Electrode Material in Supercapacitors," 1997.
- [28] J. Li, X. Wang, Q. Huang, S. Gamboa, and P. J. Sebastian, "Studies on preparation and performances of carbon aerogel electrodes for the application of supercapacitor," *Journal of Power Sources*, vol. 158, no. 1, pp. 784–788, Jul. 2006, doi: 10.1016/j.jpowsour.2005.09.045.
- [29] S. J. Kim, S. W. Hwang, and S. H. Hyun, "Preparation of carbon aerogel electrodes for supercapacitor and their electrochemical characteristics," *J Mater Sci*, vol. 40, no. 3, pp. 725–731, Feb. 2005, doi: 10.1007/s10853-005-6313-x.
- [30] P. Hao *et al.*, "Hierarchical porous carbon aerogel derived from bagasse for high performance supercapacitor electrode," *Nanoscale*, vol. 6, no. 20, pp. 12120–12129, 2014, doi: 10.1039/C4NR03574G.
- [31] R. Saliger, U. Fischer, C. Herta, and J. Fricke, "High surface area carbon aerogels for supercapacitors," *Journal of Non-Crystalline Solids*, vol. 225, pp. 81–85, Apr. 1998, doi: 10.1016/S0022-3093(98)00104-5.
- [32] E. Frackowiak, K. Metenier, V. Bertagna, and F. Beguin, "Supercapacitor electrodes from multiwalled carbon nanotubes," *Appl. Phys. Lett.*, vol. 77, no. 15, pp. 2421–2423, Oct. 2000, doi: 10.1063/1.1290146.
- [33] S. Hu, R. Rajamani, and X. Yu, "Flexible solid-state paper based carbon nanotube supercapacitor," *Appl. Phys. Lett.*, vol. 100, no. 10, p. 104103, Mar. 2012, doi: 10.1063/1.3691948.
- [34] M. Kaempgen, C. K. Chan, J. Ma, Y. Cui, and G. Gruner, "Printable Thin Film Supercapacitors Using Single-Walled Carbon Nanotubes," *Nano Lett.*, vol. 9, no. 5, pp. 1872–1876, May 2009, doi: 10.1021/nl8038579.
- [35] C. Masarapu, H. F. Zeng, K. H. Hung, and B. Wei, "Effect of Temperature on the Capacitance of Carbon Nanotube Supercapacitors," *ACS Nano*, vol. 3, no. 8, pp. 2199–2206, Aug. 2009, doi: 10.1021/nn900500n.

## Bibliography

---

- [36] C.-S. Yang, Y. S. Jang, and H. K. Jeong, "Bamboo-based activated carbon for supercapacitor applications," *Current Applied Physics*, vol. 14, no. 12, pp. 1616–1620, Dec. 2014, doi: 10.1016/j.cap.2014.09.021.
- [37] G. Wang *et al.*, "Solid-State Supercapacitor Based on Activated Carbon Cloths Exhibits Excellent Rate Capability," *Adv. Mater.*, vol. 26, no. 17, pp. 2676–2682, May 2014, doi: 10.1002/adma.201304756.
- [38] M. Zhi, F. Yang, F. Meng, M. Li, A. Manivannan, and N. Wu, "Effects of Pore Structure on Performance of An Activated-Carbon Supercapacitor Electrode Recycled from Scrap Waste Tires," *ACS Sustainable Chem. Eng.*, vol. 2, no. 7, pp. 1592–1598, Jul. 2014, doi: 10.1021/sc500336h.
- [39] M. Chen *et al.*, "Preparation of activated carbon from cotton stalk and its application in supercapacitor," *J Solid State Electrochem*, vol. 17, no. 4, pp. 1005–1012, Apr. 2013, doi: 10.1007/s10008-012-1946-6.
- [40] P. Liu, M. Verbrugge, and S. Soukiazian, "Influence of temperature and electrolyte on the performance of activated-carbon supercapacitors," *Journal of Power Sources*, vol. 156, no. 2, pp. 712–718, Jun. 2006, doi: 10.1016/j.jpowsour.2005.05.055.
- [41] D. S. Dhawale, A. Vinu, and C. D. Lokhande, "Stable nanostructured polyaniline electrode for supercapacitor application," *Electrochimica Acta*, vol. 56, no. 25, pp. 9482–9487, Oct. 2011, doi: 10.1016/j.electacta.2011.08.042.
- [42] H. Zhou, H. Chen, S. Luo, G. Lu, W. Wei, and Y. Kuang, "The effect of the polyaniline morphology on the performance of polyaniline supercapacitors," *J Solid State Electrochem*, vol. 9, no. 8, pp. 574–580, Aug. 2005, doi: 10.1007/s10008-004-0594-x.
- [43] K. Wang, J. Huang, and Z. Wei, "Conducting Polyaniline Nanowire Arrays for High Performance Supercapacitors," *J. Phys. Chem. C*, vol. 114, no. 17, pp. 8062–8067, May 2010, doi: 10.1021/jp9113255.
- [44] H. Mi, X. Zhang, S. Yang, X. Ye, and J. Luo, "Polyaniline nanofibers as the electrode material for supercapacitors," *Materials Chemistry and Physics*, vol. 112, no. 1, pp. 127–131, Nov. 2008, doi: 10.1016/j.matchemphys.2008.05.022.
- [45] F. Fusalba, P. Gouérec, D. Villers, and D. Bélanger, "Electrochemical Characterization of Polyaniline in Nonaqueous Electrolyte and Its Evaluation as Electrode Material for Electrochemical Supercapacitors," *J. Electrochem. Soc.*, vol. 148, no. 1, p. A1, 2001, doi: 10.1149/1.1339036.
- [46] H. Guan, L.-Z. Fan, H. Zhang, and X. Qu, "Polyaniline nanofibers obtained by interfacial polymerization for high-rate supercapacitors," *Electrochimica Acta*, vol. 56, no. 2, pp. 964–968, Dec. 2010, doi: 10.1016/j.electacta.2010.09.078.
- [47] L.-Z. Fan and J. Maier, "High-performance polypyrrole electrode materials for redox supercapacitors," *Electrochemistry Communications*, vol. 8, no. 6, pp. 937–940, Jun. 2006, doi: 10.1016/j.elecom.2006.03.035.
- [48] Y. Song, T.-Y. Liu, X.-X. Xu, D.-Y. Feng, Y. Li, and X.-X. Liu, "Pushing the Cycling Stability Limit of Polypyrrole for Supercapacitors," *Adv. Funct. Mater.*, vol. 25, no. 29, pp. 4626–4632, Aug. 2015, doi: 10.1002/adfm.201501709.
- [49] B. Muthulakshmi, D. Kalpana, S. Pitchumani, and N. G. Renganathan, "Electrochemical deposition of polypyrrole for symmetric supercapacitors," *Journal of Power Sources*, vol. 158, no. 2, pp. 1533–1537, Aug. 2006, doi: 10.1016/j.jpowsour.2005.10.013.
- [50] D. P. Dubal, S. H. Lee, J. G. Kim, W. B. Kim, and C. D. Lokhande, "Porous polypyrrole clusters prepared by electropolymerization for a high performance supercapacitor," *J. Mater. Chem.*, vol. 22, no. 7, p. 3044, 2012, doi: 10.1039/c2jm14470k.

- [51] Y. Huang, M. Zhu, Z. Pei, Y. Huang, H. Geng, and C. Zhi, "Extremely Stable Polypyrrole Achieved via Molecular Ordering for Highly Flexible Supercapacitors," *ACS Appl. Mater. Interfaces*, vol. 8, no. 3, pp. 2435–2440, Jan. 2016, doi: 10.1021/acsami.5b11815.
- [52] A. Laforgue, P. Simon, C. Sarrazin, and J.-F. Fauvarque, "Polythiophene-based supercapacitors," *Journal of Power Sources*, vol. 80, no. 1–2, pp. 142–148, Jul. 1999, doi: 10.1016/S0378-7753(98)00258-4.
- [53] B. H. Patil, S. J. Patil, and C. D. Lokhande, "Electrochemical Characterization of Chemically Synthesized Polythiophene Thin Films: Performance of Asymmetric Supercapacitor Device," *Electroanalysis*, vol. 26, no. 9, pp. 2023–2032, Sep. 2014, doi: 10.1002/elan.201400284.
- [54] T. Cheng, Y.-Z. Zhang, J.-D. Zhang, W.-Y. Lai, and W. Huang, "High-performance free-standing PEDOT:PSS electrodes for flexible and transparent all-solid-state supercapacitors," *J. Mater. Chem. A*, vol. 4, no. 27, pp. 10493–10499, 2016, doi: 10.1039/C6TA03537J.
- [55] A. V. Volkov *et al.*, "Understanding the Capacitance of PEDOT:PSS," *Adv. Funct. Mater.*, vol. 27, no. 28, p. 1700329, Jul. 2017, doi: 10.1002/adfm.201700329.
- [56] D. Ni, Y. Chen, H. Song, C. Liu, X. Yang, and K. Cai, "Free-standing and highly conductive PEDOT nanowire films for high-performance all-solid-state supercapacitors," *J. Mater. Chem. A*, vol. 7, no. 3, pp. 1323–1333, 2019, doi: 10.1039/C8TA08814D.
- [57] N. I. Jalal, R. I. Ibrahim, and M. K. Oudah, "A review on Supercapacitors: types and components," *J. Phys.: Conf. Ser.*, vol. 1973, no. 1, p. 012015, Aug. 2021, doi: 10.1088/1742-6596/1973/1/012015.
- [58] W. Yu, X. Jiang, S. Ding, and B. Q. Li, "Preparation and electrochemical characteristics of porous hollow spheres of NiO nanosheets as electrodes of supercapacitors," *Journal of Power Sources*, vol. 256, pp. 440–448, Jun. 2014, doi: 10.1016/j.jpowsour.2013.12.110.
- [59] Z. Yang, F. Xu, W. Zhang, Z. Mei, B. Pei, and X. Zhu, "Controllable preparation of multishelled NiO hollow nanospheres via layer-by-layer self-assembly for supercapacitor application," *Journal of Power Sources*, vol. 246, pp. 24–31, Jan. 2014, doi: 10.1016/j.jpowsour.2013.07.057.
- [60] M. Huang, F. Li, J. Y. Ji, Y. X. Zhang, X. L. Zhao, and X. Gao, "Facile synthesis of single-crystalline NiO nanosheet arrays on Ni foam for high-performance supercapacitors," *CrystEngComm*, vol. 16, no. 14, pp. 2878–2884, 2014, doi: 10.1039/C3CE42335B.
- [61] X. Zhang *et al.*, "Synthesis of porous NiO nanocrystals with controllable surface area and their application as supercapacitor electrodes," *Nano Res.*, vol. 3, no. 9, pp. 643–652, Sep. 2010, doi: 10.1007/s12274-010-0024-6.
- [62] X. Xia, J. Tu, X. Wang, C. Gu, and X. Zhao, "Hierarchically porous NiO film grown by chemical bath deposition via a colloidal crystal template as an electrochemical pseudocapacitor material," *J. Mater. Chem.*, vol. 21, no. 3, pp. 671–679, 2011, doi: 10.1039/C0JM02784G.
- [63] H. Xia, Y. Shirley Meng, G. Yuan, C. Cui, and L. Lu, "A Symmetric RuO<sub>2</sub>/RuO<sub>2</sub> Supercapacitor Operating at 1.6 V by Using a Neutral Aqueous Electrolyte," *Electrochem. Solid-State Lett.*, vol. 15, no. 4, p. A60, 2012, doi: 10.1149/2.023204esl.
- [64] V. Subramanian, "Mesoporous anhydrous RuO<sub>2</sub> as a supercapacitor electrode material," *Solid State Ionics*, vol. 175, no. 1–4, pp. 511–515, Nov. 2004, doi: 10.1016/j.ssi.2004.01.070.
- [65] C.-C. Hu, K.-H. Chang, M.-C. Lin, and Y.-T. Wu, "Design and Tailoring of the Nanotubular Arrayed Architecture of Hydrated RuO<sub>2</sub> for Next Generation Supercapacitors," *Nano Lett.*, vol. 6, no. 12, pp. 2690–2695, Dec. 2006, doi: 10.1021/nl061576a.
- [66] M. Zhang, Y. Chen, D. Yang, and J. Li, "High performance MnO<sub>2</sub> supercapacitor material prepared by modified electrodeposition method with different electrodeposition voltages," *Journal of Energy Storage*, vol. 29, p. 101363, Jun. 2020, doi: 10.1016/j.est.2020.101363.

## Bibliography

---

- [67] X. Long, Z. Zeng, E. Guo, X. Shi, H. Zhou, and X. Wang, "Facile fabrication of all-solid-state flexible interdigitated MnO<sub>2</sub> supercapacitor via in-situ catalytic solution route," *Journal of Power Sources*, vol. 325, pp. 264–272, Sep. 2016, doi: 10.1016/j.jpowsour.2016.06.024.
- [68] P. Ragupathy, H. N. Vasan, and N. Munichandraiah, "Synthesis and Characterization of Nano-MnO<sub>2</sub> for Electrochemical Supercapacitor Studies," *Journal of The Electrochemical Society*.
- [69] V. Subramanian, H. Zhu, and B. Wei, "Nanostructured MnO<sub>2</sub>: Hydrothermal synthesis and electrochemical properties as a supercapacitor electrode material," *Journal of Power Sources*, vol. 159, no. 1, pp. 361–364, Sep. 2006, doi: 10.1016/j.jpowsour.2006.04.012.
- [70] Z. Yu, B. Duong, D. Abbitt, and J. Thomas, "Highly Ordered MnO<sub>2</sub> Nanopillars for Enhanced Supercapacitor Performance," *Adv. Mater.*, vol. 25, no. 24, pp. 3302–3306, Jun. 2013, doi: 10.1002/adma.201300572.
- [71] B. Saravanakumar, K. K. Purushothaman, and G. Muralidharan, "Interconnected V<sub>2</sub>O<sub>5</sub> Nanoporous Network for High-Performance Supercapacitors," *ACS Appl. Mater. Interfaces*, vol. 4, no. 9, pp. 4484–4490, Sep. 2012, doi: 10.1021/am301162p.
- [72] H. Y. Lee and J. B. Goodenough, "Ideal Supercapacitor Behavior of Amorphous V<sub>2</sub>O<sub>5</sub>-nH<sub>2</sub>O in Potassium Chloride (KCl) Aqueous Solution," *Journal of Solid State Chemistry*, vol. 148, no. 1, pp. 81–84, Nov. 1999, doi: 10.1006/jssc.1999.8367.
- [73] K. Panigrahi, P. Howli, and K. K. Chattopadhyay, "3D network of V<sub>2</sub>O<sub>5</sub> for flexible symmetric supercapacitor," *Electrochimica Acta*, vol. 337, p. 135701, Mar. 2020, doi: 10.1016/j.electacta.2020.135701.
- [74] J. Yang, T. Lan, J. Liu, Y. Song, and M. Wei, "Supercapacitor electrode of hollow spherical V<sub>2</sub>O<sub>5</sub> with a high pseudocapacitance in aqueous solution," *Electrochimica Acta*, vol. 105, pp. 489–495, Aug. 2013, doi: 10.1016/j.electacta.2013.05.023.
- [75] B. Pandit, D. P. Dubal, and B. R. Sankapal, "Large scale flexible solid state symmetric supercapacitor through inexpensive solution processed V<sub>2</sub>O<sub>5</sub> complex surface architecture," *Electrochimica Acta*, vol. 242, pp. 382–389, Jul. 2017, doi: 10.1016/j.electacta.2017.05.010.
- [76] R. Velmurugan, J. Premkumar, R. Pitchai, M. Ulaganathan, and B. Subramanian, "Robust, Flexible, and Binder Free Highly Crystalline V<sub>2</sub>O<sub>5</sub> Thin Film Electrodes and Their Superior Supercapacitor Performances," *ACS Sustainable Chem. Eng.*, vol. 7, no. 15, pp. 13115–13126, Aug. 2019, doi: 10.1021/acssuschemeng.9b02302.
- [77] N. Maheswari and G. Muralidharan, "Supercapacitor Behavior of Cerium Oxide Nanoparticles in Neutral Aqueous Electrolytes," *Energy Fuels*, vol. 29, no. 12, pp. 8246–8253, Dec. 2015, doi: 10.1021/acs.energyfuels.5b02144.
- [78] X. Hao *et al.*, "Surfactant-mediated morphology evolution and self-assembly of cerium oxide nanocrystals for catalytic and supercapacitor applications," *Nanoscale*, vol. 13, no. 23, pp. 10393–10401, 2021, doi: 10.1039/D1NR01746B.
- [79] B. Pandit, N. Kumar, P. M. Koinkar, and B. R. Sankapal, "Solution processed nanostructured cerium oxide electrode: Electrochemical engineering towards solid-state symmetric supercapacitor device," *Journal of Electroanalytical Chemistry*, vol. 839, pp. 96–107, Apr. 2019, doi: 10.1016/j.jelechem.2019.02.047.
- [80] B. Talluri, K. Yoo, and J. Kim, "Novel rhombus-shaped cerium oxide sheets as a highly durable methanol oxidation electrocatalyst and high-performance supercapacitor electrode material," *Ceramics International*, vol. 48, no. 1, pp. 164–172, Jan. 2022, doi: 10.1016/j.ceramint.2021.09.092.
- [81] A. A. Yadav, A. C. Lokhande, R. B. Pujari, J. H. Kim, and C. D. Lokhande, "The synthesis of multifunctional porous honey comb-like La<sub>2</sub>O<sub>3</sub> thin film for supercapacitor and gas sensor

- applications," *Journal of Colloid and Interface Science*, vol. 484, pp. 51–59, Dec. 2016, doi: 10.1016/j.jcis.2016.08.056.
- [82] A. A. Yadav, V. S. Kumbhar, S. J. Patil, N. R. Chodankar, and C. D. Lokhande, "Supercapacitive properties of chemically deposited La<sub>2</sub>O<sub>3</sub> thin film," *Ceramics International*, vol. 42, no. 1, pp. 2079–2084, Jan. 2016, doi: 10.1016/j.ceramint.2015.09.098.
- [83] Y. Gogotsi and B. Anasori, "The Rise of MXenes," *ACS Nano*, vol. 13, no. 8, pp. 8491–8494, Aug. 2019, doi: 10.1021/acsnano.9b06394.
- [84] Z. Lin *et al.*, "Capacitance of Ti<sub>3</sub>C<sub>2</sub>T<sub>x</sub> MXene in ionic liquid electrolyte," *Journal of Power Sources*, vol. 326, pp. 575–579, Sep. 2016, doi: 10.1016/j.jpowsour.2016.04.035.
- [85] J. Tang *et al.*, "Optimizing Ion Pathway in Titanium Carbide MXene for Practical High-Rate Supercapacitor," *Adv. Energy Mater.*, vol. 11, no. 4, p. 2003025, Jan. 2021, doi: 10.1002/aenm.202003025.
- [86] Z. Wang *et al.*, "Unraveling and Regulating Self-Discharge Behavior of Ti<sub>3</sub>C<sub>2</sub>T<sub>x</sub> MXene-Based Supercapacitors," *ACS Nano*, vol. 14, no. 4, pp. 4916–4924, Apr. 2020, doi: 10.1021/acsnano.0c01056.
- [87] M. Hu, Z. Li, G. Li, T. Hu, C. Zhang, and X. Wang, "All-Solid-State Flexible Fiber-Based MXene Supercapacitors," *Adv. Mater. Technol.*, vol. 2, no. 10, p. 1700143, Oct. 2017, doi: 10.1002/admt.201700143.
- [88] R. B. Rakhi, B. Ahmed, M. N. Hedhili, D. H. Anjum, and H. N. Alshareef, "Effect of Postetch Annealing Gas Composition on the Structural and Electrochemical Properties of Ti<sub>2</sub>CT<sub>x</sub> MXene Electrodes for Supercapacitor Applications," *Chem. Mater.*, vol. 27, no. 15, pp. 5314–5323, Aug. 2015, doi: 10.1021/acs.chemmater.5b01623.
- [89] J. Come *et al.*, "Nanoscale Elastic Changes in 2D Ti<sub>3</sub>C<sub>2</sub>T<sub>x</sub> (MXene) Pseudocapacitive Electrodes," *Adv. Energy Mater.*, vol. 6, no. 9, p. 1502290, May 2016, doi: 10.1002/aenm.201502290.
- [90] S.-Y. Lin and X. Zhang, "Two-dimensional titanium carbide electrode with large mass loading for supercapacitor," *Journal of Power Sources*, vol. 294, pp. 354–359, Oct. 2015, doi: 10.1016/j.jpowsour.2015.06.082.
- [91] S. Wang *et al.*, "Free-standing 3D graphene/polyaniline composite film electrodes for high-performance supercapacitors," *Journal of Power Sources*, vol. 299, pp. 347–355, Dec. 2015, doi: 10.1016/j.jpowsour.2015.09.018.
- [92] B. Song, L. Li, Z. Lin, Z.-K. Wu, K. Moon, and C.-P. Wong, "Water-dispersible graphene/polyaniline composites for flexible micro-supercapacitors with high energy densities," *Nano Energy*, vol. 16, pp. 470–478, Sep. 2015, doi: 10.1016/j.nanoen.2015.06.020.
- [93] Q. Wang, J. Li, F. Gao, W. Li, K. Wu, and X. Wang, "Activated carbon coated with polyaniline as an electrode material in supercapacitors," *New Carbon Materials*, 2008.
- [94] L. Yu *et al.*, "Highly effective synthesis of NiO/CNT nanohybrids by atomic layer deposition for high-rate and long-life supercapacitors," *Dalton Trans.*, vol. 45, no. 35, pp. 13779–13786, 2016, doi: 10.1039/C6DT01927G.
- [95] M. Boota, B. Anasori, C. Voigt, M.-Q. Zhao, M. W. Barsoum, and Y. Gogotsi, "Pseudocapacitive Electrodes Produced by Oxidant-Free Polymerization of Pyrrole between the Layers of 2D Titanium Carbide (MXene)," *Adv. Mater.*, vol. 28, no. 7, pp. 1517–1522, Feb. 2016, doi: 10.1002/adma.201504705.
- [96] M. Zhu *et al.*, "Highly Flexible, Freestanding Supercapacitor Electrode with Enhanced Performance Obtained by Hybridizing Polypyrrole Chains with MXene," *Adv. Energy Mater.*, vol. 6, no. 21, p. 1600969, Nov. 2016, doi: 10.1002/aenm.201600969.

## Bibliography

---

- [97] L. Yu *et al.*, "MXene-Bonded Activated Carbon as a Flexible Electrode for High-Performance Supercapacitors," *ACS Energy Lett.*, vol. 3, no. 7, pp. 1597–1603, Jul. 2018, doi: 10.1021/acsenergylett.8b00718.
- [98] J. Fu, J. Yun, S. Wu, L. Li, L. Yu, and K. H. Kim, "Architecturally Robust Graphene-Encapsulated MXene  $\text{Ti}_2\text{CT}_x$ @Polyaniline Composite for High-Performance Pouch-Type Asymmetric Supercapacitor," *ACS Appl. Mater. Interfaces*, vol. 10, no. 40, pp. 34212–34221, Oct. 2018, doi: 10.1021/acsmi.8b10195.
- [99] Y. Li, P. Kamdem, and X.-J. Jin, "Hierarchical architecture of MXene/PANI hybrid electrode for advanced asymmetric supercapacitors," *Journal of Alloys and Compounds*, vol. 850, p. 156608, Jan. 2021, doi: 10.1016/j.jallcom.2020.156608.
- [100] X. Wang *et al.*, "In situ polymerized polyaniline/MXene (V2C) as building blocks of supercapacitor and ammonia sensor self-powered by electromagnetic-triboelectric hybrid generator," *Nano Energy*, vol. 88, p. 106242, Oct. 2021, doi: 10.1016/j.nanoen.2021.106242.
- [101] Y. Wei *et al.*, "All pseudocapacitive MXene-MnO<sub>2</sub> flexible asymmetric supercapacitor," *Journal of Energy Storage*, vol. 45, p. 103715, Jan. 2022, doi: 10.1016/j.est.2021.103715.
- [102] K. Li, P. Zhang, R. A. Soomro, and B. Xu, "Alkali-Induced Porous MXene/Carbon Nanotube-Based Film Electrodes for Supercapacitors," *ACS Appl. Nano Mater.*, vol. 5, no. 3, pp. 4180–4186, Mar. 2022, doi: 10.1021/acsnm.2c00109.
- [103] Y.-Z. Cai, Y.-S. Fang, W.-Q. Cao, P. He, and M.-S. Cao, "MXene-CNT/PANI ternary material with excellent supercapacitive performance driven by synergy," *Journal of Alloys and Compounds*, vol. 868, p. 159159, Jul. 2021, doi: 10.1016/j.jallcom.2021.159159.
- [104] G. Han *et al.*, "MnO<sub>2</sub> Nanorods Intercalating Graphene Oxide/Polyaniline Ternary Composites for Robust High-Performance Supercapacitors," *Sci Rep*, vol. 4, no. 1, p. 4824, Apr. 2014, doi: 10.1038/srep04824.
- [105] H. Jiang, Y. Dai, Y. Hu, W. Chen, and C. Li, "Nanostructured Ternary Nanocomposite of rGO/CNTs/MnO<sub>2</sub> for High-Rate Supercapacitors," *ACS Sustainable Chem. Eng.*, vol. 2, no. 1, pp. 70–74, Jan. 2014, doi: 10.1021/sc400313y.
- [106] J. Wang *et al.*, "Symmetric supercapacitors composed of ternary metal oxides (NiO/V<sub>2</sub>O<sub>5</sub>/MnO<sub>2</sub>) nanoribbon electrodes with high energy storage performance," *Chemical Engineering Journal*, vol. 426, p. 131804, Dec. 2021, doi: 10.1016/j.cej.2021.131804.
- [107] H. Zhou, Z. Yan, X. Yang, J. Lv, L. Kang, and Z.-H. Liu, "RGO/MnO<sub>2</sub>/polypyrrole ternary film electrode for supercapacitor," *Materials Chemistry and Physics*, vol. 177, pp. 40–47, Jul. 2016, doi: 10.1016/j.matchemphys.2016.03.035.
- [108] M. A. A. Mohd Abdah, N. S. Mohd Razali, P. T. Lim, S. Kulandaivalu, and Y. Sulaiman, "One-step potentiostatic electrodeposition of polypyrrole/graphene oxide/multi-walled carbon nanotubes ternary nanocomposite for supercapacitor," *Materials Chemistry and Physics*, vol. 219, pp. 120–128, Nov. 2018, doi: 10.1016/j.matchemphys.2018.08.018.
- [109] Q. Wang *et al.*, "High-performance supercapacitor based on V<sub>2</sub>O<sub>5</sub>/carbon nanotubes-super activated carbon ternary composite," *Ceramics International*, vol. 42, no. 10, pp. 12129–12135, Aug. 2016, doi: 10.1016/j.ceramint.2016.04.145.
- [110] F. Karimi, S. Korkmaz, C. Karaman, O. Karaman, and İ. Afşin Kariper, "Engineering of GO/MWCNT/RuO<sub>2</sub> ternary aerogel for high-performance supercapacitor," *Fuel*, vol. 329, p. 125398, Dec. 2022, doi: 10.1016/j.fuel.2022.125398.
- [111] K. K. Kar, Ed., *Handbook of Nanocomposite Supercapacitor Materials I: Characteristics*, vol. 300. in Springer Series in Materials Science, vol. 300. Cham: Springer International Publishing, 2020. doi: 10.1007/978-3-030-43009-2.

- [112] X. Du, C. Wang, M. Chen, Y. Jiao, and J. Wang, "Electrochemical Performances of Nanoparticle  $\text{Fe}_3\text{O}_4$ /Activated Carbon Supercapacitor Using KOH Electrolyte Solution," *J. Phys. Chem. C*, vol. 113, no. 6, pp. 2643–2646, Feb. 2009, doi: 10.1021/jp8088269.
- [113] X.-F. Wang, Z. You, and D.-B. Ruan, "A Hybrid Metal Oxide Supercapacitor in Aqueous KOH Electrolyte<sup>+</sup>," *Chin. J. Chem.*, vol. 24, no. 9, pp. 1126–1132, Sep. 2006, doi: 10.1002/cjoc.200690212.
- [114] K. Feng *et al.*, "Study on the binder-free asymmetric supercapacitors with nano- $\text{IrO}_2$ - $\text{ZnO}$ /Ti as anode and  $\text{RuO}_2$ - $\text{MoO}_3$ /Ti as cathode in  $\text{H}_2\text{SO}_4$  electrolyte," *Journal of Alloys and Compounds*, vol. 819, p. 153385, Apr. 2020, doi: 10.1016/j.jallcom.2019.153385.
- [115] P. Ge *et al.*, "Electrochemical performance of  $\text{MoO}_3$ - $\text{RuO}_2$ /Ti in  $\text{H}_2\text{SO}_4$  electrolyte as anodes for asymmetric supercapacitors," *Electrochimica Acta*, vol. 429, p. 140984, Oct. 2022, doi: 10.1016/j.electacta.2022.140984.
- [116] Q. Chen *et al.*, "Graphene quantum dots–three-dimensional graphene composites for high-performance supercapacitors," *Phys. Chem. Chem. Phys.*, vol. 16, no. 36, pp. 19307–19313, 2014, doi: 10.1039/C4CP02761B.
- [117] A. Hodaei, A. S. Dezfuli, and H. R. Naderi, "A high-performance supercapacitor based on N-doped  $\text{TiO}_2$  nanoparticles," *J Mater Sci: Mater Electron*, vol. 29, no. 17, pp. 14596–14604, Sep. 2018, doi: 10.1007/s10854-018-9595-x.
- [118] A. E. Ghazaly *et al.*, "Enhanced supercapacitive performance of  $\text{Mo}_1.33\text{C}$  MXene based asymmetric supercapacitors in lithium chloride electrolyte," *Energy Storage Materials*, vol. 41, pp. 203–208, Oct. 2021, doi: 10.1016/j.ensm.2021.05.006.
- [119] M. Sajjad, M. I. Khan, F. Cheng, and W. Lu, "A review on selection criteria of aqueous electrolytes performance evaluation for advanced asymmetric supercapacitors," *Journal of Energy Storage*, vol. 40, p. 102729, Aug. 2021, doi: 10.1016/j.est.2021.102729.
- [120] J. S. Daubert, J. Z. Mundy, and G. N. Parsons, "Kevlar-Based Supercapacitor Fibers with Conformal Pseudocapacitive Metal Oxide and Metal Formed by ALD," *Adv. Mater. Interfaces*, vol. 3, no. 21, p. 1600355, Nov. 2016, doi: 10.1002/admi.201600355.
- [121] X. Gong, S. Li, and P. S. Lee, "A fiber asymmetric supercapacitor based on  $\text{FeOOH}$ /PPy on carbon fibers as an anode electrode with high volumetric energy density for wearable applications," *Nanoscale*, vol. 9, no. 30, pp. 10794–10801, 2017, doi: 10.1039/C7NR02896B.
- [122] X. Jian, H. Yang, J. Li, E. Zhang, L. Cao, and Z. Liang, "Flexible all-solid-state high-performance supercapacitor based on electrochemically synthesized carbon quantum dots/polypyrrole composite electrode," *Electrochimica Acta*, vol. 228, pp. 483–493, Feb. 2017, doi: 10.1016/j.electacta.2017.01.082.
- [123] B. Anothumakkool, A. Torris A. T, S. N. Bhange, M. V. Badiger, and S. Kurungot, "Electrodeposited polyethylenedioxythiophene with infiltrated gel electrolyte interface: a close contest of an all-solid-state supercapacitor with its liquid-state counterpart," *Nanoscale*, vol. 6, no. 11, p. 5944, 2014, doi: 10.1039/c4nr00659c.
- [124] T. De Silva *et al.*, "Carbon Nanotube Based Robust and Flexible Solid-State Supercapacitor," *ACS Appl. Mater. Interfaces*, vol. 13, no. 47, pp. 56004–56013, Dec. 2021, doi: 10.1021/acsaem.1c12551.
- [125] J. Xu *et al.*, "Flexible Asymmetric Supercapacitors Based upon  $\text{Co}_9\text{S}_8$  Nanorod// $\text{Co}_3\text{O}_4$ @ $\text{RuO}_2$  Nanosheet Arrays on Carbon Cloth," *ACS Nano*, vol. 7, no. 6, pp. 5453–5462, Jun. 2013, doi: 10.1021/nn401450s.
- [126] X. Jing *et al.*, "KOH Chemical-Activated Porous Carbon Sponges for Monolithic Supercapacitor Electrodes," *ACS Appl. Energy Mater.*, vol. 4, no. 7, pp. 6768–6776, Jul. 2021, doi: 10.1021/acsaem.1c00868.



## Bibliography

---

- [127] S. T. Senthilkumar and R. Kalai Selvan, "Fabrication and performance studies of a cable-type flexible asymmetric supercapacitor," *Phys. Chem. Chem. Phys.*, vol. 16, no. 29, p. 15692, 2014, doi: 10.1039/c4cp00955j.
- [128] A. Lewandowski, "Supercapacitor based on activated carbon and polyethylene oxide–KOH–H<sub>2</sub>O polymer electrolyte," *Electrochimica Acta*, vol. 46, no. 18, pp. 2777–2780, May 2001, doi: 10.1016/S0013-4686(01)00496-0.
- [129] F. Tao, L. Qin, Z. Wang, and Q. Pan, "Self-Healable and Cold-Resistant Supercapacitor Based on a Multifunctional Hydrogel Electrolyte," *ACS Appl. Mater. Interfaces*, vol. 9, no. 18, pp. 15541–15548, May 2017, doi: 10.1021/acsami.7b03223.
- [130] B. Pal, S. Yang, S. Ramesh, V. Thangadurai, and R. Jose, "Electrolyte selection for supercapacitive devices: a critical review," *Nanoscale Adv.*, vol. 1, no. 10, pp. 3807–3835, 2019, doi: 10.1039/C9NA00374F.
- [131] Y.-S. Kim, Y.-G. Cho, D. Odkhuu, N. Park, and H.-K. Song, "A physical organogel electrolyte: characterized by in situ thermo-irreversible gelation and single-ion-predominant conduction," *Sci Rep*, vol. 3, no. 1, p. 1917, May 2013, doi: 10.1038/srep01917.
- [132] R. Yuksel, Z. Sarioba, A. Cirpan, P. Hiralal, and H. E. Unalan, "Transparent and Flexible Supercapacitors with Single Walled Carbon Nanotube Thin Film Electrodes," *ACS Appl. Mater. Interfaces*, vol. 6, no. 17, pp. 15434–15439, Sep. 2014, doi: 10.1021/am504021u.
- [133] P. M. DiCarmine, T. B. Schon, T. M. McCormick, P. P. Klein, and D. S. Seferos, "Donor–Acceptor Polymers for Electrochemical Supercapacitors: Synthesis, Testing, and Theory," *J. Phys. Chem. C*, vol. 118, no. 16, pp. 8295–8307, Apr. 2014, doi: 10.1021/jp5016214.
- [134] K.-F. Chiu and S.-H. Su, "Lithiated and sulphonated poly(ether ether ketone) solid state electrolyte films for supercapacitors," *Thin Solid Films*, vol. 544, pp. 144–147, Oct. 2013, doi: 10.1016/j.tsf.2013.03.135.
- [135] M.-F. Hsueh, C.-W. Huang, C.-A. Wu, P.-L. Kuo, and H. Teng, "The Synergistic Effect of Nitrile and Ether Functionalities for Gel Electrolytes Used in Supercapacitors," *J. Phys. Chem. C*, vol. 117, no. 33, pp. 16751–16758, Aug. 2013, doi: 10.1021/jp4031128.
- [136] J. Li *et al.*, "Separator Design for High-Performance Supercapacitors: Requirements, Challenges, Strategies, and Prospects," *ACS Energy Lett.*, vol. 8, no. 1, pp. 56–78, Jan. 2023, doi: 10.1021/acscenergylett.2c01853.
- [137] C. Zhao, X. Sun, W. Li, M. Shi, K. Ren, and X. Lu, "Reduced Self-Discharge of Supercapacitors Using Piezoelectric Separators," *ACS Appl. Energy Mater.*, vol. 4, no. 8, pp. 8070–8075, Aug. 2021, doi: 10.1021/acsaem.1c01373.
- [138] Z. Yang *et al.*, "Wet-spun PVDF nanofiber separator for direct fabrication of coaxial fiber-shaped supercapacitors," *Chemical Engineering Journal*, vol. 400, p. 125835, Nov. 2020, doi: 10.1016/j.cej.2020.125835.
- [139] G. Teng, S. Lin, D. Xu, Y. Heng, and D. Hu, "Renewable cellulose separator with good thermal stability prepared via phase inversion for high-performance supercapacitors," *J Mater Sci: Mater Electron*, vol. 31, no. 10, pp. 7916–7926, May 2020, doi: 10.1007/s10854-020-03330-w.
- [140] D. Xu, G. Teng, Y. Heng, Z. Chen, and D. Hu, "Eco-friendly and thermally stable cellulose film prepared by phase inversion as supercapacitor separator," *Materials Chemistry and Physics*, vol. 249, p. 122979, Jul. 2020, doi: 10.1016/j.matchemphys.2020.122979.
- [141] Q. Zhang *et al.*, "Nanocellulose-Enabled, All-Nanofiber, High-Performance Supercapacitor," *ACS Appl. Mater. Interfaces*, vol. 11, no. 6, pp. 5919–5927, Feb. 2019, doi: 10.1021/acsami.8b17414.
- [142] M. Shin *et al.*, "Metamorphosis of Seaweeds into Multitalented Materials for Energy Storage Applications," *Adv. Energy Mater.*, vol. 9, no. 19, p. 1900570, May 2019, doi: 10.1002/aenm.201900570.

- [143] M. Raja, B. Sadhasivam, J. Naik R, D. R, and K. Ramanujam, "A chitosan/poly(ethylene glycol)-ran -poly(propylene glycol) blend as an eco-benign separator and binder for quasi-solid-state supercapacitor applications," *Sustainable Energy Fuels*, vol. 3, no. 3, pp. 760–773, 2019, doi: 10.1039/C8SE00530C.
- [144] F. Lufrano and P. Staiti, "Performance improvement of Nafion based solid state electrochemical supercapacitor," *Electrochimica Acta*, vol. 49, no. 16, pp. 2683–2689, Jul. 2004, doi: 10.1016/j.electacta.2004.02.021.
- [145] Z. Algharaibeh and P. G. Pickup, "An asymmetric supercapacitor with anthraquinone and dihydroxybenzene modified carbon fabric electrodes," *Electrochemistry Communications*, vol. 13, no. 2, pp. 147–149, Feb. 2011, doi: 10.1016/j.elecom.2010.11.036.
- [146] X. Liu and P. G. Pickup, "Ru oxide supercapacitors with high loadings and high power and energy densities," *Journal of Power Sources*, vol. 176, no. 1, pp. 410–416, Jan. 2008, doi: 10.1016/j.jpowsour.2007.10.076.
- [147] J. Wen *et al.*, "Electrospun flexible aluminum silicate nanofibers as a flame-resistant separator for the high performance supercapacitor," *Ionics*, vol. 28, no. 1, pp. 433–442, Jan. 2022, doi: 10.1007/s11581-021-04329-x.
- [148] H. Li, S. Guo, L. Wang, J. Wu, Y. Zhu, and X. Hu, "Thermally Durable Lithium-Ion Capacitors with High Energy Density from All Hydroxyapatite Nanowire-Enabled Fire-Resistant Electrodes and Separators," *Adv. Energy Mater.*, vol. 9, no. 46, p. 1902497, Dec. 2019, doi: 10.1002/aenm.201902497.
- [149] M. Sharma, A. Gaur, and J. K. Quamara, "Swift heavy ions irradiated PVDF/BaTiO<sub>3</sub> film as a separator for supercapacitors," *Solid State Ionics*, vol. 352, p. 115342, Sep. 2020, doi: 10.1016/j.ssi.2020.115342.
- [150] M. Liu, K. Turcheniuk, W. Fu, Y. Yang, M. Liu, and G. Yushin, "Scalable, safe, high-rate supercapacitor separators based on the Al<sub>2</sub>O<sub>3</sub> nanowire Polyvinyl butyral nonwoven membranes," *Nano Energy*, vol. 71, p. 104627, May 2020, doi: 10.1016/j.nanoen.2020.104627.
- [151] F. Qiu *et al.*, "An Ecofriendly Gel Polymer Electrolyte Based on Natural Lignocellulose with Ultrahigh Electrolyte Uptake and Excellent Ionic Conductivity for Alkaline Supercapacitors," *ACS Appl. Energy Mater.*, vol. 2, no. 8, pp. 6031–6042, Aug. 2019, doi: 10.1021/acsaem.9b01150.
- [152] K. K. Kar, Ed., *Handbook of Nanocomposite Supercapacitor Materials II: Performance*, vol. 302. in Springer Series in Materials Science, vol. 302. Cham: Springer International Publishing, 2020. doi: 10.1007/978-3-030-52359-6.
- [153] G.-H. An, S. Cha, and H.-J. Ahn, "Surface functionalization of the terraced surface-based current collector for a supercapacitor with an improved energy storage performance," *Applied Surface Science*, vol. 478, pp. 435–440, Jun. 2019, doi: 10.1016/j.apsusc.2019.01.280.
- [154] A. Abdisattar *et al.*, "Recent advances and challenges of current collectors for supercapacitors," *Electrochemistry Communications*, vol. 142, p. 107373, Sep. 2022, doi: 10.1016/j.elecom.2022.107373.
- [155] Y. Huang *et al.*, "Hierarchically Mesostructured Aluminum Current Collector for Enhancing the Performance of Supercapacitors," *ACS Appl. Mater. Interfaces*, vol. 10, no. 19, pp. 16572–16580, May 2018, doi: 10.1021/acsaami.8b03647.
- [156] D. Yang and A. Laforgue, "Laser Surface Roughening of Aluminum Foils for Supercapacitor Current Collectors," *J. Electrochem. Soc.*, vol. 166, no. 12, pp. A2503–A2512, 2019, doi: 10.1149/2.0601912jes.
- [157] S. Pilathottathil, M. S. Thayyil, M. P. Pillai, and A. P. Jemshihhas, "Role of a Printed Circuit Board Copper Clad Current Collector in Supercapacitor Application," *Journal of Elec Materi*, vol. 48, no. 9, pp. 5835–5842, Sep. 2019, doi: 10.1007/s11664-019-07365-6.

## Bibliography

---

- [158] X. Su *et al.*, "In-situ green synthesis of CuO on 3D submicron-porous/solid copper current collectors as excellent supercapacitor electrode material," *J Mater Sci: Mater Electron*, vol. 30, no. 4, pp. 3545–3551, Feb. 2019, doi: 10.1007/s10854-018-00632-y.
- [159] J.-L. Xu *et al.*, "Embedded Ag Grid Electrodes as Current Collector for Ultraflexible Transparent Solid-State Supercapacitor," *ACS Appl. Mater. Interfaces*, vol. 9, no. 33, pp. 27649–27656, Aug. 2017, doi: 10.1021/acsami.7b06184.
- [160] Y. Jang, J. Jo, Y.-M. Choi, S. Kwon, and K.-Y. Kim, "3D (3-dimensional) porous silver nonwoven mats prepared with cellulosic templates and spray equipment for use as supercapacitor current collectors," *Energy*, vol. 93, pp. 1303–1307, Dec. 2015, doi: 10.1016/j.energy.2015.10.013.
- [161] X. Y. Lang, H. T. Yuan, Y. Iwasa, and M. W. Chen, "Three-dimensional nanoporous gold for electrochemical supercapacitors," *Scripta Materialia*, vol. 64, no. 9, pp. 923–926, May 2011, doi: 10.1016/j.scriptamat.2011.01.038.
- [162] Y. Hou, L. Chen, A. Hirata, T. Fujita, and M. Chen, "Non-aqueous nanoporous gold based supercapacitors with high specific energy," *Scripta Materialia*, vol. 116, pp. 76–81, Apr. 2016, doi: 10.1016/j.scriptamat.2016.01.016.
- [163] N. Maile *et al.*, "Capacitive property studies of electrochemically synthesized Co<sub>3</sub>O<sub>4</sub> and Mn<sub>3</sub>O<sub>4</sub> on inexpensive stainless steel current collector for supercapacitor application," *Ceramics International*, vol. 46, no. 10, pp. 14640–14649, Jul. 2020, doi: 10.1016/j.ceramint.2020.02.265.
- [164] J. Yu *et al.*, "Metallic Fabrics as the Current Collector for High-Performance Graphene-Based Flexible Solid-State Supercapacitor," *ACS Appl. Mater. Interfaces*, vol. 8, no. 7, pp. 4724–4729, Feb. 2016, doi: 10.1021/acsami.5b12180.
- [165] N. A. Salleh, S. Kheawhom, and A. A. Mohamad, "Characterizations of nickel mesh and nickel foam current collectors for supercapacitor application," *Arabian Journal of Chemistry*, vol. 13, no. 8, pp. 6838–6846, Aug. 2020, doi: 10.1016/j.arabjc.2020.06.036.
- [166] L. Liu, H. Zhao, Y. Wang, Y. Fang, J. Xie, and Y. Lei, "Evaluating the Role of Nanostructured Current Collectors in Energy Storage Capability of Supercapacitor Electrodes with Thick Electroactive Materials Layers," *Adv. Funct. Mater.*, vol. 28, no. 6, p. 1705107, Feb. 2018, doi: 10.1002/adfm.201705107.
- [167] M. K. Khawaja, M. F. Khanfar, T. Oghlenian, and W. Alnahar, "Fabrication and electrochemical characterization of graphene-oxide supercapacitor electrodes with activated carbon current collectors on graphite substrates," *Computers & Electrical Engineering*, vol. 85, p. 106678, Jul. 2020, doi: 10.1016/j.compeleceng.2020.106678.
- [168] M. Muthu Balasubramanian, M. Subramani, D. Murugan, and S. Ponnusamy, "Groundnut shell-derived porous carbon-based supercapacitor with high areal mass loading using carbon cloth as current collector," *Ionics*, vol. 26, no. 12, pp. 6297–6308, Dec. 2020, doi: 10.1007/s11581-020-03754-8.
- [169] S. Asim *et al.*, "RuO<sub>2</sub> nanorods decorated CNTs grown carbon cloth as a free standing electrode for supercapacitor and lithium ion batteries," *Electrochimica Acta*, vol. 326, p. 135009, Dec. 2019, doi: 10.1016/j.electacta.2019.135009.
- [170] K. U. Laszczyk, "Design and technology processes used for microsupercapacitors," in *Microsupercapacitors*, Elsevier, 2022, pp. 215–255. doi: 10.1016/B978-0-08-102888-9.00004-5.
- [171] H. Durou, D. Pech, D. Colin, P. Simon, P.-L. Taberna, and M. Brunet, "Wafer-level fabrication process for fully encapsulated micro-supercapacitors with high specific energy," *Microsyst Technol*, vol. 18, no. 4, pp. 467–473, Apr. 2012, doi: 10.1007/s00542-011-1415-7.

- [172] A. Noori, M. F. El-Kady, M. S. Rahmanifar, R. B. Kaner, and M. F. Mousavi, "Towards establishing standard performance metrics for batteries, supercapacitors and beyond," *Chem. Soc. Rev.*, vol. 48, no. 5, pp. 1272–1341, 2019, doi: 10.1039/C8CS00581H.
- [173] J. Yao *et al.*, "Fluorinated Ether-Based Electrolyte for Supercapacitors with Increased Working Voltage and Suppressed Self-discharge," *ChemElectroChem*, vol. 9, no. 10, May 2022, doi: 10.1002/celec.202200223.
- [174] Y. Lu, K. Jiang, D. Chen, and G. Shen, "Wearable sweat monitoring system with integrated micro-supercapacitors," *Nano Energy*, vol. 58, pp. 624–632, Apr. 2019, doi: 10.1016/j.nanoen.2019.01.084.
- [175] M. Deschanel, M. Dietrich, P. Gentile, F. Alloin, C. Iojoiu, and S. Sadki, "In-situ crosslinking of polysiloxane electrolyte within Al<sub>2</sub>O<sub>3</sub>@SiNWs for quasi-solid-state micro-supercapacitors," *Electrochimica Acta*, p. 142925, Jul. 2023, doi: 10.1016/j.electacta.2023.142925.
- [176] W. Du *et al.*, "Facile synthesis and superior electrochemical performances of CoNi<sub>2</sub>S<sub>4</sub>/graphene nanocomposite suitable for supercapacitor electrodes," *J. Mater. Chem. A*, vol. 2, no. 25, pp. 9613–9619, 2014, doi: 10.1039/C4TA00414K.
- [177] S. Min, C. Zhao, Z. Zhang, G. Chen, X. Qian, and Z. Guo, "Synthesis of Ni(OH)<sub>2</sub>/RGO pseudocomposite on nickel foam for supercapacitors with superior performance," *J. Mater. Chem. A*, vol. 3, no. 7, pp. 3641–3650, 2015, doi: 10.1039/C4TA06233G.
- [178] W. Yang *et al.*, "3D Printing of Freestanding MXene Architectures for Current-Collector-Free Supercapacitors," *Adv. Mater.*, vol. 31, no. 37, p. 1902725, Sep. 2019, doi: 10.1002/adma.201902725.
- [179] Y.-M. Wang, X. Zhang, C.-Y. Guo, Y.-Q. Zhao, C.-L. Xu, and H.-L. Li, "Controllable synthesis of 3D Ni<sub>x</sub>Co<sub>1-x</sub> oxides with different morphologies for high-capacity supercapacitors," *J. Mater. Chem. A*, vol. 1, no. 42, p. 13290, 2013, doi: 10.1039/c3ta12713c.
- [180] M. Jana *et al.*, "Growth of Ni–Co binary hydroxide on a reduced graphene oxide surface by a successive ionic layer adsorption and reaction (SILAR) method for high performance asymmetric supercapacitor electrodes," *J. Mater. Chem. A*, vol. 4, no. 6, pp. 2188–2197, 2016, doi: 10.1039/C5TA10297A.
- [181] K. Shen, J. Ding, and S. Yang, "3D Printing Quasi-Solid-State Asymmetric Micro-Supercapacitors with Ultrahigh Areal Energy Density," *Adv. Energy Mater.*, vol. 8, no. 20, p. 1800408, Jul. 2018, doi: 10.1002/aenm.201800408.
- [182] W. Xia, A. Mahmood, R. Zou, and Q. Xu, "Metal–organic frameworks and their derived nanostructures for electrochemical energy storage and conversion," *Energy Environ. Sci.*, vol. 8, no. 7, pp. 1837–1866, 2015, doi: 10.1039/C5EE00762C.
- [183] X. Mu *et al.*, "A high energy density asymmetric supercapacitor from ultrathin manganese molybdate nanosheets," *Electrochimica Acta*, vol. 211, pp. 217–224, Sep. 2016, doi: 10.1016/j.electacta.2016.06.072.
- [184] S. Ratha *et al.*, "Supercapacitors based on patronite–reduced graphene oxide hybrids: experimental and theoretical insights," *J. Mater. Chem. A*, vol. 3, no. 37, pp. 18874–18881, 2015, doi: 10.1039/C5TA03221K.
- [185] S. Abdolhosseinzadeh, R. Schneider, A. Verma, J. Heier, F. Nüesch, and C. (John) Zhang, "Turning Trash into Treasure: Additive Free MXene Sediment Inks for Screen-Printed Micro-Supercapacitors," *Adv. Mater.*, vol. 32, no. 17, p. 2000716, Apr. 2020, doi: 10.1002/adma.202000716.
- [186] E. Talaie, P. Bonnicks, X. Sun, Q. Pang, X. Liang, and L. F. Nazar, "Methods and Protocols for Electrochemical Energy Storage Materials Research," *Chem. Mater.*, vol. 29, no. 1, pp. 90–105, Jan. 2017, doi: 10.1021/acs.chemmater.6b02726.

## Bibliography

---

- [187] P. Forouzandeh, V. Kumaravel, and S. C. Pillai, "Electrode Materials for Supercapacitors: A Review of Recent Advances," *Catalysts*, vol. 10, no. 9, p. 969, Aug. 2020, doi: 10.3390/catal10090969.
- [188] W. Chen, R. B. Rakhi, L. Hu, X. Xie, Y. Cui, and H. N. Alshareef, "High-Performance Nanostructured Supercapacitors on a Sponge," *Nano Lett.*, vol. 11, no. 12, pp. 5165–5172, Dec. 2011, doi: 10.1021/nl2023433.
- [189] C. Wang *et al.*, "Metallic few-layered VSe<sub>2</sub> nanosheets: high two-dimensional conductivity for flexible in-plane solid-state supercapacitors," *J. Mater. Chem. A*, vol. 6, no. 18, pp. 8299–8306, 2018, doi: 10.1039/C8TA00089A.
- [190] Y. Wu and R. Holze, "Self-discharge in supercapacitors: Causes, effects and therapies: An overview\*".
- [191] B. E. Conway, W. G. Pell, and T.-C. Liu, "Diagnostic analyses for mechanisms of self-discharge of electrochemical capacitors and batteries," *Journal of Power Sources*, vol. 65, no. 1–2, pp. 53–59, Mar. 1997, doi: 10.1016/S0378-7753(97)02468-3.
- [192] B.-A. Mei, O. Munteshari, J. Lau, B. Dunn, and L. Pilon, "Physical Interpretations of Nyquist Plots for EDLC Electrodes and Devices," *J. Phys. Chem. C*, vol. 122, no. 1, pp. 194–206, Jan. 2018, doi: 10.1021/acs.jpcc.7b10582.
- [193] T. A. Smith, J. P. Mars, and G. A. Turner, "Using supercapacitors to improve battery performance," in *2002 IEEE 33rd Annual IEEE Power Electronics Specialists Conference. Proceedings (Cat. No.02CH37289)*, Cairns, Qld., Australia: IEEE, 2002, pp. 124–128. doi: 10.1109/PSEC.2002.1023857.
- [194] M. G. Say *et al.*, "Ultrathin Paper Microsupercapacitors for Electronic Skin Applications," *Adv Materials Technologies*, vol. 7, no. 8, p. 2101420, Aug. 2022, doi: 10.1002/admt.202101420.
- [195] F. Bu, W. Zhou, Y. Xu, Y. Du, C. Guan, and W. Huang, "Recent developments of advanced micro-supercapacitors: design, fabrication and applications," *npj Flex Electron*, vol. 4, no. 1, p. 31, Dec. 2020, doi: 10.1038/s41528-020-00093-6.
- [196] M. F. El-Kady and R. B. Kaner, "Scalable fabrication of high-power graphene micro-supercapacitors for flexible and on-chip energy storage," *Nat Commun*, vol. 4, no. 1, p. 1475, Feb. 2013, doi: 10.1038/ncomms2446.
- [197] X. Sun, K. Chen, F. Liang, C. Zhi, and D. Xue, "Perspective on Micro-Supercapacitors," *Front. Chem.*, vol. 9, p. 807500, Jan. 2022, doi: 10.3389/fchem.2021.807500.
- [198] P. Zhang, F. Wang, S. Yang, G. Wang, M. Yu, and X. Feng, "Flexible in-plane micro-supercapacitors: Progresses and challenges in fabrication and applications," *Energy Storage Materials*, vol. 28, pp. 160–187, Jun. 2020, doi: 10.1016/j.ensm.2020.02.029.
- [199] N. A. Kyremateng, T. Brousse, and D. Pech, "Microsupercapacitors as miniaturized energy-storage components for on-chip electronics," *Nature Nanotech*, vol. 12, no. 1, pp. 7–15, Jan. 2017, doi: 10.1038/nnano.2016.196.
- [200] J. Yoo, S. Byun, C.-W. Lee, C.-Y. Yoo, and J. Yu, "Precisely Geometry Controlled Microsupercapacitors for Ultrahigh Areal Capacitance, Volumetric Capacitance, and Energy Density," *Chem. Mater.*, vol. 30, no. 12, pp. 3979–3990, Jun. 2018, doi: 10.1021/acs.chemmater.7b03786.
- [201] J. Zhang, G. Zhang, T. Zhou, and S. Sun, "Recent Developments of Planar Micro-Supercapacitors: Fabrication, Properties, and Applications," *Adv. Funct. Mater.*, vol. 30, no. 19, p. 1910000, May 2020, doi: 10.1002/adfm.201910000.
- [202] S. H. Park, G. Goodall, and W. S. Kim, "Perspective on 3D-designed micro-supercapacitors," *Materials & Design*, vol. 193, p. 108797, Aug. 2020, doi: 10.1016/j.matdes.2020.108797.

- [203] N. Liu and Y. Gao, "Recent Progress in Micro-Supercapacitors with In-Plane Interdigital Electrode Architecture," *Small*, vol. 13, no. 45, p. 1701989, Dec. 2017, doi: 10.1002/smll.201701989.
- [204] Z.-S. Wu, K. Parvez, X. Feng, and K. Müllen, "Photolithographic fabrication of high-performance all-solid-state graphene-based planar micro-supercapacitors with different interdigital fingers," *J. Mater. Chem. A*, vol. 2, no. 22, p. 8288, 2014, doi: 10.1039/c4ta00958d.
- [205] W. Zhao, F. Liu, C. Liu, X. Li, L. Zhang, and G. Zhang, "Photolithographic fabrication of high-voltage output integrated all-solid-state planar on-chip micro-supercapacitors," *Ferroelectrics*, vol. 563, no. 1, pp. 87–94, Jul. 2020, doi: 10.1080/00150193.2020.1760612.
- [206] L. Zhang *et al.*, "Photolithographic fabrication of graphene-based all-solid-state planar on-chip microsupercapacitors with ultrahigh power characteristics," *Journal of Applied Physics*, vol. 126, no. 16, p. 164308, Oct. 2019, doi: 10.1063/1.5109691.
- [207] Y. Zhang, L.-D. Zhang, W.-Q. Zhao, Y.-Y. Zhou, W.-T. Jiang, and G.-Y. Zhang, "All-solid-state planar on-chip micro-supercapacitors with excellent areal power performance at ultrahigh scan rates by photolithography," *Ferroelectrics*, vol. 595, no. 1, pp. 88–94, Jul. 2022, doi: 10.1080/00150193.2022.2079459.
- [208] Y. Yang *et al.*, "Improved conductivity and capacitance of interdigital carbon microelectrodes through integration with carbon nanotubes for micro-supercapacitors," *Nano Res.*, vol. 9, no. 8, pp. 2510–2519, Aug. 2016, doi: 10.1007/s12274-016-1137-3.
- [209] Z. Niu, L. Zhang, L. Liu, B. Zhu, H. Dong, and X. Chen, "All-Solid-State Flexible Ultrathin Micro-Supercapacitors Based on Graphene," *Adv. Mater.*, vol. 25, no. 29, pp. 4035–4042, Aug. 2013, doi: 10.1002/adma.201301332.
- [210] N. Kurra, M. K. Hota, and H. N. Alshareef, "Conducting polymer micro-supercapacitors for flexible energy storage and Ac line-filtering," *Nano Energy*, vol. 13, pp. 500–508, Apr. 2015, doi: 10.1016/j.nanoen.2015.03.018.
- [211] R. Agrawal and C. Wang, "On-Chip Asymmetric Microsupercapacitors Combining Reduced Graphene Oxide and Manganese Oxide for High Energy-Power Tradeoff," *Micromachines*, vol. 9, no. 8, p. 399, Aug. 2018, doi: 10.3390/mi9080399.
- [212] S. Gu, Z. Lou, L. Li, Z. Chen, X. Ma, and G. Shen, "Fabrication of flexible reduced graphene oxide/Fe<sub>2</sub>O<sub>3</sub> hollow nanospheres based on-chip micro-supercapacitors for integrated photodetecting applications," *Nano Res.*, vol. 9, no. 2, pp. 424–434, Feb. 2016, doi: 10.1007/s12274-015-0923-7.
- [213] M. Tahir *et al.*, "Co-Electrodeposited porous PEDOT–CNT microelectrodes for integrated micro-supercapacitors with high energy density, high rate capability, and long cycling life," *Nanoscale*, vol. 11, no. 16, pp. 7761–7770, 2019, doi: 10.1039/C9NR00765B.
- [214] X. Feng *et al.*, "Ultrahigh-rate and high-frequency MXene micro-supercapacitors for kHz AC line-filtering," *Journal of Energy Chemistry*, vol. 69, pp. 1–8, Jun. 2022, doi: 10.1016/j.jechem.2021.11.012.
- [215] X. Wang and Q. Zhang, "Recent progress on laser fabrication of on-chip microsupercapacitors," *Journal of Energy Storage*, vol. 34, p. 101994, Feb. 2021, doi: 10.1016/j.est.2020.101994.
- [216] J. B. In *et al.*, "Facile fabrication of flexible all solid-state micro-supercapacitor by direct laser writing of porous carbon in polyimide," *Carbon*, vol. 83, pp. 144–151, Mar. 2015, doi: 10.1016/j.carbon.2014.11.017.
- [217] Y. Chen *et al.*, "Enhanced electrochemical performance of laser scribed graphene films decorated with manganese dioxide nanoparticles," *J Mater Sci: Mater Electron*, vol. 27, no. 3, pp. 2564–2573, Mar. 2016, doi: 10.1007/s10854-015-4059-z.

## Bibliography

---

- [218] M. F. El-Kady, V. Strong, S. Dubin, and R. B. Kaner, "Laser Scribing of High-Performance and Flexible Graphene-Based Electrochemical Capacitors," *Science*, vol. 335, no. 6074, pp. 1326–1330, Mar. 2012, doi: 10.1126/science.1216744.
- [219] B. Xie *et al.*, "Laser-processed graphene based micro-supercapacitors for ultrathin, rollable, compact and designable energy storage components," *Nano Energy*, vol. 26, pp. 276–285, Aug. 2016, doi: 10.1016/j.nanoen.2016.04.045.
- [220] R. Kumar *et al.*, "Fabrication of interdigitated micro-supercapacitor devices by direct laser writing onto ultra-thin, flexible and free-standing graphite oxide films," *RSC Adv.*, vol. 6, no. 88, pp. 84769–84776, 2016, doi: 10.1039/C6RA17516C.
- [221] V. Mishukova *et al.*, "Facile fabrication of graphene-based high-performance microsupercapacitors operating at a high temperature of 150 °C," *Nanoscale Adv.*, vol. 3, no. 16, pp. 4674–4679, 2021, doi: 10.1039/D1NA00220A.
- [222] L. Liu, H.-Y. Li, Y. Yu, L. Liu, and Y. Wu, "Silver nanowires as the current collector for a flexible in-plane micro-supercapacitor via a one-step, mask-free patterning strategy," *Nanotechnology*, vol. 29, no. 5, p. 055401, Feb. 2018, doi: 10.1088/1361-6528/aa9aaf.
- [223] L. Liu, D. Ye, Y. Yu, L. Liu, and Y. Wu, "Carbon-based flexible micro-supercapacitor fabrication via mask-free ambient micro-plasma-jet etching," *Carbon*, vol. 111, pp. 121–127, Jan. 2017, doi: 10.1016/j.carbon.2016.09.037.
- [224] H.-H. Chien *et al.*, "Nitrogen DC-pulse atmospheric-pressure-plasma jet (APPJ)-processed reduced graphene oxide (rGO)-carbon black (CB) nanocomposite electrodes for supercapacitor applications," *Diamond and Related Materials*, vol. 88, pp. 23–31, Sep. 2018, doi: 10.1016/j.diamond.2018.06.019.
- [225] Z. Wu, K. Parvez, X. Feng, and K. Müllen, "Graphene-based in-plane micro-supercapacitors with high power and energy densities," *Nat Commun*, vol. 4, no. 1, p. 2487, Dec. 2013, doi: 10.1038/ncomms3487.
- [226] C. J. Zhang *et al.*, "Stamping of Flexible, Coplanar Micro-Supercapacitors Using MXene Inks," *Adv. Funct. Mater.*, vol. 28, no. 9, p. 1705506, Feb. 2018, doi: 10.1002/adfm.201705506.
- [227] F. Li *et al.*, "Stamping Fabrication of Flexible Planar Micro-Supercapacitors Using Porous Graphene Inks," *Advanced Science*, vol. 7, no. 19, p. 2001561, Oct. 2020, doi: 10.1002/advs.202001561.
- [228] L. Jia, Y. Shi, Q. Zhang, and X. Xu, "Green synthesis of ultrafine Methyl-cellulose-derived porous carbon/MnO<sub>2</sub> nanowires for asymmetric supercapacitors and flexible pattern stamping," *Applied Surface Science*, vol. 462, pp. 923–931, Dec. 2018, doi: 10.1016/j.apsusc.2018.08.213.
- [229] Y. Chen, X. Li, Z. Bi, G. Li, X. He, and X. Gao, "Stamp-assisted printing of nanotextured electrodes for high-performance flexible planar micro-supercapacitors," *Chemical Engineering Journal*, vol. 353, pp. 499–506, Dec. 2018, doi: 10.1016/j.cej.2018.07.158.
- [230] Y. Zhang *et al.*, "Ink formulation, scalable applications and challenging perspectives of screen printing for emerging printed microelectronics," *Journal of Energy Chemistry*, vol. 63, pp. 498–513, Dec. 2021, doi: 10.1016/j.jechem.2021.08.011.
- [231] X. Lin *et al.*, "Screen-printed water-based conductive ink on stretchable fabric for wearable micro-supercapacitor," *Materials Today Chemistry*, vol. 30, p. 101529, Jun. 2023, doi: 10.1016/j.mtchem.2023.101529.
- [232] S. Bellani *et al.*, "Scalable Production of Graphene Inks via Wet-Jet Milling Exfoliation for Screen-Printed Micro-Supercapacitors," *Adv. Funct. Mater.*, vol. 29, no. 14, p. 1807659, Apr. 2019, doi: 10.1002/adfm.201807659.

- [233] J. P. Mensing, T. Lomas, and A. Tuantranont, "2D and 3D printing for graphene based supercapacitors and batteries: A review," *Sustainable Materials and Technologies*, vol. 25, p. e00190, Sep. 2020, doi: 10.1016/j.susmat.2020.e00190.
- [234] O. A. Moses *et al.*, "2D materials inks toward smart flexible electronics," *Materials Today*, vol. 50, pp. 116–148, Nov. 2021, doi: 10.1016/j.mattod.2021.08.010.
- [235] H. Li and J. Liang, "Recent Development of Printed Micro-Supercapacitors: Printable Materials, Printing Technologies, and Perspectives," *Adv. Mater.*, vol. 32, no. 3, p. 1805864, Jan. 2020, doi: 10.1002/adma.201805864.
- [236] Q. Zhang, L. Huang, Q. Chang, W. Shi, L. Shen, and Q. Chen, "Gravure-printed interdigital microsupercapacitors on a flexible polyimide substrate using crumpled graphene ink," *Nanotechnology*, vol. 27, no. 10, p. 105401, Mar. 2016, doi: 10.1088/0957-4484/27/10/105401.
- [237] Y. Xiao, L. Huang, Q. Zhang, S. Xu, Q. Chen, and W. Shi, "Gravure printing of hybrid MoS<sub>2</sub>@S-rGO interdigitated electrodes for flexible microsupercapacitors," *Appl. Phys. Lett.*, vol. 107, no. 1, p. 013906, Jul. 2015, doi: 10.1063/1.4926570.
- [238] J. Sun *et al.*, "Printable Nanomaterials for the Fabrication of High-Performance Supercapacitors," *Nanomaterials*, vol. 8, no. 7, p. 528, Jul. 2018, doi: 10.3390/nano8070528.
- [239] Y.-Y. Peng *et al.*, "All-MXene (2D titanium carbide) solid-state microsupercapacitors for on-chip energy storage," *Energy Environ. Sci.*, vol. 9, no. 9, pp. 2847–2854, 2016, doi: 10.1039/C6EE01717G.
- [240] Y. Lei, W. Zhao, Y. Zhu, U. Buttner, X. Dong, and H. N. Alshareef, "Three-Dimensional Ti<sub>3</sub>C<sub>2</sub>T<sub>x</sub> MXene-Prussian Blue Hybrid Microsupercapacitors by Water Lift-Off Lithography," *ACS Nano*, vol. 16, no. 2, pp. 1974–1985, Feb. 2022, doi: 10.1021/acsnano.1c06552.
- [241] Q. Jiang *et al.*, "MXene electrochemical microsupercapacitor integrated with triboelectric nanogenerator as a wearable self-charging power unit," *Nano Energy*, vol. 45, pp. 266–272, Mar. 2018, doi: 10.1016/j.nanoen.2018.01.004.
- [242] J. Li *et al.*, "MXene-conducting polymer electrochromic microsupercapacitors," *Energy Storage Materials*, vol. 20, pp. 455–461, Jul. 2019, doi: 10.1016/j.ensm.2019.04.028.
- [243] Z. Xiong *et al.*, "A Dynamic Graphene Oxide Network Enables Spray Printing of Colloidal Gels for High-Performance Micro-Supercapacitors," *Adv. Mater.*, vol. 31, no. 16, p. 1804434, Apr. 2019, doi: 10.1002/adma.201804434.
- [244] L. Zhou, J. Fu, and Y. He, "A Review of 3D Printing Technologies for Soft Polymer Materials," *Adv. Funct. Mater.*, vol. 30, no. 28, p. 2000187, Jul. 2020, doi: 10.1002/adfm.202000187.
- [245] K. Ghosh and M. Pumera, "MXene and MoS<sub>3-x</sub> Coated 3D-Printed Hybrid Electrode for Solid-State Asymmetric Supercapacitor," *Small Methods*, vol. 5, no. 8, p. 2100451, Aug. 2021, doi: 10.1002/smtd.202100451.
- [246] C. W. Foster *et al.*, "3D Printed Graphene Based Energy Storage Devices," *Sci Rep*, vol. 7, no. 1, p. 42233, Mar. 2017, doi: 10.1038/srep42233.
- [247] B. Lu, X. Jin, Q. Han, and L. Qu, "Planar Graphene-Based Microsupercapacitors," *Small*, vol. 17, no. 48, p. 2006827, Dec. 2021, doi: 10.1002/smll.202006827.
- [248] Y. Wang, Y.-Z. Zhang, D. Dubbink, and J. E. Ten Elshof, "Inkjet printing of δ-MnO<sub>2</sub> nanosheets for flexible solid-state micro-supercapacitor," *Nano Energy*, vol. 49, pp. 481–488, Jul. 2018, doi: 10.1016/j.nanoen.2018.05.002.
- [249] J. Li *et al.*, "Scalable Fabrication and Integration of Graphene Microsupercapacitors through Full Inkjet Printing," *ACS Nano*, vol. 11, no. 8, pp. 8249–8256, Aug. 2017, doi: 10.1021/acsnano.7b03354.
- [250] D. Pech *et al.*, "Elaboration of a microstructured inkjet-printed carbon electrochemical capacitor," *Journal of Power Sources*, vol. 195, no. 4, pp. 1266–1269, Feb. 2010, doi: 10.1016/j.jpowsour.2009.08.085.



## Bibliography

---

- [251] J. Ma *et al.*, "Aqueous MXene/PH1000 Hybrid Inks for Inkjet-Printing Micro-Supercapacitors with Unprecedented Volumetric Capacitance and Modular Self-Powered Microelectronics," *Adv. Energy Mater.*, vol. 11, no. 23, p. 2100746, Jun. 2021, doi: 10.1002/aenm.202100746.
- [252] J. Li, V. Mishukova, and M. Östling, "All-solid-state micro-supercapacitors based on inkjet printed graphene electrodes," *Appl. Phys. Lett.*, vol. 109, no. 12, p. 123901, Sep. 2016, doi: 10.1063/1.4962728.
- [253] P. Giannakou, M. G. Masteghin, R. C. T. Slade, S. J. Hinder, and M. Shkunov, "Energy storage on demand: ultra-high-rate and high-energy-density inkjet-printed NiO micro-supercapacitors," *J. Mater. Chem. A*, vol. 7, no. 37, pp. 21496–21506, 2019, doi: 10.1039/C9TA07878A.
- [254] Y. Bräuniger, S. Lochmann, J. Grothe, M. Hantusch, and S. Kaskel, "Piezoelectric Inkjet Printing of Nanoporous Carbons for Micro-supercapacitor Devices," *ACS Appl. Energy Mater.*, vol. 4, no. 2, pp. 1560–1567, Feb. 2021, doi: 10.1021/acsaem.0c02745.
- [255] L. T. Le, M. H. Ervin, H. Qiu, B. E. Fuchs, and W. Y. Lee, "Graphene supercapacitor electrodes fabricated by inkjet printing and thermal reduction of graphene oxide," *Electrochemistry Communications*, vol. 13, no. 4, pp. 355–358, Apr. 2011, doi: 10.1016/j.elecom.2011.01.023.
- [256] J. Malda *et al.*, "25th Anniversary Article: Engineering Hydrogels for Biofabrication," *Adv. Mater.*, vol. 25, no. 36, pp. 5011–5028, Sep. 2013, doi: 10.1002/adma.201302042.
- [257] X. Li, H. Li, X. Fan, X. Shi, and J. Liang, "3D-Printed Stretchable Micro-Supercapacitor with Remarkable Areal Performance," *Adv. Energy Mater.*, vol. 10, no. 14, p. 1903794, Apr. 2020, doi: 10.1002/aenm.201903794.
- [258] K. Tang *et al.*, "3D printed hybrid-dimensional electrodes for flexible micro-supercapacitors with superior electrochemical behaviours," *Virtual and Physical Prototyping*, vol. 15, no. sup1, pp. 511–519, Dec. 2020, doi: 10.1080/17452759.2020.1842619.
- [259] X. Yun *et al.*, "Direct 3D printing of a graphene oxide hydrogel for fabrication of a high areal specific capacitance microsupercapacitor," *RSC Adv.*, vol. 9, no. 50, pp. 29384–29395, 2019, doi: 10.1039/C9RA04882K.
- [260] J. Orangi, F. Hamade, V. A. Davis, and M. Beidaghi, "3D Printing of Additive-Free 2D  $\text{Ti}_3\text{C}_2\text{T}_x$  (MXene) Ink for Fabrication of Micro-Supercapacitors with Ultra-High Energy Densities," *ACS Nano*, vol. 14, no. 1, pp. 640–650, Jan. 2020, doi: 10.1021/acsnano.9b07325.
- [261] Z. Wang *et al.*, "Three-Dimensional Printing of Polyaniline/Reduced Graphene Oxide Composite for High-Performance Planar Supercapacitor," *ACS Appl. Mater. Interfaces*, vol. 10, no. 12, pp. 10437–10444, Mar. 2018, doi: 10.1021/acsaami.7b19635.
- [262] X. Tian *et al.*, "Boosting capacitive charge storage of 3D-printed micro-pseudocapacitors via rational holey graphene engineering," *Carbon*, vol. 155, pp. 562–569, Dec. 2019, doi: 10.1016/j.carbon.2019.08.089.
- [263] W. Yu, H. Zhou, B. Q. Li, and S. Ding, "3D Printing of Carbon Nanotubes-Based Microsupercapacitors," *ACS Appl. Mater. Interfaces*, vol. 9, no. 5, pp. 4597–4604, Feb. 2017, doi: 10.1021/acsaami.6b13904.
- [264] X. Li, S. Ling, W. Cao, L. Zeng, R. Yuan, and C. Zhang, "Surface-Adaptive Capillarity Enabling Densified 3D Printing for Ultra-High Areal and Volumetric Energy Density Supercapacitors," *Angewandte Chemie*, vol. 134, no. 24, Jun. 2022, doi: 10.1002/ange.202202663.
- [265] X. Aeby, A. Poulin, G. Siqueira, M. K. Hausmann, and G. Nyström, "Fully 3D Printed and Disposable Paper Supercapacitors," *Adv. Mater.*, vol. 33, no. 26, p. 2101328, Jul. 2021, doi: 10.1002/adma.202101328.
- [266] J. W. Goodwin and R. W. Hughes, *Rheology for Chemists: An Introduction*. The Royal Society of Chemistry, 2008. [Online]. Available: <https://doi.org/10.1039/9781847558046>
- [267] J. De Vicente, Ed., *Rheology*. InTech, 2012. doi: 10.5772/2065.

- [268] Y. Y. Hou and H. O. Kassim, "Instrument techniques for rheometry," *Review of Scientific Instruments*, vol. 76, no. 10, p. 101101, Oct. 2005, doi: 10.1063/1.2085048.
- [269] L. del-Mazo-Barbara and M.-P. Ginebra, "Rheological characterisation of ceramic inks for 3D direct ink writing: A review," *Journal of the European Ceramic Society*, vol. 41, no. 16, pp. 18–33, Dec. 2021, doi: 10.1016/j.jeurceramsoc.2021.08.031.
- [270] J. Yan *et al.*, "Direct-ink writing 3D printed energy storage devices: From material selectivity, design and optimization strategies to diverse applications," *Materials Today*, vol. 54, pp. 110–152, Apr. 2022, doi: 10.1016/j.mattod.2022.03.014.
- [271] B. R. Gupta, *Rheology Applied in Polymer Processing*, 1st ed. London: CRC Press, 2022. doi: 10.1201/9781003344971.
- [272] J. Mewis and N. J. Wagner, *Colloidal Suspension Rheology*, 1st ed. Cambridge University Press, 2011. doi: 10.1017/CBO9780511977978.
- [273] M. Li *et al.*, "3D Printed Supercapacitor: Techniques, Materials, Designs, and Applications," *Adv Funct Materials*, vol. 33, no. 1, p. 2208034, Jan. 2023, doi: 10.1002/adfm.202208034.
- [274] S. Tagliaferri, A. Panagiotopoulos, and C. Mattevi, "Direct ink writing of energy materials," *Materials Advances*, no. 2, pp. 540–563, 2021, doi: <https://doi.org/10.1039/D0MA00753F>.
- [275] W. Li *et al.*, "Printing assembly and structural regulation of graphene towards three-dimensional flexible micro-supercapacitors," *J. Mater. Chem. A*, vol. 5, no. 31, pp. 16281–16288, 2017, doi: 10.1039/C7TA02041D.
- [276] A. Hodaei *et al.*, "Single Additive Enables 3D Printing of Highly Loaded Iron Oxide Suspensions," *ACS Appl. Mater. Interfaces*, vol. 10, no. 11, pp. 9873–9881, Mar. 2018, doi: 10.1021/acsami.8b00551.
- [277] N. Fazeli, E. Arefian, S. Irani, A. Ardeshiryajimi, and E. Seyedjafari, "3D-Printed PCL Scaffolds Coated with Nanobioceramics Enhance Osteogenic Differentiation of Stem Cells," *ACS Omega*, vol. 6, no. 51, pp. 35284–35296, Dec. 2021, doi: 10.1021/acsomega.1c04015.
- [278] W. Liu *et al.*, "Rapid Continuous Multimaterial Extrusion Bioprinting," *Adv. Mater.*, vol. 29, no. 3, p. 1604630, Jan. 2017, doi: 10.1002/adma.201604630.
- [279] A. K. Miri *et al.*, "Microfluidics-Enabled Multimaterial Maskless Stereolithographic Bioprinting," *Adv. Mater.*, vol. 30, no. 27, p. 1800242, Jul. 2018, doi: 10.1002/adma.201800242.
- [280] L. Ouyang, C. B. Highley, W. Sun, and J. A. Burdick, "A Generalizable Strategy for the 3D Bioprinting of Hydrogels from Nonviscous Photo-crosslinkable Inks," *Adv. Mater.*, vol. 29, no. 8, p. 1604983, Feb. 2017, doi: 10.1002/adma.201604983.
- [281] A. A. Szklanny *et al.*, "3D Bioprinting of Engineered Tissue Flaps with Hierarchical Vessel Networks (VesselNet) for Direct Host-To-Implant Perfusion," *Advanced Materials*, vol. 33, no. 42, p. 2102661, Oct. 2021, doi: 10.1002/adma.202102661.
- [282] J. Park, Y. S. Kim, S. J. Sung, T. Kim, and C. R. Park, "Highly dispersible edge-selectively oxidized graphene with improved electrical performance," *Nanoscale*, vol. 9, no. 4, pp. 1699–1708, 2017, doi: 10.1039/C6NR05902C.
- [283] F. Tarannum *et al.*, "Chemically Edge-Carboxylated Graphene Enhances the Thermal Conductivity of Polyetherimide–Graphene Nanocomposites," *ACS Appl. Mater. Interfaces*, vol. 14, no. 12, pp. 14753–14763, Mar. 2022, doi: 10.1021/acsami.1c25279.
- [284] L. Wei *et al.*, "Spontaneous intercalation of long-chain alkyl ammonium into edge-selectively oxidized graphite to efficiently produce high-quality graphene," *Sci Rep*, vol. 3, no. 1, p. 2636, Dec. 2013, doi: 10.1038/srep02636.
- [285] A. Reina *et al.*, "Large Area, Few-Layer Graphene Films on Arbitrary Substrates by Chemical Vapor Deposition," *Nano Lett.*, vol. 9, no. 1, pp. 30–35, Jan. 2009, doi: 10.1021/nl801827v.

## Bibliography

---

- [286] L. M. Malard, M. A. Pimenta, G. Dresselhaus, and M. S. Dresselhaus, "Raman spectroscopy in graphene," *Physics Reports*, vol. 473, no. 5–6, pp. 51–87, Apr. 2009, doi: 10.1016/j.physrep.2009.02.003.
- [287] S. Villar-Rodil, Juan. I. Paredes, A. Martínez-Alonso, and Juan. M. D. Tascón, "Preparation of graphene dispersions and graphene-polymer composites in organic media," *J. Mater. Chem.*, vol. 19, no. 22, p. 3591, 2009, doi: 10.1039/b904935e.
- [288] R. Blume, D. Rosenthal, J.-P. Tessonnier, H. Li, A. Knop-Gericke, and R. Schlögl, "Characterizing Graphitic Carbon with X-ray Photoelectron Spectroscopy: A Step-by-Step Approach," *ChemCatChem*, vol. 7, no. 18, pp. 2871–2881, Sep. 2015, doi: 10.1002/cctc.201500344.
- [289] A. Lerf, H. He, M. Forster, and J. Klinowski, "Structure of Graphite Oxide Revisited," *J. Phys. Chem. B*, vol. 102, no. 23, pp. 4477–4482, Jun. 1998, doi: 10.1021/jp9731821.
- [290] A. S. Dezfuli, M. R. Ganjali, H. R. Naderi, and P. Norouzi, "A high performance supercapacitor based on a ceria/graphene nanocomposite synthesized by a facile sonochemical method," *RSC Adv.*, vol. 5, no. 57, pp. 46050–46058, 2015, doi: 10.1039/C5RA02957K.
- [291] D. Joung, V. Singh, S. Park, A. Schulte, S. Seal, and S. I. Khondaker, "Anchoring Ceria Nanoparticles on Reduced Graphene Oxide and Their Electronic Transport Properties," *J. Phys. Chem. C*, vol. 115, no. 50, pp. 24494–24500, Dec. 2011, doi: 10.1021/jp206485v.
- [292] R. S. Kalubarme, Y.-H. Kim, and C.-J. Park, "One step hydrothermal synthesis of a carbon nanotube/cerium oxide nanocomposite and its electrochemical properties," *Nanotechnology*, vol. 24, no. 36, p. 365401, Sep. 2013, doi: 10.1088/0957-4484/24/36/365401.
- [293] M. R. Khawar *et al.*, "Cerium oxide nanosheets-based tertiary composites (CeO<sub>2</sub>/ZnO/ZnWO<sub>4</sub>) for supercapattery application and evaluation of faradic & non-faradic capacitive distribution by using Donn's model," *Journal of Energy Storage*, vol. 55, p. 105778, Nov. 2022, doi: 10.1016/j.est.2022.105778.
- [294] M. E. Khan, M. M. Khan, and M. H. Cho, "Ce<sup>3+</sup>-ion, Surface Oxygen Vacancy, and Visible Light-induced Photocatalytic Dye Degradation and Photocapacitive Performance of CeO<sub>2</sub>-Graphene Nanostructures," *Sci Rep*, vol. 7, no. 1, p. 5928, Dec. 2017, doi: 10.1038/s41598-017-06139-6.
- [295] J. W. Kim, V. Augustyn, and B. Dunn, "The Effect of Crystallinity on the Rapid Pseudocapacitive Response of Nb<sub>2</sub>O<sub>5</sub>," *Adv. Energy Mater.*, vol. 2, no. 1, pp. 141–148, Jan. 2012, doi: 10.1002/aenm.201100494.
- [296] T. Brezesinski, J. Wang, S. H. Tolbert, and B. Dunn, "Ordered mesoporous  $\alpha$ -MoO<sub>3</sub> with iso-oriented nanocrystalline walls for thin-film pseudocapacitors," *Nature Mater*, vol. 9, no. 2, pp. 146–151, Feb. 2010, doi: 10.1038/nmat2612.
- [297] A. Chortos, E. Hajesmaili, J. Morales, D. R. Clarke, and J. A. Lewis, "3D Printing of Interdigitated Dielectric Elastomer Actuators," *Adv. Funct. Mater.*, vol. 30, no. 1, p. 1907375, Jan. 2020, doi: 10.1002/adfm.201907375.
- [298] T. Wei, B. Y. Ahn, J. Grotto, and J. A. Lewis, "3D Printing of Customized Li-Ion Batteries with Thick Electrodes," *Adv. Mater.*, vol. 30, no. 16, p. 1703027, Apr. 2018, doi: 10.1002/adma.201703027.
- [299] S. Naficy *et al.*, "Graphene oxide dispersions: tuning rheology to enable fabrication," *Mater. Horiz.*, vol. 1, no. 3, pp. 326–331, 2014, doi: 10.1039/C3MH00144J.
- [300] J. Wang, J. Polleux, J. Lim, and B. Dunn, "Pseudocapacitive Contributions to Electrochemical Energy Storage in TiO<sub>2</sub> (Anatase) Nanoparticles," *J. Phys. Chem. C*, vol. 111, no. 40, pp. 14925–14931, Oct. 2007, doi: 10.1021/jp074464w.
- [301] O. Ghodbane, J.-L. Pascal, and F. Favier, "Microstructural Effects on Charge-Storage Properties in MnO<sub>2</sub>-Based Electrochemical Supercapacitors," *ACS Appl. Mater. Interfaces*, vol. 1, no. 5, pp. 1130–1139, May 2009, doi: 10.1021/am900094e.

- [302] L. Jiang *et al.*, "Controlled Synthesis of CeO<sub>2</sub>/Graphene Nanocomposites with Highly Enhanced Optical and Catalytic Properties," *J. Phys. Chem. C*, vol. 116, no. 21, pp. 11741–11745, May 2012, doi: 10.1021/jp3015113.
- [303] N. J. Lawrence *et al.*, "Defect Engineering in Cubic Cerium Oxide Nanostructures for Catalytic Oxidation," *Nano Lett.*, vol. 11, no. 7, pp. 2666–2671, Jul. 2011, doi: 10.1021/nl200722z.
- [304] H. Lindström *et al.*, "Li<sup>+</sup> Ion Insertion in TiO<sub>2</sub> (Anatase). 2. Voltammetry on Nanoporous Films," *J. Phys. Chem. B*, vol. 101, no. 39, pp. 7717–7722, Sep. 1997, doi: 10.1021/jp970490q.
- [305] S. Fleischmann *et al.*, "Pseudocapacitance: From Fundamental Understanding to High Power Energy Storage Materials," *Chem. Rev.*, vol. 120, no. 14, pp. 6738–6782, Jul. 2020, doi: 10.1021/acs.chemrev.0c00170.
- [306] Y. Wang *et al.*, "Direct Graphene-Carbon Nanotube Composite Ink Writing All-Solid-State Flexible Microsupercapacitors with High Areal Energy Density," *Adv. Funct. Mater.*, vol. 30, no. 16, p. 1907284, Apr. 2020, doi: 10.1002/adfm.201907284.
- [307] Z. Peng *et al.*, "Flexible Boron-Doped Laser-Induced Graphene Microsupercapacitors," *ACS Nano*, vol. 9, no. 6, pp. 5868–5875, Jun. 2015, doi: 10.1021/acsnano.5b00436.
- [308] L. Liu *et al.*, "All-Printed Solid-State Microsupercapacitors Derived from Self-Template Synthesis of Ag@PPy Nanocomposites," *Adv. Mater. Technol.*, vol. 3, no. 1, p. 1700206, Jan. 2018, doi: 10.1002/admt.201700206.
- [309] S. Zhu, Y. Li, H. Zhu, J. Ni, and Y. Li, "Pencil-Drawing Skin-Mountable Micro-Supercapacitors," *Small*, vol. 15, no. 3, p. 1804037, Jan. 2019, doi: 10.1002/smll.201804037.
- [310] E. Paparazzo, "Use and mis-use of x-ray photoemission spectroscopy Ce3d spectra of Ce<sub>2</sub>O<sub>3</sub> and CeO<sub>2</sub>," *J. Phys.: Condens. Matter*, vol. 30, no. 34, p. 343003, Aug. 2018, doi: 10.1088/1361-648X/aad248.
- [311] S. Ardizzone, G. Fregonara, and S. Trasatti, "'Inner' and 'outer' active surface of RuO<sub>2</sub> electrodes," *Electrochimica Acta*, vol. 35, no. 1, pp. 263–267, Jan. 1990, doi: 10.1016/0013-4686(90)85068-X.
- [312] P. Cabanach *et al.*, "Zwitterionic 3D-Printed Non-Immunogenic Stealth Microrobots," *Adv. Mater.*, vol. 32, no. 42, p. 2003013, Oct. 2020, doi: 10.1002/adma.202003013.
- [313] Y. Fang *et al.*, "3D Printing of Cell-Laden Microgel-Based Biphasic Bioink with Heterogeneous Microenvironment for Biomedical Applications," *Adv Funct Materials*, vol. 32, no. 13, p. 2109810, Mar. 2022, doi: 10.1002/adfm.202109810.
- [314] G. Cidonio, M. Glinka, J. I. Dawson, and R. O. C. Oreffo, "The cell in the ink: Improving biofabrication by printing stem cells for skeletal regenerative medicine," *Biomaterials*, vol. 209, pp. 10–24, Jul. 2019, doi: 10.1016/j.biomaterials.2019.04.009.
- [315] K. Huang *et al.*, "Anisotropy of graphene scaffolds assembled by three-dimensional printing," *Carbon*, vol. 130, pp. 1–10, Apr. 2018, doi: 10.1016/j.carbon.2017.12.120.
- [316] M. Zhang *et al.*, "Spontaneous Alignment of Graphene Oxide in Hydrogel during 3D Printing for Multistimuli-Responsive Actuation," *Adv. Sci.*, vol. 7, no. 6, p. 1903048, Mar. 2020, doi: 10.1002/advs.201903048.
- [317] B. Zhou *et al.*, "Controlling surface porosity of graphene-based printed aerogels," *npj 2D Mater Appl*, vol. 6, no. 1, p. 34, May 2022, doi: 10.1038/s41699-022-00312-w.
- [318] C. Zhang *et al.*, "Additive-free MXene inks and direct printing of micro-supercapacitors," *Nat Commun*, vol. 10, no. 1, p. 1795, Dec. 2019, doi: 10.1038/s41467-019-09398-1.
- [319] X. Tang *et al.*, "Generalized 3D Printing of Graphene-Based Mixed-Dimensional Hybrid Aerogels," *ACS Nano*, vol. 12, no. 4, pp. 3502–3511, Apr. 2018, doi: 10.1021/acsnano.8b00304.



# Amin Hodaei

Route Cantonale 25, CH-1025 St-Sulpice (Vaud)

Phone: +41787940202

amin.hodaei@epfl.ch

amin.hodaei@gmail.com

Work Permit B (avec activité)



## Areas of Research Competence

---

- Advanced Fabrication of Miniaturized Energy Storage Systems, Advanced Material Development and Characterization (Ceramics, Polymers, and Ceramic-based Composites), Precision Fabrication
- Young materials scientist with extensive working experience on synthesis and colloidal processing of inorganic nanoparticles, fabrication of electrochemical energy devices, ink formulations (ceramic- and composite-based) for additive fabrication of electronic and microelectrochemical systems with complex structures

## Education

---

- **Swiss Federal Institute of Technology in Lausanne (EPFL), Lausanne, Switzerland**  
PhD in Materials Science & Engineering (2018 – 2023)
- **Sabanci University, Istanbul, Turkey**  
MSc in Materials Science & Engineering (2015 – 2018)
- **University of Tehran, Tehran, Iran**  
BSc in Metallurgical & Materials Engineering (2010 – 2015)

## Professional Experiences

---

### Doctoral Research Assistant

Laboratory for Advanced Fabrication Technologies (LAFT), EPFL, Switzerland

**Thesis:** Additive fabrication of microsupercapacitors

**Supervisor:** Prof. Vivek Subramanian

Full additive fabrication of millimeter-scale high-performance microsupercapacitors (smallest with the best performance in the world), by design, synthesis, and formulation of novel inks for their components, i.e., electrodes, electrolytes, and current collectors — performing electro-chemical, rheological, spectroscopic (e.g., Raman and XPS) characterizations, in addition to scanning and transmission electron microscopy

### **Graduate Research Assistant**

Sabanci University, Istanbul, Turkey

**Thesis:** Synthesis and characterization of grafted copolymers as rheology modifiers for the preparation of highly loaded ceramic inks for 3D printing

**Supervisor:** Prof. Ozge Akbulut

Synthesis, characterization, and optimization of grafted copolymers to be used as rheology modifiers for preparation of highly loaded ceramic inks (e.g. iron oxide, alumina, barium titanate — ink formulations and 3D printing functional systems with intricate 3D structures thereof with optimized performance

### **Undergraduate Research Assistant**

Magnetic Materials Laboratory, University of Tehran, Tehran, Iran

**Thesis:** Intermediate milling energy optimization to enhance the characteristics of barium hexaferrite magnetic nanoparticles

**Supervisor:** Prof. Abolghasem Ataie

Mechanochemical Synthesis of barium hexaferrite nanoparticles and investigating of the effect of mechanical milling energy on structural, morphological, and compositional characteristics of barium hexaferrite nanoparticles using electron microscopy, X-ray diffraction, thermal (e.g., DTA/TGA) and magnetic (e.g., VSM) characterization techniques

### **Patent(s)**

---

- US10954377B2- “An admixture and ink comprising such admixture”

Inventors: Ozge Akbulut, Omid Akhlaghi, **Amin Hodaei**, Dilek Sezer (published 03/2021)

### **Special Courses and Certificates**

---

- Innosuisse Start-up Training: Business Concept, EPFL, Lausanne, Switzerland (2018)
- PRINCE2 Project Management training (2023)

### **Honors and Awards**

---

- One of the two delegates of Swiss Chemical Society (SCS) to the European Young Chemists' Network (EYCN), (12/2018 – 12/2019).
- Full Scholarship throughout MSc study covering full tuition fee exemption, monthly stipend, and dormitory support, Sabanci University, Istanbul, Turkey, 2015.
- Ranked within the top 1% among 317,605 participants of the Iranian University Entrance Exam (Physics and Math), Ministry of Education, Iran, 2010.

## Publications and Presentations

---

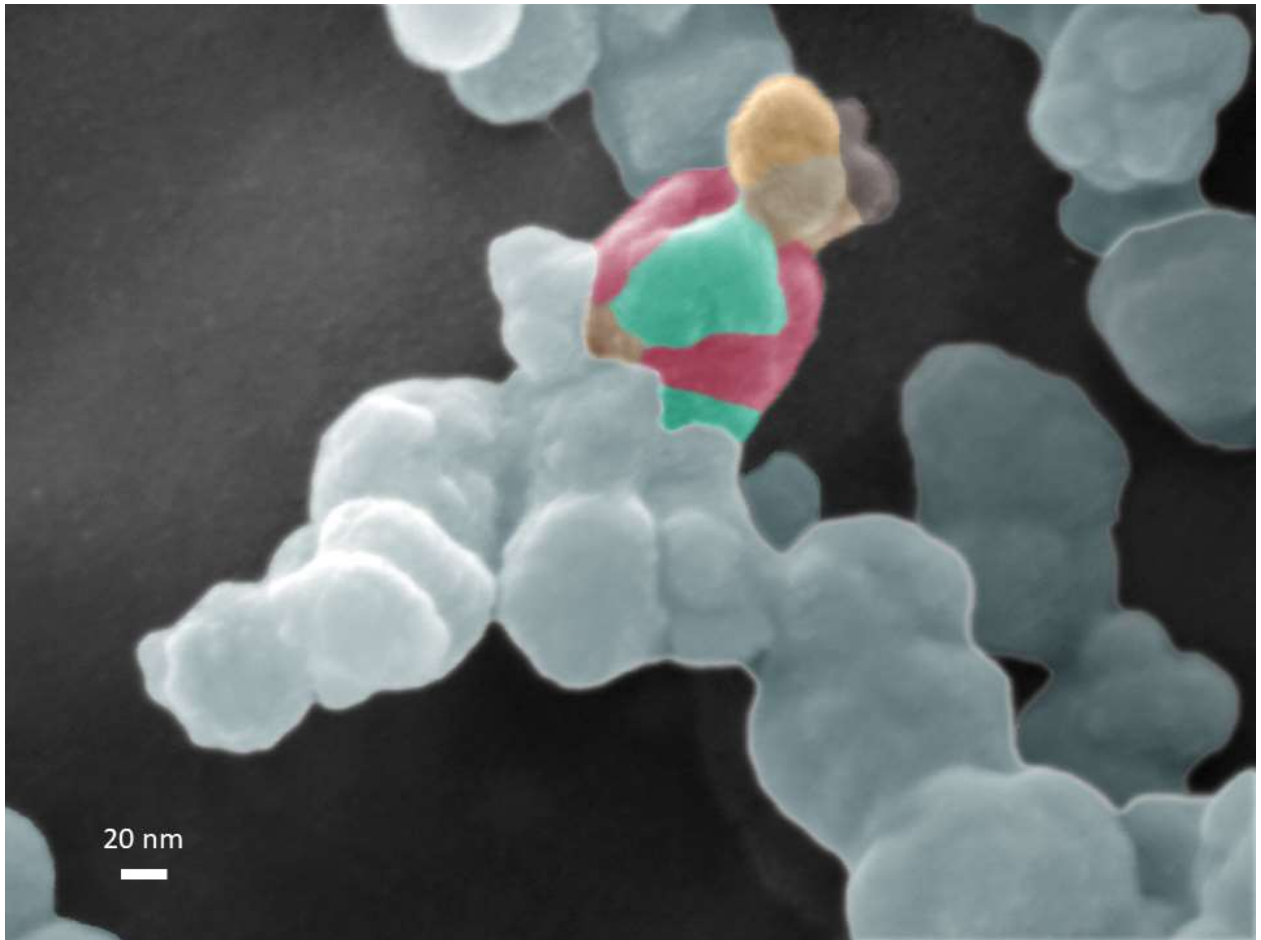
- **Hodaei, A.**, Subramanian, V., “Additive Fabrication of Fully-integrated High-Performance Millimeter-Scale Microsupercapacitors: Fine-Tuning Chemistry to Maximize Performance”, (under review), 2023.
- **Hodaei, A.**, Subramanian, V., “Sub-mm<sup>3</sup> Dimensional Scaling of Additively Fabricated Microsupercapacitors for Embedded Energy Applications”, 23<sup>rd</sup> IEEE International Conference on Nanotechnology (IEEE-NANO 2023), Jeju Island, Korea, July 2023.
- **Hodaei, A.**, Subramanian, V., “All-Additively-Fabricated Microsupercapacitors: Fine-Tuning Chemistry to Maximize Performance”, EMRS Spring Meeting, Strasbourg, France, May/June 2023.
- **Hodaei, A.**, Subramanian, V., “Sub-mm<sup>3</sup> Dimensional Scaling of All-Additively-Fabricated Microsupercapacitors”, (submitted), 2023.
- Goharibajestani, Z., Akhlaghi, O., Akaoglu, C., Afghah, F., Khani, N., **Hodaei, A.**, Koc, B., Akbulut, O. “Incorporating steric hindrance into the additive design enables a robust formulation of alumina ink for extrusion-based 3D printing”, ACS Applied Polymer Materials, 1, 12, 3279–3285 (2019).
- **Hodaei, A.**, Akhlaghi, O., Khani, N., Aytas, T., Sezer, D., Koc, B., Menciloglu, Y. Z., Akbulut, O. “Single additive enables 3D printing of highly loaded iron oxide suspensions”, ACS Applied Materials and Interfaces, 10 (11), 9873–9881 (2018).
- **Hodaei, A.**, Shiralizadeh Dezfouli, A., Naderi, H. R. “A high-performance supercapacitor based on N- doped TiO<sub>2</sub> nanoparticles”, Journal of Materials Science: Materials in Electronics, 29 (17), 14596–14604 (2018).
- Akhlaghi, O., Aytas, T., Tatli, B., Sezer, D., **Hodaei, A.**, Rosine, F. A., Scrivener, K., Akbulut, O. “Modified poly(carboxylate ether)-based superplasticizer enhances flowability of calcined clay-limestone gypsum blended cement”, Cement and Concrete Research, 101, 114–122 (2017).
- **Hodaei, A.**, Ataie, A., Mostafavi E. “Intermediate milling energy optimization to enhance the characteristics of barium hexaferrite magnetic nanoparticles”, Journal of Alloys and Compounds, 640 (15), 162–168 (2015).
- Teng, L., Zirhli, O., Ustbas, B., Sezer, D., **Hodaei, A.**, Akbulut, O., Stokes, A. A. “Towards hard and soft packaging for die-scale ICs”, MicroTech-Sensors, MEMS & Advanced Packaging, at Heriot-Watt University- Edinburgh, Scotland, March 2016 (poster presentation).

## References

---

- Prof. Vivek Subramanian ([vivek.subramanian@epfl.ch](mailto:vivek.subramanian@epfl.ch))
- Prof. Ozge Akbulut ([ozgeakbulut@sabanciuniv.edu](mailto:ozgeakbulut@sabanciuniv.edu))
- Prof. Abolghasem Ataie ([aataie@ut.ac.ir](mailto:aataie@ut.ac.ir))





**From the bottom to the skies, love is the essence. (Amin Hodaei, 2018)**

Floating on the clouds, at the bottom of the matter, two lovers united. These lovers are made up of calcium carbonate nanoparticles which have been synthesized using a microfluidic spray-drier fabricated at the Center of MicroNanoTechnology (CMi), EPFL. (<https://www.epfl.ch/research/facilities/cmi/organisation/picture-of-the-month/picture-of-the-month-honorable-runner-ups-2018/>)